

https://dspace.org/

Iinvestigation of ZnO, and AZnO and rare earth doped ZnO thin films for spectral conversion and application to solar cells

Otieno, Francis Otieno

2018

https://hdl.handle.net/10539/27141

Otieno, Francis Otieno (2018) Investigation of ZnO, AZnO and rare earth doped ZnO thin films for spectral conversion and application to solar cells,University of the Witwatersrand, Johannesburg, https://hdl.handle.net/10539/27141

Downloaded from a DSpace repository. https://dspace.org/



Investigation of ZnO, AZnO and Rare earth doped ZnO thin films for spectral conversion and application to solar cells.

By

Francis Otieno Otieno

Submitted in partial fulfillment of the requirements for the degree of

DOCTOR OF PHILOSOPHY IN PHYSICS

In the School of Physics

Faculty of Science

University of the Witwatersrand

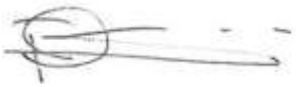
Johannesburg – South Africa

Supervisor: Prof. Daniel Wamwangi
Co-supervisor: Prof. Alexander Quandt

Declaration

I declare that "Investigation of ZnO, AZnO and Rare earth doped ZnO thin films for spectral conversion and application to solar cells." is my own, unaided work submitted at the University of the Witwatersrand, Johannesburg. And that this work has not been submitted for any degree or examination in any other institution of higher learning. Moreover, that all sources used or quoted have been indicated and acknowledged with complete references.

Name: Francis Otieno (748845)

Date: 22nd October 2018 Signature: 

Abstract

Recently Zinc oxide has drawn a resurgent attention in semiconductor industry due to its interesting properties with diverse application potential. These properties include high exciton binding energy, high resistance against radiation, high breakdown voltage, insensitivity to visible light, and easy wet chemical etching. The high quantum efficiency for emission by ZnO has seen it being considered a strong candidate for solid-state white lighting applications as well as transparent conductor electrode in solar cells.

In order to realize efficient utilization of the multi-functional properties of ZnO for electronic and opto-electric applications, ZnO is usually doped with different elements. Such doping is aimed at enhancing and controlling its electrical, optical and multi-functional properties. Typical dopants widely used are trivalent atoms categorized as group III in the periodic table (Al, In, Ga) through substitution of cations. The as-grown ZnO thin film is usually n-type semiconductor with structural, electrical and optical properties that can be varied depending on the growth conditions as well as post deposition treatment such as thermal annealing. The use of RF sputtering for ZnO deposition has been explored in this work through varying deposition time, RF power and the partial pressure of oxygen. The films were then subjected to ex-situ thermal annealing in Argon filled furnace leading to a significant increase in grain size.

Rare earth (RE) doping of materials has been widely investigated owing to the prominent and desirable optical and magnetic properties. Typically trivalent rare earths elements such as Sm^{+}, Tb^{3+} and Eu^{3+} are investigated in this research project. ZnO doped with RE has exhibited electroluminescence, thus highlighting its potential for photovoltaic applications as a bi-functional layer. A doped ZnO layer is thus simultaneously utilized as transparent conducting electrode and as a spectral conversion layer. The RE doped luminescent materials provide an opportunity to

effectively use the high energy and sub-band gap energy photons from the solar spectrum that would have otherwise been lost in direct band gap absorbers. In solar cells, they have been applied with an intention to reduce the fundamental thermalization losses arising as a result of the intrinsic properties of the semiconductor material namely: (a) sub-bandgap photon loss (b) thermalization of charge carriers resulting from absorption of high energy photons.

From the X-ray diffraction (XRD) patterns both pristine and doped ZnO thin films showed growth along the *c*-axis of the wurtzite structure. The peaks were found to match the reflection planes of (100), (002) and (102) with all the diffraction peaks being well indexed to the wurtzite structure of ZnO of the space group P63mc, which is consistent with the standard values reported in JCPDS, card no. 03-0888. The structural properties of the material were investigated using a -scanning electron microscope (SEM) and Atomic force microscopy (AFM) where the particle size, roughness, skewness and kurtosis were found to change with growth condition and annealing temperature. Most importantly, the results indicated that the photoluminescence (PL) properties reflect the quality of the pristine and doped ZnO. The films were then used in the fabrication of the solar cells as a bi-functional layer and thus as a proof of concept of good transparent conducting oxides (TCOs) and for spectral conversion. RBS measurements indicated the depth profile distribution of Zn, O and various rare earths which showed homogeneity in depth distribution without any external impurity.

Acknowledgments

All thanks and glory to Almighty God for His kind grace to grant me and my family good health and gave me the chance to start and complete the PhD degree. The strength, the patience, the capability to work all day long and long nights, the gift with insatiable desire to learn about physics complexities and to surround myself with great many people was just amazing plus many more favors makes me owe God an enormous debt of gratitude.

My sincere gratitude goes to my advisor then Dr. but now Prof. Daniel Wamwangi. Thank you for teaching and training me in thin film lab. Your kindness, patience but firm corrections made me a better person both as a researcher and personal life enabling me think critically and analyze data effectively. In deed you were more than an advisor and you will always remain a great big brother, friend and counsellor. Thank you for your steadfast belief in my ability to complete the degree even when I faced many obstacles. When I first applied to Wits for an MSc, I was twice denied an admission, but later your faith in my ability through the strong recommendation made it possible for me to be in Wits. Every time I got a chance to teach my juniors in the lab, the memory of your great depth of patience with me when I was completely green always made be a better humbled teacher. I owe a lot to you 'Ahsante sana mkubwa.'

A particular debt of gratitude goes to my co-supervisor Prof. Alex Quandt. Through you, we were able to obtain funding from MERG that always enable me to meet the harsh cost of living in Johannesburg. Your kind words and encouragement coupled with effective and prompt corrections to my work were quite instrumental in making this dream a reality. I can't fail to mention that your harsh but healthy criticism expressed using lengthy emails always made me a better person. Thanks Prof.

I wish express my deep gratitude to a number of Wits lecturers such as Prof. Neil Covile, Prof Nosipho Moloto for their encouragement, wisdom and kindness. I was indeed astounded to know

professors who meticulously care for all students in multiple aspects to achieve scientific development. Their inspiration was quite vital in making me a strong and capable man in science. Gratitude and the utmost respect to team of dedicated researchers and friends, Mr. Lesias Kotane, Mr. Ibrahim Usman, Ms Rudo Kadzutu, Ms Lerato Machogo, Ms Siziwe, Partrick Mwonga, Nhluvuko Mayimele and many others from both Wits school of Physics and Chemistry. You indeed made my time in the lab the happiest and non-forgettable moment. Thank you for your kindness and help both in and out of Wits. Together, we all have overcome many difficulties in Wits, collaborated on research projects, and shared life as graduate students. I would not have made it this far without your friendship.

I wish to express my sincere gratitude to our collaborators who gave me the much need support and exposure as well as travelling opportunities. These include Historical Museum of Physics and Study & Research Centre "Enrico Fermi", 00184 Roma, Italy, committee of the International School for Materials for Energy and Sustainability IV (ISMES IV) – Colorado school of Mines – USA and the organizing committee of the 5th School Materials for Energy and Sustainability-" and 3rd "EPS-SIF International School on Energy held at Ettore Majorana Foundation and Centre for Scientific Culture in Erice, Italy. Also special and hearty "thank you" to Giancarlo Righini, Maurizio Ferrari, Antinio Terrasi, Francesco Enrichi. Thanks so much.

Nobody has been more important to me in the pursuit of this work than the members of my family, especially my wife Dr. Mildred, my father (wuon Oluoch), my brothers (Jacktone, Mike, Leonard, Lo), sisters (Rose, Jocinter), in-laws (Annementation and mama Angelina), my pretty niece Herah and my adorable son Hawi. You all imprinted on me as an example of hard work, determination and perseverance and indeed you all deserve the most credit for your laudable sacrifice. A special thanks for your encouragement, constant support and faith in me.

To my wife Dr. Mildred, you were indeed a God sent and your coming into my life has always brought good luck. Thank you for always being there for me, for filling my heart with kind words, for praying for and with me and inspiring me to love through your unconditional love and trust. Thank you Darloh for brightening up my life with your sincere care, comfort, and granting me hope. Thank you for your laudable sacrifice and great help that enabled me overcome many obstacles. This degree would not have been possible without you.

To my joy and adorable son Hawi, no words can truly express the great happiness you brought since your coming. Every day, your smile always brightens my heart, gives me hope and determination to overcome many study obstacles and keep going and more significantly put in me the vigor to be a role model dad. You are indeed the best gift in my life and best luck to me in conformity to your name mean. You gave me the much needed joy and comfort during the strenuous thesis writing period.

Table of contents

Declaration i
Abstract ii
Acknowledgments iv
Table of contents vii
Dedication xiii
List of Publications xiv
List of conference/workshop presentations xvi
Research visits xvii
Summer schools attended xvii
List of figures xviii
List of tables xxviii
List of symbols and abbreviations xxx
Thesis synopsis xxxii
Chapter 1: Background and Rationale 1
1.1 Background 1
1.1.1. Organic solar cells 4
1.1.2. Dye-Sensitized Solar Cells (DSSCs) and perovskites 4
1.2. Problem statement 5
1.3. Aim and objectives 6
1.3.1. Aim 6
1.3.2. Objectives 6
1.4. Motivation 7
1.5. References (for chapter 1) 9
Chapter 2: Introduction to ZnO, AZnO and Rare earth doped ZnO thin films 13
2.1. Introduction to Fundamentals on TCOs. 13
2.2. Properties of ZnO 17
2.2.1. Structural properties of ZnO 17
2.2.2. Electronic properties 19
2.2.3. Optical properties 23
2.2.4. Thermal properties 24

2.2.5. Lattice Dynamics 25
2.3. Native point defects in ZnO 26
2.3.1. Introduction to point defects. 26
2.3.2. Defect concentrations and formation energies 26
2.3.3. Migration barriers and activation energies related to diffusion. 27
2.3.4. Introduction to various intrinsic point defects in ZnO 28
2.4. Luminescence properties of ZnO 33
2.4.1. Introduction. 33
2.4.2. Classification of luminescence 35
2.4.3. Fluorescence quenching 36
2.4.4. Advantages of Luminescence Techniques 37
2.4.5. Photoluminescence spectra of ZnO 38
2.5. Evolution of thin films 39
2.5.1. Nucleation and growth of isolated islands. 39
2.5.2. Island coalescence. 40
2.5.3. Film thickening. 41
3.5.4. Grain growth. 41
2.6. Effect of annealing temperature on grain growth. 43
2.6.1. Effects of thermal annealing on film stress 45
2.7. Effect of Oxygen concentration on ZnO film quality 47
2.8. Doping of ZnO 47
2.8.1. Aluminum doping of ZnO 47
2.8.2. Rare earth doping. 48
2.8.3. Rare earths, RE 49
2.8.4. Energy transfer in phosphors 53
2.9. Applications of nanostructured ZnO based material. 60
2.9.1. Energy losses in solar cells 60
2.9.2. Effect of varying solar air-mass using up and down-conversion 62
2.9.3. Down-conversion process. 64
2.9.4. Down-shifting process. 67
2.9.5. Up-conversion process 68

2.9.6. State of art on the recent progress on doping on rare earth ions in the oxide nanomaterials 69
2.9.7. Rare earth metals used for doping of ZnO 72
2.9.8. Applications of ZnO and rare earth doped ZnO in solar cells. 76
2.9.9. Parameters used in the various solar cells 81
2.10. References (for chapter 2). 82
Chapter 3: Film Growth Methods and Materials Characterization 102
3.1. Thin films deposition methods 102
3.2. Thin Film deposition techniques used in this project. 103
3.2.1. RF magnetron sputtering 103
3.2.2. Basic Principles of RF sputtering 103
3.2.3. Advantages of magnetron sputtering 107
3.3. Ion implantation of Rare earth ions 108
3.3.1. Ion range 109
3.3.2. Implantation procedure 110
3.4. Substrate Cleaning 112
3.5. Thermal Annealing of the films 112
3.6. Thin film Characterization 114
3.6.1. Film Thickness Measurement 114
3.6.2. X-Ray Diffraction Studies (XRD) 116
3.6.3. Raman Spectroscopy 119
3.6.4. Chemical Compositional Analysis 121
3.6.5. Rutherford backscattering spectroscopy (RBS) 124
3.6.6. Morphological Studies using Scanning Electron Microscopy (SEM) 128
3.6.7. Atomic Force Microscopy (AFM) 131
3.6.8. Optical properties using UV-Vis-NIR Spectrophotometry 134
3.6.9. Photoluminescence Spectroscopy 137
3.7. References (for chapter 3) 140
Chapter 4: Structural and Optical characterization of ZnO thin films. 144
4.1. Introduction 144
4.2. Growth conditions 145

4.3. Characterization techniques 146
4.4. Results and discussion 147
4.4.1. EDS and RBS measurements 147
4.4.2. Atomic Force Microscopy & Scanning Electron Microscopy. 149
4.4.3. X-Ray Diffraction analysis 161
4.4.4. Raman spectroscopy 171
4.4.5. Photoluminescence studies 180
4.5. The Effect of the Oxygen Concentration on the Zinc Oxide Films 188
4.5.1. Raman studies on oxygen variation. 192
4.5.2. VIS/NIR Analysis studies on oxygen variation 196
4.6. Application of ZnO thin films into perovskites solar cells 199
4.6.1. Preparation procedure 199
4.7. Conclusion 201
4.8. References (for chapter 4) 203
Chapter 5: Structural and spectroscopic analysis of ex-situ annealed RF sputtered Al doped ZnO thin film. 210
5.1 Introduction 210
5.2. Experimental details 212
5.3. Characterization of the films. 212
5.4. Results and discussion 213
5.4.1. Morphology studies by AFM and SEM 213
5.4.2. Raman Spectroscopy 219
5.4.3. XRD measurements 222
5.4.4. XRR measurements. 230
5.4.5. Photoluminescence measurements 231
5.5. Conclusion 241
5.6. References (for chapter 5) 241
Chapter 6: Structural and optical study of annealed ZnO:Tb^{3+} and Zn:Eu^{3+} nano-polycrystalline thin films and their application for down conversion in solar cells. 245
6.1 Introduction 245
6.2. Experimental procedure 247

6.2.1. Materials 247
6.2.2. The growth of ZnO:Tb^{3+} and ZnO:Eu^{3+} thin films. 247
6.2.3. Characterization 248
6.3.1 Morphology Studies 248
6.3.2 Rutherford Backscattering Spectroscopy Measurements 251
6.3.3 Grazing incidence XRD measurements 252
6.3.4 Optical properties 254
6.3.5 Photoluminescence studies 256
6.4. Application of ZnO:Tb^{3+} thin films into organic solar cells 261
6.4.1. Device fabrication and characterization 261
6.4.2. Current –Voltage (*I-V)* Characteristics 261
6.5. Results and discussion of ZnO: Eu^{3+} thin films 264
6.5.1. Morphological studies 264
6.5.2. Rutherford Backscattering Spectroscopy Measurements 265
6.5.3. X-Ray Diffraction Analysis 266
6.5.4. Optical studies 268
6.5.5. Photoluminescence properties 270
6.6. Application of ZnO:Eu^{3+} thin layer into Dye sensitized solar cells 274
6.6.1. Fabrication procedure. 274
6.6.2. Results and discussion. 276
6.7. Conclusion 277
6.8. References (for chapter 6) 278
Chapter 7: Implantation of Sm^{+} ions into ZnO matrix for spectral conversion. 283
7.1. Introduction 283
7.2. Experimental procedure 285
7.2. Stopping and Range of Ions in Matter (SRIM) calculation 286
7.2.1. Introduction to SRIM and analysis of Sm based implantations in ZnO 286
7.3 Results and discussion. 287
7.3.1 Morphology Studies using Atomic force microscopy 287
7.3.2. Scanning Electron Microscopy (SEM). 291
7.3.3 Rutherford Backscattering Spectroscopy measurements 293

7.3.4. Grazing incidence XRD measurements. 297
7.3.5. Raman Spectroscopy 299
7.3.6. Photoluminescence studies 300
7.4. Conclusion 303
7.5. References (for chapter 7) 304
Chapter 8: Conclusion and future work 308
8.1. Conclusion 308
8.2. Future work 311
Appendix 313

In loving memory of mama Nyogola

Dedication

To my adorable son Hawi and pretty niece Herah, my beloved wife Dr. Mildred and my amazing father Mzee wuon Oluoch together with the entire big and loving family.

List of Publications

i) **Otieno, Francis**, Mildred Airo, Kamalakannan Ranganathan, and Daniel Wamwangi. "Annealed silver-islands for enhanced optical absorption in organic solar cell." *Thin Solid Films* 598 (2016): 177-183.

ii) **Francis Otieno**, Bridget Mutuma, Mildred Airo, Kamalakannan Ranganathan, Neil Coville and Daniel Wamwangi, "Enhancement of organic photovoltaic device performance via P3HT:PCBM solution heat treatment." *Thin Solid Films* 625 (2017): 62-69.

iii) **F. Otieno**, K. Kamalakan, D. Wamwangi, 'Enhancing light absorption and life-time stability of organic solar cells using pentacene encapsulation. Proceedings of SAIP2015 - ISBN: 978-0-620-70714-5.

iv) Airo, Mildred, Siziwe Gqoba, **Francis Otieno**, Makwena Justice Moloto, and Nosipho Moloto. "Structural modification and band-gap crossover in indium selenide nanosheets." *RSC Advances 6.47 (2016): 40777-40784*.

v) Airo MA, Rodrigues R, Gqoba S, Ntholeng N, **Otieno F**, Moloto MJ, Greenshields MW, Hümmelgen IA, Moloto N. Colloidal InSe nanostructures: Effect of morphology on their chemical sensitivity to methanol and formaldehyde fumes. Sensors and Actuators B: Chemical. 2016 Nov 29; 236:116-25.

vi) **Francis Otieno**, Shumbula N Prince, Mildred Airo, Mlambo Mbuso, Nosipho Moloto, Rudolph Erasmus, Alex Quandt and Daniel Wamwangi. "Improved efficiency of organic solar cells using Au NPs incorporated into PEDOT:PSS buffer layer." AIP Advances. 7.8 (2017): 085302

vii) **Francis Otieno**, Mildred Airo, Rudolph M. Erasmus, David G. Billing, Alexander Quandt, and Daniel Wamwangi. "Structural and spectroscopic analysis of ex-situ annealed RF sputtered aluminium doped zinc oxide thin films." *Journal of Applied Physics* 122.7 (2017): 075303.

viii) **Otieno, Francis**, Mildred Airo, Rudolph M. Erasmus, David G. Billing, Alexander Quandt, and Daniel Wamwangi. "Effect of thermal treatment on ZnO: Tb^{3+} nano-crystalline thin films and application for spectral conversion in inverted organic solar cells." *RSC Advances* 8, no. 51 (2018): 29274-29282.

ix) Nhluvuko Mayimele, **Francis Otieno**, Alex Quandt and Daniel Wamwangi Localized surface plasmon resonance for better efficiency of organic solar cell. Journal of applied Physics. Under review

x) **Francis Otieno**, Mildred Airo, Eric G. Njoroge, Rudolph Erasmus, Theodore Ganetsos, Alexander Quandt and Daniel Wamwangi. Effect of implantation of Sm^{+} ions into RF sputtered ZnO thin film. *Journal of Materials Chemistry and Physics*. Under review.

xi) **Francis Otieno**, Mildred Airo, Rudolph Erasmus, Theodore Ganetsos, Alexander Quandt and Daniel Wamwangi. The Effect of the Oxygen Concentration on the structural and optical properties of RF magnetron sputtered Zinc Oxide thin films. Journal of *Royal Society Open Science*. Under review.

xii) **Francis Otieno**, Mildred Airo and Daniel Wamwangi. Annealing effect on the structural and optical behavior of ZnO-Eu^{3+} thin film grown using RF magnetron sputtering technique. Journal of *Thin solid films - Elsevier*. Under review

xiii) **Francis Otieno**, Mildred Airo and Daniel Wamwangi. Raman spectroscopy analysis of RF sputtered ZnO thin film of varied thickness annealed at different temperature. Journal of *Thin solid films - Elsevier*. Under review

List of conference/workshop presentations

i) Oral presentation: Held (23/10-27/05/2014). 7th International Symposium On Macro- and Supramolecular Architectures and Materials entitled (MAM-14): *Surface Plasmon Resonance effect to enhance photo-conversion efficiency of organic solar cells*

ii) Oral presentation: Held (29/10-31/10/2014). Material for energy research group annual workshop. '*Enhancement of photo-conversion efficiency of organic solar cells by surface Plasmon resonance effect*'. held in Free- State in South Africa

iii) Poster presentation: Held (28/10-29/10/2014). The 6th Cross faculty graduate symposium showcasing graduate research at Wits. '*Enhancement of photo-conversion efficiency of organic solar cells by surface Plasmon resonance effect*'.

iv) Poster presentation: Held (13 – 20th July 2015). International School for Materials for Energy and Sustainability IV (ISMES IV) held in Colorado school of Mines – USA. "*Annealed silver-islands for enhanced optical absorption in organic solar cell*."

v) Poster presentation: Held (1-2nd March 2016). The 6th Cross faculty graduate symposium showcasing graduate research at Wits. '*Enhancement of organic photovoltaic device performance via P3HT:PCBM solution heat treatment*'.

vi) Poster presentation: Held (13-19 July 2016). 5th School Materials for Energy and Sustainability-" and 3rd "EPS-SIF International School on Energy. 'Improved efficiency of organic solar cells using Au NPs incorporated into PEDOT:PSS buffer layer.' Held in: Erice, Italy.

vii) Oral presentation: Held on 01-11-2017. Material for energy research group annual workshop. '*Efficiency enhancement of inverted ZnO:Tb^{3+} based organic solar cells through down conversion*'. held at Societa Dante Alighieri, Johannesburg- South Africa.

viii) Poster presentation: Held (November 30 - December 2, 2017). 7th International Workshops on Photoluminescence of Rare-Earth: Photonic Materials and Applications 2017. '*Efficiency enhancement of inverted ZnO:Tb^{3+} based organic solar cells through down conversion.'* Held at Sapienza University of Rome, Roma, Italy.

Research visits

i) 3 months Research visit to University of West Attica - Technological Educational Institute of Piraeus, Perou Ralli & Thevon 250, Egaleo, Greece. From 23rd April to 20th May 2018 to carry our VIS/NIR and Raman spectroscopy measurements

ii) Visit to the laboratory of the Istituto di Fotonica e Nanotecnologie del Consiglio Nazionale delle Ricerche (IFN CNR) in Povo (Trento)-Italy between 20-27th July 2016.

iii) Visit to Mintek Nanotechnology Innovation Centre (NIC). 200 Malibongwe Drive, Strijdom Park, Randburg. South Africa on the 8 March 2015.

iv) Visit to the National Centre for Nano-Structured Materials based at the Council for Scientific and Industrial Research (CSIR), Meiring Naudé Road; Brummeria; Pretoria; South Africa on the 26th August 2015.

Summer schools attended

i) International School for Materials for Energy and Sustainability IV (ISMES IV) held in Colorado school of Mines – Colorado, USA. Held (13 – 20 July 2015). The aim of the School was to present the state-of-the-art and the future perspectives for materials as they can be applied to energy generation and storage for sustainable energy technologies.

ii) 5th School Materials for Energy and Sustainability-" and 3rd "EPS-SIF International School on Energy held at Ettore Majorana Foundation and Centre for Scientific Culture in Erice, Italy. Held (13-19 July 2016). The aim of the School was to present the state-of-the-art and the future perspectives for materials applied to the generation and storage of renewable and sustainable energy. Lectures were given by some of the most recognized academic and industrial experts, merging physics, chemistry and engineering knowledge in several fields.

List of figures

Figure 1-1: Mechanisms of photon luminescent conversion processes and simplified view of schemes of application into solar cells..... 4

Figure 2-1: The wurtzite crystal structure ZnO with: (a) four atoms per unit cell, (b) tetrahedral coordination, (c) hexagonal symmetry and the lattice parameters a and c, (d) top view of (c) [38]. 18

Figure 2-2: Schematics of typical TCOs band structure 19

Figure 2-3: (a) the assumed band structure of TCOs in the vicinity of the top of the valence band and the bottom of the conduction band. (b) valence band shifted upwards by many body effects while the conduction band is shifted downwards. Shaded areas denote occupied states [43]. 21

Figure 2-4: The local density approximation band structure of bulk wurtzite ZnO [51]. 23

Figure 2-5: Thermodynamic transition levels for native defects in ZnO [78]. 32

Figure 2-6: Band diagram illustration of the different processes that make up the photoluminescence spectra [79]..... 34

Figure 2-7: Grain growth in a continuous film with an in-plane grain size adapted from Ref. [102] 42

Figure 2-8: Overview of possible grain structure evolution during deposition of polycrystalline thin film adapted from ref [102]. 43

Figure 2-9: Schematic representation of the splitting of the 4fn state of a free rare earth ion as a result of atomic and crystal field forces ref [155]. 51

Figure 2-10: An energy-level diagram, called Dieke diagram, for trivalent lanthanide rare earth ions adapted from Ref [152]. The green frames indicate RE studied in this study. 52

Figure 2-11: Resonant energy transfer by the quantum mechanical exchange interaction with overlapping D and A wave functions (shaded area). 55

Figure 2-12: Phonon-assisted non-radiative transfer where ε is the energy mismatch [171]. 56

Figure 2-13: Cross-relaxation between two identical ions [176]. 59

Figure 2-14: Energy loss processes in a single-junction solar cell [180] 60

Figure 2-15: Spectral irradiance and power contained within various solar spectra [181]. 62

Figure 2-16: AM1.5G spectrum showing the fraction that is currently absorbed by a thick silicon device and the additional regions of the spectrum that can contribute towards up- and down-conversion [181]. 63

Figure 2-17: Overview of different resonant down-conversion mechanisms demonstrated using two ions, I and II, with hypothetical energy level schemes [203]. 65

Figure 2-18: The interband Auger process. (a) A high energy photon creates an electron–hole pair and excites the electron deep into the conduction band. (b) This is followed by a non-radiative relaxation to the band edge of the conduction band, the excess energy is used to create a second electron–hole pair. (c) The radiative recombination of both electron–hole pairs via energy levels of the active ion leads to the emission of two low energy photons of wavelength, λ_{em}. [191]. ... 66

Figure 2-19: Schematic energy diagram of a solar cell in combination with active luminescence down-converter/down-shifter layer that precede the TCO layer in the device [207]. 67

Figure 2-20: Energy level schemes for various two-photon up-conversion processes with quantum efficiency normalized to the incident power (1 W cm^2). Transitions between energy levels are indicated by vertical arrows, and curved arrows connecting different ions indicate energy transfer. Horizontal lines are real energy levels [215]. 68

Figure 2-21: (a) Terbium ore (b) Schematic energy level diagram of Tb^{3+} ion [236]. 73

Figure 2-22: Illustration of proposed emission mechanism in Eu^{3+} doped ZnO [243]. 75

Figure 2-23: Band diagram and main processes in Organic Solar Cells: 1 Absorption of photon followed by exciton formation; 2 Exciton diffusion; 3 Charge separation; 4 Charge extraction [251]. 77

Figure 2-24: Band diagram and main processes and Perovskites solar cells: 1 Absorption of photon and free charges generation; 2 Charge transport; 3 Charge extraction [251]. 79

Figure 2-25: Energy diagram of the working principle of a dye sensitized solar cell [220]. 80

Figure 2-26: The J-V characteristics of solar cell in the dark and under illumination the equivalent circuit diagram. 81

Figure 3-1: Photograph of vacuum system used in the present study and view of inside the deposition chamber. 104

Figure 3-2: Schematic representation of a RF magnetron sputtering system [4]. 105

Figure 3-3: Depth distribution of implanted ions in a target for; (a) the ion mass m_1 < mass m_2 of the substrate [19]. The mean depth Rp depends only on m_1 and E_1 whereas $\Delta Rp/Rp$ depends on the ratio m_1:m_2. 110

Figure 3-4: General schematic of an ion implantation equipment..... 111

Figure 3-5: Summary of furnace annealing process where (a), (b) and (c) depicts the ramping, dwelling and cooling time respectively. 113

Figure 3-6: The Filmetrics F20 instrument used for thickness measurements 114

Figure 3-7: Representation of light reflectance from two layers 115

Figure 3-8: An example of reflectance spectrum showing both raw and fitted (calculated) spectrum. 116

Figure 3-9: The geometrically description of the direction of the diffraction beam due to the constructive interference between atoms located on the planes with interplanar spacing d(hkl). 118

Figure 3-10: A sketch of the instrumental setup for a θ /2θ scan 119

Figure 3-11: Energy diagram for inelastic (Raman) and elastic (Rayleigh) scattering. 120

Figure 3-12: Optical diagram of JY T64000 monochromator in a triple additive and subtractive mode (adapted from the Instruction Manual for the Jobin-Yvon T64000 Raman Spectrograph). 121

Figure 3-13: (a) and (b) Characteristic x-ray radiation..... 122

Figure 3-14: Example of an EDS spectrum of ZnO implanted with Sm rare earth. 123

Figure 3-15: A schematic illustration of RBS experimental set-up used in this work. 125

Figure 3-16: Schematic illustration of backscattered alpha particles and energy loss at a depth x. 125

Figure 3-17: Typical RBS spectrum for ZnO thin film 127

Figure 3-18: Schematic illustration of the phenomena resulting from the interaction of highly energetic electrons with matter. 128

Figure 3-19: Schematic illustration of Scanning Electron Microscope. 130

Figure 3-20: Schematic operation principle of atomic force microscopy. 131

Figure 3-21: Illustration of absorption and transmitted light. 135

Figure 3-22: Schematic representation of a dual-beam UV-Vis spectrophotometer 136

Figure 3-23: Principle of photoluminescence spectroscopy (PL). 138

Figure 3-24: Schematic diagram of a fluorescence spectrometer 139

Figure 4-1: EDS analysis of the ZnO thin film grown using RF sputtering on Si wafer substrate. 147

Figure 4-2: RBS image spectrum of ZnO layer on Si showing experimental curve (black) and simulated curve (red) using XRump code. 148

Figure 4-3: AFM images of ZnO thin film grown at 100 W, 1 minute and annealed at different temperatures (600-900 ˚C). 149

Figure 4-4: SEM images of ZnO thin film grown at 100 W, 1 minute and annealed at different temperatures (600-900 ˚C) using beam energy of 30000 in each case, working distance of 4.8mm, 5.0 mm, 5.2 mm, 4.8 mm and beam energy magnification of 36 000, 20 000, 20 000, 20 000 for 500 ˚C, 600 ˚C, 700 ˚C, 800 ˚C and 900 ˚C respectively. 152

Figure 4-5: AFM images of ZnO thin film grown at 100 W at different deposition time ranging from 1-20 minutes. 153

Figure 4-6: SEM images of ZnO thin film grown at 100 W at different deposition times, (1-20 minutes) 155

Figure 4-7: AFM images of ZnO thin film grown at a deposition time of 5 minutes at different RF sputtering power 157

Figure 4-8: SEM image of ZnO thin film grown at a deposition time of 5 minutes at different RF sputtering power 160

Figure 4-9: XRD patterns of ZnO thin film grown at 100 W, 1 minute unannealed and annealed at different temperatures (600-900 ˚C). 161

Figure 4-10: XRD patterns of ZnO thin film grown at 100 W, 5 minutes unannealed and annealed at different temperatures (600-900 ˚C). 164

Figure 4-11: XRD patterns of ZnO thin film grown at 100 W, 20 minutes unannealed and annealed at different temperatures (600-900 ˚C). 166

Figure 4-12: XRD patterns of ZnO thin film grown at 100 W with varied deposition time. 168

Figure 4-13: XRD patterns of ZnO thin film grown at deposition time of 5 minutes with varied RF power in the (100-260 W) range. 169

Figure 4-14: Eigenvectors of the ZnO optical phonon modes. For every mode, the red arrows represent the dominating displacement vectors. The A_1, B_1 (high), E_1, and E(high) modes are oxygen-dominated while B (low) and E_2 (low) modes are Zn-displacement dominated [39]. .. 173

Figure 4-15: Unpolarized Raman spectrum of bulk ZnO showing Raman active modes with the corresponding vibrations of the ions. The red arrows specify the dominant ions displacements adopted from [40]. 173

Figure 4-16: Raman spectra of ZnO thin film grown at 100 W for 1 minute before and after annealing at temperature 600-900 ˚C. 174

Figure 4-17: Raman spectra of ZnO thin film grown at 100 W for 5 minutes before and after annealing at temperature 600-900 ˚C. 175

Figure 4-18: Raman spectra of ZnO thin film grown at 100 W for 20 minute before and after annealing at temperature 600-900 ˚C. 176

Figure 4-19: Raman spectra of ZnO thin film grown at 100 W for different time variation (1-20 minutes)..... 178

Figure 4-20: Raman spectra of ZnO thin film grown for 5 minutes at different RF power (100-260 W). 179

Figure 4-21: Room temperature photoluminescence study of ZnO films deposited on silicon substrate for 1 minute then annealed at 600-900 ˚C. 181

Figure 4-22: Room temperature photoluminescence study of ZnO films deposited on silicon substrate for 5 minutes then annealed at 600-900 ˚C. 184

Figure 4-23: Room temperature photoluminescence study of ZnO films deposited on silicon substrate for 20 minutes then annealed at 600-900 ˚C. 185

Figure 4-24: Room temperature photoluminescence study of ZnO films deposited on silicon substrate at different deposition time then annealed at 750 ˚C. 187

Figure 4-25: Room temperature photoluminescence study of ZnO films deposited on silicon substrate at constant Argon flow rate of 13 sccm but varied Oxygen flow rate (0-15 sccm) then annealed at 700 ˚C in Ar ambient. 189

Figure 4-26: The schematic diagram of the suggested emission mechanisms of green and red light in ZnO thin films adapted from ref. [61]. 191

Figure 4-27: Raman spectroscopy of unannealed ZnO thin films grown at different O_2 concentration. 192

Figure 4-28: Raman spectroscopy of ZnO thin films grown at different O_2 concentration then annealed in Ar filled furnace at 700 ˚C. 195

Figure 4-29 Optical reflectance spectrum of ZnO thin film deposited using different oxygen flow rates into the RF chamber. 196

Figure 4-30: Spectrum fitting to derive thickness of the film and refractive index. 197

Figure 4-31: Film thickness variation with oxygen flow rate. 198

Figure 4-32: Energy level diagram and device structure of perovskite solar cells. (a) Energy diagram of individual layers used in perovskite devices. (b) Perovskite device structure. (c) Surface groups on the ZnO film and the crystalline structure of perovskite cry stalline structure of perovskite crystals. 200

Figure 4-33: J-V characteristics of perovskites solar cell composed of ZnO as electron transport layer. 201

Figure 5-1: AFM images of the Al doped ZnO before and after annealing at temperature range of 600-1000 ˚C in air. 213

Figure 5-2: AFM images of the Al doped ZnO grown an RF power of 100 W over different deposition time ranging from 5 minutes to 1 hour. 216

Figure 5-3: SEM images of the Al doped ZnO before and after annealing at temperature range of 600-1000 ˚C in air and EDS spectra. 217

Figure 5-4: Energy Dispersive Spectroscopy (EDS) spectra of the pristine and annealed ZnO thin film (1000 ˚C). 218

Figure 5-5: Raman spectra of Aluminium doped ZnO thin film before and after annealing at 600-1000 ˚C. The spectra were collected at normal incidence (at 90 ˚ to the surface). 220

Figure 5-6: Raman spectra of Al doped ZnO thin film deposited at 100 W at different deposition time. 221

Figure 5-7: Schematic representation of a wurtzitic ZnO structure having lattice constants a in the basal plane and c in the basal direction; u parameter is expressed as the bond length [21].. 223

Figure 5-8: X-ray diffraction (XRD) pattern of (a) the Al doped ZnO thin film before and after annealing at temperature between 600-1000 ˚C in air, (b) curve fit of the (100) peak before and after annealing at 1000 ˚C. 224

Figure 5-9: X-ray diffraction (XRD) pattern of the Al doped ZnO thin film grown using varied deposition time. 229

Figure 5-10: Experimental (black) and simulated (blue) XRR spectra of as-deposited Al doped thin film deposited at 100 W for 5 minutes 230

Figure 5-11: Room temperature photoluminescence spectra of Al doped ZnO thin film grown for 20, 30 and 40 minutes before and after annealing at temperature between 600-1000 ˚C in air. 234

Figure 5-12: Room temperature photoluminescence spectra of Al doped ZnO thin film grown for 20,30 and 40 minutes before and after annealing at 900 ˚C 236

Figure 5-13: PL spectrum showing the effect of variation of deposition time on the emission spectrum. 237

Figure 5-14: Room temperature photoluminescence spectra of Al doped ZnO thin film grown for 40 minutes before and after annealing at temperature between 600-1000 °C in air. The spectra have been stacked for clarity 239

Figure 5-15: Room temperature photoluminescence spectra of Al doped ZnO thin film as-grown at an RF power of 100 W at different deposition time. 240

Figure 6-1: AFM images of pristine ZnO:Tb3+ films (room temperature) and after annealing in Ar filled furnace for 2 hours in the range between 600 and 900 ˚C. 249

Figure 6-2: RBS spectrum of an 190 nm ZnO:Tb^{3+} layer on Si showing experimental data and computer simulation using XRump code. The sample structure and the thicknesses of the layers were derived. 251

Figure 6-3: Grazing incidence X-ray diffraction of ZnO:Tb^{3+} thin films deposited by RF sputtering at room temperature then annealed different temperatures (600-900 ˚C). 253

Figure 6-4: Transmission spectra of pristine ZnO:Tb^{3+} thin films and upon annealing at different temperatures, 600-900 ˚C in Ar filled furnace. 254

Figure 6-5: Plot of $(\alpha h\nu)^2$ versus hν for the pristine ZnO:Tb^{3+} thin film and after annealing at 600-900 ˚C. The inset shows the variation of optical band gap as a function of annealing temperature. 256

Figure 6-6: PL spectra of the ZnO:Tb^{3+} thin films annealed at different temperatures excited at 244 nm together with that of the ZnO:Tb^{3+} thin film annealed at temperature range of 600-900 ˚C. 258

Figure 6-7: schematic of the energy level diagram of the ZnO:Tb^{3+} thin films. 260

Figure 6-8: J–V characteristics (a) under illumination of devices formed from pristine and heat treated P3HT:PCBM blends. 262

Figure 6-9: Scanning Electron Microscopy micrographs of Eu doped ZnO films annealed at temperature range of 500-900 ˚C. 264

Figure 6-10: Random and simulated RBS spectra from the ZnO:Eu^{3+} thin film annealed at 900 ˚C. 265

Figure 6-11: Room temperature XRD pattern of pristine and annealed ZnO:Eu^{3+} thin films compared to the undoped ZnO. 267

Figure 6-12: Optical transmittance of pristine and ZnO:Eu^{3+} annealed at 500-900 ˚C. 268

Figure 6-13: Plot of $(\alpha h\nu)^2$ versus hν for the pristine ZnO:Eu^{3+} thin film and after annealing at 500-900 ˚C. The inset shows the variation of optical band gap as a function of annealing temperature. 269

Figure 6-14: Schematic illustration of the proposed mechanism of energy transfer from the ZnO host to the Eu^{3+} ions. 271

Figure 6-15: Room temperature PL spectrum of ZnO:Eu^{3+} annealed at 500-700 ˚C measured at 244 nm excitation wavelength. 272

Figure 6-16: Room temperature PL spectrum of ZnO:Eu^{3+} annealed at 500-700 ˚C using 244 nm excitation wavelength. 273

Figure 6-17 J-V characteristics curves of pristine and Eu^{3+} doped ZnO used in dye sensitized solar as a photoanode. 276

Figure 7-1: SRIM profile illustrating the estimated ion distribution with penetration depth for Sm+ ions of energy 80 keV. 286

Figure 7-2: Tapping mode AFM images of ZnO and ZnO:Sm^{+} thin films. 288

Figure 7-3: SEM micrographs of the undoped ZnO Sm^{+} - doped ZnO films implanted at different fluences. 291

Figure 7-4: EDS of ZnO thin film before and after Sm ion implantation 292

Figure 7-5: RBS spectrum of an 154 nm Sm implanted ZnO layer on Si showing experimental data at a fluence of 2×10^{15} ions/cm^2. Inset is a zoom plot of channel range 450-500 293

Figure 7-6: RBS spectrum of an 154 nm Sm implanted ZnO layer on Si showing experimental data and computer simulation using XRump code. 294

Figure 7-7: RBS spectra of Sm implanted ZnO layer at different fluences at energy of 80 keV. Inset is a zoom plot of channel range 450-500. 296

Figure 7-8: GIXRD patterns of pristine-, unannealed Sm implanted- - and annealed Sm implanted ZnO thin films. The dose used for Sm implantation is ions/cm^2. 297

Figure 7-9: Raman spectra of RF sputtered ZnO films grown on Si (100), as grown and after ion implantation with Sm^{+} to form ZnO:Sm^{+}. 299

Figure 7-10: Room temperature PL spectra of the ZnO and Sm^{+}-doped ZnO thin films both of average thickness of 152 nm. 301

Figure 7-11: schematic of the energy level diagram of the ZnO:Sm^{+} thin films. 302

List of tables

Table 2-1: summary of basic physical properties of ZnO..... 25

Table 2-2: Various forms of luminescence adapted from Ref [79]. 36

Table 2-3: Electronic configuration of rare earth ions in their ground state [154]. 50

Table 3-1: Post-treatment parameters of furnace annealing used in this study 114

Table 4-1: XRump Simulation parameters of thickness and fractional elemental compositions. 148

Table 4-2: Summary of tapping mode AFM analysis after annealing at 600-900 ˚C temperature range..... 151

Table 4-3: Summary of tapping mode AFM analysis for films grown at different deposition time ranging from 1-20 minutes..... 154

Table 4-4: Summary of tapping mode AFM analysis for films deposited at time of 5 minutes at different RF sputtering power. 158

Table 4-5: Summary of statistical values of ZnO thin film grown at 100 W, 1 minute and annealed at different temperatures (600-900 ˚C). 163

Table 4-6: Summary of statistical values of ZnO thin film grown at 100 W, 5 minutes and annealed at different temperatures (600-900 ˚C). 165

Table 4-7: Summary of statistical values of ZnO thin film grown at 100 W, 20 minutes and annealed at different temperatures (600-900 ˚C). 167

Table 4-8: Summary of statistical values of ZnO thin film grown at 100 W with varied deposition time. 168

Table 4-9: Summary of statistical values of ZnO thin film grown at deposition time of 5 minutes with varied RF power in the (100-260 W) range. 170

Table 4-10: Peak positions of the NBE and DL emission peaks. 183

Table 4-11: Intrinsic defects concentration against oxygen concentration variation. 189

Table 5-1: Summary of tapping mode AFM analysis..... 214

Table 5-2: Summary of tapping mode AFM analysis for AZnO deposited at varied time. 216

Table 5-3: Characteristics of Al doped ZnO annealed at 600-1000 ˚C in air as estimated from XRD patterns 225

Table 5-4: Estimated crystallite size, lattice parameters, dislocation density and strain from XRD data. 228

Table 6-1: Summary of Rms and grain height from taping mode AFM 250

Table 6-2: Characteristics of Tb^{3+} doped ZnO estimated from XRD measurements. 253

Table 6-3: Summary of peak center position and FWHM for the NBE PL peak. 258

Table 6-4: Summary of the performance of the P3HT:PCBM bulk heterojunction solar cells device with pure ZnO and ZnO: Tb^{3+} as the cathode buffer layer. 263

Table 6-5: Derived atomic composition at various film depth from XRump code 266

Table 7-1: Summary of tapping mode AFM analysis with varied fluence 289

Table 7-2: Simulated Sm concentration using varied fluences. 295

List of symbols and abbreviations

AFM	atomic force microscopy
ALD	atomic layer deposition
AM 1.5G	Solar Spectral Irradiance: Air Mass
APTE	addition de photon par transferts d'energie
AZO	Al-doped zinc oxide
c-Si	crystalline silicon
CVD	chemical vapor deposition
DL	Deep level emission
EA	electron affinity
E_{CBM}	conduction band minimum
EDS	Energy-dispersive X-ray spectroscopy
E_F	Fermi level
Eg	Energy band gap
E_{g0}	intrinsic band gap
ETU	energy transfer up-conversion
E_{VBM}	valence band maximum
E_{vsc}	vacuum level
FPDs	Flat panel displays
FTO	Flourine - doped Tin Oxide
FWHM	Full width at half maxima

GSA ground state absorption

I_p ionization potential

ITO Indium Tin Oxide

LEDs Light emitting diode

NIR near infra-red (light)

OSCs Organic solar cells

P3HT Poly(3-hexylthiophene-2,5-diyl) regioregular

PCBM [6,6]-phenyl-C_{61}-butyric acid methyl ester

PLD pulsed laser deposition

PV Photovoltaic

RBS Rutherford backscattering spectroscopy

RE Rare earth

Rku kurtosis

Rms root mean square SEM scanning electron microscopy

Rsk skewness

SEM scanning electron microscope

TCOs transparent conducting oxides

UV ultra violet

UV-Vis ultra violet – visible (referred to light)

WF work function

XRD X-ray diffraction

Thesis synopsis

This thesis is partitioned into 8 chapters as follows:

Chapter 1: a survey of the background studies of rare earth doped ZnO as well as the aims and objectives of the project.

Chapter 2: an overview of the fundamentals of the wide bandgap oxides, the choice of rare earth ions used and their radiative properties as well as the state-of-the art research on rare earth doping effects in wide bandgap oxide materials and also highlights the visible outcome of the research carried out, which serves as a good platform for future perspectives.

Chapter 3: the experimental details used for the growth of thin films by RF sputtering and gives a brief explanation of the principles of the characterization technique used with an outline of the principle of their operation.

Chapter 4: an elaborate study on the effect of ex-situ annealing of ZnO on its structural, morphological, optical and photoluminescence properties. As a proof of concept, the films were used to fabricate perovskite solar cells.

Chapter 5: the investigation of the effects of Aluminium concentration on the structural, morphological, optical and photoluminescence properties of ZnO thin films grown at different parameters. Only doping with low concentrations is generally pursued in order to avoid luminescence quenching.

Chapter 6: the Structural and optical properties of annealed ZnO:Tb^{3+} and Zn:Eu^{3+} nano-polycrystalline thin films grown using RF sputtering and their application for down conversion in solar cells.

Chapter 7: the effect of implantation of Sm^{+} ions into ZnO matrix on the structural and optical properties. The energy used for implantation was 80 *keV* at different fluence ranging from $\approx 10^{14}$ - 10^{16} ions/cm^2 and SRIM was used to calculate the particle distribution.

Chapter 8: a summary of our findings and outlook on future work.

Chapter 1: Background and Rationale

1.1 Background

The surge in modernity has brought the quest for modern electronics which are ultra-portable and efficient, combining communication, storage, and multimedia technologies in one package [1]. This led to intensified research into transparent conducting oxides (TCOs) which have been a subject of great interest for their potential applications in devices such as light emitting diodes (LEDs), flat panel displays, solar cells etc where transparent electrodes and circuitry remain a necessary and sufficient condition for portability and enhanced performance at very low voltages [2-8]. Generally, the term TCOs refers to wide bandgap semiconductor oxides (Eg > 3.1 eV). This could be attained through doping (sometimes to degeneracy) through the introduction of dopants. These dopants enable these materials to possess high carrier concentrations and high mobility [3, 6, 8]. A wide bandgap ensures transparency throughout the visible portion of the electromagnetic spectrum (400 nm < λ < 700 nm). These important properties make TCO widely applicable for any device that requires optical access behind electrical circuitry [9].

TCOs discovery can be traced back to 1907 when K. Badeker [10] deposited cadmium thin film before heating it in air. This was resulted in a partial oxidation of the cadmium to non-stoichiometric cadmium oxide, leaving oxygen vacancies in its structure. This generates occupied defect energy levels from which electronic promotion into the cadmium oxide conduction band could easily take place. Although this was the first report of an n-type transparent conducting material, the films had a relatively high electrical resistance compared to metals and were susceptible to oxidation. Current TCOs include tin-doped indium oxide In_2O_3:Sn (ITO), fluorine doped tin oxide SnO_2:F (FTO) and aluminium doped zinc oxide ZnO:Al (AZO). These materials, instead of relying on intrinsic vacancies within the metal oxide structure, use the defect energy

levels created by the extrinsic dopant species to generate n-type conduction. ITO was the first modern TCOs material discovered by Rupperecht in 1954 [11] , and a few years later the TCOs market was flooded by indium tin oxide (ITO) due to its high optical transparency (> 90%) and electrical conductivity and low surface resistivity (8-12 Ω/sq). This saw the consumption of several tons of indium which had limited reserves in the world. Owing to the dwindling global reserves of indium and the degradation of the films at the high temperatures required for certain device processing steps, attention was diverted to Zinc Oxide, a naturally n-type semiconductor, having a direct band gap of 3.37 eV and low threshold voltage [12, 13]. Apart from these essential properties for a TCO, ZnO offers a plethora of advantages compared to ITO such as availability, low cost, chemical inertness and non-toxicity [14]. Studies on heavily doped TCOs continue to stimulate tremendous interest due to their immense application potential due to metal-like conductive behavior. In this state, the TCOs are referred to as degenerate semiconductor in which the Fermi level, or average charge carrier energy, is either above the conduction band (in the case of electrons) or below the valence band (in the case of electron holes) [15]. An example of such doping is the use of Aluminium as reported in this work.

Another aspect of doping involves the use of Rare earth (RE) elements to ensure energy transfer from the host material (ZnO) to the RE such that the emitted photon from the RE earth can be within the absorption spectrum of solar cells.

Photovoltaic (PV) technologies incorporated with solar energy conversion approaches present an a promising alternative towards the realization of green and renewable energy generation [16]. Although the technology is not new, solar cell production remains costly, largely due to their low power conversion efficiencies [17-19]. The main challenge to realizing high conversion efficiency of PV cells is their insensitivity to the full solar emission spectrum. The spectral distribution of

sunlight at Air Mass 1.5 global (AM 1.5G) is made of photons of wide wavelengths ranging from ultraviolet to infrared (280–2500 nm, 4.4-0.5eV), while on the other hand the PVs only utilize a relatively small fraction of the photons due to their limited absorption of a narrow range of solar photons with energy matching the characteristic bandgap of the material [20].

Notably, the theoretical maximum level of efficiency for crystalline silicon (*c-Si*) with a bandgap energy (*E*g) of 1.1 eV is approximately 31% as defined by the Shockley–Queisser limit [21]. There has been intensive research aimed at overcoming the energy losses mainly attributed to non-absorption of low energy photons ($E < E_g$) and thermalization of above band gap photons. This was motivated by Trupke *et al* theoretical extension of conversion efficiency to 38.6% through modification of the solar spectrum [22, 23].

In recent years, luminescent materials capable of converting a broad spectrum of light into photons of a particular wavelength have been reported. This has paved the way for applications to minimize the losses in the solar-cell-based energy conversion processes. Rare earth doped TCOs present explicit examples of such developments due to their capacity to enhance spectral conversion through up-conversion, quantum cutting and down-shifting as illustrated in figure 1-1.

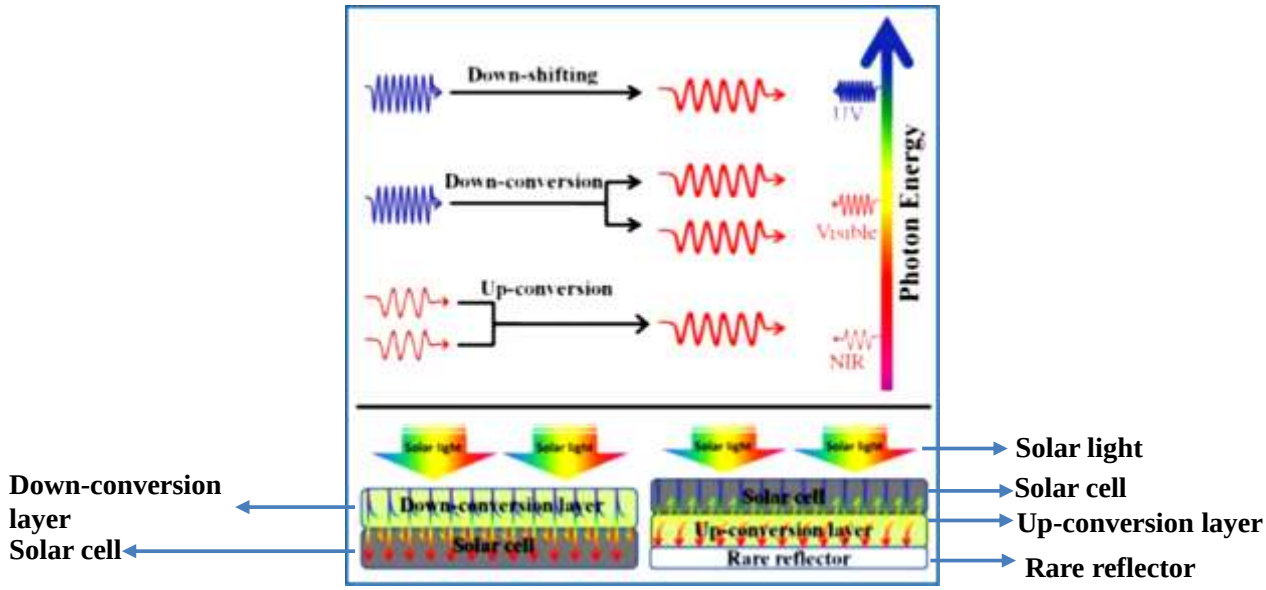


Figure 1-1: Mechanisms of photon luminescent conversion processes and simplified view of schemes of application into solar cells.

In this work, optimized TCOs thin films and spectral conversion layers have been incorporated into three solar cell device structures namely: organic solar cells (OSCs), Dye-Sensitized Cells (DSCs) and Perovskites solar cells and investigated for photoconversion efficiency enhancement.

1.1.1. Organic solar cells

In organic solar cells, the typical thickness of the active layer (P3HT:PCBM) is of the order of few hundred nanometers and hence the transparent electrode needs to have low surface roughness to avoid the occurrence of short circuits in the cell [24]. To minimize internal energy losses, the control of band alignment (work function) becomes a matter of great importance in these devices as well. Furthermore, these devices have the peculiarity of being fabricated at room temperature to be compatible with flexible substrates which remains a formidable challenge.

1.1.2. Dye-Sensitized Solar Cells (DSSCs) and perovskites

In Dye-Sensitized solar Cells (DSSCs), the oxide based layers constitute two main aspects: the

transparent electrode and the electron transport layer/photoanode. The electrode, apart from conventional high transparency and conductivity, requires a careful energy level matching to collect photogenerated charges from the dye. The transport layer constituted in this project by ZnO and RE doped ZnO also requires the fundamental properties of large surface area and mesoscale porosity for realization of maximum dye infiltration [25]. In the development of oxides for DSSCs, 3-dimensional architectures are of late replacing compact TCOs and commercial pastes [26, 27], which can also be used to perform the task of light scattering. Lately, new DSSCs-like devices employing perovskite-based materials as an active layers have been developed with promising efficiencies, but they are still far from application [28].

1.2. Problem statement

Transparent conducting oxides remain the electrode material of choice for optoelectronic and photovoltaic applications. The electrical and optical properties require optimization either through modification of film properties by the growth deposition and ion implantation methods. The first problem that is addressed in this thesis is a control of the growth process of ZnO thin films for the reproducible formation of a desired morphology amid highly sensitive growth environment as well as how to control native defects. The control of the ZnO crystallite size and size distribution is essential for tailoring optical and electrical properties to achieve effective incorporation into solar cells as transparent conducting electrodes (TCOs) for instance as excellent application as the buffer layer. Secondly, the thesis investigates the doping of wide band gap materials with trivalent rare earth (RE) ions to obtain optical activity. As such the effects of incorporation of Rare earth ions into the ZnO matrix in order to obtain RE-based efficient light emitters in red, green and blue spectral regions is explored in detail and also optimized.

The third problem is to explore the fact that the utilization of renewable energy sources is one of

the best eco-friendly options to refrain from using fossil fuels and emerging as the most feasible ways to mitigate the world's energy crisis. This is possible by ensuring enhanced efficiency of third generation solar cells such as dye-sensitized solar cell (DSSCs) and organic solar cell (OSC) which have received great attention as a promising technology for renewable energy exploration as a result of their flexibility, low toxicity to the environment and simple fabrication with low cost. This can be achieved through spectral conversion ensuring matching solar spectrum to the solar cell photon absorption window.

1.3. Aim and objectives

1.3.1. Aim

This work seeks to develop optically active materials and explore approaches to increase the photo conversion efficiency of solar cells. The harnessing of all the parts of the solar emission spectrum through application of efficient photo converters to match the absorption characteristic of the solar cells will be explored. To this end we carried out ion doping of the host semiconductor materials (ZnO) to enhance spectral conversion. The ZnO samples were first to be doped with Aluminium to enhance conductivity and thereafter with Rare earths ions (Tb^{3+}, Eu^{3+} and Sm^{+}) energy transfer in order to realize active materials for the efficient absorption and conversion of the solar radiation in solar cell.

1.3.2. Objectives

- To optimize the growth mechanisms of the host material to accommodate luminescent centres as well characterization of the grown ZnO thin films.

- To demonstrate the practical possibility to use the developed ZnO as TCOs in perovskite solar cells.
- To study both growth process & doping conditions for optimization of rare earth (RE) doped oxide films by RF sputtering and ion implantation processes, aiming primarily to develop highly luminescent materials and to study their structural and optical properties.
- Characterisation of the deposited thin films to establish suitable parameters for efficient energy transfer process of the excitation energy. This step was to enable the attainment of efficient spectral conversion.
- To develop a deeper understanding on the dominant factors in the doping process that determines luminescence and losses (i.e. the relationship between luminescence properties, and the matrix excitation energy transfer characteristics will be established).
- As a proof of concept, study the application of the developed materials in solar cells as efficient spectral down converter layers with functional photo-activity in organic and dye sensitized solar cells.

1.4. Motivation

The primary motivation is to search for optimized bi-functional layers of ZnO and RE doped ZnO thin films capable to be incorporated into solar cell devices with the aim of enhancing their efficiency. The solar cells do suffer losses which can be reduced through minimizing the mismatch between the active layer absorption spectrum and the solar emission spectrum

There is a huge potential in utilizing the abundant solar energy resource. Although the research on photovoltaics is at a mature stage, there are still opportunities to improve the technology to commensurate with the global energy demand. Higher efficiencies, lower costs, implementation of non-toxic and abundant materials as replacement of some of the present expensive and toxic

materials such as Indium are bound to further improve the technology and its implementation.

The application of ZnO layers in solar cells is expected to provide a window of opportunity due to the following attributes;

- it is readily available and inexpensive,
- high electrical conductivity,
- high excitonic binding energy,
- high electron mobility with undoped state
- versatile routes of fabrication.

Indeed it is regarded as a cheap replacement of silicon and gallium nitride based solar which give quite costly devices. In the recent years, ZnO nanostructures have been fronted as an alternative to TiO_2 when it comes to electron transport layers. Some of the unique combination of electrical and optical properties of bulk ZnO is the relatively high electron mobility (more than 1 order of magnitude larger than anatase TiO_2) [29, 30]. Furthermore ZnO has a very rich family of nanostructures [31-34] with diverse applications in optoelectronics and photovoltaics. Currently, ZnO is emerging as an efficient electron transport material in technologies, such as Dye-Sensitized Solar Cells (DSSCs) and inverted polymer solar cells [35][36], Quantum dot solar cells (QDSSCs) [37], biomedical applications, [38] and light emitting diodes [39, 40].

The role of various film growth parameters form the motivation of this work as they are crucial in the control of quantum size effects such as control over the nanoparticles size and size distribution which is essential for tailoring the electrical, chemical, optical and magnetic properties for desired applications of the nanomaterials devices. The target was to obtain enhanced physical and optical properties as well as to utilize the possibility and flexibility of controlling various growth

conditions in order to obtain more efficient but cheaper semiconducting devices capable of being produced in relatively larger volume. The ZnO thin films are then doped with different rare earths and the energy transfer from the host ZnO to the rare earth ions studied for the purpose of potential application into solar cell since the spectrally converted light energy matches the solar cell absorption spectrum range. The properties are investigated using a number of different characterization techniques.

1.5. References (for chapter 1)

[1] K. Siraj, J.Z. Hashmi, S. Naseem, M.S. Rafique, S. Shaukat, Microstructure and optical properties of rare-earth doped ZnO thin films, Materials Today: Proceedings, 2 (2015) 5365-5372.

[2] D.S. Ginley, C. Bright, Transparent conducting oxides, MRS bulletin, 25 (2000) 15-18.

[3] B.G. Lewis, D.C. Paine, Applications and processing of transparent conducting oxides, MRS bulletin, 25 (2000) 22-27.

[4] H. Kawazoe, H. Yanagi, K. Ueda, H. Hosono, Transparent p-type conducting oxides: design and fabrication of pn heterojunctions, Mrs Bulletin, 25 (2000) 28-36.

[5] T. Minami, New n-type transparent conducting oxides, MRS bulletin, 25 (2000) 38-44.

[6] R.G. Gordon, Criteria for choosing transparent conductors, MRS bulletin, 25 (2000) 52-57.

[7] A. Freeman, K. Poeppelmeier, T. Mason, R. Chang, T. Marks, Chemical and thin-film strategies for new transparent conducting oxides, MRS bulletin, 25 (2000) 45-51.

[8] T.J. Coutts, D.L. Young, X. Li, Characterization of transparent conducting oxides, Mrs Bulletin, 25 (2000) 58-65.

[9] H. Liu, V. Avrutin, N. Izyumskaya, Ü. Özgür, H. Morkoç, Transparent conducting oxides for electrode applications in light emitting and absorbing devices, Superlattices and Microstructures, 48 (2010) 458-484.

[10] K. Badeker, Electrical conductivity and thermo-electromotive force of some metallic compounds, Ann. Phys, 22 (1907) 749.

[11] G. Rupprecht, Untersuchungen der elektrischen und lichtelektrischen Leitfähigkeit dünner Indiumoxydschichten, Zeitschrift für Physik, 139 (1954) 504-517.

[12] M. Godlewski, E. Guziewicz, K. Kopalko, G. Łuka, M. Łukasiewicz, T. Krajewski, B. Witkowski, S. Gierałtowska, Zinc oxide for electronic, photovoltaic and optoelectronic applications, Low Temperature Physics, 37 (2011) 235-240.

[13] E. Senthil Kumar, S. Venkatesh, M. Ramachandra Rao, Oxygen vacancy controlled tunable magnetic and electrical transport properties of (Li, Ni)-codoped ZnO thin films, Applied Physics Letters, 96 (2010) 232504.

[14] D. Dimova-Malinovska, ZnO—An Advanced Material for Solar Cell, Optoelectronic and Sensor Applications, in: Nanostructured and Advanced Materials for Applications in Sensor, Optoelectronic and Photovoltaic Technology, Springer, 2005, pp. 139-154.

[15] D.S. Ginley, Nanoparticle derived contacts for photovoltaic cells, in: Electrochemical Society Proceedings, 1999, pp. 103-110.

[16] X. Huang, S. Han, W. Huang, X. Liu, Enhancing solar cell efficiency: the search for luminescent materials as spectral converters, Chemical Society Reviews, 42 (2013) 173-201.

[17] P.K. Nayak, G. Garcia-Belmonte, A. Kahn, J. Bisquert, D. Cahen, Photovoltaic efficiency limits and material disorder, Energy & Environmental Science, 5 (2012) 6022-6039.

[18] A.J. Nozik, J. Miller, Introduction to solar photon conversion, in, ACS Publications, 2010.

[19] H.A. Atwater, A. Polman, Plasmonics for improved photovoltaic devices, Nature materials, 9 (2010) 205.

[20] B. Richards, Enhancing the performance of silicon solar cells via the application of passive luminescence conversion layers, Solar energy materials and solar cells, 90 (2006) 2329-2337.

[21] W. Shockley, H.J. Queisser, Detailed balance limit of efficiency of p-n junction solar cells, Journal of applied physics, 32 (1961) 510-519.

[22] T. Trupke, M. Green, P. Würfel, Improving solar cell efficiencies by down-conversion of high-energy photons, Journal of applied physics, 92 (2002) 1668-1674.

[23] T. Trupke, M. Green, P. Würfel, Improving solar cell efficiencies by up-conversion of sub-band-gap light, Journal of Applied Physics, 92 (2002) 4117-4122.

[24] D.C. Olson, D.S. Ginley, Nanostructured TCOs (ZnO, TiO 2, and Beyond), in: Handbook of Transparent Conductors, Springer, 2011, pp. 425-457.

[25] M. Grätzel, Recent advances in sensitized mesoscopic solar cells, Accounts of chemical research, 42 (2009) 1788-1798.

[26] F. Sauvage, F. Di Fonzo, A. Li Bassi, C. Casari, V. Russo, G. Divitini, C. Ducati, C. Bottani, P. Comte, M. Graetzel, Hierarchical TiO2 photoanode for dye-sensitized solar cells, Nano letters, 10 (2010) 2562-2567.

[27] N. Memarian, I. Concina, A. Braga, S.M. Rozati, A. Vomiero, G. Sberveglieri, Hierarchically assembled ZnO nanocrystallites for high-efficiency dye-sensitized solar cells, Angewandte Chemie, 123 (2011) 12529-12533.

[28] H.J. Snaith, Perovskites: the emergence of a new era for low-cost, high-efficiency solar cells, The Journal of Physical Chemistry Letters, 4 (2013) 3623-3630.

[29] L. Forro, O. Chauvet, D. Emin, L. Zuppiroli, H. Berger, F. Levy, High mobility n-type charge carriers in large single crystals of anatase (TiO2), Journal of Applied Physics, 75 (1994) 633-635.

[30] D.C. Look, D.C. Reynolds, J. Sizelove, R. Jones, C.W. Litton, G. Cantwell, W. Harsch, Electrical properties of bulk ZnO, Solid state communications, 105 (1998) 399-401.

[31] Y. Mishra, S. Mohapatra, R. Singhal, D. Avasthi, D. Agarwal, S. Ogale, Au–ZnO: A tunable localized surface plasmonic nanocomposite, Applied Physics Letters, 92 (2008) 043107.

[32] C. Klingshirn, ZnO: From basics towards applications, physica status solidi (b), 244 (2007) 3027-3073.

[33] V.-M. Guérin, T. Pauporté, From nanowires to hierarchical structures of template-free electrodeposited ZnO for efficient dye-sensitized solar cells, Energy & Environmental Science, 4 (2011) 2971-2979.

[34] X. Jin, M. Götz, S. Wille, Y.K. Mishra, R. Adelung, C. Zollfrank, A Novel Concept for Self-Reporting Materials: Stress Sensitive Photoluminescence in ZnO Tetrapod Filled Elastomers, Advanced Materials, 25 (2013) 1342-1347.

[35] O. Lupan, T. Pauporté, B. Viana, Low-Voltage UV-Electroluminescence from ZnO-Nanowire Array/p-GaN Light-Emitting diodes, Advanced Materials, 22 (2010) 3298-3302.

[36] O. Lupan, T. Pauporté, T. Le Bahers, B. Viana, I. Ciofini, Wavelength-emission tuning of ZnO nanowire-based light-emitting diodes by Cu doping: experimental and computational insights, Advanced Functional Materials, 21 (2011) 3564-3572.

[37] J. A Makawana, C. B Sangani, Y.-F. Yao, Y.-T. Duan, P.-C. Lv, H.-L. Zhu, Recent Developments of Metal and Metal Oxide Nanocatalysts in Organic Synthesis, Mini reviews in medicinal chemistry, 16 (2016) 1303-1320.

[38] S. Zhu, Q. Meng, L. Wang, J. Zhang, Y. Song, H. Jin, K. Zhang, H. Sun, H. Wang, B. Yang, Highly photoluminescent carbon dots for multicolor patterning, sensors, and bioimaging, Angewandte Chemie, 125 (2013) 4045-4049.

[39] A. Lansdown, A. Taylor, Zinc and titanium oxides: promising UV-absorbers but what influence do they have on the intact skin?, International journal of cosmetic science, 19 (1997) 167-172.

[40] J.H. Kim, Y.C. Hong, H.S. Uhm, Synthesis of oxide nanoparticles via microwave plasma decomposition of initial materials, Surface and Coatings Technology, 201 (2007) 5114-5120.

Chapter 2: Introduction to ZnO, AZnO and Rare earth doped ZnO thin films

2.1. Introduction to Fundamentals on TCOs.

Transparent conductive oxides (TCOs) have gained extensive interest owing to a combination of high transparency in the visible range of light as well as their high electrical conductivity [1]. Since visible light has a wavelength range of 380-750 nm (3.26-1.65 eV), the transparent material needs to have a higher band gap energy of more than 3.26 eV. This transparency can be obtained due to intrinsic defects as well as extrinsic defects.

Transparent conductive oxide (TCOs) thin film was first reported more than 100 years ago in 1907 by Badeker [2]. This was a thin film of CdO prepared by thermally oxidizing a vacuum sputtered film of cadmium metal. Even though CdO has been of great theoretical interest because of its high electron mobility apparently caused by its low effective electron mass, is not widely used today due to toxicity concerns. In the initial stages of the discovery of TCOs, the deposition was carried out using post-oxidation of evaporated metal films to form the metal oxide [3]. In 1937 saw the first deposition of Tin Oxide (TO) using this method [4] followed by transparent conductive layer of indium oxide (IO) made by post-oxidation of metal thin films in 1954 [5]. There was little practical development of TCOs during the first 50 years following CdO discovery until the 1940s that saw the development of a chemical deposition method (pyrolysis) for TO, SnO_2, from $SnCl_4$ [3, 6]. During the second 50 years following its discovery (i.e., since 1957), TCOs films have developed significantly and now they are seen virtually in everyday applications ranging from digital watches to computer screens or other types of displays.

For the last 50 years up until today, Tin doped indium oxide, In_2O_3:Sn typically called indium-tin-oxide or ITO has remained the most highly used TCOs with varied applications used as a

transparent electrode in nearly all flat panel displays (FPDs). During the late 1950s and 1960s, ITO was mainly deposited using vacuum evaporation of In/Sn metal and via DC diode and RF sputtering of metal In/Sn alloy targets. The challenge was to control the deposition process in order to attain precise electrical and optical properties. For RF sputtering the coating thickness was controlled using fixed deposition time and power while for evaporation thickness estimation was made by visual detection of a specific color or color change that gave the order of interference in the coating [7, 8].

In the 1970s interest on TCOs was raised by the successful deposition of undoped ZnO films [9] and Al doped, AZnO [10] with good electrical and optical properties. However, the thermally evaporated ZnO coatings were quite unstable hence hindering wide spread application at this time. This led to intensive broad investigations of various dopants in ZnO and deposition methods beginning in the 1980s [11]. Zinc Oxide, besides being one of the most important wide band gap materials continues to be regarded as the most promising Transparent Conductive Oxides (TCOs). Being abundant in nature it is available at lower cost compared to the Tin and Indium based counterparts. Additionally it has the added advantage of being non-toxic and that it can be deposited at relatively low temperatures. ZnO will therefore be more preferred to ITO in making front electrodes of solar cells. This is because whereas ITO usually undergo reduction when exposed to hydrogen leading to additional absorption of light [12], ZnO is very stable in hydrogen atmosphere [13, 14].

With these advantages, the usage of ZnO and Al-doped ZnO is increasing in the industry day by day. As a semiconductor, ZnO has range of useful properties that greatly distinguish it from other semiconductor or oxides such as:

- *Direct and wide band gap*. This has been found to be 3.37 eV at room temperature and 3.44 eV at low temperatures. This wide band gap as stated earlier enables ZnO to be used in optoelectric applications in the blue/UV region such as in light emitting diodes, laser diodes and photodetectors [15-17].
- *Large exciton binding energy*. ZnO has a higher free-exciton binding energy of 60 meV [18, 19], even greater than GaN (25 meV). This allows for efficient excitonic emission at room temperature hence making ZnO a good candidate for optical devices which are based on excitonic effects.
- *Large piezoelectric constants*. In piezoelectric materials, an applied voltage generates a deformation in the crystal and vice versa. Such materials are useful in making sensors that detect, e.g., pressure or acceleration or serves as transducers and actuators. The low symmetry of the wurtzite crystal structure combined with a large electromechanical coupling in ZnO gives rise to strong piezoelectric and pyroelectric properties [20-23].
- *Strong luminescence*. The strong luminescence in the green-white spectral region makes it suitable for phosphor applications. The luminescence centres in ZnO are speculated to originate from oxygen vacancies or zinc interstitials [24]. This has been extensively studied in this project in subsequent chapters.
- *High sensitivity of surface conductivity to the presence of adsorbed species*. ZnO has a sensitive conductivity when its surface is exposed to various gases surfaces. This make it possible to detect freshness of food and drinks when used as a smell sensor since ZnO is sensitive to trimethylamine present in the odor from sea foods, and in the fragrance from wine and coffee [25].

- *Large non-linear optical coefficients*. According to Larciprete, M. C., *et al*. analysis of the second and third harmonic generation experiments, ZnO crystals and, in particular, thin films exhibit non-linear optical behavior, suitable for non-linear optical devices which are dependent on the crystallinity of the films. Among the deposition techniques capable of producing films with strong second-order non-linear response are laser deposition, reactive sputtering and spray pyrolysis [26]. Such non-linear optical response in ZnO thin films make it attractive for integrated non-linear optical devices.
- *High thermal conductivity*. This property makes it useful as an additive to avoid damage of materials at high temperatures. ZnO is a major component of the tires along with rubber which led to many inventions in the rubber industry and ceramic industry [27]. It removes heat during device operation with high efficiency. ZnO has a co-efficient of expansion and melting point close to that of Silica of about $3.16\times10^{-6}/^{\circ}C$ and 2000 ˚C respectively [28]. Usually its vapor pressure reaches 760 mm (normal atmospheric pressure) at around 1700 ˚C which is almost 300 ˚C below its melting point. According to Leverenz [29], the high thermal conductivity is as a result of the difficulty to break the Zn-O bonds along the *c*-axis where it possess directional strength unlike the non-directional strength of Zn-O bonds in the other directions.
- *Large single crystal availability*. Large area single crystals ZnO are readily available as wells as commercial epi-ready substrates. Bulk crystals can be achieved using various methods such as hydrothermal growth [30], vapor-phase transport [31] and melt growth at high pressure [32]. Thin films on the other hand can be grown by molecular-beam epitaxy, chemical vapor deposition (MOCVD), laser ablation or sputtering [33, 34].

- *Amenability to wet chemical etching*. ZnO thin films can be easily etched using acidic, alkaline as well as mixture solutions. This ensures flexibility in the process, design and integration of ZnO layers into electronic and optoelectronic devices. Amenability to low-temperature wet chemical etching greatly helps in device fabrication [35].
- *Radiation hardness*. High radiation hardness is crucial for high altitude applications or in space. According to Tuomisto, Filip, et al ZnO exhibits exceptionally high radiation hardness enabling irradiation-induced defects to fully recover upon annealing at 600 K [36]. According to Anderson Janotti and Chris G Van de Walle ZnO has a higher radiation hardness compared to GaN [35].

The above attributes of ZnO validate the intense focus on ZnO as a promising candidate material for optoelectronics, transparent electronics and spintronic applications.

2.2. Properties of ZnO

2.2.1. Structural properties of ZnO

The chemical binding character of ZnO lies between covalent and ionic bonding. Since there exists a strong ionicity of the bonds between Zn and O atoms (i.e about 0.62 on the Phillips scale), the two binding partners of ZnO can be denoted as Zn^{2+} and O^{2-} ions, respectively [37]. At ambient temperatures and pressure, ZnO crystallizes in the thermodynamically stable phase with a wurtzite structure, which belongs to the hexagonal system [38]. The wurtzite structure is based on the space group C_{6v}^4 in the Schoenflies notation and $P6_3mc$ in the Hermann–Mauguin notation. Figure 2-1 shows some of its characteristics: (a) It has four atoms per unit cell, two of similar element (b) Every atom is tetrahedrally coordinated, i.e. the four nearest neighbors are of the other atom sort.

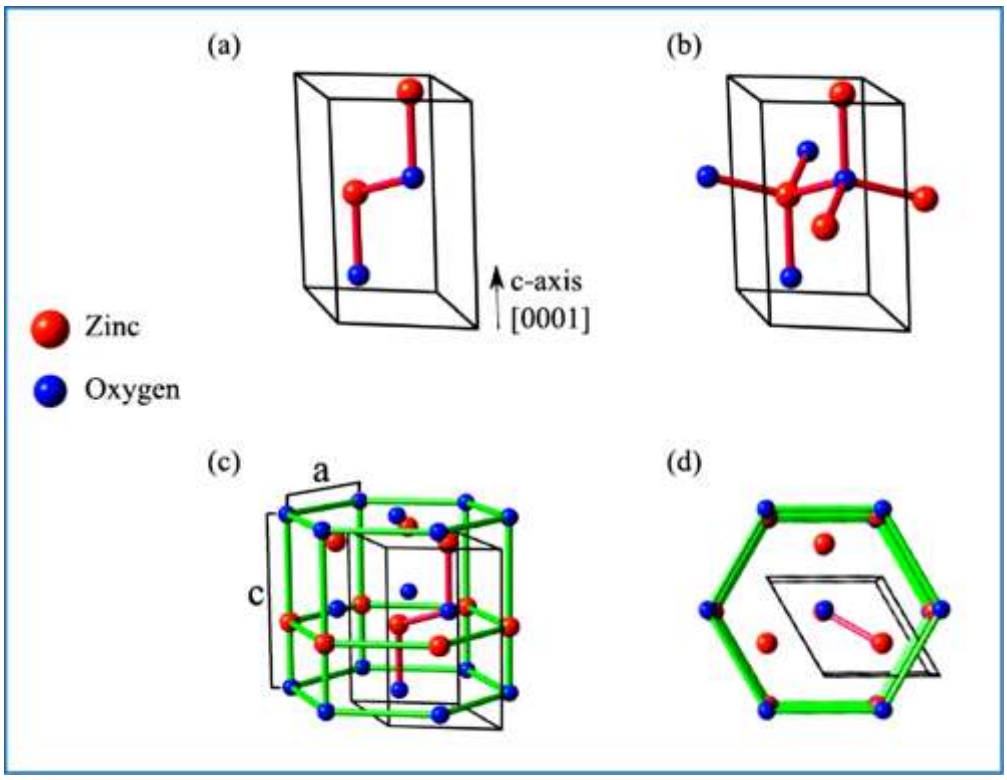


Figure 2-1: The wurtzite crystal structure ZnO with: (a) four atoms per unit cell, (b) tetrahedral coordination, (c) hexagonal symmetry and the lattice parameters a and c, (d) top view of (c) [38].

Figure 2-1 illustrates the wurtzite lattice of ZnO and the coordination of the constituent elements at various perspectives. There are lattice parameters *a*, *b* and *c*, and the internal parameter u and bond angles α and $\beta = 109.47^{\circ}$. The internal parameter u is defined as the ratio of the length of the bond parallel to the *c*-axis divided to the lattice parameter *c* (i.e *a/c*). The lattice constants of the ZnO unit cell are $a = b = 3.25$ Å and $c = 5.21$ Å, yielding a *c/a* ratio of 1.60, which is close to the ideal value of 1.63 [39-41].

From figure 2-1 (c) there are two faces of opposite polarity along the *c*-axis which are a Zn-terminated plane of (001) and a O- terminated labeled (001). There is no polarity in the planes of (100) along a-axis and (101) since Zn and O atoms are of equal number [1]. The interplanar distance between (100) and (002) and (101) are theoretically 0.2816, 0.2602 and 0.2476 nm, respectively. Usually the other plane (100) corresponding to the (300) family lies at about 0.1408

nm away from the other (100) [11]. This implies that a single monolayer of ZnO grown on this plane has a thickness of about 0.14 nm. This value is used for comparison with the growth rate that will be reported in this thesis during RF sputter deposition. Furthermore, ZnO oxide has a specific mass density of 5.675 g/cm^3, this will become important when simulating the film thickness using the X-Ray reflectometry techniques as discussed later in this thesis. Apart from the intrinsic material properties, the lattice parameters may vary depending on the extrinsic properties like the free electron concentration (via the deformation potential of the conduction band minimum), the foreign impurities concentration which may possess varied ionic radii capable of replacing the host atom, substrate-induced strain and annealing temperature [42].

2.2.2. Electronic properties

Figure 2-2 shows crucial surface potentials and energy transitions of a generic n-type TCOs. The fundamental band gap (Eg_0) gives the lowest energy (long wavelength) limit of optical transparency.

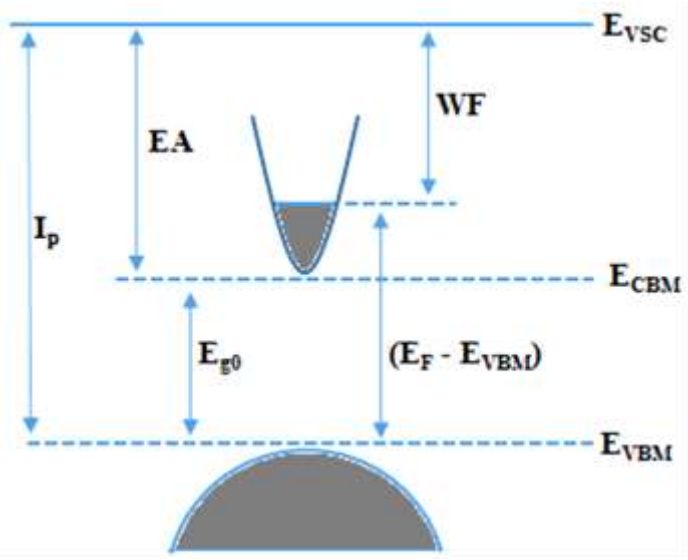


Figure 2-2: Schematics of typical TCOs band structure

Where I_p, WF, EA, E_{g0}, E_{vsc}, E_{CBM}, E_{VBM}, and E_F denote ionization potential, work function, electron affinity, intrinsic band gap, vacuum level, conduction band minimum, valence band maximum, and Fermi level, respectively. The WF is essentially the Fermi level measured from the vacuum level ($\phi = E_{vsc} - E_F$). This value is not a materials constant and can be modified using:

- Carrier-doping. This raises the Fermi level and hence lowering the work function (for a fixed ionization potential).
- Modification of the surface dipole. This can increase the ionization potential and therefore the work function (for a fixed Fermi level)
- A combination of both methods above.

In order to attain the much required transparency throughout the visible spectrum for application of TCOs, Eg_0 must be ≥3 eV [43]. According to Sernelius, Bo E., et al.[44], the optical band gaps could be widened in proportion to the added dopant as shown in figure 2-3. In their study, these authors used Al doping evaluated from spectrophotometric data which gave a wider band gap due to the high dispersion of the conduction band. The band gap can be stretched by ~5 eV or greater as shown in figure 2-2 as ($E_F - E_{VBM}$) where E_F is the Fermi level and E_{VBM} is the valence band maximum. This phenomenon is the well-known Burstein-Moss shift of the Fermi level with doping. The Fermi level ($E_F - E_{VBM}$) therefore gives the concentration of the carrier doping. A similar study of varying the band gap was carried out by Hamberg, I., *et al.* [45] in their study of Sn-doped semiconducting In_2O_3 and Berggren, K-F., *et al*. [46] who observed a shrinkage counteracted by the Burstein-Moss effect which gives a bandgap widening as a result of the blocking of the lowest states in the conduction band as shown in figure 2-3. In general, the higher the Fermi level, the more conductive the TCOs whereas excess doping level may cause free

carrier absorption and shift the associated plasma frequency into the visible from the infrared which limits the optical transparency [43].

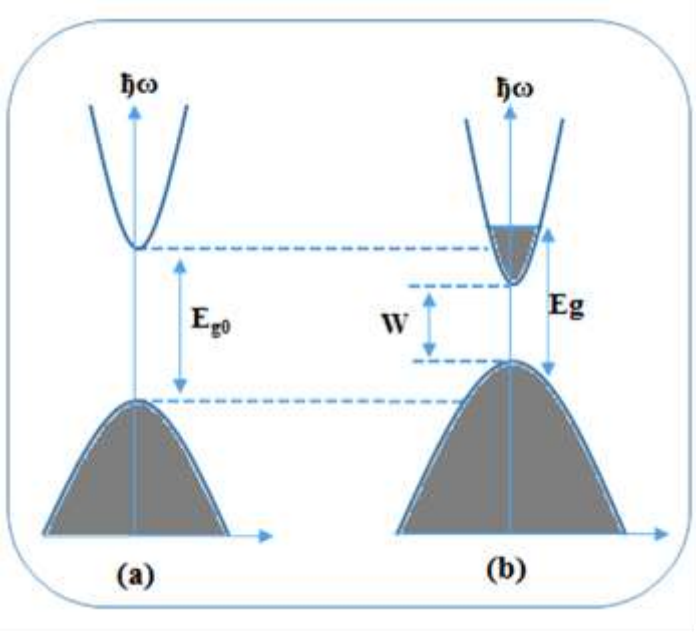


Figure 2-3: (a) the assumed band structure of TCOs in the vicinity of the top of the valence band and the bottom of the conduction band. (b) valence band shifted upwards by many body effects while the conduction band is shifted downwards. Shaded areas denote occupied states [43].

ZnO has deviations in stoichiometry caused by defects such that even if a stoichiometric phase is an insulator at room temperature, with a carrier concentration of the order of $10^{13}/10^{14}$ cm^{-3}, it exists as an n-type conductor. The crystal defects are attributed to the difference in the ion radii of Oxygen (1.4Å) and Zinc (0.74Å) which introduces voids/defects in the structure. Such deviations do also lead to the formation of free charge carriers as a result of the shallow donor levels associated with oxygen vacancies and interstitial zinc. To make ZnO conducting, the oxide must be doped to degeneracy by increasing the free carrier density enough to move the Fermi level into the conduction band [47] as shown in figure 2-2.

Theoretically the electronic band structures of ZnO have been calculated by several research groups [48-50]. By use of the standard density functional approach in the local density

approximation (LDA) the band gap have always been underestimated by ~3 eV due to the failure of LDA to model Zn 3d electrons accurately. This can however be corrected by the use of atomic self-interaction corrected pseudopotentials such that the Zn 3d electrons can be accurately accounted for [50]. Figure 2-4 shows an example of the calculation of the band structure along the high symmetry lines in the hexagonal Brillouin Zone. Both the valence band maxima and the lowest conduction band minima occur at the Γ point,(k = 0), an indication that ZnO is a direct band gap semiconductor [51]. The band gap as determined from this calculation is 3.56 eV which is relatively close to that measured in this work. Since the lattice constants vary with temperature and pressure, the electronic band structure also changes with temperature and pressure. The bandgap (at Γ point) shrinks with increasing temperature as given by the empirical relationship [52]:

$$E_g(T) = E_g(T=0) - \frac{\alpha T^2}{T+\beta} \quad \ldots\ldots\ldots\ldots\ldots\ldots \text{2-1}$$

where E_g (T=0) is the energy gap which may be direct (E_{gd}) or indirect (E_{gi}), Eo is its value at O˚K, and α and β are temperature coefficients which are given as $\alpha = -5.5\times10^{-4}$ eVK^{-1}while $\beta = -900K$ for temperature ranging to 300 K [53].

The variations in the band gap can also be attributed to the following changes in the lattice:

- shift in the relative position of the conduction and valence bands due to the temperature-dependent dilatation of the lattice.
- shift in the relative position of the conduction and valence bands due to a temperature-dependent electron phonon interaction [52].

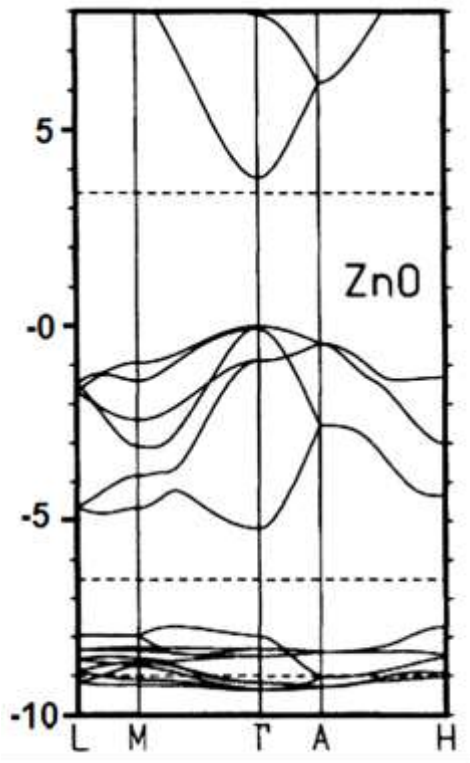


Figure 2-4: The local density approximation band structure of bulk wurtzite ZnO [51].

2.2.3. Optical properties

The optical transitions in TCOs can either be intrinsic or extrinsic. Intrinsic transitions involves transitions from conduction to valence band, including excitonic effects due to coulomb interactions while extrinsic transitions are created in the bandgap by dopants/impurities or point defects and complexes, which usually influence both optical absorption and emission processes as they create discrete energy levels inside the band gap. For the sake of ZnO thin films investigated in this thesis the strong emission peak around 380 nm as a result of band-to-band transition and green-yellow emission band related to the oxygen vacancy are reported.

ZnO is transparent to light in the visible region with a sharp cut-off in the UV region. The transparent region corresponds to wavelengths region from 0.3-2.5 μm [54]. Thus ZnO is transparent to visible light and absorbs ultra-violet light (photoconductive under UV light). The

typical optical transmittance of 90% can be attained for films deposited under optimum conditions. This property together with a refractive index of 2.0 makes it possible to use ZnO as the white pigment in the paint industry [28]. This combination of excellent optoelectronic properties makes doped ZnO suitable for applications as next generation novel devices capable of replacing their expensive indium tin oxide based counterparts.

Intrinsic optical properties of ZnO nanostructures have been intensively investigated in this thesis for possible application in photonic devices. Photoluminescence (PL) spectra of ZnO nanostructures have been probed with varied excitation wavelength sources. Excitonic emissions were observed from the PL spectra of ZnO showing that quantum size confinement can significantly enhance the exciton binding energy.

2.2.4. Thermal properties

ZnO has lattice constants *a* and *c* that are dependent on temperature and are quantified by thermal expansion coefficients, which are denoted as $\Delta a/a$ and $\Delta c/c$ for the in-plane and out-of-plane cases, respectively. They depend on the stoichiometry, presence of extended defects, and free carrier concentration. The typical room temperature values for ZnO are $\Delta a/a = 4.75\times10^{-6}K^{-1}$ and $\Delta c/c = 2.9\times10^{-6}K^{-1}$ [55]. These lattice constants also contribute to the lattice thermal conductivity κ as per equation 2-2 [56].

$$\kappa_{ph}(T) = TL_T \frac{1}{3} v_s C_{ph} \quad \ldots\ldots\ldots\ldots \text{2-2}$$

Where *T* is the temperature, v_s is the velocity of sound (almost independent of temperature), C_{ph} *(T)* is the lattice specific heat, and L_T is the phonon mean free path. Usually, the conductivity *k (T)* is known to first increase with temperature upto a particular maximum value (k_{max}) at certain

characteristic temperature T_{ch} before decreasing. Apart from the lattice parameters, point defects also play a significant role in thermal conductivity [57].

2.2.5. Lattice Dynamics

For wurtzite ZnO, there are 4 atoms per unit cell and this leads a total of 12 phonon modes, namely, 1 longitudinal acoustic (LA), 2 transverse acoustic (TA), 3 longitudinal optical (LO), and 6 transverse optical (TO) branches, the details of which are discussed in section 4-5. Infrared (IR) reflection and Raman spectroscopies have been commonly employed to derive zone center and some zone boundary phonon modes in ZnO. In the hexagonal structures with C_{6v}^4 symmetry, group theory predicts eight sets of phonon normal modes at the G point, namely, $2A_1 + 2E_1 + 2B_1 + 2E_2$. Among these, one set of A_1 and E_1 modes are acoustic, while the remaining six modes, namely, $A_1 + E_1 + 2B_1 + 2E_2$ are optical modes [58].

A summary of basic physical properties of ZnO is as shown in table 2-1

Table 2-1: summary of basic physical properties of ZnO

Physical Parameters	Values
Stable phase at 300K	Wurtzite
Lattice Parameters	a= 0.32495 nm, c= 0.52069 nm, u= 0.345, c/a = 1.602
Density	5.606 g/cm3
Melting point	1975°C
Refractive index	2.008
Energy gap	3.4eV, direct
Exciton binding energy	60meV
Electron effective mass	0.24

2.3. Native point defects in ZnO

2.3.1. Introduction to point defects.

Native or intrinsic defects can be described as imperfections in the crystal lattice involving the constituent elements only [59]. They include:

- Vacancies. These are missing atoms at regular lattice positions/sites
- Interstitials. These are additional atoms occupying interstices within the lattice
- Antisites. These are O atoms occupying Zn lattice sites or vice versa.

Native defects within a crystal strongly affect their electrical and optical properties and hence have a bearing on doping, minority carrier lifetime and luminescence efficiency. It is therefore crucial to understand the incorporation and behavior of ZnO point defects for successful application in semiconductor devices [35, 60, 61].

2.3.2. Defect concentrations and formation energies

The concentrations of point defects are highly determined by the formation energy of the defects. Thus the defect concentrations and their formation energies are not constant but also highly dependent on the growth or annealing conditions of the materials [62]. In thermodynamic equilibrium and in the dilute regime not taking into considerations the defect-defect interactions, point defect concentration can be described by the equation 2-3 [63] while formation energy of a charged point defect in ZnO is described by equation 2-4 [64]:

$$c = N_{sites} \exp(-\frac{E^f}{k_B T}) \quad \text{.....2-3}$$

where E^f is the formation energy, N_{sites} the number of sites the defect can be incorporated on, k_B is the Boltzmann constant, and T is the temperature.

From equation 2-3, the defects with high formation energies will occur in low concentrations while high concentration of defects will result from low formation energies.

$$\triangle E_f = E(N_{Zn}, N_o) - N_{Zn}\mu_{Zn} - N_o\mu_o + q\epsilon_F \quad \ldots\ldots\ldots \text{2-4}$$

where $E(N_{Zn}, N_O)$ is the total energy of a system containing zinc (N_{Zn}) and oxygen (N_O)atoms, μ_{Zn} and μ_O are the external zinc and oxygen chemical potentials, q is the charge of the defect (its sign included), and ϵ_F is the Fermi energy which is regarded as the energy of the reservoir (chemical potential) from which an electron is taken to form a charged defect [64].

2.3.3. Migration barriers and activation energies related to diffusion.

Point defects are known to migrate within the crystal. Neumann, G., and E. Kaldis summarized the experimental results for self-diffusion in ZnO up to 1981 where they reported a range of 1.9 to 3.3 eV for the activation energies of zinc self-diffusion and a wider range of 1.5 to 7.5 eV for oxygen self-diffusion [65]. The activation energy for self-diffusion or impurity diffusion (Q) is the sum of the formation energy of the defect that aid the process of diffusion, E^f as well as the migration energy barrier E^b as given by equation 2-5 [66].

$$Q = E^f + E^b \quad \ldots\ldots\ldots\ldots\ldots\ldots\ldots\ldots\ldots\ldots\ldots\ldots \text{2-5}$$

Where the migration energy barrier E^b is the energy difference between the equilibrium configuration and the configuration at the saddle point along the migration path and can be accurately obtained from density-functional calculations [62, 67] while E^f is often variable depending on the experimental conditions, such as the position of the Fermi level, and the Zn or O chemical potentials (μ_{Zn} and μ_O) [35].

2.3.4. Introduction to various intrinsic point defects in ZnO

2.3.4.1. The oxygen Vacancy V_O

This is a very common low energy of formation type of defect in ZnO and it is often considered the source of n-type conductivity. However this assertion has also been challenged by several research groups based on density-functional calculations that describes this vacancy as a deep donor with high formation energy in n-type ZnO (~ 3.5 eV) and hence it cannot contribute to n-type conductivity [68, 69]. Under n-type condition, the fermi level is near the bottom of the conduction band and the V_O is in the neutral charge state located at ~1 eV below the CBM. However its formation energy is much lower in p-type ZnO, where it assumes the 2+ charge state making it to be a source of compensation in p-type ZnO [68]. Formation of V_O^{2+} can be avoided during growth and annealing. This done by making the chemical potential approach oxygen rich atmosphere and/or by otherwise keeping the Fermi level away from the VBM, in such a way that the V_O^{2+} formation energy increases.

The migration of oxygen vacancy involves jumping of the nearest-neighbor oxygen atom of the oxygen lattice into the original vacant site leaving a vacancy behind. According to Janotti, Anderson, and Chris G. Van de Walle [69], the V_O migration is isotropic, i.e. migration barriers involving oxygen atoms from the basal plane of the vacancy and from planes above or below the basal plane of the vacancy have the same value. These authors reported a migration barrier of 2.4 eV and 1.7 eV for V_O^0 and V_O^{2+} respectively. The former is useful in n-type materials whereas the latter is relevant in semi-insulating or p-type materials. The V_O^0 defect is thus mobile at temperatures above 900 K while the V_O^{2+} defect is mobile at temperatures above 650 K.

2.3.4.2. The Zinc Vacancy V_{Zn}

Zinc vacancies are often formed in n-type samples prepared in oxygen-rich conditions. They are found in modest concentrations in n-type ZnO where they act as compensating centers. They introduce partly occupied states in the band gap as a result of broken bonds to 4 oxygen neighbor's. However they have high formation energy of 3.7 eV even in the most favorable extreme O-rich limit in p-type materials and therefore they occur in low concentrations. Migration of V_{Zn} usually takes place when a nearest-neighbor Zn atom moves into the vacant site leaving a vacancy behind. According to Anderson, and Chris G. Van de Walle [69], V_{Zn}^{2-} has a migration barrier of 1.4 eV, an indication that V_{Zn} is mobile at 540 K and above. Neutral V_{Zn} centres have a very high formation energy (~3.5 eV) even under oxygen rich conditions but slightly lower in n-type materials [70]. Experimentally, V_{Zn} is identified in ZnO by a broad and weak green luminescence centered around 2.4-2.5 eV although there seems to be no single source of this luminescence [71-74].

2.3.4.3. Zinc Interstitial Zn_i

The Zn_i defects have two occupancies in the wurtzite structure of ZnO, namely:

- At the tetrahedral interstitials site, also designated as "tet". This site contains one zinc and oxygen as nearest-neighbor atoms, at a distance ~ $0.833d_0$, where d_0 is the Zn-O bond length along the *c* axis. Thus the placement of the zinc atom at this site will most likely suffer severe geometrical constraints and thus in most cases it turns out to be unstable.
- At the octahedral interstitial site. The octahedral site is in the interstitial channel along the c axis at an equidistance from 3 zinc and 3 oxygen atoms by $1.07d_0$. Since this distance is less than that at the tetrahedral, Zn_i would preferably form at this site with a geometrical constraints of less than severity [63].

Zn interstitial has a thermodynamic transition level of ε (2+ / + /0) in the vicinity of the CBM,

where the three charge states have nearly identical formation energies of ~ 0.05 eV. Hence it is usually regarded as a shallow donor with experimental donor energy of 30 meV [75]. It has low formation energy of ~ 0.5 eV in p-type conditions in O-rich limit and is even negative at the O-poor limit. This enables Zn_i to compensate for holes in p-type ZnO. However, this defect has a high formation energy of ~4 eV under n-type conditions even at the O-poor limit. The migration barrier of Zn_i of 0.22 eV [76] or 0.57 eV [68] for the 2+ charge state makes it easier to diffuse and to bind with other defects/impurities [77].

2.3.4.4. Oxygen Interstitial O_i

This occurs when excess oxygen atoms are accommodated in the ZnO lattice. Just like zinc interstitial, O_i may occupy the tetrahedral interstitial site, octahedral site or form split interstitials. At the tetrahedral site, O_i is unstable and spontaneously relaxes into a split-interstitial configuration that shares a lattice site with one of the nearest-neighbor substitutional oxygen atoms with an O-O bond length of ~ 1.46 Å.

O_i at the octahedral site introduces states in the lower part of the band gap that may accept 2 electrons. Such states result from the oxygen *p* orbitals and give deep acceptor transition levels ε(0/-) and ε(-/2-) at 0.72 and 1.59 eV above the *VBM* [63]. O_i can exist either as electrically inactive O_i^0 (split) mainly in semi-insulating and p-type materials, or as deep acceptors at the octahedral interstitial site O_i^{2-} (oct) in n-type materials (E_F > 2.8 eV) [35]. At octahedral and tetrahedral sites, the O_i have high formation energies and may be electrically inactive except under extreme oxygen rich atmosphere and we do not expect oxygen interstitials to be present in significant concentrations under equilibrium conditions [59]. In this thesis, the role of oxygen interstitials on film properties after introducing excess oxygen during thin film growth is investigated.

The reported migration energy barrier for O_i^0 (split) is 0.9 eV, while that of O_i^{2-} (oct) through the hexagonal channel along the *c* axis is 1.1 eV. From these values it can be derived that O_i^0 (split) will become mobile at 340 K and above while O_i^{2-} (oct) will become mobile at 440 K and above [63].

2.3.4.5. Zinc Antisite Zn_O

The Zn_O antisite defect is formed when a zinc atom substitutes an oxygen host atom. They exist exclusively in the 2+ charge state, Zn_O^{2+} with the transition levels ε (2+/+) and ε (+/0) located above the conduction band minimum. Their formation energies are higher than that of Zn_i. However, they have shown a higher thermal stability. Anderson Janotti, Chris G. Van de Walle suggested that Zn_O diffusion mechanism can be split into Zn_i and V_O constituents. For n-type material under zinc rich environment reaction, the condition for the endothermic process as prescribed by equation 2-6 applies at an energy of ~ 2.8 eV. Hence it is quite difficult to annihilate the Zn_O as compared to Zn_i [68] defect.

$$Zn_O^{2+} \rightarrow Zn_i^{2+} + V_O^0 \quad \text{..... 2-6}$$

According to Sizelove *et al*. [75] the Zn_O contributes to n-type conductivity under non equilibrium conditions especially when created under irradiation ambient. Compared to Zn_i and V_{Zn} they diffuse at a slower pace and hence may accumulate in the crystal.

2.3.4.6. Oxygen Antisite O_{Zn}

This defect is prevalent in instances where an oxygen atom occupies a site on the zinc sub-lattice. It has the highest formation energy among native point defects even under the most favorable oxygen rich environment. O_{Zn} are deep acceptors and are quite unstable as they spontaneously

relax to off-site configurations. Just like Zn_O, they can be created under non-equilibrium conditions for instance irradiation or implantation and since they migrate quite slowly, they may accumulate in the crystal [68].

2.3.4.7. Summary of the point defects.

In summary, it has been shown that the native point defects represent one of the controversial thematic areas in majority semiconductors, and ZnO is no exception. This is because the measurement techniques are usually unable to correlate electrical or optical manifestation of defects to their origin specifically as summarized in figure 2-5. Probably it can be noted that the point defects in ZnO are also not well understood. While several assignments of the defect-related luminescence bands can be found in the literature, only a few of them are reliable.

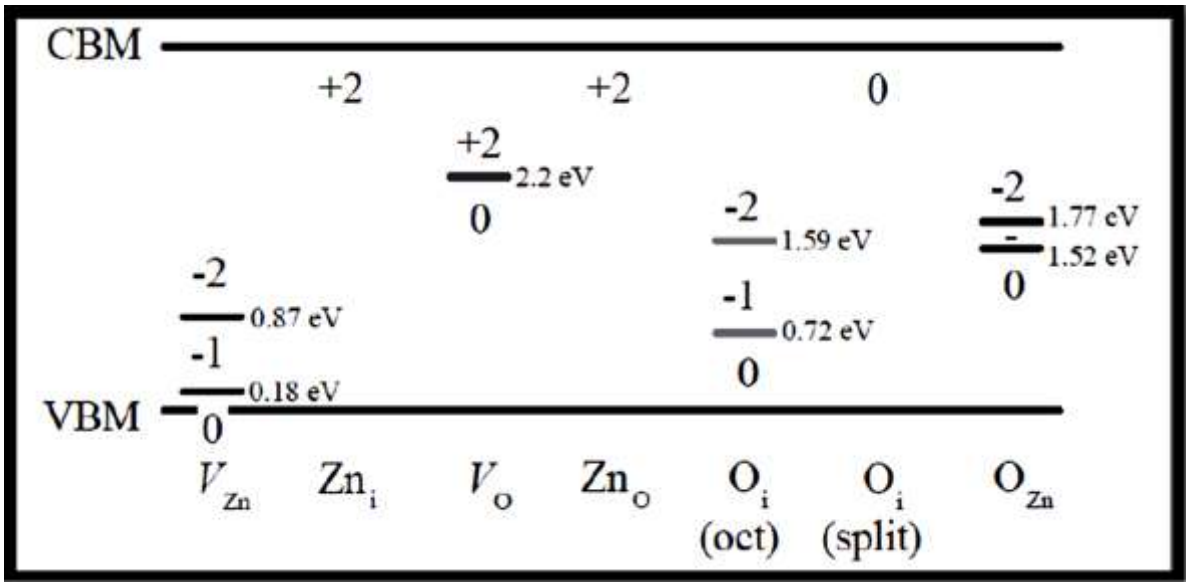


Figure 2-5: Thermodynamic transition levels for native defects in ZnO [78].

2.4. Luminescence properties of ZnO

2.4.1. Introduction.

Luminescence is defined as the emission of light by bodies usually in the excess of that attributed to black body radiation and it may persist for relatively longer time compared to electromagnetic radiations in the visible range upon the termination of an excitation [79].

In semiconductors, luminescence is the direct product of interband electron transitions from higher to lower energy levels under select Fermi Golden rules. Figure 2-6 shows the simplified band structure of a semiconductor near the centre of the first Brillouin zone, where a material with band gap energy *Eg* is irradiated by a laser with energy $hv>Eg$, leading to the following effects;

(a) The excitation of an electron into the higher energy levels of the conduction band (b) the formation of a hole in the valence band. An electron-hole pair (excitons) is therefore created.

(c) Thermalization of electrons and holes through the intraband transitions towards the lowest energy state of their respective bands via phonon emission.

d) Recombination of the exciton across the fundamental band gap or the defect levels within the band gap through either a radiative or non-radiative phonon related process (e).

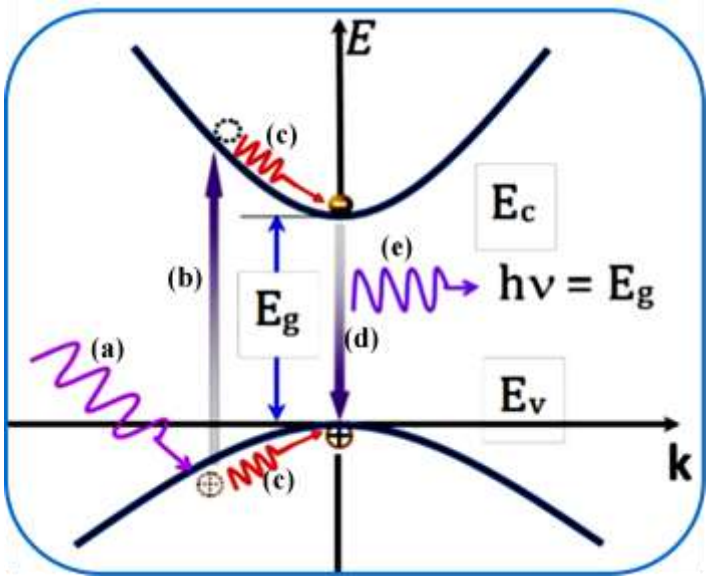


Figure 2-6: Band diagram illustration of the different processes that make up the photoluminescence spectra [79].

In a radiative mechanism, one photon with energy equal to or near the bandgap energy of the semiconductor is emitted due to electron–hole recombination [80] while in non-radiative recombination energy is exchanged with the lattice as heat through phonon emissions within defect states in semiconductor or transferred to other carriers without emission of any photon. This can take place through physical mechanisms, Auger recombination, recombination at defects in the bulk and surface recombination all of which cannot be detected by PL. Photoluminescence can help in band gap approximation, impurity levels and defect detection, thus determining the recombination mechanisms as well as the material quality.

Luminescence is classified as fluorescence and phosphorescence. Fluorescence is characterized by emission of relatively short persistence (10^{-6}-10^{-12} seconds) concerning the emission of light whereas phosphorescence persists for a considerable longer time up to seconds. Fluorescence usually obeys the decay equation 2-7:

$$I(t) = I_O \exp(-\alpha t) \quad \text{..... 2-7}$$

Where I_o is the initial intensity, *I (t)* is the intensity at time *t*, and α is a constant related to the absorption of the material. Luminescence occurs by simple excitation followed by an optical emission from the active centre with excitation energy remaining closely localized within the centre between excitation and emission.

On the other hand phosphorescence usually obeys the decay equation 2-8.

$$I(t) = \frac{I_o}{(\beta t + 1)^n} \quad \text{..... 2-8}$$

Where I_o is the initial intensity, *I (t)* is the intensity at time *t*, and β and *n* are constants. β depends on temperature. Here the atoms are ionized during excitation and luminescent radiation is emitted during recombination of the free electrons and the ionized centres. According to Johnson, R. P.[81], all centres may be ionized during excitation with majority of the free electrons being captured in a state with a much longer lifetime(~milliseconds) since optical transition to the ground state is forbidden.

2.4.2. Classification of luminescence

Further classification depends on the excitation source with a prefix is added for instance as shown in table 2-2:

Table 2-2: Various forms of luminescence adapted from Ref [79].

Luminescence type	Excitation source	Applications
Photoluminescence	Photons	Fluorescent lamps PL-LCD, Plasma display, Lasers, Luminescent solar concentrator (LSCs), paints
Radio luminescence	Ionising radiations e.g. X-ray or Gamma rays	X-ray imaging, Scintilators, dosimetry.
Cathodoluminescence	Electrons	TV set, Monitors, Field Emission Display (FED)
Electroluminescence	Electric field	Light emitting diodes (LEDs), Electroluminescent Display (ELDs), Diode lasers
Sonoluminescence	Ultrasound	Ultrasound diagnosis
Lyoluminescence	Chemical reaction energy	Detectors, Analytical devices, Lyoluminescence dosimetry
Chemiluminescence	Chemical reaction energy	Analytical chemistry
Bioluminescence	Biochemical reaction energy	Analytical chemistry
Triboluminescence	Mechanical energy	Certain types of sugar crystals.

Among the various luminescence, the phenomena of photoluminescence has found more application compared to others and has also been the preferred technique in this thesis. A detailed analysis of its working is given in section 3-5.

2.4.3. Fluorescence quenching

Quenching may defined as the decrease in intensity of light in a fluorescent compound at its maximum wavelength. When one material makes the fluorescence of another material to be diminished or abolished, then it is said to quench the fluorescence. There are 5 possible causes of quenching:

- Inner filter effect. This is an instrumental effect which has no influence on the primary process of emission but simply reduces the observed intensity of luminescence within the material being tested [82-84].
- Energy degradation. This quenching process involves the transition of singlet excited state molecule into triplet state by energy or electron transfers such that the fluorophores no longer emits its energy as fluorescence [85, 86].
- Energy transfer. Since the donor-acceptor pairs are such that they satisfy the conditions required for efficient transfer of energy, the acceptor molecule accepts the energy from donor by which the donor gets deactivated to its ground state and the acceptor is raised to a singlet excited level. The excited acceptors de-excite to the ground level either radiatively or non-radiatively. In a non-radiative process the fluorescence characteristics of the acceptor molecule is exhibited. The systematic variation of the acceptor concentration gradually quenches the fluorescence of the donor by energy transfer with simultaneous sensitization of acceptor fluorescence [87-89].

2.4.4. Advantages of Luminescence Techniques

Although all substances that show photoluminescence also experience absorption, luminescence only provides some of the most sensitive and specific spectroscopic techniques with the possible exception of radioactive labeling procedures. Advantages of luminescence include:

- High sensitivity. In highly luminescent materials low concentration of the luminescence centers to the level of 10^{-9} -10^{-12} can be detected. This is 10^{4} times greater than absorption spectroscopy.

- Better selectivity. The technique is more specific due to the fact that only about 10% of all substances that absorb radiation re-emit it as light and there are two selectable wavelengths (excitation and emission) in luminescence as opposed to only one in absorbance. Therefore, it is highly unlikely that two substances will share both a similar excitation and emission spectrum. This is because the difference between excitation and emission peaks can range anywhere from several nanometers to hundreds of nanometers.
- Environmental qualitative information. Since the lifetimes involved in the electronic transitions of luminescence is longer, it is far more sensitive to the local environment than absorbance. This allows luminescence to be an excellent local probe vehicle for its environment.
- Large linear quantitative range. Compared to spectrophotometers, luminescence instruments have a greater linear measurement range for quantitative analysis. A typical spectrophotometer has a usable range of between 0.1 to 3 absorbance units (less than 3 orders of magnitude). Furthermore, the absorbance errors are usually quite high and might even extend to 50% whereas luminescence instruments have greater linear ranges of 6 to 7 orders of magnitude with little error at the extremes.
- Multidimensional information. Photoluminescence is composed of two separate electronic transitions which give rise to the excitation and emission spectra of a given substance. This represents twice the amount of information contained in absorbance spectra and is quite useful in substance identification via various fingerprint techniques [90].

2.4.5. Photoluminescence spectra of ZnO

At room temperature, the photoluminescence spectrum of ZnO typically exhibits two luminescence bands namely;

- Short wavelength band located near the absorption edge of the material, this emission is also referred to as near band edge (NBE) luminescence.
- The second band is a broad wavelength band usually in the green spectral range (420 nm to 700 nm). This is attributed to the deep level emission band (DL) as a result of the native defects as discussed above. The DL band has previously been attributed to several defects in the crystal structure such as V_O [91-93], V_{Zn} [94-96], O_i [97, 98], Zn_i [99] and extrinsic impurities such as substitutional Cu [100].

2.5. Evolution of thin films

Polycrystalline films are composed of randomly oriented grains or crystallites with a particular size distribution. Each grain possesses a given crystallographic orientation relative to a fixed reference direction which is mostly the surface normal of the film. A non-random orientation of the grains in the film leads to crystallographic texture. During deposition of a polycrystalline film, several fundamental kinetic processes exist through which the micro- or nanostructure evolves. These may be classified into three stages:

2.5.1. Nucleation and growth of isolated islands.

During deposition, some atoms are adsorbed on arrival at the substrate surface. When stable clusters of adatoms form, nucleation takes place, which may eventually grow into islands. The nucleation rate and rate of islands growth depend mainly on several process parameters such as the deposition rate, the substrate temperature, total working gas pressure and the energy of particles impinging on the substrate. For instance, the nucleation rate generally increases with increase in deposition rate (coverage) and decreases with increase in temperature [101]. In the case of

nanocrystalline film deposition used in this thesis, a high nucleation rate is often desirable since it promotes a fine-grained structure.

The nucleation rate can be analyzed using classical methods based on the capillarity approximation or more appropriately in the current context, based on an atomistic analysis. Both approaches leads to nucleation rate given by equation 2-9.

$$I = I_0 R^{n^*} \exp\left(\frac{-\Delta G_{n^*}}{kT}\right) \quad \text{..... 2-9}$$

where I_0 is a temperature and deposition-flux-independent constant, k is Boltzmann's constant, and T is the temperature of the substrate and ΔG_{n^*} is the energy of formation of a cluster of size n^*, where n^* is the critical cluster size which is dependent on the dimensionality of the critical nuclei. For physical vapor deposition processes, n^* has a low integer value, often only 1 [102].

2.5.2. Island coalescence.

As the islands continue to grow, they reach a particular size at which they eventually begin to impinge on each other. The impingement of these islands with varied surface energies produces a driving force that leads to the formation of a grain boundary. At this point the islands with higher free surface energy are annihilated to coalesce to a continuous thin film. For a relatively low diffusivity, the attraction between the islands is usually accompanied by great strain in the developing film. This is the reason behind the intrinsic tensile stress mostly seen during the early stages of thin film growth [101]. In case of sufficient diffusivity, the growth can happen through grain boundary motion leading to complete elimination of the smaller islands. However, for low diffusivity, the grain boundary will remain intact resulting in relatively small grain sizes after coalescence. Since the energy of the individual islands is dependent on size and orientation,

structure evolution during coalescence can affect both the developing grain size distribution and the orientation distribution [103].

2.5.3. Film thickening.

Once the polycrystalline film has totally coalesced into a continuous film, any subsequent depositions will lead to the increase in film thicknesses. During this process of thickening, the film structure may evolve in various ways, depending on the actual deposition conditions and the adatom mobility in the system, i.e. the ability of atom to diffuse on the surface, grain boundaries as well as the grains interior [102]. Atoms arriving at the film surface may either undergo nucleation of new grains on top of existing grains, or contribute to “local epitaxial growth", i.e. join an already formed grain serving as a template with low-energy sites for further (growth-induced) grain growth. The mode involving nucleation of new grains is usually caused by impurities or the defects created during deposition, which serves as favorable nucleation sites; the resulting grain shapes are then predominantly equiaxed. However, for pure metals deposited under conditions with high atomic mobility “local epitaxial growth" growth mode is most common, resulting in columnar grains.

3.5.4. Grain growth.

Consider a fully coalesced polycrystalline film with an equiaxed grain structure. Grain coarsening may take place through movement of grain boundaries leading to shrinking and elimination of small grains hence resulting in increased average size of the remaining grains as shown in figure 2-7. Grain growth has been the subject of several reviews [104-106], and grain growth in polycrystalline thin films has also been the subject of a comprehensive review [107]. Grain growth in pure defect-free bulk materials is driven by the reduction in the total grain boundary area and in

the corresponding reduction in the total grain boundary energy that accompanies the area decrease. At a more microscopic scale this process is accomplished when individual boundaries move toward their centers of curvature in order to reduce boundary curvature and therefore boundary energy.

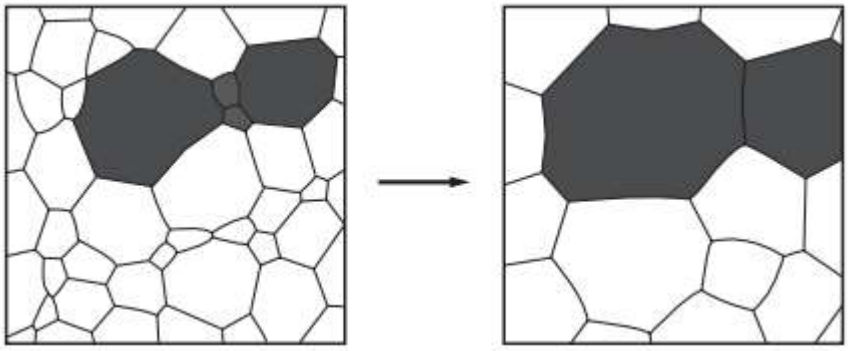


Figure 2-7: Grain growth in a continuous film with an in-plane grain size adapted from Ref. [102]

In addition, thin film structure may also develop during post-deposition processing leading to growth of the grains, recrystallization and defect annihilation. The mode of film structure evolves during the different processes depending on the exact processing conditions such as choice of materials, deposition rate, deposition and annealing temperatures, ion bombardment etc. Each of these growth conditions affects the diffusivity and mobility in the evolving thin film.

A summary of the three stages of growth is diagrammatically shown in figure 2-8.

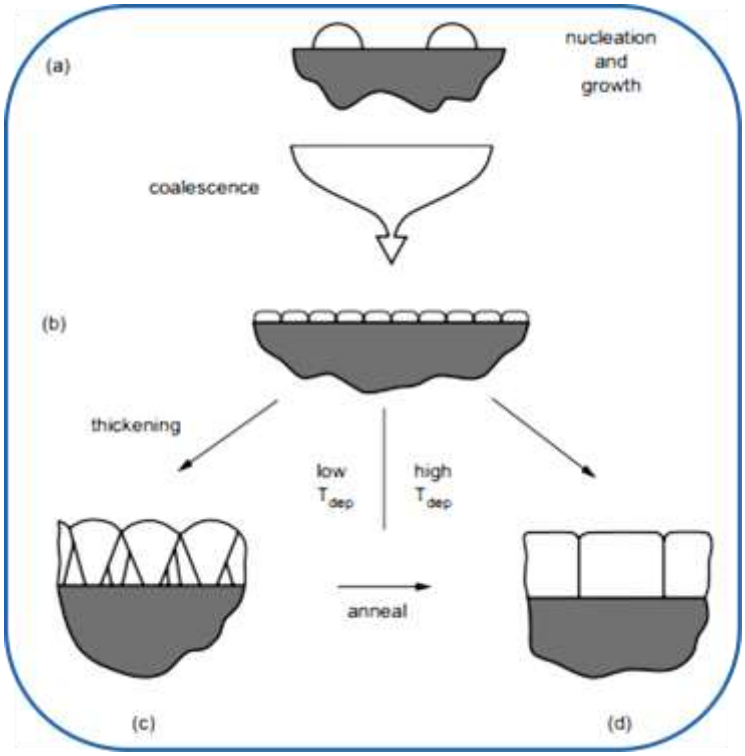


Figure 2-8: Overview of possible grain structure evolution during deposition of polycrystalline thin film adapted from ref [102].

2.6. Effect of annealing temperature on grain growth.

Annealing induces grain growth which is driven by the reduction in the total grain boundary area hence leading to a reduction in total free energy associated with the grain boundaries. Grain boundary migration is driven by the pressure difference formed by a curved grain boundary, which is proportional to γ_{gb}/r, where γ_{gb} is the grain boundary energy and r being the grain curvature radius (proportional to the grain size). The resulting driving force makes the boundaries to shift towards their center of curvature. Assuming that the velocity of grain boundary migration (or grain growth rate) dD/dt is proportional to the driving force, $dD/dt = K \cdot \gamma gb/r$, the grain size D at time t and constant temperature T can be defined by equation 2-10 [108].

$$D^2 - D_o^2 = K(T)t \quad \ldots\ldots\ldots\ldots\ldots\ldots\ldots\ldots \text{2-10}$$

Here D_0 is the initial mean grain size, and $K(T)$ is a thermally activated rate constant.

The rate constant is equivalent to the grain boundary mobility and can be expressed by an Arrhenius-type equation 2-11:

$$K = K_O \exp\left(\frac{-Q}{k_B T}\right) \quad \text{..... 2-11}$$

where K_0 is a pre-exponential constant, k_B is Boltzmann's constant, and Q is the activation energy for the rate limiting atomic process required for grain boundary migration. Grain growth that follows the parabolic expression in equation 2-10 is called normal grain growth [109] and usually also characterized by a time-invariant shape of the grain size distribution. The normal grain growth is quite rare except for high purity bulk metals at high homologous temperatures. However the most common temperature dependent grain growth is described by the empirical formula of equation 2-12

$$D^{1/n} - D_O^{1/n} = K_1(T)t \quad \text{..... 2-12}$$

where the growth exponent n usually deviates from the normal-grain-growth value 0.5. Observed values for n in nano-crystalline materials are mostly found in the range $n \leq 0.5$ [110], but also linear growth ($n = 1$) has been reported [111]. Usually n has a trend to increase towards the ideal value 0.5 as annealing temperature increases. The deviation from the ideal normal grain growth may be attributed to the fact that the velocity of grain boundary motion is not a linear function of the driving force, i.e. the mobility rate constant is not a constant but varies with the driving force (hence with D as well).

Other factors such as the interfacial energies associated with the film-surface interface may also contribute to the grain-growth behavior. For thin films studied in this project, particles impurity, pores or defects such as dislocations, vacancies, and stacking faults may also exert a drag or pinning force hence hindering the migration of grain boundaries. Such pinning forces are not

factored in equation 2-10 and 2-12. According to model proposed by Burke J. E. [112], grain growth with due regard to pinning forces may expressed as equation 2-13 where a limiting grain size is introduced.

$$\frac{D_o - D}{D_m} + \ln\left(\frac{D_m - D_o}{D_m - D}\right) = K_2 t \quad \text{..... 2-13}$$

where D_m is the maximum grain size resulting from to the pinning forces, and K_2 is again an Arrhenius-type rate constant.

Apart from drag or pinning forces the resistance to grain growth in nanocrystalline materials results may also be due to insufficient driving force as a result of structural factors such as equiaxed grain morphology, narrow grain-size distribution, relatively flat grain boundary configurations as well as low-energy grain boundary structures [113]. In these additional scenarios it may not be energetically favorable for one grain to grow at the expense of another yielding a metastable structure. With this variation of factors affecting grain growth, the activation energy values (Q) for isothermal grain growth may show a wide dispersion. Abnormal grain growth also termed as secondary recrystallization may occur due to these varied factors as a result of a combination of the inhibition of normal grain growth (such as because of impurity pinning) and the presence of a small number of special grains in the film that have a lower free energy which may contribute a net driving force for their growth [105, 114].

2.6.1. Effects of thermal annealing on film stress

In solids, atoms interact with each other via repulsive and attractive forces. In a crystalline material each atom is bound to an equilibrium position by those interatomic forces. Those forces can be seen as springs, which allow the atoms to vibrate near their equilibrium position. As the temperature rises the atoms gain more kinetic energy and their vibration amplitude grows. At

elevated temperature, excess kinetic energy of the atoms allows them to rearrange in the crystal lattice. Moreover, there is an increase in the diffusion of atoms in the material which enables the reduction of fluctuations in concentration. Thermal treatment also aids in improving the crystallinity of polycrystalline materials by reducing defects in the crystal lattice and allowing grain growth of polycrystalline material [115].

When films are annealed, the thermal mismatch between the film and the substrate must be taken into consideration. This is because the film and the substrates may possess different thermal expansion coefficients which induce thermal stresses. A typical examples arises when the deposited film possesses a higher coefficient of thermal expansion than the substrate such that the deposited film experiences compressive stress as the annealing temperature increases and vice versa. Such stress realized during annealing, compressive or tensile, is called thermal stress. Thin films may form cracks or other defects to relieve excessive stress. On the other side a thin film is deposited on a substrate with lower coefficient of thermal expansion than that of the thin film the assumption is that the thin film is relaxed during the steady state of the annealing hence the thin film will be in tensile stress after the annealing process [116].

2.7. Effect of Oxygen concentration on ZnO film quality

Oxygen partial pressure or flow rate plays a pivotal role in determining the deposition rate of ZnO as well as the structural, optical and electrical characteristics of ZnO. It is therefore necessary and sufficient to add oxygen during RF sputtering in order to attain a semiconducting ZnO film. According to Carcia *et al*., [117], the absence of oxygen or excess of it may make the ZnO film exhibiting either metallic or insulating properties. From their investigation on the dependence of electrical resistivity for sputtered ZnO thin films on oxygen partial pressure, the resistivity showed a transition from semiconducting at low oxygen partial pressure to semi-insulating at higher partial pressure [118, 119]. For ZnO thin films in this project we varied oxygen pressure from 0-15 sccm and analyzed the variation in film properties in chapter 4.

2.8. Doping of ZnO

2.8.1. Aluminum doping of ZnO

ZnO as a transparent conductive oxide (TCOs) has been under investigation for potential application in electronic and optoelectronic devices [120, 121], such as solar cells [122], liquid crystal displays [123], and high-definition displays and touch screens [124], due to its low resistivity (like a metal) and high optical transparency in the visible and near-infrared spectral region (like an insulator) [125]. Among the TCOs, indium tin oxide (ITO) film is the most widely used TCO material [126]. Therefore a breakthrough in understanding ZnO has a great potential of replacing the commonly used ITO which are scarce and toxic in nature. In order to realize conductivities above 5×10^{3} Scm^{-1} as well as high transmission in the near-infrared spectral range with high electron mobility, ZnO films have to be highly doped up to carrier concentrations of more than 5×10^{20} cm^{-3} [127]. For these reasons films doped with trivalent metal cations have attracted considerable attentions [128-131] and Al-doped ZnO (AZO) film has emerged as one of

the most promising candidates since it has many advantages, such as low cost, abundant resource, non-toxicity, and good stability in a hydrogen plasma [132]. Doping is the addition of foreign atoms or impurities to a compound by creating defect for enhancing its electrical and optical [133]. Importantly, the optical and electrical behaviors of AZO films can be improved or modified by controlling their doping level [134], which is critical to achieve functionality and tunability of TCOs-based devices. Therefore, it is useful to investigate the correlation between the properties of AZO films and the concentration of Al doping. Various research groups have applied different routes to preparing AZO films, including atomic layer deposition (ALD) [135, 136], chemical vapor deposition (CVD) [137, 138], magnetron sputtering [139, 140], and pulsed laser deposition (PLD) [141]. Comparatively, magnetron sputtering has been widely used since the charged particles are contained by a closed magnetic field and high density plasma is produced in the vicinity of the cathode. This results in;

- a strong decrease of the plasma impedance and a decrease of the discharge voltage, typically up to ~ 500 V
- a strong increase in the deposition rate
- excellent plasma confinement enabling sputtering at lower pressures compared to diode sputtering systems, typically at 0.1-1 Pa [142].

2.8.2. Rare earth doping.

Another aspect of doping ZnO is the use of trivalent rare earth elements due to their optical and high conductivity properties [143-146]. Rare earth metals doping for providing wide bandgap semiconductors continues to be of interest for display applications involving UV, visible, and infrared light emission. Wide band gap semiconductors such as ZnO also exhibit less thermal quenching of emissions than narrow band gap semiconductors [133]. Rare earths (e.g., La, Tb, Er,

Eu, Dy and Sm) provide many interesting properties of ZnO materials, which includes the efficient modulation of the emission in the visible range due to their unique optical properties [147].

2.8.3. Rare earths, RE

The discovery of light emission from rare earth (RE) ions dates back to the 19th century. Rare earths "RE" refers to a group of chemically similar (same number of electrons in their outer atomic shell) metallic elements that occur naturally [148, 149].

Rare Earths are isotopically stable with an outer electronic configuration of trivalent ions and are known to have RE^{3+} as the dominant oxidation state. RE earths include both actinium (Z=89-103) and lanthanides (Z= 57-70) and have a general form of $[Xe]5s^2 5p^6 4f^n$ where [Xe] represents the electronic configuration of the xenon atom and *n* refers to the number of 4f electrons. These partially filled 4f orbitals have different energies exhibiting a rich energy level structure, with a typical wavelength covering from ultraviolet, visible to infra-red part of the spectrum making them perfect "photon managers" that can be used to efficiently convert radiation into photons of any desired wavelength [150, 151]. The characteristic energy level structure of rare earth ions called Dieke Diagram [152, 153]86] is shown in figure 2-10. These partially filled 4f electronic levels are completely shielded by the filled outer $5s^2$ and $5p^6$ levels. The latter levels have larger radial extensions than the 4f shell and the latter are thus weakly affected by the ions in the surrounding medium in the host matrix. As a result of this all the trivalent ions result in very narrow and sharp optical absorption and emission bands which are relatively independent of the host matrix [154].

From the vector sum of the orbital angular momentum of all 4f electrons, the orbital angular momentum quantum number, L and spin quantum number, S can be calculated where the total angular momentum quantum number denoted as J is vectorially given by equation 2-14.

$$J = L + S \quad \ldots\ldots\ldots\ldots\ldots\ldots\ldots \text{2-14}$$

Where L can take the values $L = 0 - (n-1)$. On the other hand S by arrows as below:

$\uparrow is(+1/2)$ while $\downarrow is(-1/2)$. There are $(2S+1)$ degenerate levels in each electronic state, the $(2S+1)$ term is also called the spin multiplicity where the states having $S = 0$ are called singlets while states with $S=1$ are known as triplets. States with $L= 0, 1, 2, 3, 4, 5$ are spectroscopically denoted by letters S, P, D …. For instance, the ground state of Sm^{3+} is denoted by $^4G_{5/2}$ which means $S = 5/2$, $L = 5$ and $J = 5/2$. Table 2-3 shows the values of S, L, J of some RE^{3+} ions in their ground state.

Table 2-3: Electronic configuration of rare earth ions in their ground state [154].

Ion	Number of electrons (n)	$S = \sum_{i=1}^{n} s_i$	$L = \sum_{i=1}^{n} l_i$	$J = L - S$ (if n < 7) $J = L + S$ (if n ≥ 7)
Ce^{3+}	↑	1/2	3	5/2
Pr^{3+}	↑ ↑	1	5	4
Nd^{3+}	↑ ↑ ↑	3/2	6	9/2
Pm^{3+}	↑ ↑ ↑ ↑	2	6	4
Sm^{3+}	↑ ↑ ↑ ↑ ↑	5/2	5	5/2
Eu^{3+}	↑ ↑ ↑ ↑ ↑ ↑	3	3	0
Gd^{3+}	↑ ↑ ↑ ↑ ↑ ↑ ↑	7/2	0	7/2
Tb^{3+}	↑ ↓ ↑ ↑ ↑ ↑ ↑ ↑	3	3	6
Dy^{3+}	↑ ↓ ↑ ↓ ↑ ↑ ↑ ↑ ↑	5/2	5	15/2
Ho^{3+}	↑ ↓ ↑ ↓ ↑ ↓ ↑ ↑ ↑ ↑	2	6	8
Er^{3+}	↑ ↓ ↑ ↓ ↑ ↓ ↑ ↓ ↑ ↑ ↑	3/2	6	15/2

However, when a rare earth atom/ion is embedded in a chemical environment for instance a crystal (ordered structure) or a glass (amorphous) their spherical symmetry is disturbed by the crystal field of the host (i.e. electrostatic field of the atomic arrangements). This leads to a shift and splitting of the energy of these free-ion atomic states into a numerous states that are dependent on the site symmetry of the ions inside the host matrix. These induced electronic states are called Stark levels. Figure 2-9 shows a simple schematic representation of the splitting of the $4f^n$ electronic configuration [155]. The electrostatic crystal forces are two orders of magnitude lower than the atomic forces (spin-orbit interaction). These smaller forces split the free-ion atomic (spin-orbit) levels into a collection of Stark levels.

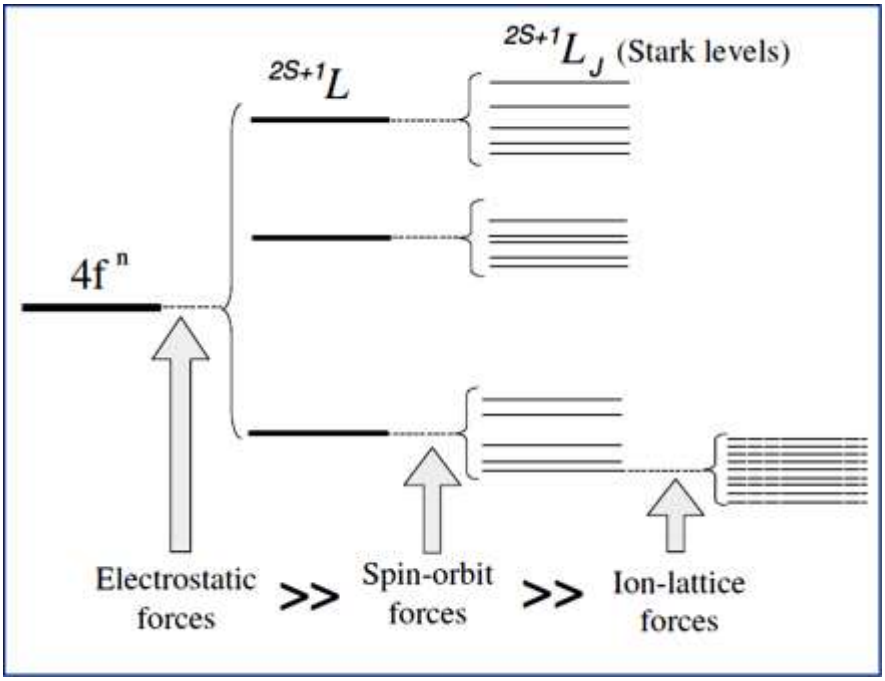


Figure 2-9: Schematic representation of the splitting of the 4fn state of a free rare earth ion as a result of atomic and crystal field forces ref [155].

The optical properties of Rare earth ions are usually dominated by the radiative transitions within the 4f manifolds. As a result, various research groups have investigated RE-related transitions. Dieke and co-workers [156] carried out intensive studies on the optical transitions of different

trivalent lanthanide ions embedded into lanthanum chloride ($LaCl_3$) bulk crystals and reported an energy level diagram detailing the energy of the different $(^{2S+1})L_J$ states for various RE^{3+} ions. The relative positions of the low-lying 4f energy levels of trivalent lanthanides ions are shown in figure 2-10.

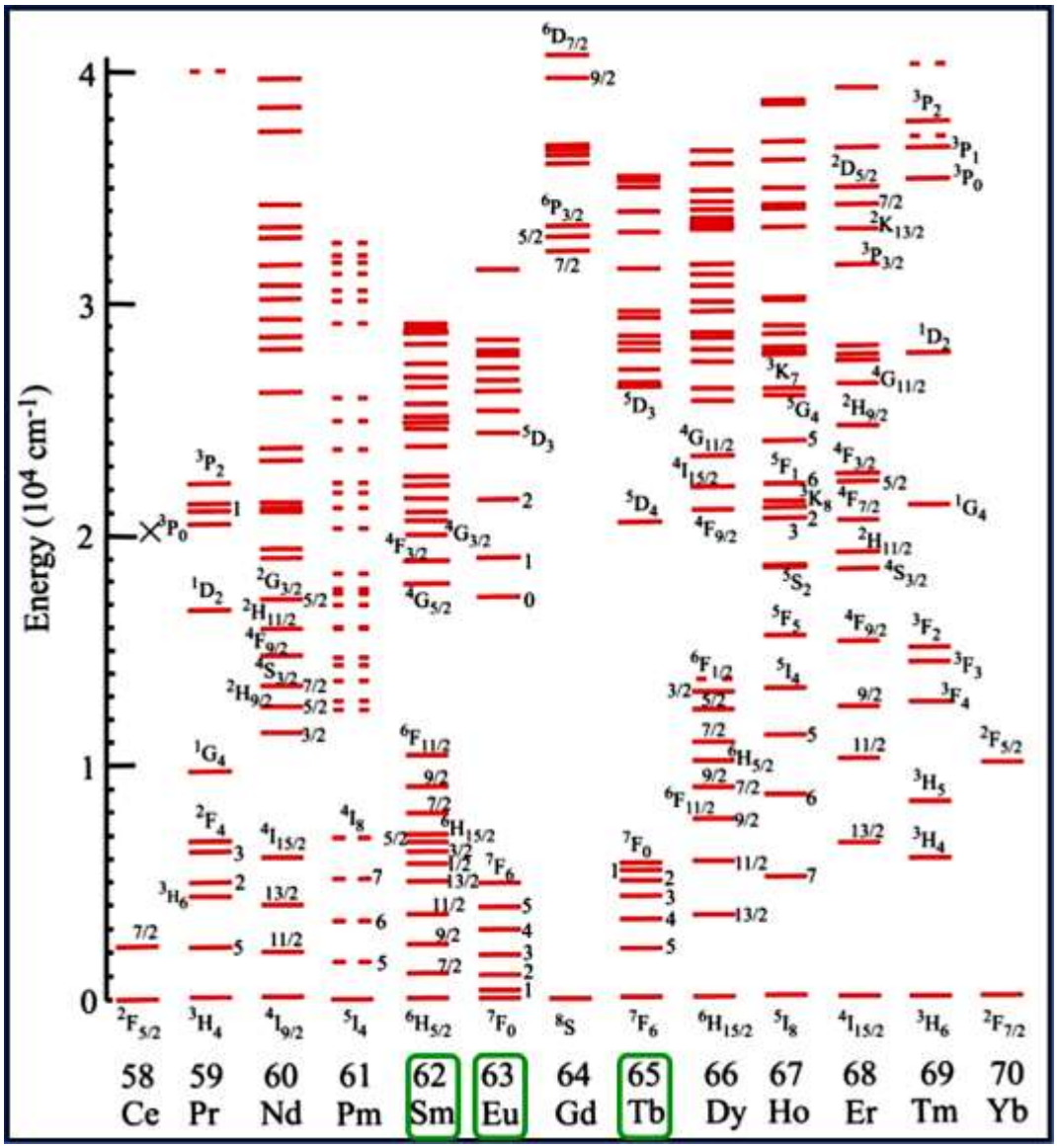


Figure 2-10: An energy-level diagram, called Dieke diagram, for trivalent lanthanide rare earth ions adapted from Ref [152]. The green frames indicate RE studied in this study.

2.8.4. Energy transfer in phosphors

2.8.4.1. Background

Energy transfer between and to the rare earth ions has widely applied in sensitizing solid state materials such as glass, infrared quantum counters and infrared to visible convertors. Although energy transfer between like and unlike rare earth ions is more understood at the present stage, the crucial transfer between ions enhancing transitions to the rare earth ions still needs thorough investigation [157]. The study of the excitation of rare-earth (RE) ions through energy transfers from semiconductor nanocrystals such as ZnO has received lots of interest lately. However, the energy transfer mechanism from ZnO to RE ions is still not well understood. Huang et al. [158] report that the energy transfer from ZnO to RE ions, specifically Eu^{3+} ions, is mainly due to the defects in the ZnO. Luo et al. [159] on the other hand have attributed the energy transfer to a combination of the band edge emission from the ZnO and the defects in the ZnO. Studies on ZnO-RE energy transfer have been based on steady-state photoluminescence (PL) emission from the nanocrystals to the rare earth [160].

During an excitation, ions may relax to the ground state through two channels namely; either radiatively or non-radiatively, the latter process being subdivided into internal non-radiative transitions and energy transfer. Non-radiative transfer from donors to acceptors depletes the population of the excited state of the donor and decreases the intensity and lifetime of the transition. In order that the transfer is significant and measurable, the rate of energy transfer must be of the same order of magnitude as the radiative transition in the donor ion.

In general, Semiconductor nanocrystals such as ZnO may be used as sensitizers to excite rare earth ions as a result of their intrinsic properties such as size-dependent luminescent properties [161], large absorption cross sections [162-164], and broad excitation spectra [165]. In this process, semiconductor nanocrystals are photoexcited to transfer the energy to the RE ions which

subsequently reemit light at a different wavelength [166]. The transfer mechanisms are discussed below.

2.8.4.2. Dexter energy transfer

The theory of energy transfer resonance according to the Dexter theory assumes two interacting luminescence centres, a Donor and an Acceptor within a distance *R*. These interactions can be either exchange or multipole-multipole interactions. When in resonance an energy transfer from one (donor) to another (acceptor) luminescence center may occur, however the nature of the energy transfer is also determined by the distance, *R* between the two ions. In the case of *R*<20 Å, the energy transfer may occur through the exchange interaction. On the other hand, multipolar interactions emerge in donor – acceptor separation distance, *R* in excess 20 Å. Thus there exists a critical distance *Rc* at which these events can be prevalent in the material and it is usually approximated to twice the radius of a sphere. *Rc* can be obtained using equation 2-15:

$$R_C = 2\left(\frac{3V}{4\pi X_c N}\right)^{1/3} \quad \ldots\ldots\ldots\ldots\ldots\ldots\ldots\ldots\ldots\ldots \text{2-15}$$

where *Xc* is the critical concentration at which the quenching occurs, *V* is the volume of the sphere, *N* is the number of lattice sites in the unit cell that can be occupied by activator ions [167-169].

For a case where the energy of the donor, *D* and acceptor, *A* are close to each other such that their electronic wave functions overlap each other as shown in figure 2.11, the excitation energy of the sensitizer *D* can be transferred to an acceptor *A* via exchange interaction.

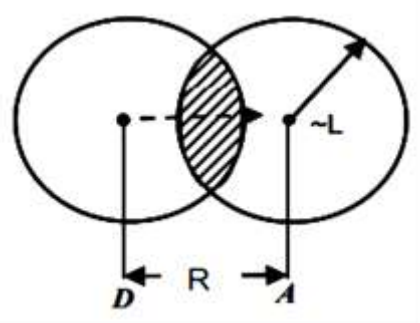


Figure 2-11: Resonant energy transfer by the quantum mechanical exchange interaction with overlapping D and A wave functions (shaded area).

The rate of energy transfer between a donor and an acceptor due to this interaction as derived by Dexter in the form of equation 2-16:

$$P_{DA}(ex) = 2\pi \left| \langle a'b | H_{DA} | ab' \rangle \right|^2 \int f_D(E) f_A(E) dE \quad \text{..... 2-16}$$

Where the integral represents the donor-acceptor absorption spectral overlap, $f_D(E)$ and $f_A(E)$ are the normalized shape of the donor emission and acceptor absorption spectra respectively. According to Inokuti, Mitio, and Fumio Hirayama [170], the exchange interaction has a time dependent fluorescence decay. In their approach the *S* ion is surrounded by a set of *A* ions at distance R_K. During energy transfer, the surrounding of the excited *A* is altered with time leading into a non-exponential decay as described by equation 2-17:

$$I = I_O \exp\left\{ \frac{-t}{\tau_A} - \gamma^{-3} \frac{C}{C_O} g\left(\frac{e^{\gamma} t}{\tau_A} \right) \right\} \quad \text{..... 2-17}$$

Where τ_A the decay time of the pure donor, C is the acceptor concentration expressed in the form:

$$C = \frac{3N}{4\pi R V^3} \quad \text{..... 2-18}$$

and C_0 describes the critical transfer concentration of an acceptor and is given by equation 2-19 as:

$$C_O = \frac{3}{4\pi R_O^3} \quad \text{.....2-19}$$

Where R_O and γ are constants described by Dexter quantities given by equation 2-20.

$$\gamma = 2\frac{R_O}{L} \quad \text{..... 2-20}$$

R_0 represents the critical distance which gives same radiative and non-radiative transfers probability. From equation 2-14 only the initial decay due to donors with closest acceptors is predicted while the slower portion of fluorescence decay is dominated by the contributions of the more distant acceptors [170].

2.8.4.2. Phonon-assisted energy transfer

Phonon assisted energy transfer is a process in which the mismatch of energy between the donor and acceptor is compensated by simultaneous emission and absorption of one or more phonons [171]. If the difference in ground state and excited state energy is large, then non-resonant energy transfer may also occur as shown in figure 2-12.

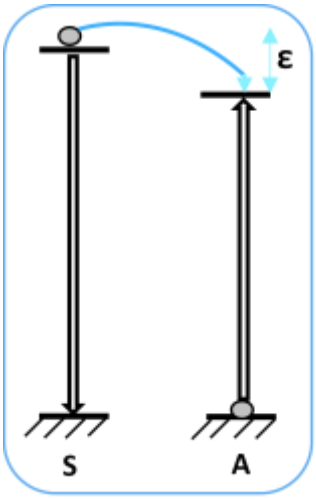


Figure 2-12: Phonon-assisted non-radiative transfer where ε is the energy mismatch [171].

For two rare earths ions with different excited states, the overlay in the $\int f_D(E) f_A(E) dE$ in equation 2-18 disappears causing the energy transfer probability to reduce to zero. Experimentally,

it is possible to have energy transfer in the absence of phonon-broadened electronic overlap so as long as the overall energy conservation is maintained by production or annihilation of phonons with energies is approaching $k_B\Theta_d$ where Θ_d is the Debye temperature of the host matrix [172]. However, energy transfer assisted by one or two phonons may take place in case of smaller energy mismatch (~100 cm^{-1}) [173]. Usually rare earth ions have high energy mismatches in the order of several thousand wave numbers which is much higher than the Debye cut off frequency found in many host matrix hence the need to consider multiphonon phenomena. This was carried out by Miyakawa and Dexter [157, 174]. In their theoretical analysis of multiphonon processes, Miyakawa and Dexter derived a comparative relaxation analogue of the multiphonon gap dependence. From their theoretical findings, the probability of phonon-assisted transfer (PAT) is given by equation 2-21:

$$W_{PAT}(\Delta E) = W_{PAT}(0)\exp(-\beta\Delta E) \quad \text{..... 2-21}$$

where ΔE is the energy gap between the electronic levels of donor and acceptor ions and β is a parameter dependent on the electron– (phonon) coupling strength and the nature of the phonon involved.

Equation 2-23 is similar to equation 2-22 that gives multiphonon relaxation dependent on the energy band gap also suggested by Miyakawa and Dexter.

$$W_{MPR}(\Delta E) = W_{MPR}(0)\exp(-\beta\Delta E) \quad \text{..... 2-22}$$

Another parameter α is described by equation 2-23:

$$\alpha = \frac{1}{\hbar\omega}\left\{\ln\left[\frac{N}{g}(n+1)\right]-1\right\} \quad \text{.....2-23}$$

where α and β are related by equation 2-24 and γ is described by equation 2-25.

$$\beta = \alpha - \gamma \quad \text{..... 2-24}$$

$$\gamma = \frac{1}{\hbar\omega}\ln\left(1+\frac{g_S}{g_A}\right) \quad \text{..... 2-25}$$

Where g_S and g_A are the electron–lattice coupling constants for the sensitizer and activator ions, respectively. n is the amount of phonons excited at the system temperature, $\hbar\omega$ is the energy of the phonon contributing mainly to the multi-phonon processes while N is the number of emitted phonons described by equation 2-26 [175].

$$N = \frac{\Delta E}{\hbar\omega} \quad \text{.....2-26}$$

2.8.4.3. Cross-relaxation

Cross relaxation also known as cooperative quenching is an energy transfer process between identical ions in which the non-radiative energy is simultaneously transferred from a single ion (donor) to two (or more) ions representing a cooperative acceptor. In this mechanism, the excitation energy of the electron that is initially a single localized donor ion is instantaneously shared between two (or more) acceptor ions, whereby the excitation is multiplicated and delocalized in space. The concentration which usually depend of the rate of the non-radiative energy transfer in the kinetic stage shows a parabolic behavior for the twinned cooperative acceptors and a cubic law for the triple cooperative acceptors [176]. The rare earth ions are known to undergo cross-relaxation because of their complicated energy level structure. For similar rare earth ions, cross-relaxation may experience quenching at higher concentrations. This effect is also permissible between identical rare earth ions with two pairs of energy levels that are separated by the same amount of energy. The two bandgap energies may be equal or can be matched by one or two phonons. This process has been observed in many ions and it is a dominating factor in non-radiative relaxations especially at high concentrations. Figure 2-13 shows diagrammatic representation of the cross-relaxation process.

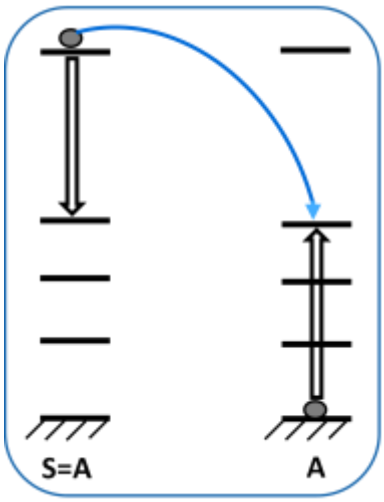


Figure 2-13: Cross-relaxation between two identical ions [176].

2.8.4.4. Migration of excitation energy

Relaxation of excitation energy by migration is a multistep process that involves the resonant energy transfer from one ion to another of the same species in a random walk manner culminating into a transfer to the acceptor acting as the quenching centre. According to Soules, Thomas F., et al. [177], the energy transfer from one donor to another is more likely to take place at low acceptor concentrations taking into account concentration quenching of fluorescence. When the two ions have comparable concentration and especially in the rare earth ions where the Stoke's shift is small, the $S \rightarrow S$ transfer is likely to be more rapid compared to the $S \rightarrow A$ transfer because of the resonant condition. As a result the excitation energy may then migrate among the sensitizer ions prior to passing to the activator hence decreasing the effective $S \rightarrow A$ distance. The diffusion of electrons over the donor energy levels may further increase the transfer efficiency. The migration of energy may also be treated as diffusion or a hopping process as reported in depth by Yokota M. and Osamu T. [178].

2.9. Applications of nanostructured ZnO based material.

2.9.1. Energy losses in solar cells

The theoretical maximum efficiency possible for a single junction solar cell consisting of a semiconducting material with a bandgap of ~1.1 eV (Si) is ~31%. This is called the Shockley–Queisser limit of the device [179]. However practically there exist a mismatch between the conventional single-junction solar cell spectral response (SR) and the solar emission spectrum. This is as a result of the limited efficiency absorption of the semiconducting material used in various active layers of the solar cell. Other sources of energy loses are depicted in figure 2-14.

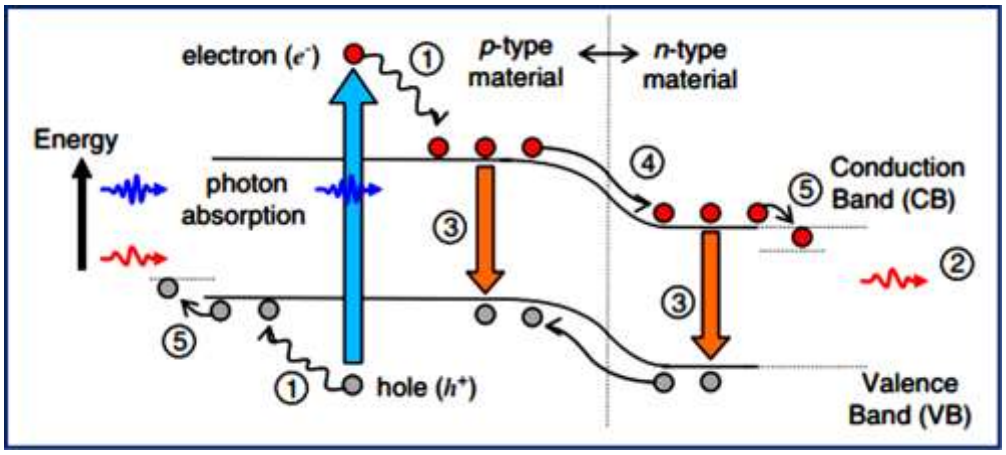


Figure 2-14: Energy loss processes in a single-junction solar cell [180]

Process (1) and (2) represent the major loss mechanisms in single junction solar cells amounting to over 70%. These losses in process (1) arise from the absorption of high energy (short wavelength) photons leading to the formation of hot carriers in the lattice. For photons with energy higher than the bandgap *Eg*, thermalisation loss is experienced in smaller band gap material based solar cells where photons are lost through non radiative relaxation of the excited electrons towards the conduction band in the form of heat. Process (2) indicates the transmission loss, in which the photons having energy lower than the bandgap *Eg* are not absorbed. Process (3) is the recombination loss while (4) and (5) corresponds to junction and contact voltage losses [180, 181].

These critical spectral losses limits the theoretical efficiency to $\eta = 25\%$ recorded experimentally with respect to AM 1.5G [182].

There have been numerous attempts to reduce the spectral mismatch accounting for the over 70% loss in energy. Out of these attempts, two basic approaches have been outstanding: (a) adaption of solar cell to better use the solar spectrum and (b) adapt the solar spectrum to better match the solar cell [180]. The application of the first approach has been successfully carried out in so-called multi-junction tandem solar cells for which efficiencies over 40% under concentrated solar light have been realized [183]. This has been possible using a combination of multiple semiconductor materials, each absorbing different portions of the solar spectrum [184, 185]. Even though tandem (two junction) solar cells are costly, they have gradually emerged as cost-competitive for terrestrial concentrated solar applications. Still under approach (a) other more recently proposed options include multiple exciton generation (MEG), and space-separated quantum cutting (SSQC). The former process involves the absorption of a high energy photon by the solar cell followed by a generation of multiple electron–hole pairs in the cell. MEG has attracted interest in various kinds of semiconductor nanocrystals ('quantum dots', *e.g.* CdSe, PbSe, and PbS) [186, 187] and has reported high efficiency of single junction solar cells to the tune of 44% [188, 189]. Another concept is space separated quantum cutting (SSQC) which has been investigated in Silicon nanocrystals [190]. Through SSQC, a high energy photon absorbed is split into two or more electron – hole pairs through the interaction of two spatially separated neighboring Si nanocrystals. SSQC has a potential to reduce energy loss resulting from thermalization in solar cells as well as multiply the number of charge carriers produced per absorbed photon in a solar cell. This however still needs further investigation to increase the efficiency of charge carrier generation [180].

The second approach (b) to raise the theoretical efficiency beyond the Shockley–Queisser limit has been under investigation through an attempt to modify incoming solar spectrum through incorporation of passive luminescence layers optically coupled above (for down-conversion and photoluminescence/downshifting) or below (for up-conversion) without altering the existing solar cells architecture for better utilization [191].

2.9.2. Effect of varying solar air-mass using up and down-conversion

Figure 2-15 shows the spectral irradiance of the solar spectrum modeled by a 6000 K black body, the extraterrestrial solar spectrum of air-mass zero (AM0), and also the terrestrial solar spectrum for various positions of the sun throughout the day as reflected by the solar air-mass [192, 193]. We see that the total power density shows a great reduction in the spectral irradiance at ultraviolet (UV) and visible wavelengths and an indication that the power contained in the AM10G spectrum is only one-fifth of that in the AM1G spectrum. Looking at a totally overcast day, the spectrum appears blue-shifted due to the higher component of scattered light under cloudy skies [181].

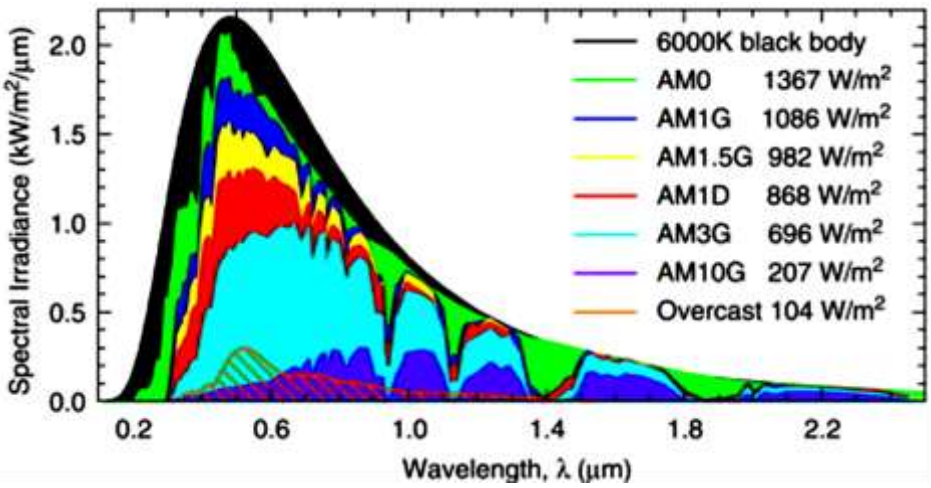


Figure 2-15: Spectral irradiance and power contained within various solar spectra [181].

Looking at AM1.5G spectrum plots in figure 2-16 the maximum fraction of light that can be absorbed by a bulk Si device is 468 W/m^2. Since silicon possesses an indirect band gap, a value of 1150 nm is used as the cut-off response, to realize a two-photon emission through down conversion, each incident high-energy photon must possess energy of at least twice the Si band gap, or a wavelength of shorter than 550 nm. This extra fraction of the AM1.5G spectrum that is available to a down conversion to a maximum value of 149 W/m^2 is shown in figure 2-16. Similarly, for the up-conversion of two sub-band gap photons resulting in the emission of a single above-band gap photon, the former must exhibit an energy of at least half the Si band gap, or longer than 2210 nm [181]. So far the best lab-scale Si solar cells with a one-Sun efficiency of $\eta = 24.7\%$ has been realized. Motivated by the predicted dominance of Si PV technologies for the next decades, several research groups have been actively pursuing the application of luminescence up-conversion (UC) [194-197] and down-conversion (DC) [181, 198-200].

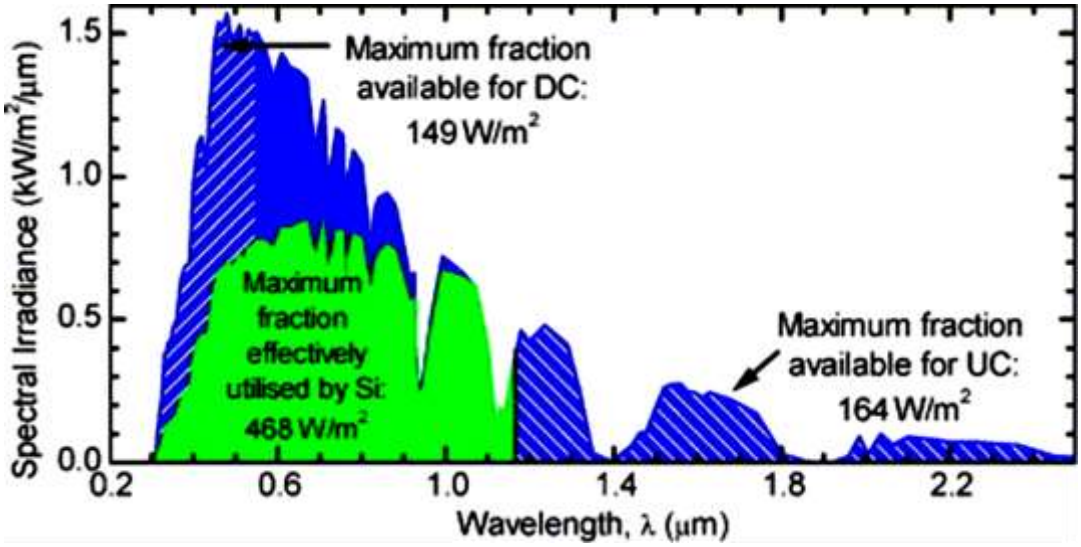


Figure 2-16: AM1.5G spectrum showing the fraction that is currently absorbed by a thick silicon device and the additional regions of the spectrum that can contribute towards up- and down-conversion [181].

2.9.3. Down-conversion process.

The theoretical feasibility of down-conversion was first proposed by Dexter in 1957 [201]. Currently, this process is also known as quantum cutting, quantum splitting, multi-photon emission (MPE) or photon cascade emission (PCE) [191].

Down-conversion mechanism involves the simultaneous energy transfer from a donor to two acceptors, each accepting half the energy of the excited donor. Despite its discovery in 1957, the experimental evidence for quantum yields above 100% was first realized in 1974 for $YF_3:Pr^{3+}$ through a different mechanism to that of Dexter. It involved two sequential emission steps from the high energy $^1S_0$ level of Pr^{3+} ($^1S_0 \rightarrow {}^1I_6$) followed by a relaxation to the $^3P_0$ level and a subsequent emission of a second emission from $^3P_0$ to the $^3P_2$ [202, 203]. Later, Wegh, Rene T., et al. reported quantum cutting using two sequential energy transfer steps in the Gd^{3+}–Eu^{3+} couple [204].

Figure 2-17 shows the different kinds of down-conversion mechanisms for a pair of lanthanide ions. Figure 2-17(b) indicates the emission of two photons from ion pairs through cross-relaxation between ions (I) to (II), this is marked in the figure as process (1) which subsequently followed by an energy transfer from ions (I) to (II) denoted by (2). Both of these energy transfer steps are followed by radiative emission from ion (II). Alternatively a single energy transfer mechanism between ions (I) and (II) accompanied by photoemission by both ions can be prevalent as adduced in Figure 2-17 (c,d).

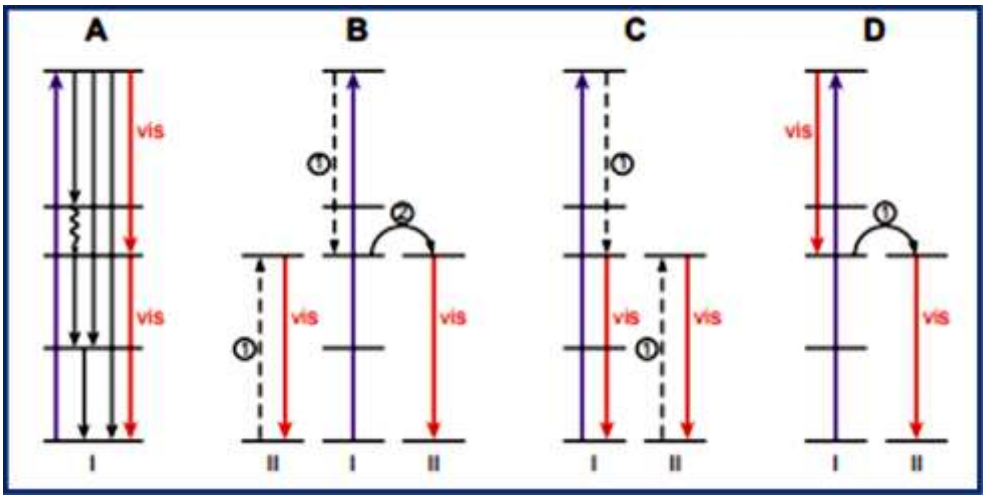


Figure 2-17: Overview of different resonant down-conversion mechanisms demonstrated using two ions, I and II, with hypothetical energy level schemes [203].

The solid vertical arrows indicate the transitions between energy levels while the dashed vertical arrows and solid curved arrows connecting different ions indicate the energy transfer. Horizontal lines are real energy levels. In the case of visible quantum cutting, the higher energy transitions are in the ultraviolet while the lower energy transitions are in the visible spectrum [203].

One aspect of down-conversion is the use of band-like down-converters where absorption occurs through excitation of the host-material. For incoming energy in excess of twice the energy of the band gap, Auger processes may be realized leading to creation of a second electron hole pair using the excess energy of the first excited electron [205]. This is also known as interband Auger transition (figure 2-18). Neglecting non-radiative relaxations, the quantum efficiency of the interband Auger process is the integer part of the ratio of excitation energy to band gap energy although just a few materials show a quantum efficiency greater than 1 practically [191].

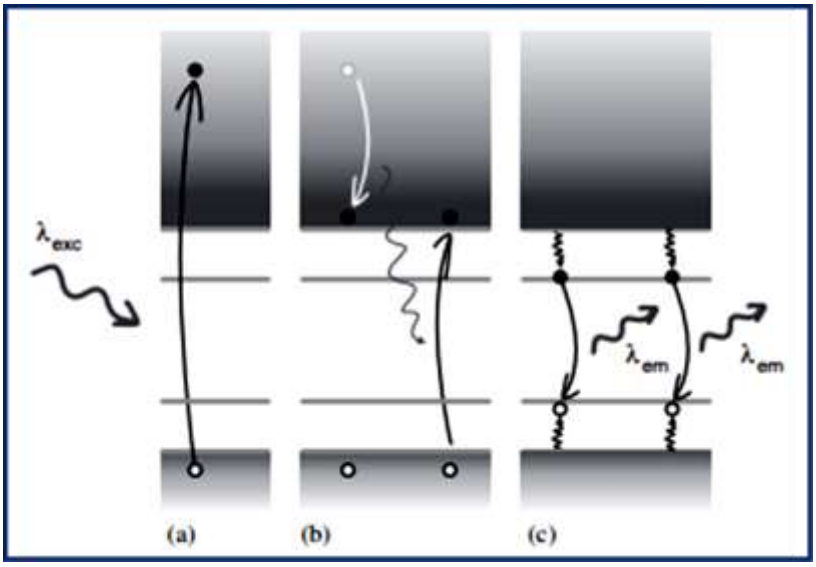


Figure 2-18: The interband Auger process. (a) A high energy photon creates an electron–hole pair and excites the electron deep into the conduction band. (b) This is followed by a non-radiative relaxation to the band edge of the conduction band, the excess energy is used to create a second electron–hole pair. (c) The radiative recombination of both electron–hole pairs via energy levels of the active ion leads to the emission of two low energy photons of wavelength, λ_{em}. [191].

For application in solar cells, a large number of ideal materials are available for luminescent down-converters layers for all existing types of solar cells but preference should be given to those that possess the following characteristics [191, 198, 206]:

- A wide band absorption (UV- blue region), particularly to cover the region where the spectral response (IQE) is low
- High absorption coefficient.
- High transmittance and narrow band emission where the IQE is high
- Large Stokes shift, i.e. the energy difference between the absorption and emission should be large enough to avoid re-absorption

Figure 2-19 shows a schematic representation of photovoltaic down-conversion/-shifting based device [207]:

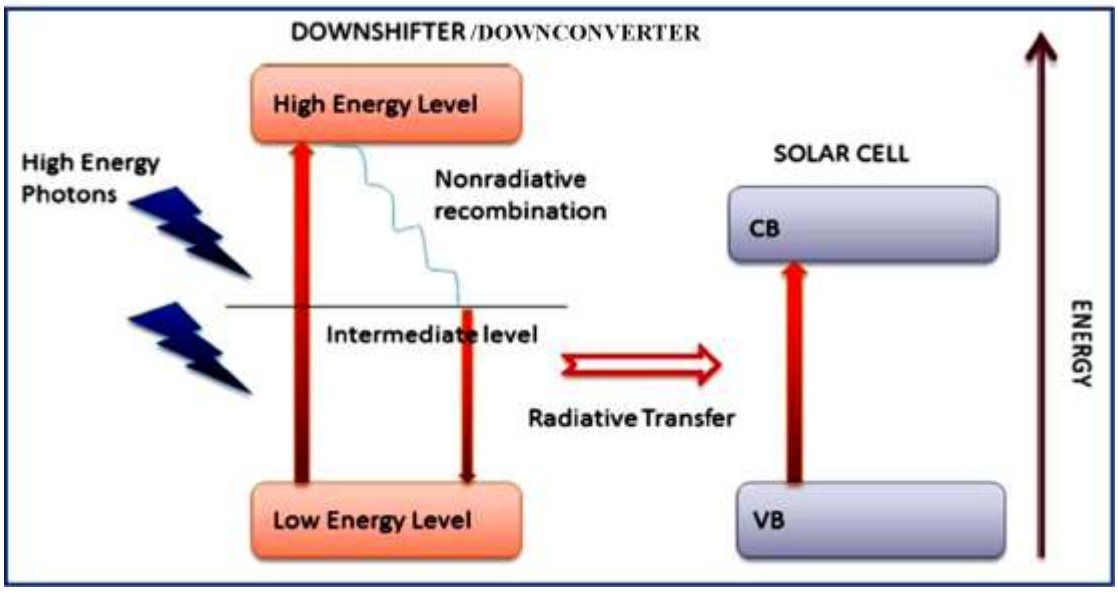


Figure 2-19: Schematic energy diagram of a solar cell in combination with active luminescence down-converter/down-shifter layer that precede the TCO layer in the device [207].

2.9.4. Down-shifting process.

Down-shifting is similar to down-conversion except for the fact that its external quantum efficiency cannot exceed unity. It involves the conversion of a (one) higher energy photon into a (one) lower energy photon such that when applied to a solar cell, it can enhance its efficiency by ensuring emission of photons that can be efficiently absorbed by the cell [197], although it could not be used to surpass the Shockley – Queisser efficiency limit. Various means can be used to realize downshifting such as the use of quantum dots [208, 209], lanthanide ions [210, 211], and other types of inorganic [212, 213] and organic materials [214].

2.9.5. Up-conversion process

The concept of up-conversion was first discovered by Auzel in the 1960s and has been particularly well investigated for lanthanide and transition metal ions doped into solids [215, 216]. It is based on the emission of at least one highly energetic photon by the absorption of two or more incoming photons by an up-converter layer. This can be obtained through various up-conversion mechanisms as summarized in figure 2-20.

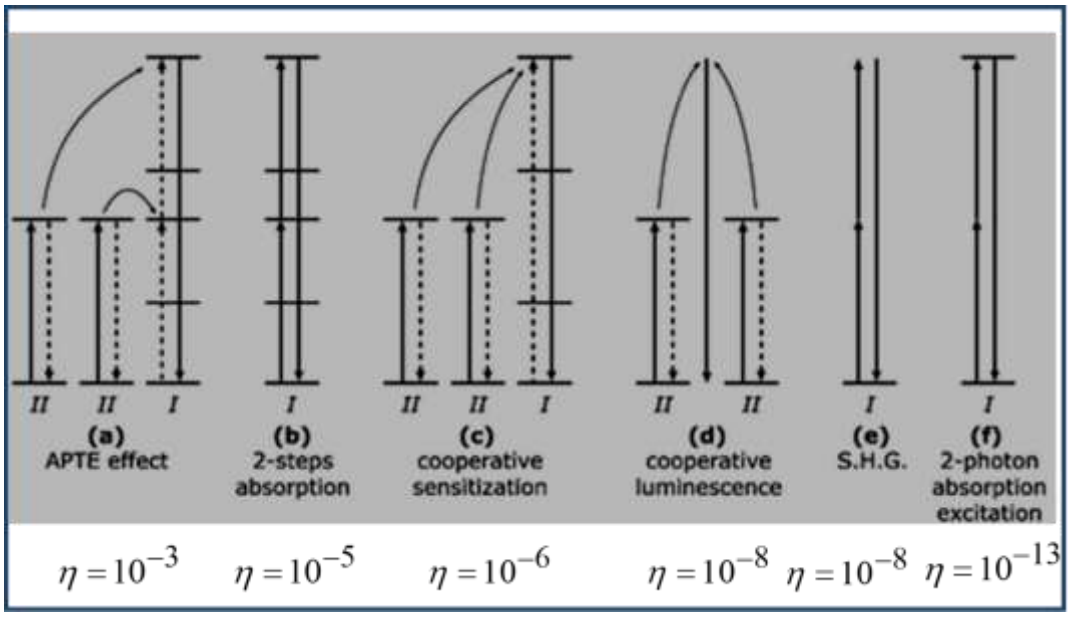


Figure 2-20: Energy level schemes for various two-photon up-conversion processes with quantum efficiency normalized to the incident power (1 W cm^2). Transitions between energy levels are indicated by vertical arrows, and curved arrows connecting different ions indicate energy transfer. Horizontal lines are real energy levels [215].

From figure 2-20, the efficiency of the up conversion processes appears to decrease from left to right as indicated by the efficiency (η) approximation. The APTE (*addition de photon par transferts d'energie*) or ETU (energy transfer up-conversion) process is most efficient mechanism followed by a two-step absorption, which is also referred to as ground state absorption (GSA) then excited state absorption (ESA). APTE is a GSA followed by an energy transfer, often written GSA/ETU. The APTE process, two-step-absorption and cooperative sensitization take place through real,

existing energetic levels and hence gives higher efficiencies compared to other competing processes occurring through virtual levels such as the second harmonic generation (SHG), cooperative luminescence and two-photon absorption (TPA) or multi-photon-excitation (MPE) since the latter require high excitation energies. For instance SHG occurs only at excitation intensities in the range of 10^{13} Wm^{-2} [217].

For application to silicon solar cells, a large number of ideal materials are available as luminescent up-converter layers, however they should possess the following characteristics:

- Absorption range higher than 1100 nm (E<1.12 eV).
- Emission that is lower than 1100 nm
- High up-conversion efficiency (>10^{-3})
- High transmittance of the up-converted light.

For crystalline silicon (*c-Si*), E_g is 1.12 eV (1110 nm) [191] while amorphous forms of silicon have wider band-gap energies, typically up to 1.7 eV . Other semiconductor materials for solar cells have their Eg falling in this range, for instance Cu_2S (1.2 eV; 1033 nm), GaAs (1.4 eV; 886 nm), and CdTe (1.5 eV; 826 nm) [218, 219]. Organic solar cells may possess a diverse range of values for Eg and typically have an absorption edge not lower than 1.5 eV. The Gra¨tzel cell is based on the use of TiO_2 (Eg = 3.0–3.2 eV; 413–387 nm); with a strategic choice of dye sensitizer, the photocurrent onset can be reduced in energy to be as low as 1.35 eV (920 nm) [220].

2.9.6. State of art on the recent progress on doping on rare earth ions in the oxide nanomaterials

Down-conversion presents the capability of cutting high energy photon into multiple lower energy photons with conversion efficiency reported being higher than 100% [175]. This enables the excess energy of the high-energy photons to be reclaimed and absorbed into the solar cells thus

minimizing the energy loss leading to improvement of solar cell efficiency. On the other hand, the up-conversion process provides a potential to minimize transmission loss by converting two low energy photons into one high energy photon falling within a range where a photovoltaic cell has high light responsivity. The down-conversion process is meant to enhance the solar cell efficiency by improving its short-wavelength spectral response. These approaches enable us to reach the Shockley−Queisser fundamental limit of a single-junction solar cell (~31% for non-concentrated sunlight irradiation on a semiconductor material with an optimized band gap of ~1.35 eV) [221]. According to Trupke et al., their theoretical model for up-conversion of the solar spectrum showed an elevated theoretical efficiency limit of a single-junction silicon solar cell to as high as 40.2% under non concentrated sunlight [222]. This surpasses the Shockley−Queisser limit set at ~30%. Recently, lots of research have been published on up- and down-conversion nanoparticles applied in crystalline silicon, dye sensitized solar cells (DSSCs), organic solar cells (OSCs) and the more nascent perovskite solar cells (PSCs) [221, 223-225].

Wu et al. investigated the fabrication of a ZnO:Eu^{3+} bifunctional layer for use in the organic solar cells [226]. The bifunctional layer is used as a spectral conversion layer as well as an electron transport layer. To study the Eu^{3+} doping influence on performance of the photoactivity, ZnO:Eu^{3+} was used as an electron buffer layer in layered organic solar cells with layer configuration ITO/ZnO:Eu^{3+}/P3HT:$PC_{61}BM$/MoO_3/Al, and they showed an increase in the short circuit current density (J_{SC}) from 8.94 to 9.11 mA/cm^2 when using ZnO and ZnO:Eu^{3+} as a buffer layers respectively which was attributed to a down-conversion process [227].

Yao et al. reported the use of rare earth doped ZnO in DSSCs for up- and down-conversion giving an efficiency increment of ~5.13% [228]. This enhancement was attributed to the increment in light harvesting through conversion of the UV and NIR into visible emission. The champion

DSSCs fabricated using up-conversion showed enhancements of ~12.5% when sensitization was done using black/N749 dye and ~5.5% with N719 [221].

Lidia et al. [229] also studied the correlation between the structure and the luminescence properties in Eu doped ZnO nano-powders prepared by sol-gel method. In their report there was simultaneous green and red luminescence at an excitation wavelength of 394 nm. According to this authors, it is possible to synergistically exploit the low-energy transfer efficiency from the ZnO host to the Eu^{3+} centres for single or multi-coloured emissions using the correct choice of excitation wavelength.

According to study by Subramanian *et al* [230] of the doping effects on the structural, optical and electronic properties of Nd doped ZnO films prepared by spray pyrolysis technique, there was a strong evidence for hybridization of Nd ions with O ions in the ZnO lattice. This was obtained using Near Edge X-ray Absorption Fluorescence Spectroscopy (NEXAFS).

Ungureanu *et al* [231] reported on the electrical and magnetic properties of Nd doped ZnO thin films which indicated a reduction on Nd doped ZnO resistivity with increasing film thickness. Shahmoradi *et al.* [232] fabricated neodymium doped ZnO hybrid nanoparticles under mild hydrothermal conditions at 150 ˚C using two surface modifiers. They showed that these surface modifiers altered the morphology and size of the nanoparticles as well as the surface charges increasing the nanoparticles stability. They reported a reduction in the band gap energy upon doping with Nd^{3+} increasing the feasibility of photodegradation in the visible light.

Achamma *et al.,* [233] reported on the luminescence properties in Ce embedded into ZnO nanocrystals prepared by simple refluxing technique. The decrease in emission intensity in these materials was attributed to the formation of additional surface defects (surface bound states) that mediated non-radiative relaxations.

Chao *et al.*, [234] reported on the effect of annealing on the properties of Nd containing ZnO prepared by sol gel route. In their studies Nd^{3+} emission intensity at 899 nm was observed to reach a maximum upon annealing at 600 ˚C. Higher annealing temperature (1000 ˚C) caused a separate phase segregation of Nd_2O_3 in the ZnO matrix.

2.9.7. Rare earth metals used for doping of ZnO

2.9.7.1. Terbium

Terbium was discovered in 1843 by Carl Mosander and is named after Ytterby, a village in Sweden, the place where this element was mined and harvested. It has an atomic number of 65 and an atomic mass of 158.93 AMU with electronic configuration of [Xe] $4f^9 6s^2$.

The trivalent Tb^{3+} ion has been under investigation by numerous research groups [152, 235] as a result of its potential as a dopant for many solid-state devices such as light emitting diodes (LEDs), fluorescent lamps and television screens and solar cells. When excited using ultra-violet wavelength (244 nm) in this study, the Tb^{3+} ions in ZnO produced showed narrow emission lines in both green spectral region. These lines have been attributed potentially to the $^5D4 \rightarrow {}^7F_J$ (J = 6, 5, 4, 3) transitions while the blue spectral region was assigned to the $^5D3 \rightarrow {}^7F_J$ (J = 6, 5, 4, 3, 2) transitions. Figure 2-21 shows a typical absorption and emission diagram of Tb^{3+} ions.

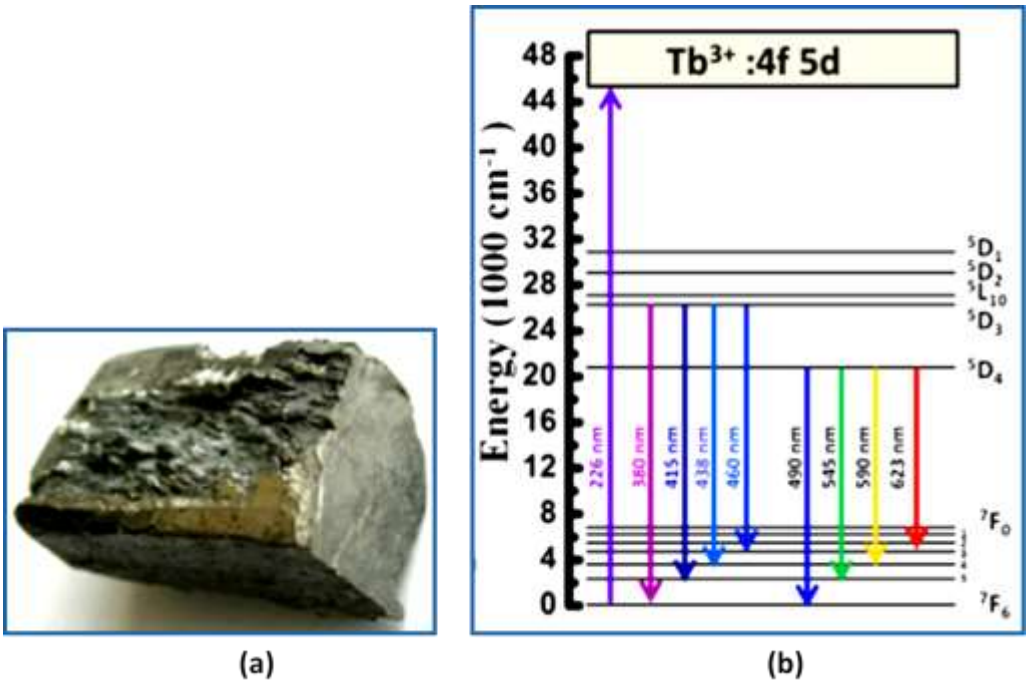


Figure 2-21: (a) Terbium ore (b) Schematic energy level diagram of Tb^{3+} ion [236].

Previous studies on Tb doped oxides include: Liu *et al*. [236] synthesized terbium-doped zinc oxide nanocrystals and reported on their structural and optical properties. Tb^{3+} ions showed green luminescence due to 4f –4f absorption transitions. Liu et al. [237] also looked at Tb-doped ZnO NPs synthesized through wet chemical route and reported on their PL properties. They attributed relaxation of carriers from excited states of ZnO hosts to rare earth dopants. The emission intensity of Tb^{3+} centers was observed to increase with increasing Tb content at the expense of the emission from surface defect states in the ZnO matrix. Jia *et al.* [238] report on photoluminescence properties of Tb doped ZnO showed strong UV emission peak. The red-shifted UV emission was attributed to defects and the presence of shallow energy level induced by Tb doping.

Wu *et al*. [239] also investigated the ferromagnetic properties of Tb-doped ZnO nanocrystalline films at room temperature. They suggest that the observed ferromagnetism was induced by Tb incorporation into the ZnO lattice. They reported a magnetization saturation of about 0.38 Tesla

per Tb ion. Ziani *et al*. [240] reported the effect of annealing on the photoluminescence properties of Tb-doped ZnO films synthesized by radio frequency magnetron sputtering at low temperatures. Their findings corroborate our observations that annealing favors optimal distribution of the ions in the matrix.

2.9.7.2. Europium

Europium was discovered by Eugène-Antole Demarçay, a French chemist, in 1896. He was not able to produce reasonably pure europium in 1901 since it usually exist as ores monazite sand. Trivalent europium ion (Eu^{3+}) is well known for red-emission as a result of the $^5D_0 \rightarrow {}^7F_2$ transition [241]. It has been widely used as a source of red light in preparing phosphors used in many light emitting devices. Its potential application as the source of red light in Eu doped GaN laser was reported by Park *et al*.[242]. Shahroosvand, H., and Ghorbani-asl, M. [243] ascribed the correlation between the red emission and the synthesis method due to the efficient energy transfer from the intrinsic defects in ZnO host to the Eu^{3+} ions. Their study also established that the three peaks in the region of $^5D_0$-^7F_J emerged from the occupancy of Eu^{3+} on the surface lattice sites ZnO. They proposed an energy transfer mechanism shown in Figure 2-22. The spectroscopic properties of the Eu^{3+} ions in this study were attributed to the transitions between its intra-4f electron energy levels. The right-hand side gives the partial energy level of Eu^{3+} ions, where the common $^{2S+1}L_J$ notion is used for the energy level, *S*, *L* and *J* referring to spin, orbital and total angular momentum, respectively while the left-hand side shows ZnO host with band-edge emission and the surface defects emission.

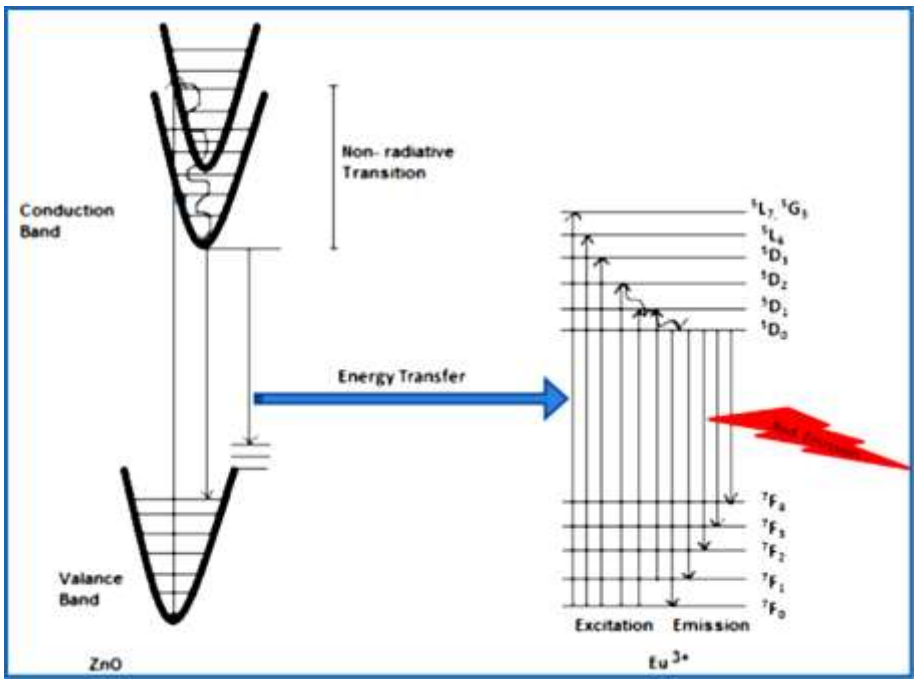


Figure 2-22: Illustration of proposed emission mechanism in Eu^{3+} doped ZnO [243].

Other previous studies on Eu doped ZnO include: Pearton *et al.* [244], who reported green luminescence of the ZnO nanowires using Eu diffusion process and they observed a peak at about 515 nm which was attributed to Eu. The thermal annealing of diffusion process caused a red shift of the NBE emission from the nanowires. Najafi *et al.*, [245] study of the photoluminescence properties of CVD fabricated Eu-doped ZnO demonstrated the correlation between defect states and energy transfer from the ZnO host to the Eu^{3+} ions. This interaction was posited to lead to the strong red emission thereby collaborating the results of Assadi *et al.* [246] in the study on the electronic, structural, and magnetic properties of Eu-doped ZnO NPs.

2.9.7.3. Samarium

The discovery of Samarium began with the discovery of cerium in 1803. This was suspected of harbouring other metals, and in 1839 Carl Mosander claimed to have obtained lanthanum and didymium from it. Although he was right about lanthanum, didymium was not true. It was until

1879, that Paul-Émile Lecoq de Boisbaudran extracted didymium from the mineral samarskite. He then made a solution of didymium nitrate and added ammonium hydroxide. Samarium itself was eventually to yield other rare-earths: gadolinium in 1886 and europium in 1901. It has an electronic configuration [Xe] $4f^6 6s^2$ [247]. Previous studies on Sm doped ZnO include: Lin *et al.*, [248] reported the PL behavior of Sm^{3+} doped ZnO (ZnO:Sm^{3+}) synthesized by the hydrothermal method. They reported that the slight substitution of Sm^{3+} into the Zn site enhanced the lattice distortion and increased the amount of defects, which suppressed the excitonic emission. Piao *et al.* [249] also investigated the ferromagnetic properties of Sm-doped ZnO nanorods produced via hydrothermal method. They observed ferromagnetic coupling in all the samples and for high doping concentrations. The segregation or formation of small clusters of Sm was associated with the observed ferromagnetic signal except that Sm substitution induced ferromagnetic ordering. Tsuji *et al.* [250] also investigated the photoluminescence properties of Sm-doped ZnO using the CVD technique. In their PL measurements of annealed ZnO:Sm, sharp emission lines from intra-4f transitions in Sm^{3+} ions were observed at room temperature under the excitation energy above the band gap energy of ZnO.

2.9.8. Applications of ZnO and rare earth doped ZnO in solar cells.

2.9.8.1. Organic solar cells

A typical OSC is made of an active layer, charge transporting layers and electrodes. The active layer is composed of a p type and an n-type material blend which serves a dual purpose in the device namely as a light harvester and simultaneously as a preferential charge separating/transport layer. Figure 4-23 shows a representation of the working principle of organic solar cells.

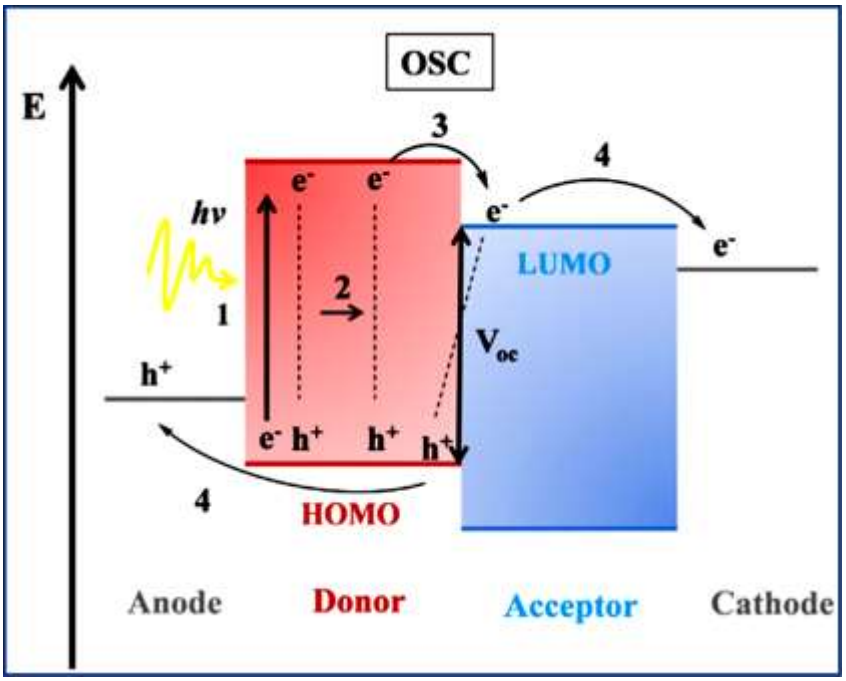


Figure 2-23: Band diagram and main processes in Organic Solar Cells: 1 Absorption of photon followed by exciton formation; 2 Exciton diffusion; 3 Charge separation; 4 Charge extraction [251].

Upon light absorption by the active layer, an electron is excited from the highest occupied molecular orbital (HOMO) to the lowest unoccupied molecular orbital (LUMO) similar to the process of promotion of an electron from the valence band to the conduction band experienced in inorganic semiconductors. This results in the formation of a tightly bound electron-hole pair called exciton with a relatively large binding energy (0.3–1 eV) [251]. This exciton then diffuses to the D/A interface where the potential difference enables it overcome its binding energy and it dissociates into free electrons and holes which then collected at respective electrodes [252-254].

2.9.8.2. Perovskites solar cells

Perovskite is a name derived from the Russian mineralogist L.A. Perovski. It has a particular crystal structure with the ABX_3 formula (X = oxygen, halogen).The larger A cation occupies a cubo-octahedral site which it shares with 12 X anions while the smaller B cation is stabilized in an

octahedral site shared with 6 X anions. The intensive interest into perovskites is motivated by the dramatic improvement in its performance that stunned the entire photovoltaic community from ~3% to ~22% [255-258] (certified 21.02% [257]), merely in a short span of less than 10 years.

The highly investigated perovskites are oxides as a result of their electrical properties of ferroelectricity or superconductivity. Halide perovskites on the other hand received little attention until the report on the layered organometal halide perovskites was found to exhibit a semiconductor-to-metal transition with increasing dimensionality [259]. In addition to changes in electrical properties, the band gap decreased with increased dimensionality from *2D* to *3D*. A narrow band gap is beneficial for solar cell applications. Park *et al.* [260] have reported a PCE of 6.5% using CH3NH3PbI3 applied as an inorganic sensitizer in dye sensitized solar cells applications. Using TiO_2 film thickness of about 3.6 mm as the transparent conducting layer, $CH_3MH_3PbI_3$ perovskite reported absorption coefficient which was 10 times greater than that of the conventional ruthenium-based molecular dye. Figure 6-23 shows the working principle of a perovskites solar cells.

Contrary to OSCs, the absorption of photons in perovskite materials within PSCs does not lead to the formation of a large lifetime exciton.

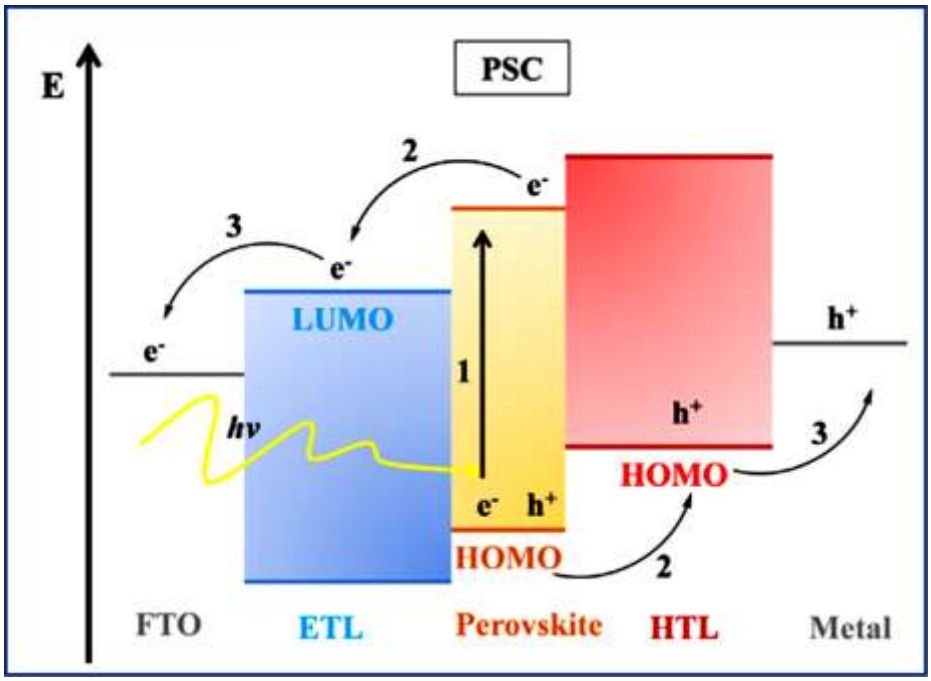


Figure 2-24: Band diagram and main processes and Perovskites solar cells: 1 Absorption of photon and free charges generation; 2 Charge transport; 3 Charge extraction [251].

The most common active layer material is the methylammonium lead iodide perovskite, (MAPbI3) put between electron transporting layer (ETL), usually mesoporous, but also planar TiO_2, and hole transporting layer (HTL). In the standard device configuration, the front transparent electrode is FTO-coated glass and the back electrode is a thermally evaporated gold layer [261]. In our studies the fabrication involves the use of RF sputtered ZnO thin films as a proof of concept.

2.9.8.3. Dye sensitized solar cells

The name implies that its working mechanism is based on the photo electrochemical processes. Figure 2-25 depicts an energy diagram of a dye sensitized solar cell. The working principle of dye sensitized solar cells (DSSC) is based on the photo generation of an electron by a dye and its injection to the semiconductor. This principle of operation is akin to photosynthesis [220].

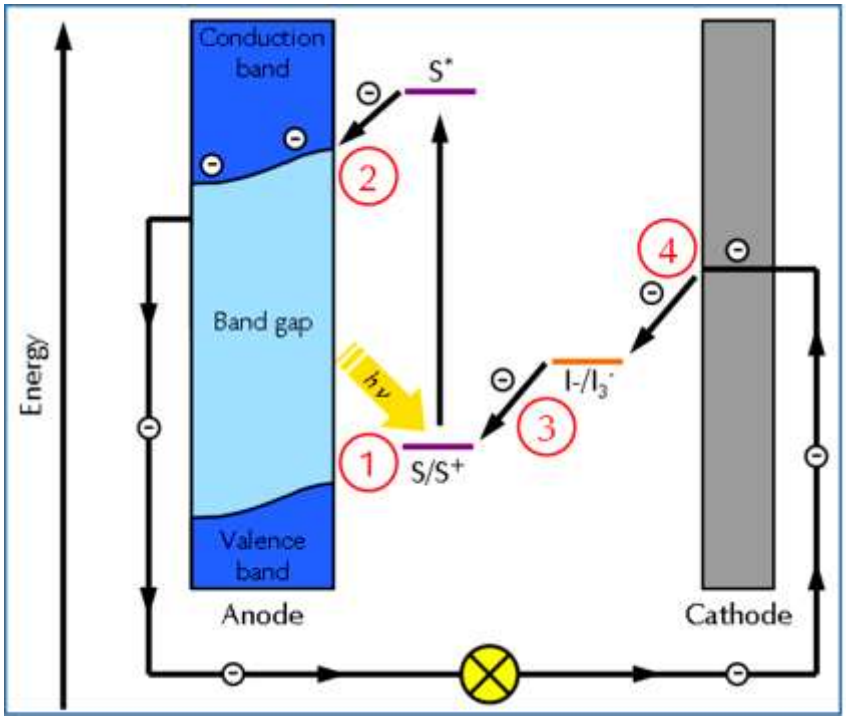


Figure 2-25: Energy diagram of the working principle of a dye sensitized solar cell [220].

Upon photo absorption, the dye molecules undergo excitation from their ground state (*S*) to a higher energy state (S^*). The increased internal energy of the excited dye molecule commensurate to the conduction band of the dye adsorbed semiconductor enables the electron to be efficiently injected into the semiconductor. [262]. Photoabsorption can also be represented by the expression of equation 4-27.

$$S \xrightarrow{h\nu} S^* \quad \ldots\ldots\ldots\ldots\ldots\ldots \text{4-27}$$

The process of photo-excitation of the dye molecule (S^*) analogous to the oxidation of the dye molecule and it is presented in the form:

$$S^* \longrightarrow S^+ + e^- \quad \ldots\ldots\ldots\ldots\ldots\ldots \text{4-28}$$

The injection of electrons into the semiconductor enhances their mobility at this energy level. The subsequent charge transport to the anode is mediated by diffusion processes to produce a potential

difference or photocurrent in the presence of a load. The oxidized dye molecule (S^+) is again regenerated by electron donation from the iodine in the electrolyte as per equation 4-29.

$$S^+ + \frac{3}{2}I^- \rightarrow S + \frac{1}{2}I_3^- \quad \ldots\ldots\ldots\ldots\ldots\ldots \text{4-29}$$

In return, the iodide is regenerated by reduction of tri-iodide on the cathode as per equation 4-30

$$\frac{1}{2}I_3^- + e^- \rightarrow \frac{3}{2}I^- \quad \ldots\ldots\ldots\ldots\ldots\ldots \text{4-30}$$

2.9.9. Parameters used in the various solar cells

The main parameters used in characterization of solar cell performance include; peak power P_{max}, short circuit current density, J_{sc}, open circuit voltage, V_{oc}, fill factor *FF and the* Power conversion efficiency. These parameters are obtained from the illuminated as well as dark *J-V* characteristic as defined by equations 4-31 to 4-34 given below.

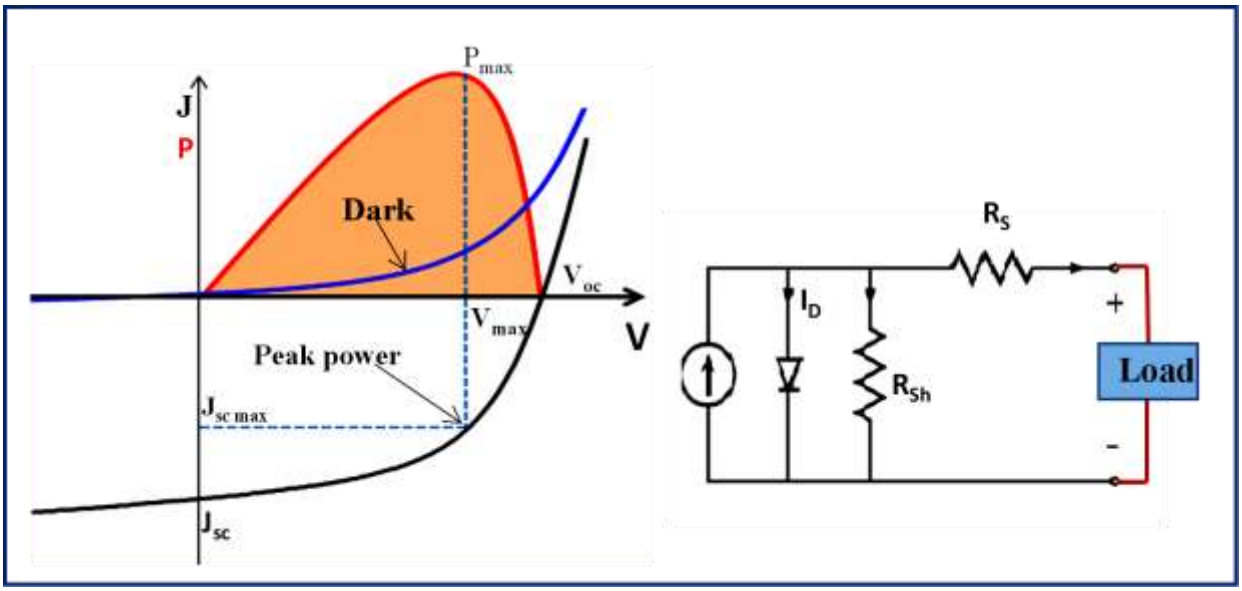


Figure 2-26: The J-V characteristics of solar cell in the dark and under illumination the equivalent circuit diagram.

Assuming that the solar cell behaves as an ideal diode, the device characteristics shown on figure 2-26 can be expressed as follows:

$$\text{Short circuit Current density } J = J_{SC} - J_O(e^{qV/K_BT} - 1) \quad \ldots\ldots\ldots \text{2-31}$$

Where *Jo* is a constant, q is electron charge while V is voltage across the terminals

$$\text{Open circuit current density, } V_{OC} = \frac{K_B T}{q}\ln\left(\frac{J_{sc}}{J_o} + 1\right) \quad \ldots\ldots\ldots\ldots \text{2-32}$$

$$\text{Fill factor, } FF = \frac{J_{\max} V_{\max}}{J_{sc} V_{oc}} \quad \ldots\ldots\ldots\ldots\ldots\ldots\ldots\ldots\ldots\ldots \text{2-33}$$

$$\text{Power conversion efficiency, } \eta = \frac{P_{\max}}{P_{in}} = \frac{J_{\max} V_{\max}}{J_{sc} V_{oc}} = \frac{J_{sc} V_{oc} FF}{P_{in}} \quad \ldots\ldots\ldots\ldots\ldots\ldots \text{2-34}$$

The efficiency of the solar cell is also affected by resistive effects that usually leads the dissipation of power in the resistances. The most common parasitic resistances are series resistance and shunt resistance. The value of series resistance depends on the resistivity of the metallic contacts and the surface layer while the shunt resistance value depends on the junction construction. An ideal solar cell has an infinite shunt resistance while the series resistance is zero.

The current density–voltage (*J*–*V*) characteristics were obtained using HP 4141B source measure unit (SMU) under 100 mW/cm^2 illumination (AM 1.5G). All the measurements were carried out at room temperature under standard conditions.

2.10. References (for chapter 2).

[1] S.K. Gurram, Atomic Layer Deposition of Zinc Based Transparent Conductive Oxides, BoD–Books on Demand, 2017.

[2] K. Badeker, Concerning the electricity conductibility and the thermoelectric energy of several heavy metal bonds, Annalen der Physik, 22 (1907) 749.

[3] D.M. Mattox, V.H. Mattox, Review of Transparent Conductive Oxides (TCO), in, DOI.

[4] G. Bauer, Elektrisches und optisches Verhalten von Halbleitern. XIII Messungen an Cd-, Tl- und Sn-Oxyden, Annalen der Physik, 422 (1937) 433-445.

[5] G. Rupprecht, Untersuchungen der elektrischen und lichtelektrischen Leitfähigkeit dünner Indiumoxydschichten, Zeitschrift für Physik, 139 (1954) 504-517.

[6] J.M. Mochel, Coated resistance, in, Google Patents, 1951.

[7] J. Vossen, Transparent conducting films, in, AVS, 1976.

[8] P.J. Silvey, G.E. John, Transparent conducting films, in, Google Patents, 1958.

[9] J. Aranovich, A. Ortiz, R.H. Bube, Optical and electrical properties of ZnO films prepared by spray pyrolysis for solar cell applications, Journal of Vacuum Science and Technology, 16 (1979) 994-1003.

[10] K. Wasa, S. Hayakawa, T. Hada, Electrical and optical properties of sputtered np ZnO–Si heterojunctions, Japanese Journal of Applied Physics, 10 (1971) 1732.

[11] T. Minami, New n-type transparent conducting oxides, MRS bulletin, 25 (2000) 38-44.

[12] S. Zafar, C. Ferekides, D. Morel, Characterization and analysis of ZnO: Al deposited by reactive magnetron sputtering, Journal of Vacuum Science & Technology A: Vacuum, Surfaces, and Films, 13 (1995) 2177-2182.

[13] M. Kubon, E. Boehmer, F. Siebke, B. Rech, C. Beneking, H. Wagner, Solution of the ZnO/p contact problem in a-Si: H solar cells, Solar Energy Materials and Solar Cells, 41 (1996) 485-492.

[14] T. Subramanyam, B.S. Naidu, S. Uthanna, Effect of substrate temperature on the physical properties of DC reactive magnetron sputtered ZnO films, Optical Materials, 13 (1999) 239-247.

[15] Ü. Özgür, Y.I. Alivov, C. Liu, A. Teke, M. Reshchikov, S. Doğan, V. Avrutin, S. Cho, H. Morkoçd, Applied physics reviews, Journal of Applied Physics, 98 (2005) 041301.

[16] N.H. Nickel, E. Terukov, Zinc Oxide-A Material for Micro-and Optoelectronic Applications: Proceedings of the NATO Advanced Research Workshop on Zinc Oxide as a Material for Micro-and Optoelectronic Applications, held in St. Petersburg, Russia, from 23 to 25 June 2004, Springer Science & Business Media, 2006.

[17] C. Jagadish, S.J. Pearton, Zinc oxide bulk, thin films and nanostructures: processing, properties, and applications, Elsevier, 2011.

[18] D.C. Reynolds, D.C. Look, B. Jogai, Optically pumped ultraviolet lasing from ZnO, Solid State Communications, 99 (1996) 873-875.

[19] D. Bagnall, Y. Chen, M. Shen, Z. Zhu, T. Goto, T. Yao, Room temperature excitonic stimulated emission from zinc oxide epilayers grown by plasma-assisted MBE, Journal of crystal growth, 184 (1998) 605-609.

[20] T. Yamamoto, T. Shiosaki, A. Kawabata, Characterization of ZnO piezoelectric films prepared by rf planar-magnetron sputtering, Journal of Applied Physics, 51 (1980) 3113-3120.

[21] J. Molarius, J. Kaitila, T. Pensala, M. Ylilammi, Piezoelectric ZnO films by rf sputtering, Journal of Materials Science: Materials in Electronics, 14 (2003) 431-435.

[22] R. Ondo-Ndong, G. Ferblantier, F. Pascal-Delannoy, A. Boyer, A. Foucaran, Electrical properties of zinc oxide sputtered thin films, Microelectronics journal, 34 (2003) 1087-1092.

[23] J.G. Gardeniers, Z. Rittersma, G. Burger, Preferred orientation and piezoelectricity in sputtered ZnO films, Journal of Applied physics, 83 (1998) 7844-7854.

[24] S. Talam, S.R. Karumuri, N. Gunnam, Synthesis, characterization, and spectroscopic properties of ZnO nanoparticles, ISRN Nanotechnology, 2012 (2012).

[25] H. Nanto, H. Sokooshi, T. Usuda, Smell sensor using zinc oxide thin films prepared by magnetron sputtering, in: Solid-State Sensors and Actuators, 1991. Digest of Technical Papers, TRANSDUCERS'91., 1991 International Conference on, IEEE, 1991, pp. 596-599.

[26] M. Larciprete, D. Haertle, A. Belardini, M. Bertolotti, F. Sarto, P. Günter, Characterization of second and third order optical nonlinearities of ZnO sputtered films, Applied Physics B, 82 (2006) 431-437.

[27] D.I. Florescu, L. Mourokh, F.H. Pollak, D.C. Look, G. Cantwell, X. Li, High spatial resolution thermal conductivity of bulk ZnO (0001), Journal of applied physics, 91 (2002) 890-892.

[28] Z.O. Rediscovered, H. Brown, The New Jersey Zinc Company, New York, (1957).

[29] H. Leverenz, Luminescence of solids, in, ACS Publications, 1950.

[30] K. Maeda, M. Sato, I. Niikura, T. Fukuda, Growth of 2 inch ZnO bulk single crystal by the hydrothermal method, Semiconductor science and technology, 20 (2005) S49.

[31] D.C. Look, D.C. Reynolds, J. Sizelove, R. Jones, C.W. Litton, G. Cantwell, W. Harsch, Electrical properties of bulk ZnO, Solid state communications, 105 (1998) 399-401.

[32] D. Reynolds, C. Litton, D.C. Look, J. Hoelscher, B. Claflin, T. Collins, J. Nause, B. Nemeth, High-quality, melt-grown ZnO single crystals, Journal of applied physics, 95 (2004) 4802-4805.

[33] H.K. Ardakani, Electrical conductivity of in situ “hydrogen-reduced” and structural properties of zinc oxide thin films deposited in different ambients by pulsed excimer laser ablation, Thin Solid Films, 287 (1996) 280-283.

[34] F. Quaranta, A. Valentini, F.R. Rizzi, G. Casamassima, Dual-ion-beam sputter deposition of ZnO films, Journal of Applied Physics, 74 (1993) 244-248.

[35] A. Janotti, C.G. Van de Walle, Fundamentals of zinc oxide as a semiconductor, Reports on progress in physics, 72 (2009) 126501.

[36] F. Tuomisto, K. Saarinen, D.C. Look, G.C. Farlow, Introduction and recovery of point defects in electron-irradiated ZnO, Physical Review B, 72 (2005) 085206.

[37] J.R. Chelikowsky, J.K. Burdett, Ionicity and the structural stability of solids, Physical review letters, 56 (1986) 961.

[38] D.R. Lide, Handbook of organic solvents, CRC Press, 1994.

[39] Ü. Özgür, Y.I. Alivov, C. Liu, A. Teke, M. Reshchikov, S. Doğan, V. Avrutin, S.-J. Cho, H. Morkoc, A comprehensive review of ZnO materials and devices, Journal of applied physics, 98 (2005) 11.

[40] Z.G. Yu, H. Gong, P. Wu, Lattice dynamics and electrical properties of wurtzite ZnO determined by a density functional theory method, Journal of crystal growth, 287 (2006) 199-203.

[41] M. Mehrabian, R. Azimirad, K. Mirabbaszadeh, H. Afarideh, M. Davoudian, UV detecting properties of hydrothermal synthesized ZnO nanorods, Physica E: Low-dimensional Systems and Nanostructures, 43 (2011) 1141-1145.

[42] M.H. Huang, Y. Wu, H. Feick, N. Tran, E. Weber, P. Yang, Catalytic Growth of Zinc Oxide Nanowires by Vapor Transport, Science, 277 (1997) 1978.

[43] A. Klein, C. Körber, A. Wachau, F. Säuberlich, Y. Gassenbauer, S.P. Harvey, D.E. Proffit, T.O. Mason, Transparent conducting oxides for photovoltaics: manipulation of Fermi level, work function and energy band alignment, Materials, 3 (2010) 4892-4914.

[44] B.E. Sernelius, K.-F. Berggren, Z.-C. Jin, I. Hamberg, C. Granqvist, Band-gap tailoring of ZnO by means of heavy Al doping, Physical Review B, 37 (1988) 10244.

[45] I. Hamberg, C. Granqvist, K.-F. Berggren, B.E. Sernelius, L. Engström, Band-gap widening in heavily Sn-doped In 2 O 3, physical Review B, 30 (1984) 3240.

[46] K.-F. Berggren, B. Sernelius, L. Engström, I. Hamberg, C. Granqvist, Bandgap Widening in Heavily Sn-Doped In 2 O 3, in: Proceedings of the 17th International Conference on the Physics of Semiconductors, Springer, 1985, pp. 1051-1054.

[47] C. Charpentier, Investigation of deposition conditions and annealing treatments on sputtered ZnO: Al thin films: Material properties and application to microcristalline silicon solar cells, in, Ecole Polytechnique X, 2012.

[48] J.E. Jaffe, J.A. Snyder, Z. Lin, A.C. Hess, LDA and GGA calculations for high-pressure phase transitions in ZnO and MgO, Physical Review B, 62 (2000) 1660.

[49] I. Ivanov, J. Pollmann, Electronic structure of ideal and relaxed surfaces of ZnO: A prototype ionic wurtzite semiconductor and its surface properties, Physical Review B, 24 (1981) 7275.

[50] D. Vogel, P. Krüger, J. Pollmann, Ab initio electronic-structure calculations for II-VI semiconductors using self-interaction-corrected pseudopotentials, Physical Review B, 52 (1995) R14316.

[51] R. Chen, Synthesis Of Zinc Oxide Nanostructures By Wet Oxidation Process, in, ResearchSpace@ Auckland, 2011.

[52] Y.P. Varshni, Temperature dependence of the energy gap in semiconductors, physica, 34 (1967) 149-154.

[53] N. Data, Functional Relationships in Science and technology, Landolt-B. ornstein, Group III, Vol. 17a, Group III, 22.

[54] H. Hartnagel, Semiconducting transparent thin films, CRC Press, 1995.

[55] H. Ibach, Thermal expansion of silicon and zinc oxide (II), physica status solidi (b), 33 (1969) 257-265.

[56] C.M. Bhandari, Thermal conduction in semiconductors, John Wiley & Sons, 1988.

[57] H. Morkoç, Ü. Özgür, General properties of ZnO, Zinc Oxide: Fundamentals, Materials and Device Technology, (2009) 1-76.

[58] K. Thoma, B. Dorner, G. Duesing, W. Wegener, Lattice dynamics of ZnO, Solid State Communications, 15 (1974) 1111-1114.

[59] M. Lannoo, J. Bourgoin, Point Defects in Semiconductors I—Theoretical Aspects, volume 22 of Springer Series in Solid-State Sciences, in, Springer, Berlin, 1981.

[60] S.T. Pantelides, Deep centers in semiconductors, CRC Press, 1992.

[61] A. Alkauskas, M.D. McCluskey, C.G. Van de Walle, Tutorial: Defects in semiconductors—Combining experiment and theory, Journal of Applied Physics, 119 (2016) 181101.

[62] C.G. Van de Walle, J. Neugebauer, First-principles calculations for defects and impurities: Applications to III-nitrides, Journal of applied physics, 95 (2004) 3851-3879.

[63] A. Janotti, C.G. Van de Walle, Native point defects in ZnO, Physical Review B, 76 (2007) 165202.

[64] A. Kohan, G. Ceder, D. Morgan, C.G. Van de Walle, First-principles study of native point defects in ZnO, Physical Review B, 61 (2000) 15019.

[65] G. Neumann, E. Kaldis, Current Topics in Materials Science, in, North-Holland Amsterdam, 1981.

[66] M.E. Glicksman, Diffusion in solids: field theory, solid-state principles and applications, Wiley, 2000.

[67] S. Limpijumnong, C.G. Van de Walle, Diffusivity of native defects in GaN, Physical Review B, 69 (2004) 035207.

[68] A. Janotti, C.G. Van de Walle, New insights into the role of native point defects in ZnO, Journal of Crystal Growth, 287 (2006) 58-65.

[69] A. Janotti, C.G. Van de Walle, Oxygen vacancies in ZnO, Applied Physics Letters, 87 (2005) 122102.

[70] R.-Y. Tian, Y.-J. Zhao, The origin of p-type conduction in (P, N) codoped ZnO, Journal of Applied Physics, 106 (2009) 043707.

[71] R. Lauer, The IR photoluminescence emission band in ZnO, Journal of Physics and Chemistry of Solids, 34 (1973) 249-253.

[72] D.C. Reynolds, D.C. Look, B. Jogai, H. Morkoc, Similarities in the bandedge and deep-centre photoluminescence mechanisms of ZnO and GaN, Solid State Communications, 101 (1997) 643-646.

[73] D. Reynolds, D. Look, B. Jogai, J. Van Nostrand, R. Jones, J. Jenny, Source of the yellow luminescence band in GaN grown by gas-source molecular beam epitaxy and the green luminescence band in single crystal ZnO, Solid state communications, 106 (1998) 701-704.

[74] B. Lin, Z. Fu, Y. Jia, Green luminescent center in undoped zinc oxide films deposited on silicon substrates, Applied Physics Letters, 79 (2001) 943-945.

[75] D.C. Look, J.W. Hemsky, J. Sizelove, Residual native shallow donor in ZnO, Physical review letters, 82 (1999) 2552.

[76] P. Erhart, K. Albe, Diffusion of zinc vacancies and interstitials in zinc oxide, Applied physics letters, 88 (2006) 201918.

[77] F. Oba, M. Choi, A. Togo, I. Tanaka, Point defects in ZnO: an approach from first principles, Science and technology of advanced materials, 12 (2011) 034302.

[78] A. Tsurkan, N. Fedotova, L. Kicherman, P. Pas' ko, Injection electroluminescence in n-ZnO-p-ZnTe heterojunctions, Fizika i Tekhnika Poluprovodnikov, 9 (1975) 1183-1185.

[79] A. Lakshmanan, Luminescence and Display Phosphors: Phenomena and Applications, Nova Publishers, 2008.

[80] J. Ungula, Growth and characterization of ZnO nanoparticles by sol-gel process, in, University of the Free State (Qwaqwa Campus), 2015.

[81] R. Johnson, Luminescence of sulphide and silicate phosphors, JOSA, 29 (1939) 387-391.

[82] S. Deshpande, Principles and applications of luminescence spectroscopy, Critical reviews in food science and nutrition, 41 (2001) 155-224.

[83] G.C. Pimentel, Hydrogen bonding and electronic transitions: the role of the Franck-Condon principle, Journal of the American Chemical Society, 79 (1957) 3323-3326.

[84] G.C. Pimentel, A.L. McClellan, The hydrogen bond, (1960).

[85] T. Effio, U. Trociewitz, X. Wang, J. Schwartz, Quench induced degradation in Bi2Sr2CaCu2O8+ x tape conductors at 4.2 K, Superconductor Science and Technology, 21 (2008) 045010.

[86] M. Kastantin, B. Ananthanarayanan, P. Karmali, E. Ruoslahti, M. Tirrell, Effect of the lipid chain melting transition on the stability of DSPE-PEG (2000) micelles, Langmuir, 25 (2009) 7279-7286.

[87] S. Bhattar, G. Kolekar, S. Patil, Fluorescence resonance energy transfer between perylene and riboflavin in micellar solution and analytical application on determination of vitamin B2, Journal of Luminescence, 128 (2008) 306-310.

[88] U. Mote, S. Bhattar, S. Patil, G. Kolekar, Interaction of fluorescein with felodipine: a spectrofluorometric and thermodynamic study, Journal of solution chemistry, 38 (2009) 619-628.

[89] I. Akai, A. Okada, K. Kanemoto, T. Karasawa, H. Hashimoto, M. Kimura, Quenching of energy transfer by freezing molecular vibrations in light-harvesting small dendrimer, Journal of luminescence, 119 (2006) 283-287.

[90] H.W. Leverenz, F. Urbach, Introduction to the Luminescence of Solids, Physics Today, 3 (1950) 32.

[91] P.H. Kasai, Electron spin resonance studies of donors and acceptors in ZnO, Physical review, 130 (1963) 989.

[92] K. Vanheusden, W. Warren, C. Seager, D. Tallant, J. Voigt, B. Gnade, Mechanisms behind green photoluminescence in ZnO phosphor powders, Journal of Applied Physics, 79 (1996) 7983-7990.

[93] S. Yamauchi, Y. Goto, T. Hariu, Photoluminescence studies of undoped and nitrogen-doped ZnO layers grown by plasma-assisted epitaxy, Journal of Crystal Growth, 260 (2004) 1-6.

[94] M. Liu, A. Kitai, P. Mascher, Point defects and luminescence centres in zinc oxide and zinc oxide doped with manganese, Journal of Luminescence, 54 (1992) 35-42.

[95] E. Bylander, Surface effects on the low-energy cathodoluminescence of zinc oxide, Journal of Applied Physics, 49 (1978) 1188-1195.

[96] X. Yang, G. Du, X. Wang, J. Wang, B. Liu, Y. Zhang, D. Liu, D. Liu, H. Ong, S. Yang, Effect of post-thermal annealing on properties of ZnO thin film grown on c-Al2O3 by metal-organic chemical vapor deposition, Journal of Crystal Growth, 252 (2003) 275-278.

[97] Z.L. Wang, J. Song, Piezoelectric nanogenerators based on zinc oxide nanowire arrays, Science, 312 (2006) 242-246.

[98] O. Schirmer, D. Zwingel, The yellow luminescence of zinc oxide, Solid State Communications, 8 (1970) 1559-1563.

[99] J.L. Freeouf, Far-Ultraviolet Reflectance of II-VI Compounds and Correlation with the Penn—Phillips Gap, Physical Review B, 7 (1973) 3810.

[100] R. Dingle, Luminescent transitions associated with divalent copper impurities and the green emission from semiconducting zinc oxide, Physical Review Letters, 23 (1969) 579.

[101] M. Ohring, Materials Science of Thin Films 2nd edn (New York: Academic), (2002).

[102] C. Thompson, Structure evolution during processing of polycrystalline films, Annual review of materials science, 30 (2000) 159-190.

[103] C.V. Thompson, R. Carel, Texture development in polycrystalline thin films, Materials Science and Engineering: B, 32 (1995) 211-219.

[104] H. Atkinson, Overview no. 65: Theories of normal grain growth in pure single phase systems, Acta Metallurgica, 36 (1988) 469-491.

[105] H. Frost, Microstructural evolution in thin films, Materials characterization, 32 (1994) 257-273.

[106] V. Holy, T. Baumbach, U. Pietsch, High-resolution X-ray scattering from thin films and multilayers, Springer, 1999.

[107] H. Natter, M. Schmelzer, M.-S. Löffler, C. Krill, A. Fitch, R. Hempelmann, Grain-growth kinetics of nanocrystalline iron studied in situ by synchrotron real-time X-ray diffraction, The Journal of Physical Chemistry B, 104 (2000) 2467-2476.

[108] K.P. Almtoft, Structural characterization of nanocrystalline thin films grown by magnetron sputtering, University of Aarhus, (2006).

[109] C. Suryanarayana, Nanocrystalline materials, International Materials Reviews, 40 (1995) 41-64.

[110] T. Malow, C. Koch, Grain growth in nanocrystalline iron prepared by mechanical attrition, Acta Materialia, 45 (1997) 2177-2186.

[111] C. Krill III, L. Helfen, D. Michels, H. Natter, A. Fitch, O. Masson, R. Birringer, Size-dependent grain-growth kinetics observed in nanocrystalline Fe, Physical review letters, 86 (2001) 842.

[112] J. Burke, Some factors affecting the rate of grain growth in metals, AIME TRANS, 180 (1949) 73-91.

[113] C. Suryanarayana, C. Koch, Nanocrystalline materials–Current research and future directions, Hyperfine Interactions, 130 (2000) 5.

[114] C.C. Wong, H.I. Smith, C. Thompson, Surface-energy-driven secondary grain growth in thin Au films, Applied physics letters, 48 (1986) 335-337.

[115] H.D. Young, R.A. Freedman, L. Ford, University Physics Vol 2 (Chapters 21-37), Pearson Education, 2007.

[116] M. Sopanen, Thermal Annealing of AlN Thin Films Fabricated by Plasma-Enhanced Atomic Layer Deposition for GaN Epitaxy, in, Aalto University, 2010.

[117] P. Carcia, R. McLean, M. Reilly, G. Nunes Jr, Transparent ZnO thin-film transistor fabricated by rf magnetron sputtering, Applied Physics Letters, 82 (2003) 1117-1119.

[118] R. Hong, J. Huang, H. He, Z. Fan, J. Shao, Influence of different post-treatments on the structure and optical properties of zinc oxide thin films, Applied Surface Science, 242 (2005) 346-352.

[119] J. Zhang, G. He, L. Zhu, M. Liu, S. Pan, L. Zhang, Effect of oxygen partial pressure on the structural and optical properties of ZnO film deposited by reactive sputtering, Applied surface science, 253 (2007) 9414-9421.

[120] W. He, C. Ye, Flexible transparent conductive films on the basis of Ag nanowires: design and applications: a review, Journal of Materials Science & Technology, 31 (2015) 581-588.

[121] D.S. Ginley, J.D. Perkins, Transparent conductors, in: Handbook of transparent conductors, Springer, 2011, pp. 1-25.

[122] K. Schulze, B. Maennig, K. Leo, Y. Tomita, C. May, J. Hüpkes, E. Brier, E. Reinold, P. Bäuerle, Organic solar cells on indium tin oxide and aluminum doped zinc oxide anodes, Applied physics letters, 91 (2007) 073521.

[123] M. Katayama, Tft-lcd technology, Thin Solid Films, 341 (1999) 140-147.

[124] U. Betz, M.K. Olsson, J. Marthy, F. Atamny, Thin films engineering of indium tin oxide: large area flat panel displays application, Surface and Coatings Technology, 200 (2006) 5751-5759.

[125] P.P. Edwards, A. Porch, M.O. Jones, D.V. Morgan, R.M. Perks, Basic materials physics of transparent conducting oxides, Dalton transactions, (2004) 2995-3002.

[126] J.-J. Lin, Z.-Q. Li, Electronic conduction properties of indium tin oxide: single-particle and many-body transport, Journal of Physics: Condensed Matter, 26 (2014) 343201.

[127] K. Ellmer, A. Bikowski, Intrinsic and extrinsic doping of ZnO and ZnO alloys, Journal of Physics D: Applied Physics, 49 (2016) 413002.

[128] A.J. Leenheer, J.D. Perkins, M.F. Van Hest, J.J. Berry, R.P. O'Hayre, D.S. Ginley, General mobility and carrier concentration relationship in transparent amorphous indium zinc oxide films, Physical Review B, 77 (2008) 115215.

[129] V. Bhosle, A. Tiwari, J. Narayan, Metallic conductivity and metal-semiconductor transition in Ga-doped ZnO, Applied Physics Letters, 88 (2006) 032106.

[130] D. Kim, I. Yun, H. Kim, Fabrication of rough Al doped ZnO films deposited by low pressure chemical vapor deposition for high efficiency thin film solar cells, Current Applied Physics, 10 (2010) S459-S462.

[131] J. Steinhauser, S. Fay, N. Oliveira, E. Vallat-Sauvain, C. Ballif, Transition between grain boundary and intragrain scattering transport mechanisms in boron-doped zinc oxide thin films, Applied Physics Letters, 90 (2007) 142107.

[132] C.-H. Zhai, R.-J. Zhang, X. Chen, Y.-X. Zheng, S.-Y. Wang, J. Liu, N. Dai, L.-Y. Chen, Effects of Al doping on the properties of ZnO thin films deposited by atomic layer deposition, Nanoscale research letters, 11 (2016) 407.

[133] D. Daksh, Y.K. Agrawal, Rare earth-doped zinc oxide nanostructures: a review, Reviews in Nanoscience and Nanotechnology, 5 (2016) 1-27.

[134] B. Benhaoua, A. Rahal, S. Benramache, The structural, optical and electrical properties of nanocrystalline ZnO: Al thin films, Superlattices and Microstructures, 68 (2014) 38-47.

[135] R.M. Mundle, H.S. Terry, K. Santiago, D. Shaw, M. Bahoura, A.K. Pradhan, K. Dasari, R. Palai, Electrical conductivity and photoresistance of atomic layer deposited Al-doped ZnO films, Journal of Vacuum Science & Technology A: Vacuum, Surfaces, and Films, 31 (2013) 01A146.

[136] Y. Wu, S. Potts, P. Hermkens, H. Knoops, F. Roozeboom, W. Kessels, Enhanced doping efficiency of Al-doped ZnO by atomic layer deposition using dimethylaluminum isopropoxide as an alternative aluminum precursor, Chemistry of Materials, 25 (2013) 4619-4622.

[137] H.C. Knoops, B.W. van de Loo, S. Smit, M.V. Ponomarev, J.-W. Weber, K. Sharma, W.M. Kessels, M. Creatore, Optical modeling of plasma-deposited ZnO films: Electron scattering at different length scales, Journal of Vacuum Science & Technology A: Vacuum, Surfaces, and Films, 33 (2015) 021509.

[138] X.J. Qin, L. Zhao, G.J. Shao, N. Wang, Influence of solvents on deposition mechanism of Al-doped ZnO films synthesized by cold wall aerosol-assisted chemical vapor deposition, Thin Solid Films, 542 (2013) 144-149.

[139] A. Bikowski, T. Welzel, K. Ellmer, The impact of negative oxygen ion bombardment on electronic and structural properties of magnetron sputtered ZnO: Al films, Applied Physics Letters, 102 (2013) 242106.

[140] K. Sago, H. Kuramochi, H. Iigusa, K. Utsumi, H. Fujiwara, Ellipsometry characterization of polycrystalline ZnO layers with the modeling of carrier concentration gradient: Effects of grain boundary, humidity, and surface texture, Journal of Applied Physics, 115 (2014) 133505.

[141] Y. Liu, Q. Li, H. Shao, Optical and photoluminescent properties of Al-doped zinc oxide thin films by pulsed laser deposition, Journal of Alloys and Compounds, 485 (2009) 529-531.

[142] J. Musil, S. Kadlec, W.D. Münz, Unbalanced magnetrons and new sputtering systems with enhanced plasma ionization, Journal of Vacuum Science & Technology A: Vacuum, Surfaces, and Films, 9 (1991) 1171-1177.

[143] S. Zhang, S.-H. Wei, A. Zunger, Microscopic origin of the phenomenological equilibrium "doping limit rule" in n-type III-V semiconductors, Physical review letters, 84 (2000) 1232.

[144] S.J. Pearton, D.P. Norton, M.P. Ivill, A.F. Hebard, J.M. Zavada, W.M. Chen, I.A. Buyanova, ZnO doped with transition metal ions, IEEE Transactions on Electron Devices, 54 (2007) 1040-1048.

[145] T. Minami, H. Sato, H. Nanto, S. Takata, Group III impurity doped zinc oxide thin films prepared by RF magnetron sputtering, Japanese journal of applied physics, 24 (1985) L781.

[146] B.D. Yuhas, D.O. Zitoun, P.J. Pauzauskie, R. He, P. Yang, Transition-Metal Doped Zinc Oxide Nanowires, Angewandte Chemie, 118 (2006) 434-437.

[147] A. Manikandan, E. Manikandan, B. Meenatchi, S. Vadivel, S. Jaganathan, R. Ladchumananandasivam, M. Henini, M. Maaza, J.S. Aanand, Rare earth element (REE) lanthanum doped zinc oxide (La: ZnO) nanomaterials: synthesis structural optical and antibacterial studies, Journal of Alloys and Compounds, 723 (2017) 1155-1161.

[148] N. Krishnamurthy, C.K. Gupta, Extractive metallurgy of rare earths, CRC press, 2004.

[149] G. Accorsi, Trivalent lanthanide ions: luminescence and applications, in, alma, 2007.

[150] A. Meijerink, R. Wegh, P. Vergeer, T. Vlugt, Photon management with lanthanides, Optical Materials, 28 (2006) 575-581.

[151] G. Blasse, B. Grabmaier, Luminescent materials, Springer Science & Business Media, 2012.

[152] K. Ogasawara, S. Watanabe, H. Toyoshima, M.G. Brik, First-principles calculations of 4fn→ 4fn− 15d transition spectra, Handbook on the Physics and Chemistry of Rare Earths, 37 (2007) 1-59.

[153] A.L. Allenic, Structural, Electrical and Optical Properties of p-Type ZnO Epitaxial Films, (2008).

[154] M.M.M. Almotari, Fabrication and Characterisation of Zinc Oxide Thin Films Singly doped With Trace amounts of Rare Earth Materials, (2013).

[155] P.M. Becker, A.A. Olsson, J.R. Simpson, Erbium-doped fiber amplifiers: fundamentals and technology, Academic press, 1999.

[156] G.H. Dieke, Spectra and Energy Levels of Rare Earth Ions in Crystals, (1968).

[157] R. Reisfeld, Excited states and energy transfer from donor cations to rare earths in the condensed phase, in: Rare Earths, Springer, 1991, pp. 65-97.

[158] J. Huang, S. Liu, B. Gao, T. Jiang, Y. Zhao, S. Liu, L. Kuang, X. Xu, Synthesis and optical properties of eu3+ doped zno nanoparticles used for white light emitting diodes, Journal of nanoscience and nanotechnology, 14 (2014) 3052-3055.

[159] L. Luo, F. Huang, G. Dong, Y. Wang, Z. Hu, J. Chen, White light emission and luminescence dynamics in eu3+/dy3+ codoped zno nanocrystals, Journal of nanoscience and nanotechnology, 16 (2016) 619-625.

[160] V. Mangalam, K. Pita, Energy Transfer Efficiency from ZnO-Nanocrystals to Eu3+ Ions Embedded in SiO2 Film for Emission at 614 nm, Materials, 10 (2017) 930.

[161] B. Bendre, S. Mahamuni, Luminescence in ZnO quantum particles, Journal of materials research, 19 (2004) 737-740.

[162] D. Chen, Y. Wang, E. Ma, F. Bao, Y. Yu, Luminescence of an Er3+-doped glass matrix containing CdS quantum dots, Scripta materialia, 55 (2006) 891-894.

[163] J. Bang, H. Yang, P.H. Holloway, Enhanced luminescence of SiO 2: Eu 3+ by energy transfer from ZnO nanoparticles, The Journal of chemical physics, 123 (2005) 084709.

[164] M. Chong, A. Abiyasa, K. Pita, S. Yu, Visible red random lasing in Y 2 O 3: Eu 3+/ZnO polycrystalline thin films by energy transfer from ZnO films to Eu 3+, Applied Physics Letters, 93 (2008) 151105.

[165] Y. Yu, Y. Wang, D. Chen, P. Huang, E. Ma, F. Bao, Enhanced emissions of Eu3+ by energy transfer from ZnO quantum dots embedded in SiO2 glass, Nanotechnology, 19 (2008) 055711.

[166] V. Mangalam, K. Pita, C. Couteau, Study of energy transfer mechanism from ZnO nanocrystals to Eu 3+ ions, Nanoscale research letters, 11 (2016) 73.

[167] G. Blasse, Energy transfer in oxidic phosphors, Physics Letters A, 28 (1968) 444-445.

[168] X. Zhang, X. Qiao, H.J. Seo, Luminescence properties of novel Ce3+, Mn2+ doped NaSr4 (BO3) 3 phosphors, Current Applied Physics, 11 (2011) 442-446.

[169] Q. Pang, J. Shi, M. Gong, Photoluminescent properties of SrTiO3: Pr, Al nanophosphors synthesized by microemulsion–microwave heating, Journal of the American Ceramic Society, 90 (2007) 3943-3946.

[170] M. Inokuti, F. Hirayama, Influence of energy transfer by the exchange mechanism on donor luminescence, The journal of chemical physics, 43 (1965) 1978-1989.

[171] X. Ruan, M. Kaviany, Enhanced nonradiative relaxation and photoluminescence quenching in random, doped nanocrystalline powders, Journal of applied physics, 97 (2005) 104331.

[172] J. Axe, P. Weller, Fluorescence and energy transfer in Y2O3: Eu3+, The Journal of Chemical Physics, 40 (1964) 3066-3069.

[173] R. Orbach, Relaxation and energy transfer, in: Optical properties of ions in solids, Springer, 1975, pp. 355-399.

[174] T. Miyakawa, D. Dexter, Phonon sidebands, multiphonon relaxation of excited states, and phonon-assisted energy transfer between ions in solids, Physical Review B, 1 (1970) 2961.

[175] Q. Zhang, X. Huang, Recent progress in quantum cutting phosphors, Progress in Materials Science, 55 (2010) 353-427.

[176] T. Basiev, M. Doroshenko, V. Osiko, Cooperative nonradiative cross-relaxation in crystals of La (1− x) Ce x F 3 solid solutions, Journal of Experimental and Theoretical Physics Letters, 71 (2000) 8-11.

[177] T.F. Soules, R.L. Bateman, R.A. Hewes, E.R. Kreidler, Energy transfer between antimony and manganese in the fluorophosphate phosphors, Physical Review B, 7 (1973) 1657.

[178] M. Yokota, O. Tanimoto, Effects of diffusion on energy transfer by resonance, Journal of the physical society of Japan, 22 (1967) 779-784.

[179] W. Shockley, H.J. Queisser, Detailed balance limit of efficiency of p-n junction solar cells, Journal of applied physics, 32 (1961) 510-519.

[180] B.M. Van Der Ende, L. Aarts, A. Meijerink, Lanthanide ions as spectral converters for solar cells, Physical Chemistry Chemical Physics, 11 (2009) 11081-11095.

[181] B. Richards, Enhancing the performance of silicon solar cells via the application of passive luminescence conversion layers, Solar energy materials and solar cells, 90 (2006) 2329-2337.

[182] M.A. Green, K. Emery, Y. Hishikawa, W. Warta, Solar cell efficiency tables (version 36), Progress in photovoltaics: research and applications, 18 (2010) 346-352.

[183] M.A. Green, K. Emery, Y. Hishikawa, W. Warta, E.D. Dunlop, Solar cell efficiency tables (Version 45), Progress in photovoltaics: research and applications, 23 (2015) 1-9.

[184] M.A. Green, Photovoltaic principles, Physica E: Low-dimensional Systems and Nanostructures, 14 (2002) 11-17.

[185] F. Dimroth, High-efficiency solar cells from III-V compound semiconductors, Physica Status solidi (c), 3 (2006) 373-379.

[186] V.I. Klimov, S.A. Ivanov, J. Nanda, M. Achermann, I. Bezel, J.A. McGuire, A. Piryatinski, Single-exciton optical gain in semiconductor nanocrystals, Nature, 447 (2007) 441.

[187] R.D. Schaller, V.M. Agranovich, V.I. Klimov, High-efficiency carrier multiplication through direct photogeneration of multi-excitons via virtual single-exciton states, Nature physics, 1 (2005) 189.

[188] M. Hanna, A. Nozik, Solar conversion efficiency of photovoltaic and photoelectrolysis cells with carrier multiplication absorbers, Journal of Applied Physics, 100 (2006) 074510.

[189] A. Nozik, Quantum dot solar cells, Physica E: Low-dimensional Systems and Nanostructures, 14 (2002) 115-120.

[190] D. Timmerman, I. Izeddin, P. Stallinga, I. Yassievich, T. Gregorkiewicz, Space-separated quantum cutting with silicon nanocrystals for photovoltaic applications, Nature Photonics, 2 (2008) 105.

[191] C. Strümpel, M. McCann, G. Beaucarne, V. Arkhipov, A. Slaoui, V. Švrček, C. Del Cañizo, I. Tobias, Modifying the solar spectrum to enhance silicon solar cell efficiency—An overview of available materials, Solar energy materials and solar cells, 91 (2007) 238-249.

[192] R.E. Bird, C. Riordan, Simple solar spectral model for direct and diffuse irradiance on horizontal and tilted planes at the earth's surface for cloudless atmospheres, Journal of climate and applied meteorology, 25 (1986) 87-97.

[193] R. Bird, R. Hulstrom, A. Kliman, H. Eldering, Solar spectral measurements in the terrestrial environment, Applied Optics, 21 (1982) 1430-1436.

[194] A. Shalav, B. Richards, T. Trupke, K. Krämer, H.-U. Güdel, Application of NaYF 4: Er 3+ up-converting phosphors for enhanced near-infrared silicon solar cell response, Applied Physics Letters, 86 (2005) 013505.

[195] A. Shalav, B. Richards, T. Trupke, R. Corkish, K. Kramer, H. Gudel, M. Green, The application of up-converting phosphors for increased solar cell conversion efficiencies, in: Photovoltaic Energy Conversion, 2003. Proceedings of 3rd World Conference on, IEEE, 2003, pp. 248-250.

[196] R. Martín-Rodríguez, S. Fischer, A. Ivaturi, B. Froehlich, K.W. Krämer, J.C. Goldschmidt, B.S. Richards, A. Meijerink, Highly efficient IR to NIR upconversion in Gd2O2S: Er3+ for photovoltaic applications, Chemistry of materials, 25 (2013) 1912-1921.

[197] B. Richard, A. Shalav, The role of polymers in the luminescence conversion of sunlight for enhanced solar cell performance, Synthetic metals, 154 (2005) 61-64.

[198] T. Trupke, M. Green, P. Würfel, Improving solar cell efficiencies by down-conversion of high-energy photons, Journal of applied physics, 92 (2002) 1668-1674.

[199] B. Richards, Luminescent layers for enhanced silicon solar cell performance: Down-conversion, Solar energy materials and solar cells, 90 (2006) 1189-1207.

[200] V. Rodríguez, V. Tikhomirov, J. Méndez-Ramos, A. Yanes, V. Moshchalkov, Towards broad range and highly efficient down-conversion of solar spectrum by Er3+–Yb3+ co-doped nano-structured glass-ceramics, Solar Energy Materials and Solar Cells, 94 (2010) 1612-1617.

[201] D. Dexter, Possibility of luminescent quantum yields greater than unity, Physical Review, 108 (1957) 630.

[202] J. Sommerdijk, A. Bril, A. De Jager, Two photon luminescence with ultraviolet excitation of trivalent praseodymium, Journal of Luminescence, 8 (1974) 341-343.

[203] W. Piper, J. DeLuca, F. Ham, Cascade fluorescent decay in Pr3+-doped fluorides: Achievement of a quantum yield greater than unity for emission of visible light, Journal of Luminescence, 8 (1974) 344-348.

[204] R.T. Wegh, H. Donker, K.D. Oskam, A. Meijerink, Visible quantum cutting in LiGdF4: Eu3+ through downconversion, Science, 283 (1999) 663-666.

[205] J. Berkowitz, J. Olsen, Investigation of luminescent materials under ultraviolet excitation energies from 5 to 25 eV, Journal of luminescence, 50 (1991) 111-121.

[206] T. Trupke, M. Green, P. Würfel, Improving solar cell efficiencies by up-conversion of sub-band-gap light, Journal of Applied Physics, 92 (2002) 4117-4122.

[207] Y. Jestin, Down-Shifting of the Incident Light for Photovoltaic Applications, (2012).

[208] W. Van Sark, A. Meijerink, R. Schropp, J. Van Roosmalen, E. Lysen, Enhancing solar cell efficiency by using spectral converters, Solar energy materials and solar cells, 87 (2005) 395-409.

[209] W. Van Sark, Enhancement of solar cell performance by employing planar spectral converters, Applied Physics Letters, 87 (2005) 151117.

[210] S. Ye, B. Zhu, J. Luo, Y. Teng, J. Chen, G. Lakshminarayana, G. Qian, J. Qiu, Energy transfer between silicon–oxygen-related defects and Yb 3+ in transparent glass ceramics containing Ba 2 TiSi 2 O 8 nanocrystals, Applied Physics Letters, 93 (2008) 181110.

[211] J. Liu, Q. Yao, Y. Li, Effects of downconversion luminescent film in dye-sensitized solar cells, Applied physics letters, 88 (2006) 173119.

[212] M. Peng, L. Wondraczek, Bismuth-doped oxide glasses as potential solar spectral converters and concentrators, Journal of Materials Chemistry, 19 (2009) 627-630.

[213] V. Švrček, A. Slaoui, J.-C. Muller, Silicon nanocrystals as light converter for solar cells, Thin Solid Films, 451 (2004) 384-388.

[214] G. Maggioni, S. Carturan, M. Tonezzer, M. Buffa, A. Quaranta, E. Negro, G. Della Mea, Porphyrin-containing polyimide films deposited by high vacuum co-evaporation, European Polymer Journal, 44 (2008) 3628-3639.

[215] F. Auzel, Upconversion and anti-stokes processes with f and d ions in solids, Chemical reviews, 104 (2004) 139-174.

[216] F. Auzel, Upconversion processes in coupled ion systems, Journal of Luminescence, 45 (1990) 341-345.

[217] G. Zhou, D. Wang, S. Yang, Y. Ren, X. Xu, X. Zhao, Z. Shao, M. Jiang, Y. Tian, F. Hao, Spectral and temporal properties of two-photon pumped amplified spontaneous emission and cavity lasing of a new organic dye, Journal of Modern Optics, 50 (2003) 847-855.

[218] A. Goetzberger, C. Hebling, H.-W. Schock, Photovoltaic materials, history, status and outlook, Materials Science and Engineering: R: Reports, 40 (2003) 1-46.

[219] X. Mathew, Band gap of CdTe thin films—The dependence on temperature, Journal of materials science letters, 21 (2002) 529-531.

[220] M. Grätzel, Dye-sensitized solar cells, Journal of Photochemistry and Photobiology C: Photochemistry Reviews, 4 (2003) 145-153.

[221] N. Chander, A.F. Khan, V.K. Komarala, S. Chawla, V. Dutta, Enhancement of dye sensitized solar cell efficiency via incorporation of upconverting phosphor nanoparticles as spectral converters, Progress in Photovoltaics: Research and Applications, 24 (2016) 692-703.

[222] M. Tsuda, K. Soga, H. Inoue, S. Inoue, A. Makishima, Upconversion mechanism in Er 3+-doped fluorozirconate glasses under 800 nm excitation, Journal of applied physics, 85 (1999) 29-37.

[223] N. Chander, S.K. Sardana, P.K. Parashar, A. Khan, S. Chawla, V.K. Komarala, Improving the short-wavelength spectral response of silicon solar cells by spray deposition of YVO 4: Eu 3+ downshifting phosphor nanoparticles, IEEE Journal of Photovoltaics, 5 (2015) 1373-1379.

[224] N. Chander, A.F. Khan, V.K. Komarala, Improved stability and enhanced efficiency of dye sensitized solar cells by using europium doped yttrium vanadate down-shifting nanophosphor, RSC Advances, 5 (2015) 66057-66066.

[225] N. Chander, A. Khan, P. Chandrasekhar, E. Thouti, S.K. Swami, V. Dutta, V.K. Komarala, Reduced ultraviolet light induced degradation and enhanced light harvesting using YVO4: Eu3+ down-shifting nano-phosphor layer in organometal halide perovskite solar cells, Applied Physics Letters, 105 (2014) 033904.

[226] N. Wu, Q. Luo, X. Qiao, C.-Q. Ma, The preparation of a Eu3+-doped ZnO bi-functional layer and its application in organic photovoltaics, Materials Research Express, 2 (2015) 125901.

[227] H. Zhou, Y. Qu, T. Zeid, X. Duan, Towards highly efficient photocatalysts using semiconductor nanoarchitectures, Energy & Environmental Science, 5 (2012) 6732-6743.

[228] N. Yao, J. Huang, K. Fu, X. Deng, M. Ding, M. Shao, X. Xu, Enhanced light harvesting of dye-sensitized solar cells with up/down conversion materials, Electrochimica Acta, 154 (2015) 273-277.

[229] L. Armelao, G. Bottaro, M. Pascolini, M. Sessolo, E. Tondello, M. Bettinelli, A. Speghini, Structure− luminescence correlations in europium-doped sol− gel ZnO nanopowders, The Journal of Physical Chemistry C, 112 (2008) 4049-4054.

[230] Y. Tian, B. Chen, R. Hua, J. Sun, L. Cheng, H. Zhong, X. Li, J. Zhang, Y. Zheng, T. Yu, Optical transition, electron-phonon coupling and fluorescent quenching of La2 (MoO4) 3: Eu3+ phosphor, Journal of Applied Physics, 109 (2011) 053511.

[231] M. Subramanian, P. Thakur, S. Gautam, K. Chae, M. Tanemura, T. Hihara, S. Vijayalakshmi, T. Soga, S. Kim, K. Asokan, Investigations on the structural, optical and electronic properties of Nd doped ZnO thin films, Journal of Physics D: Applied Physics, 42 (2009) 105410.

[232] B. Shahmoradi, K. Soga, S. Ananda, R. Somashekar, K. Byrappa, Modification of neodymium-doped ZnO hybrid nanoparticles under mild hydrothermal conditions, Nanoscale, 2 (2010) 1160-1164.

[233] A. George, S.K. Sharma, S. Chawla, M. Malik, M. Qureshi, Detailed of X-ray diffraction and photoluminescence studies of Ce doped ZnO nanocrystals, Journal of Alloys and Compounds, 509 (2011) 5942-5946.

[234] L.-C. Chao, J.-W. Huang, C.-W. Chang, Annealing effects on the properties of Nd containing ZnO nanoparticles prepared by sol–gel process, Physica B: Condensed Matter, 404 (2009) 1301-1304.

[235] R. Verma, K. Kumar, S. Rai, Pulsed laser ablation synthesis of silver nanoparticles and their use in fluorescence enhancement of Tb3+-doped aluminosilicate glass, Solid State Communications, 150 (2010) 1947-1950.

[236] S.-M. Liu, F.-Q. Liu, H.-Q. Guo, Z.-H. Zhang, Z.-G. Wang, Correlated structural and optical investigation of terbium-doped zinc oxide nanocrystals, Physics Letters A, 271 (2000) 128-133.

[237] S.-M. Liu, F.-Q. Liu, Z.-G. Wang, Relaxation of carriers in terbium-doped ZnO nanoparticles, Chemical physics letters, 343 (2001) 489-492.

[238] T. Jia, W. Wang, F. Long, Z. Fu, H. Wang, Q. Zhang, Synthesis, characterization and luminescence properties of Y-doped and Tb-doped ZnO nanocrystals, Materials Science and Engineering: B, 162 (2009) 179-184.

[239] Z. Wu, X. Liu, J. Huang, Room temperature ferromagnetism in Tb doped ZnO nanocrystalline films, Journal of Magnetism and Magnetic Materials, 324 (2012) 642-644.

[240] A. Ziani, C. Davesnne, C. Labbé, J. Cardin, P. Marie, C. Frilay, S. Boudin, X. Portier, Annealing effects on the photoluminescence of terbium doped zinc oxide films, Thin Solid Films, 553 (2014) 52-57.

[241] S. Gao, H. Zhang, R. Deng, X. Wang, D. Sun, G. Zheng, Engineering white light-emitting Eu-doped ZnO urchins by biopolymer-assisted hydrothermal method, Applied physics letters, 89 (2006) 123125.

[242] J. Park, A. Steckl, Demonstration of a visible laser on silicon using Eu-doped GaN thin films, in, AIP, 2005.

[243] H. Shahroosvand, M. Ghorbani-asl, Solution-based synthetic strategies for Eu doped ZnO nanoparticle with enhanced red photoluminescence, Journal of Luminescence, 144 (2013) 223-229.

[244] C. Pan, C. Chen, J. Chen, P. Huang, G. Chi, C. Chang, F. Ren, S. Pearton, Optical and structural properties of Eu-diffused and doped ZnO nanowires, Applied Surface Science, 256 (2009) 187-190.

[245] M. Najafi, H. Haratizadeh, The effect of growth conditions and morphology on photoluminescence properties of Eu-doped ZnO nanostructures, Solid State Sciences, 41 (2015) 48-51.

[246] M.H.N. Assadi, Y. Zhang, R.-K. Zheng, S.P. Ringer, S. Li, Structural and electronic properties of Eu-and Pd-doped ZnO, Nanoscale research letters, 6 (2011) 357.

[247] V.R. Murthy, R. Schmitt, Isotope abundances of rare-earth elements in meteorites: 1. Implications of samarium, europium, and gadolinium to the early history of the solar system, Journal of Geophysical Research, 68 (1963) 911-917.

[248] C. Lin, S. Young, C. Kung, L. Horng, H. Chen, M. Kao, Y. Shih, C. Ou, Phonon spectra and magnetic behaviors of hydrothermally synthesized Sm-doped ZnO nanorods, Vacuum, 87 (2013) 178-181.

[249] J. Piao, L.-T. Tseng, J. Yi, Ferromagnetism in Sm doped ZnO nanorods by a hydrothermal method, Chemical Physics Letters, 649 (2016) 19-22.

[250] T. Tsuji, Y. Terai, M. hakim bin Kamarudin, M. Kawabata, Y. Fujiwara, Photoluminescence properties of Sm-doped ZnO grown by sputtering-assisted metalorganic chemical vapor deposition, Journal of Non-Crystalline Solids, 358 (2012) 2443-2445.

[251] G.v. Sauvé, R. Fernando, Beyond fullerenes: designing alternative molecular electron acceptors for solution-processable bulk heterojunction organic photovoltaics, The journal of physical chemistry letters, 6 (2015) 3770-3780.

[252] N.S. Sariciftci, L. Smilowitz, A.J. Heeger, F. Wudl, Photoinduced electron transfer from a conducting polymer to buckminsterfullerene, Science, 258 (1992) 1474-1476.

[253] K.A. Mazzio, C.K. Luscombe, The future of organic photovoltaics, Chemical Society Reviews, 44 (2014) 78-90.

[254] K.A. Mazzio, C.K. Luscombe, Correction: The future of organic photovoltaics, Chemical Society Reviews, 44 (2015) 5744-5744.

[255] W.S. Yang, J.H. Noh, N.J. Jeon, Y.C. Kim, S. Ryu, J. Seo, S.I. Seok, High-performance photovoltaic perovskite layers fabricated through intramolecular exchange, Science, 348 (2015) 1234-1237.

[256] N.J. Jeon, J.H. Noh, W.S. Yang, Y.C. Kim, S. Ryu, J. Seo, S.I. Seok, Compositional engineering of perovskite materials for high-performance solar cells, Nature, 517 (2015) 476.

[257] D. Bi, C. Yi, J. Luo, J.-D. Décoppet, F. Zhang, S.M. Zakeeruddin, X. Li, A. Hagfeldt, M. Grätzel, Polymer-templated nucleation and crystal growth of perovskite films for solar cells with efficiency greater than 21%, Nature Energy, 1 (2016) 16142.

[258] D.-Y. Son, J.-W. Lee, Y.J. Choi, I.-H. Jang, S. Lee, P.J. Yoo, H. Shin, N. Ahn, M. Choi, D. Kim, Self-formed grain boundary healing layer for highly efficient CH 3 NH 3 PbI 3 perovskite solar cells, Nature Energy, 1 (2016) 16081.

[259] D.B. Mitzi, C. Feild, W. Harrison, A. Guloy, Conducting tin halides with a layered organic-based perovskite structure, Nature, 369 (1994) 467.

[260] J.-H. Im, C.-R. Lee, J.-W. Lee, S.-W. Park, N.-G. Park, 6.5% efficient perovskite quantum-dot-sensitized solar cell, Nanoscale, 3 (2011) 4088-4093.

[261] N. Marinova, S. Valero, J.L. Delgado, Organic and perovskite solar cells: Working principles, materials and interfaces, Journal of colloid and interface science, 488 (2017) 373-389.

[262] J. Bisquert, D. Cahen, G. Hodes, S. Rühle, A. Zaban, Physical chemical principles of photovoltaic conversion with nanoparticulate, mesoporous dye-sensitized solar cells, The Journal of Physical Chemistry B, 108 (2004) 8106-8118.

Chapter 3: Film Growth Methods and Materials Characterization

In this chapter, a brief description of the different techniques used in the growth and characterization of thin films will be presented. The thin films growth techniques discussed include RF magnetron technique, thermal evaporation. Particle morphology, elemental composition, and structure of the pristine and Al and Rare earth doped ZnO were studied using scanning electron microscopy (SEM), Rutherford Backscattering spectroscopy (RBS), energy dispersive spectrometer (EDS), and X-Ray diffraction (XRD). The optical properties were studied were studied using the UV-Vis spectroscopy while optical reflectance to attain thickness, refractive index, color were analyzed using FR-Basic-VIS/NIR fitted with FR-Monitor software for fittings. Luminescent properties were studied using a fluorescence spectroscopy and the data was collected both at room temperature. The current density-voltage characteristics of all the devices were measured by a computer interfaced HP 4141B Source Measure Unit (SMU) under 100 mW/cm^2 illumination (AM 1.5G).

3.1. Thin films deposition methods

Thin films of rare earth ion doped semiconducting metal oxides can be prepared by a wide range of preparation techniques, mainly classified into (i) Physical Vapour Deposition (PVD) methods and (ii) Chemical Vapour Deposition (CVD). PVD methods include DC (Direct Current) and RF (Radio Frequency) Sputtering, Pulsed Laser Deposition (PLD), Electron Beam Evaporation, Thermal Evaporation, Molecular Beam Epitaxy (MBE) etc. Thin film preparation by chemical route includes Chemical vapour deposition (CVD) and their derivatives like metal organic chemical vapour deposition (MOCVD) and halide vapour phase epitaxy (HVPE), low pressure CVD (LPCVD), atmospheric pressure CVD (APCVD), Sol-gel, electro deposition etc. Among all

the PVD techniques, the RF magnetron sputtering, (industrial viable technique) is superior to the other techniques and was subsequently used in the deposition of films discussed in this thesis.

3.2. Thin Film deposition techniques used in this project.

3.2.1. RF magnetron sputtering

Sputtering is a type of Physical Vapor Deposition that is based on the principle of momentum transfer to remove neutral atoms from a target. Magnetron sputtering of transparent conductive oxides (zinc oxide) is a promising technique which allows the deposition of films at low temperatures with good optical and electronic properties. A special advantage is its scalability to large areas [1]. The planar magnetron sputtering source was invented at the beginning of the 70s. Only some years later magnetron sputtering was a well-established commercial technique for the deposition of metals and optical films. Much later the urge for high quality semiconducting thin films saw the use for the deposition of semiconductors (transparent conductive oxides (TCOs). The fundamental difference between magnetron sputtering as a plasma process and thermally excited thin-film preparation methods (evaporation, chemical deposition methods) is the much higher energy input into the growing film, that can be achieved by magnetron sputtering [2, 3].

3.2.2. Basic Principles of RF sputtering

Figure 3-1 shows a pictorial view of the RF sputtering set-up used for film deposition while figure 3-2 gives the schematic representation.

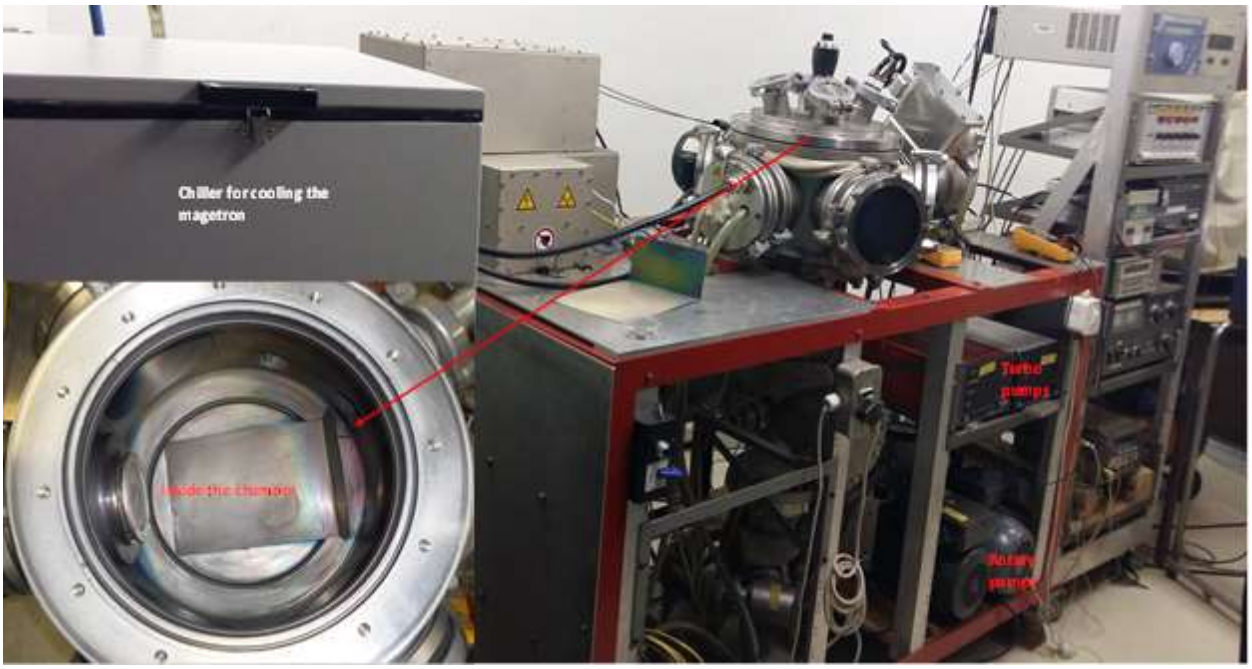


Figure 3-1: Photograph of vacuum system used in the present study and view of inside the deposition chamber.

The material to be deposited (target) acts as the cathode and is connected to a negative voltage supply which could be either direct current (DC) or radio frequency (RF). The substrate is placed on a substrate holder and it can be grounded, floating, biased, heated, cooled, or could be a combination of these. The substrates are placed directly facing the target at a distance of 6 mm. This setup is placed inside a vacuum system which is pumped down and maintained at high vacuum. An inert gas Argon is introduced into the system as the medium for glow discharge. This is because an inert gas like Argon has its metastable energy greater than its first ionization potential which helps in producing a sufficient supply of ions for self-sputtering. When this glow discharge is initiated, ions with high kinetic energy strike the cathode and the subsequent collisions knock loose the neutral atoms from the material by momentum transfer. These neutral atoms then condense on the substrate to form thin films. The principle of momentum transfer used to deposit materials has made the sputtering technique very attractive. Figure 3-2 shows the schematic illustration of the sputtering process.

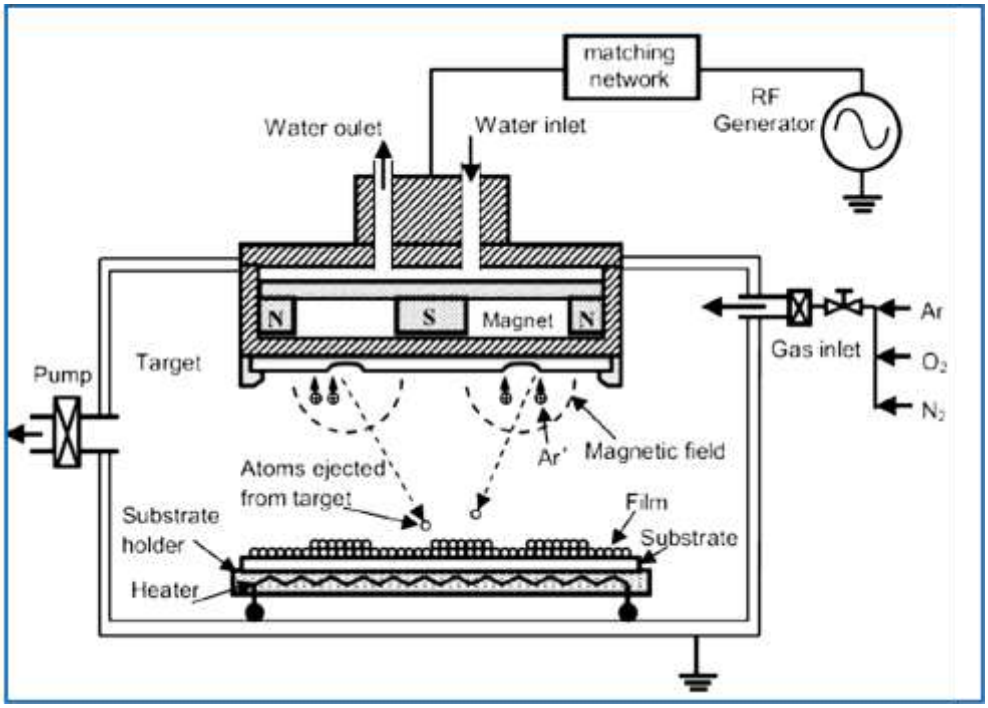


Figure 3-2: Schematic representation of a RF magnetron sputtering system [4].

When ionized gas species (Ar^+) hit the target, an atom is ejected from the surface as a result of momentum transfer from Ar^+ ions to the target atoms through a collision cascade in the near-surface region of the target usually about 10 Å. The average number of sputtered neutral atoms for every Ar^+ ion is described as the sputter yield *S*. With an assumption that the kinetic energy of the incident Ar^+ ions is $E_{ions} < 1$ keV, the sputter yield is expressed by Sigmund [4] in equation 3-1 for amorphous and polycrystalline targets.

$$S = \frac{3\alpha}{4\pi^2} \frac{4M_{ion}M_{target}}{\left(M_{ion}+M_{target}\right)^2} \frac{E_{ion}}{U_{sub}} \quad \text{..... 3-1}$$

where U_{sub} is the heat of sublimation of the target material, and $\alpha\left(\frac{M_{target}}{M_{ion}}\right)$ usually have values ranging between 0.2 and 1.4 depending on the target-to-ion mass ratio.

From equation 3-1, the sputter yield is proportional to the ion energy, but inversely proportional to the sublimation energy of the target material, some sputter yields of various materials are reported in Ref [5]. Generally compounds such as nitrides and oxides (such as ZnO) have lower sputter yields than pure metals. This is because the compounds materials possess higher sublimation or binding energy [6].

The energy distribution of the sputtered neutral atoms is described by equation 3-2 [7]

$$f\left(E_{sput}\right) \propto \frac{E_{SB}E_{sput}}{\left(E_{SB}+E_{sput}\right)^{3}} \quad \text{..... 3-2}$$

where E_{sput} is the energy of the sputtered particle, and E_{SB} is the surface binding energy of the target atoms. For E_{sput} larger than the E_{SB}, $f(E_{sput})$ decreases as $1/E_{sput}^{2}$. From equation 3-2, the energy distribution is independent of the energy of the incident ions. The maximum in this distribution occurs when $E_{sput} = 1/2E_{SB}$, which is about 0.5–2 eV for most metals. Thus, if the mean free path of the sputtered atoms is sufficiently large to avoid collisions, the majority of sputtered atoms reach the substrate with kinetic energies in the range of 1–20 eV. However, due to the high-energy tail of the energy distribution, target atoms with even higher energy also impinge on the substrate.

Apart from the sputtered target atoms, the film being grown is also hit by backscattered neutral working-gas atoms, which are vital as a result of their relatively high kinetic energy. On striking the target, part of the gas ions are neutralized and reflected because of the binary collision with target atoms. The energy of these backscattered neutrals (for scattering angle of 180˚) is given by equation 3-3 [8].

$$E_{neutral} = E_{ion}\left(\frac{M_{ion} - M_{target}}{M_{ion} + M_{target}}\right)^2 \quad \ldots\ldots\ldots\ldots\ldots\ldots\ldots\ldots\ldots\ldots \text{3-3}$$

where M_{ion}, E_{ion} and M_{target} are the mass and energy of the incident gas ion and mass of the target atom, respectively.

The proportion of the neutrals that arrive at the growing film have an energy corrected for losses during collisions with the working gas. However, due to the broad energy distribution of the impinging Ar^+ ions, the energy distribution of backscattered neutrals will also be rather broad and the average energy is typically 10–40 eV [9]. Therefore, the calculated values using equation 3-3 should be considered as extreme values. Winters et al. [10] calculated the ratio of the energy carried away from the target by reflected neutrals to that carried away by sputtered particles versus the incident ion kinetic energy.

From this discussion, the sputtered atoms and reflected neutrals are far more energetic than for example evaporated atoms (~ 0.1 eV) during thermal evaporation. Therefore, the atoms impinging on the substrate using sputter deposition system are relatively more energetic with higher adatom mobility.

3.2.3. Advantages of magnetron sputtering

When compared to other thin-film deposition methods such as thermal evaporation, chemical vapour deposition (CVD) or spray pyrolysis, magnetron sputtering has the following advantages:

- low substrate temperatures (down to room temperature)
- good adhesion of films on substrates
- high deposition rates (up to 12 µm min^{-1}) [11].
- Very good thickness uniformity and high mass density of the films.

- Good controllability and long-term stability of the process.
- Alloys and compounds of materials with very different vapour pressures can be sputtered easily without preferential sputtering of a particular component.
- By reactive sputtering in rare/reactive gas mixtures many compounds can be deposited from elemental (metallic) targets.
- Relatively cheap deposition method
- Scalability to large areas [12].

3.3. Ion implantation of Rare earth ions

Ion implantation is a common technique used to incorporate foreign ions into a host material. When an energetic ion impinges upon the surface of condensed matter, it experiences a series of inelastic and elastic collisions with atoms along its path. This results in the loss of kinetic energy of the projectile and excitation of the solid material as well as momentum transfer between the interacting bodies [13]. Implantation has a number of advantages [14]:

- Speed, homogeneity and reproducibility of the doping process.
- Exact control of the implantation fluence by integration of the beam current.
- Isotopically selectively ion beams due to mass separation.
- Possibility to exceed the solubility limit by operating far from thermal equilibrium.
- Simple masking methods to make lateral patterns for devices.

The energy lost by the projectile as it travels through a solid is determined by the "stopping power", defined as the energy transfer per unit path length of a particle along its trajectory and denoted by equation 3-4.

$$S(E) = -\frac{dE}{dx} \quad \text{..... 3-4}$$

Where the negative sign indicates an energy loss change along the path length.

Consider maximum possible energy transfer during collision to be T_{max} and target atoms per unit volume to be N_{ions}, then the stopping power is given by equation 3-5.

$$-\frac{dE}{dx} = -N_{ions}\int T_{\max} d\varepsilon \quad \ldots\ldots\ldots\ldots\ldots\ldots \text{3-5}$$

where $d\varepsilon$ the differential implanted cross section by the trajectory. N_{ions} is also called the implant density. Expressing equation 3-5 in terms of the atomic density, then N_{ions} can be approximated as a Gaussian range distribution as predicted by Lindhart, Scharff and Schiott [15] given by equation 3-6.

$$N(x) = \frac{\varphi}{\Delta R_p \sqrt{2\pi}} \exp\left[-\frac{\left(x - R_p\right)^2}{2\left(\Delta R_p\right)^2}\right] \quad \ldots\ldots\ldots\ldots\ldots\ldots \text{3-6}$$

where φ is the ion fluence, ΔR_p is the standard deviation for the mean projected range (projected range straggle) defining the position of the peak measured from the target's surface, R_p the mean perpendicular penetration depth also known as the projected range and x the ion depth of penetration [16].

3.3.1. Ion range

As the incident ion travels into the solid target matrix, it encounters multiple collisions with the substrate's atoms hence does not travel linearly till the end of range position. The implanted range R(E), therefore defines the total integrated distance the ion travels through the solid before coming to rest [17, 18] and is defined by equation 3-7.

$$R(E) = \int \frac{dE}{S_n(E) + S_e(E)} \quad \ldots\ldots\ldots\ldots\ldots\ldots\ldots\ldots \text{3-7}$$

where $S_n(E)$ and $S_e(E)$ are the nuclear and electronic stopping powers respectively.

The projected range defines the net perpendicular peak position measured from the target's surface or in other words, the mean penetration depth relative to the surface. However, due to the statistics of the process, not all the ions reach the same depth and the ion distribution obtained after implantation can be approximated by a Gaussian distribution being characterized by mean projected range R_p and the straggling $\Delta Rp(E)$ defined in equation 3-6 [17, 19, 20]. The depth distribution of implanted ions is as shown in figure 3-3.

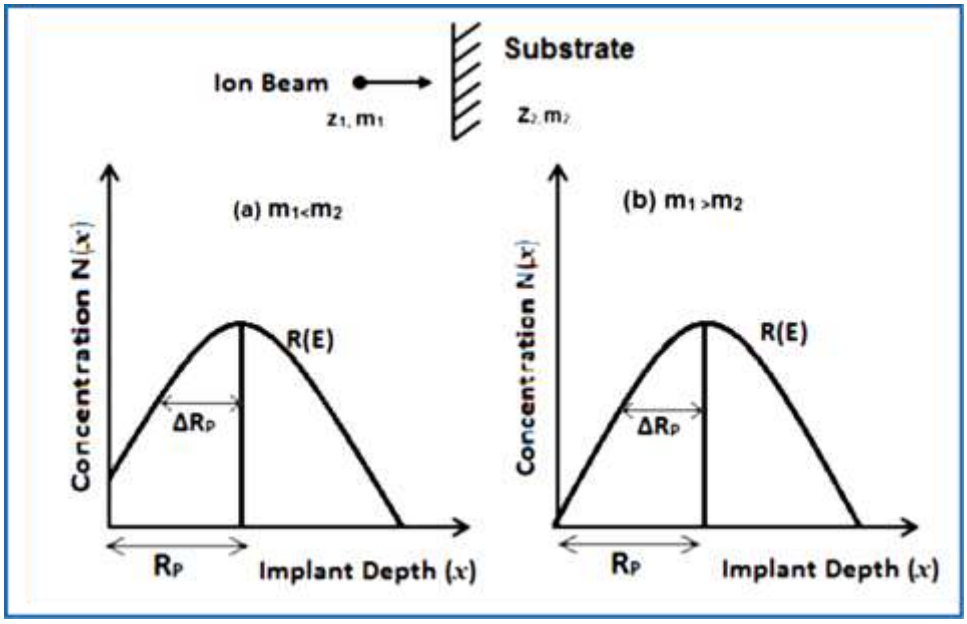


Figure 3-3: Depth distribution of implanted ions in a target for; (a) the ion mass m_1 < mass m_2 of the substrate [19]. The mean depth Rp depends only on m_1 and E_1 whereas ΔRp/Rp depends on the ratio m_1:m_2.

3.3.2. Implantation procedure

During ion implantation, ions of desired species (Sm, Eu and Tb in our case) are formed by stripping electrons from source atoms (Sm_2O_3, ZnO (97%): Eu (3%) and ZnO (97%): Tb (3%) sputter target respectively), in the plasma. They are subsequently extracted and mass selected by an analyzing magnet before being accelerated towards the target via a potential gradient column. The ion beam is scanned over an area and the sample to be implanted is positioned in the end

station within the scanned area of the beam. The ions are usually injected at the cost of some structural damage to the crystal lattice of the target as discussed in the beginning, forming vacancies and interstitials in the target. This structural disorder can be removed by a subsequent thermal annealing process in an inert atmosphere at high temperature, which also helps to segregate the implanted species and the host material phases. Accurate tailoring of the depth and size distribution and the concentration of implanted ions can be achieved by controlling implantation parameters (ion energy and flux and beam current) and annealing parameters (temperature, time and atmosphere conditions) [21]. A schematic representation of the generation and control of the ion beam is shown in figure 3-4 [22].

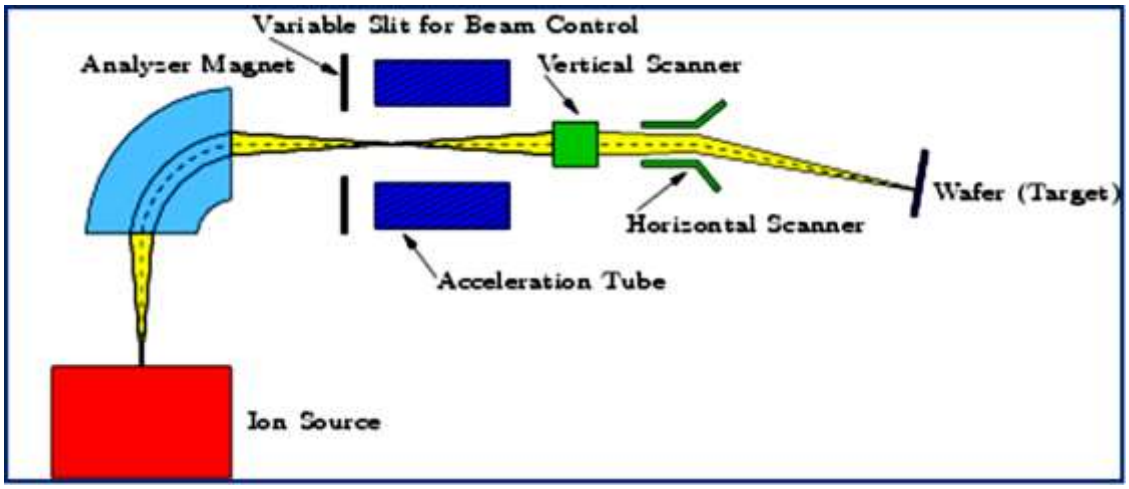


Figure 3-4: General schematic of an ion implantation equipment

3.4. Substrate Cleaning

Substrate cleaning is a crucial step in the preparation of high quality thin films as well as for high adherence to the substrate. In the present study, we have used silicon (100), ITO coated glass and quartz substrates for all the analysis. Firstly all the samples were cleaned by normal water, then the silicon substrates were separately immersed and rinsed using de-ionized water. They were subsequently cleaned by an ultrasonic cleaner in an ethanol alcohol bath for 15 minutes and then washed thoroughly with deionized water and allowed to dry with nitrogen flush. These quartz and ITO substrates were first cut in small pieces measuring 125 mm^2. For ITO each piece had a portion wet etched through a reaction between the HCl and Zn paste embossed on the film. The etched ITO and cut quartz were then ultra-sonicated in a soap solution then rinsed thoroughly in deionized water bath. After rinsing they were cleaned in acetone bath for 15 minutes, rinsed in deionized water followed cleaning in ethanol solution for 15 minutes. Finally they were rinsed in deionized water bath for 15 minutes and then allowed to dry with nitrogen flush. The main aim of cleaning the substrates by acetone is to remove the inorganic/organic impurities respectively and finally acetone is removed by ethanol cleaning. Ultrasonic cleaning in deionized water bath was done to remove any other foreign particles that stays on the surface of the substrates.

3.5. Thermal Annealing of the films

After the RF thin film deposition, the annealing treatment was an efficient approach to improve the crystalline quality and optical property of as-deposited films [23, 24]. A commercial annealing furnace (Carbolite Gero model) was used for post-treatment of the deposited films under various gases at ambient pressure. It is most often utilized in laboratories as a compact means of creating suitable post-treatment high temperature atmospheres. The furnace can be fine pre-turned to hold and stable temperatures in the range 500-1000 ˚C at a resolution of ± 5 ˚C. These were the selected

temperature range used in this work. The films were placed in a quartz glass boat before inserted into a ceramic tube of dimensions, 10 cm in diameter and length 75 cm. The samples were placed at the centre of the zone furnace for homogenous temperature distribution. The Alumina tube was subsequently sealed using vacuum sealing flanges prior to the bleeding of nitrogen gas in the furnace during annealing. Annealing was carried out at a ramping rate of 10 ˚C/minute to the set point temperature to the desired set point temperature. The fluctuations at the set point temperature were marginal for high annealing temperatures (± 5 ˚C) due to the high sensitivity of the PID programme parameters at these temperature ranges. The annealing process is summarized in figure 3-5 while table 3-1 shows a summary of the conditions used in this work.

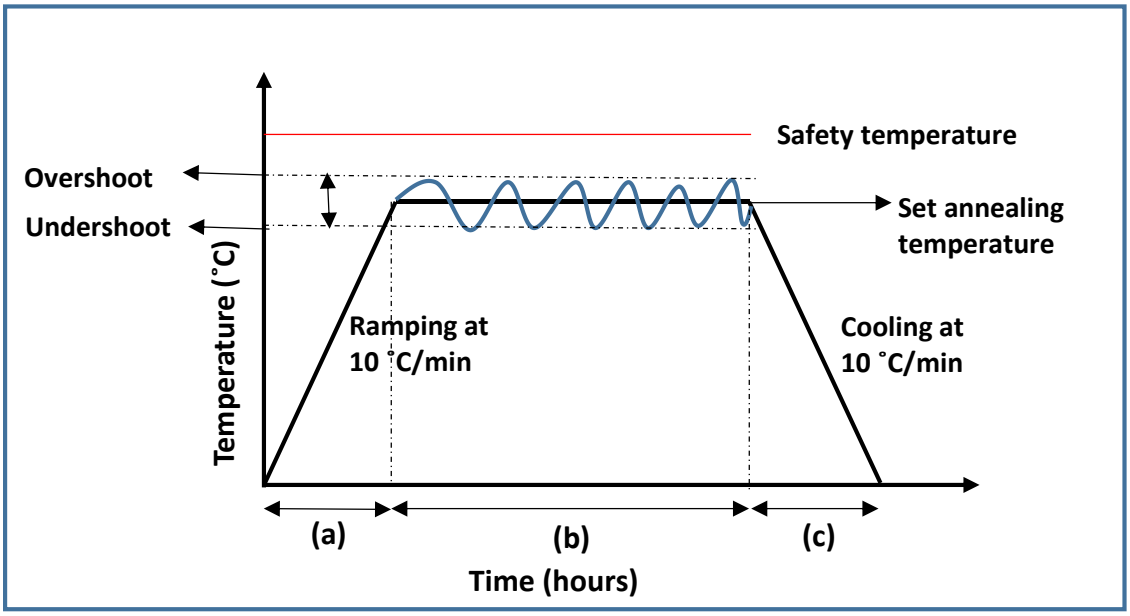


Figure 3-5: Summary of furnace annealing process where (a), (b) and (c) depicts the ramping, dwelling and cooling time respectively.

Table 3-1: Post-treatment parameters of furnace annealing used in this study

Substrate	Quartz glass, p-type silicon (001)(0.02 Ω.cm), ITO (30-60 Ω/sq), FTO
Gas flow rate	N_2 at about 100 sccm
Temperature	300-1000 ˚C
Annealing time	0.5-2 hours

3.6. Thin film Characterization

3.6.1. Film Thickness Measurement

The film thickness measurement was carried out using Filmetrics F20 shown in figure 3-6



Figure 3-6: The Filmetrics F20 instrument used for thickness measurements

Principle behind Filmetrics F20

Considering a thin film of ZnO on Si substrate as shown in figure 3-7, the monochromatic light incident to the film-substrate system of optical constants, n_1 and k_1 for the film and n_2 and k_2 for the substrate undergoes reflection and transmission at their interfaces and in the media. The light that is simultaneously reflected and transmitted through the thin film and then again transmitted and back reflected at the ZnO-Si interface experiences a phase shift that is determined by the difference in the path length of the two reflections at the air-ZnO interfaces. The quantitative aspects of these reflections can be combined as shown in equation 3-8.

$$R = A + B\cos\left(\frac{4\pi}{\lambda}\right)nd \quad \ldots\ldots\ldots\ldots\ldots\ldots\ldots\ldots\ldots\ldots \text{3-8}$$

Where n is the refractive index and d is the thickness

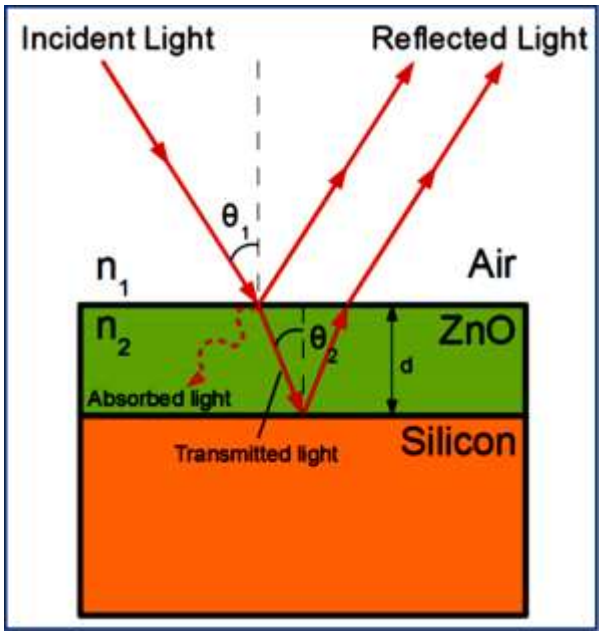


Figure 3-7: Representation of light reflectance from two layers

Reflected light from ZnO and Si thin film will interfere with one another and form a new wave that is sent back to the spectrometer with information about the film's thickness and the refractive

index. The film's thickness, optical constants, and roughness will determine the amplitude and periodicity of the measured reflectance spectrum. The reflectance spectrum is a film's percent reflectance versus the wavelength of light, where 1 is equivalent to 100% reflectance. The film's properties are approximated using mathematical models defined in Ref [25] which shows refractive index *(n)* and extinction coefficient *(k)* change in a material over a range of wavelengths. The mathematical model uses theoretical values for thickness, *n*, and *k* used to calculate a theoretical reflectance spectrum and adjusts the calculated spectrum until it matches the measured reflectance spectrum for instance as shown in figure 3-8.

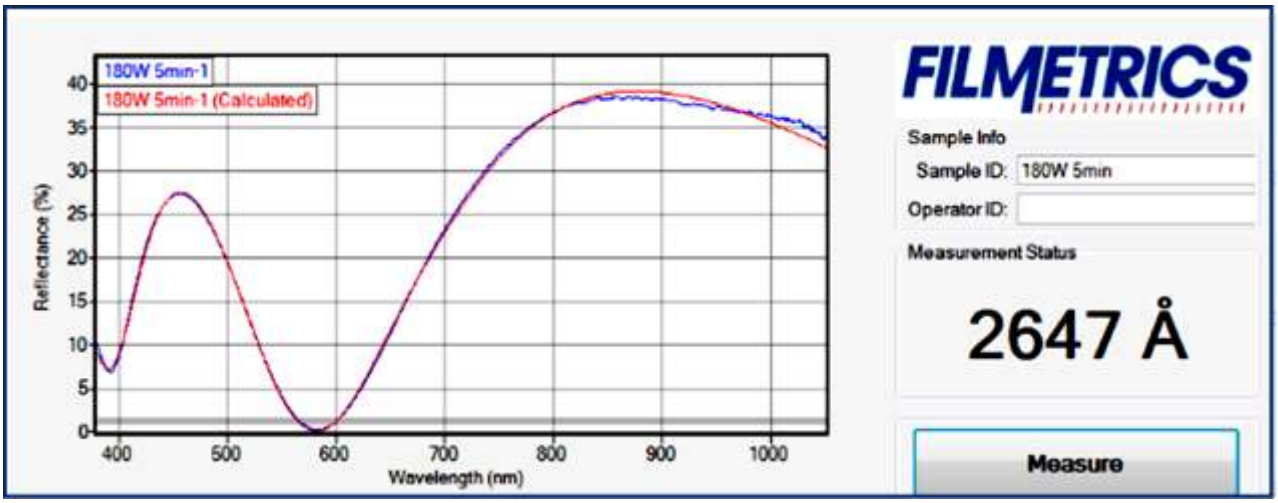


Figure 3-8: An example of reflectance spectrum showing both raw and fitted (calculated) spectrum.

3.6.2. X-Ray Diffraction Studies (XRD)

In Grazing incidence X-ray diffraction (XRD) and X-ray reflectivity (XRR) measurements the thin films are subjected to X-ray radiation. X-ray radiation used in these measurements consists of X-ray photons from the $K_{\alpha 1}$-line of copper with wavelength 1.5405 Å [26].

The concept of the X-ray diffraction in crystals is derived from elastic scattering processes where the scattered X-rays have the same wavelength as the incident beam but have momentum transferred in the scattering process. These scattered X-rays carry information about the electron

distribution in materials and are produced by elastic scattering only when certain geometrical conditions are fulfilled [27]. By measuring the angle and intensity of the output radiation with respect to the incident, the structural properties of a sample can be determined where the maximum intensity can be described by equation 3-9.

$$\frac{|Q|}{2\pi} = \frac{\sqrt{h^2+k^2+l^2}}{a} \quad \text{..... 3-9}$$

Where Q is the vector of momentum transfer also called scattering vector ($Q = S - S_0$, S and S_o describes direction of incident and outgoing beam respectively). Q can be expressed as in equation 3-10.

$$|Q| = \frac{4\pi \sin\theta}{\lambda} \quad \text{..... 3-10}$$

The wavelength of the incoming x-ray (λ), the scattering angle (θ) and the crystal properties (represented by the Miller indices) are related using equation 3-11.

$$\lambda = \frac{a}{\sqrt{h^2+k^2+l^2}} \sin\theta \quad \text{..... 3-11}$$

But since the distance between two adjacent planes d_{hkl} for a cubic lattice is given by equation 3-12, equation 3-11 can be expressed as equation 3-13.

$$d_{hkl} = \frac{a}{\sqrt{h^2+k^2+l^2}} \quad \text{..... 3-12}$$

$$2d_{hkl} \sin\theta_B = \lambda \quad \text{..... 3-13}$$

This is the Bragg relation, where θ_B is the Bragg angle which is the position of maximum reflected x-ray intensity. For an x-ray plane wave scattered from an atom plane in a crystal with a spacing of d_{hkl} between the planes, the phase shift of the wave is $2d\sin\theta$ for any angle θ. However

constructive interference can only be realized when the phase shift is equal to a multiple, n, of the wavelength as expressed in equation 3-14.

$$2d\sin\theta_B = n\lambda \quad \text{..... 3-14}$$

where *n* is a integer. This concept may be visualized as shown in figure 3-9.

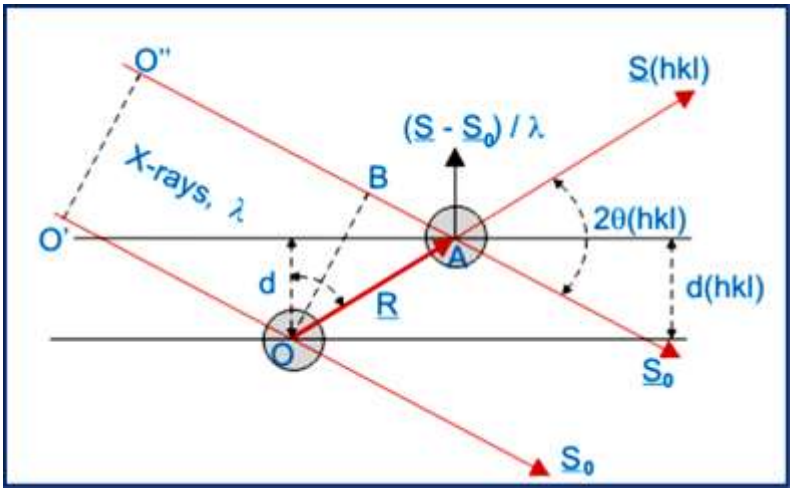


Figure 3-9: The geometrically description of the direction of the diffraction beam due to the constructive interference between atoms located on the planes with interplanar spacing d(hkl).

The setup for a $\theta/2\theta$ scan is shown in figure 3-10. Because the scattered intensity depends on the distance between the sample and detector, the detector is moved on a constant radius hemisphere around the sample. Any intensity variations are thus mainly due to beam-sample interactions. During the scan, the angle of the incoming beam and detector angle with respect to the sample is varied, but kept equal to each other, i.e. $\theta_{\text{incoming}} = \theta_{\text{detector}}$, with maximum intensity occurring when equation 3-14 is satisfied. The width of a Bragg reflection peak also provide information regarding the crystallite size and distortion of the crystal structure such as micro strain and dislocations.

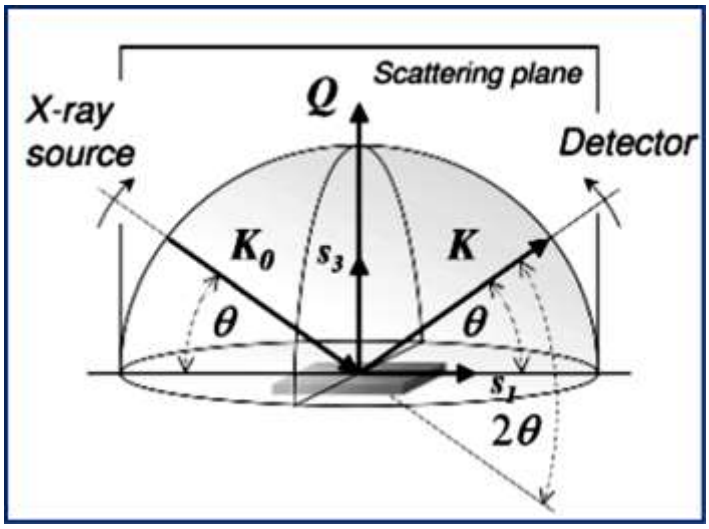


Figure 3-10: A sketch of the instrumental setup for a $\theta/2\theta$ scan

In the case of thin films, the penetration depth of X-rays mostly exceeds the thickness of the film. This causes a large fraction of the intensity to reflect from the substrate. The path travelled by X-ray in the sample can be significantly decreased by utilizing small angles of incident. This technique is known as the grazing incidence X-ray diffraction (GIXRD), and it makes it possible to obtain depth-resolved structural information by probing the sample under shallow angles of incidence.

3.6.3. Raman Spectroscopy

Consider a monochromatic light incident onto a sample, the light may be absorbed, transmitted, reflected or scattered. The scattering may be inelastic (Raman) or/and elastic (Rayleigh) as shown in figure 3-11. Raman spectroscopy is a non-invasive scattering technique used for chemical analysis or in solid state Physics [28-30]. It is based on the Raman Effect where frequency of a small fraction of scattered radiation is different from frequency of monochromatic incident radiation. Raman spectroscopy was named in the honor of its inventor, C.V. Raman, who, along

with K.S. Krishnan, published the first paper on this technique in 1928 who observed that a minute fraction of the incident light was shifted from its initial wavelength upon interacting with a liquid under observation [31]. In this project the elementary excitations are vibrations, particularly Raman active lattice vibrations (phonons). Raman spectroscopy then provides access to the lattice dynamics of a sample and therewith delivers information on structural properties. In a typical Raman spectrum, the intensity (proportional to the number of photons of a certain frequency reaching the detector) is plotted against Raman shift (frequency difference between the scattered light and the monochromatic excitation source).

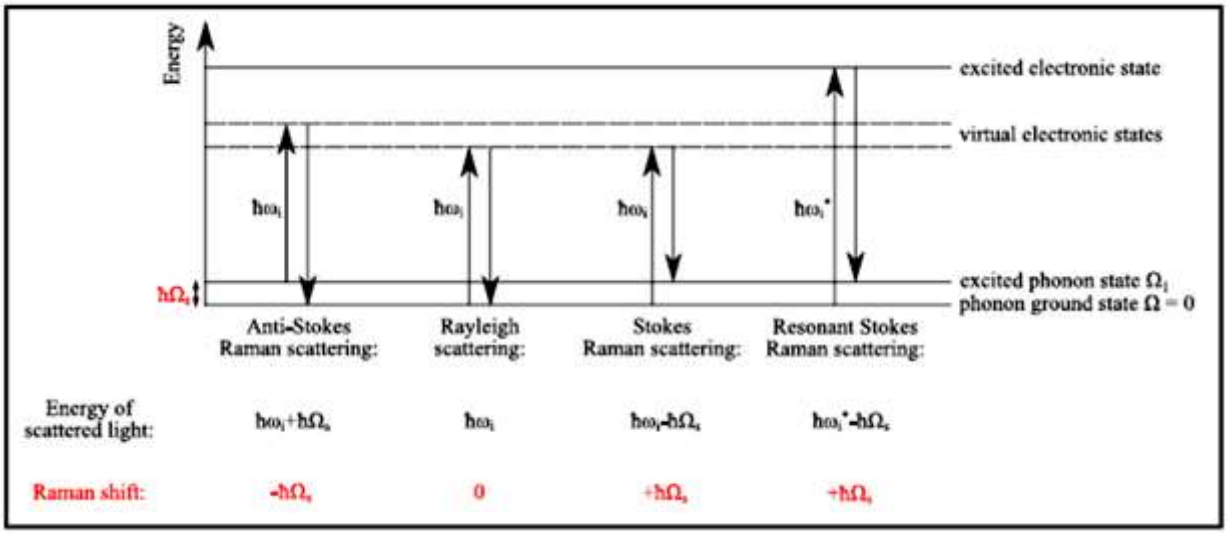


Figure 3-11: Energy diagram for inelastic (Raman) and elastic (Rayleigh) scattering.

In this study Jobin-Yvon T64000 spectrometer was used with a triple monochromatic dispersive system as shown in figure 3-12. Laser light is first incident to the spectrometer using an Olympus BX40 microscope attached to the spectrograph. Scattered light from the film returns through the microscope into the spectrometer where it is processed. The processing involves the single spectrograph mode where light is directed to a holographic notch filter. This filter suppresses the elastic scattered light but allows the Raman scattered light to pass through. The transmitted light then passes through an entrance slit and falls on the grating where it is dispersed [32]. The

dispersed light falls on the Charge Coupled Device (CCD) detector, which detects the scattered light thus producing a spectrum. The CCD is made of 1024-256 pixels where each pixel is a silicon photosensor. Scattered radiation falling on the pixels produces photoelectrons in numbers proportional to the radiation intensity. In order to achieve optimal spectrometer performance, the CCD is cooled to 140 K [33]. The output from the detector is analyzed on a computer using Labspec scientific software supplied by Jobin-Yvon.

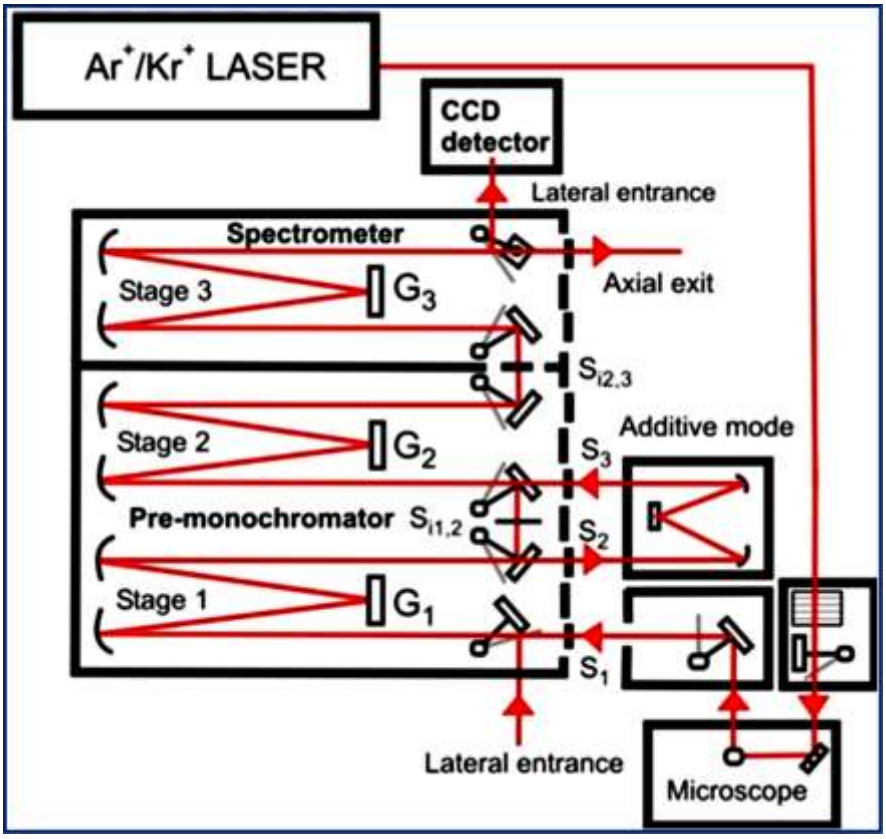


Figure 3-12: Optical diagram of JY T64000 monochromator in a triple additive and subtractive mode (adapted from the Instruction Manual for the Jobin-Yvon T64000 Raman Spectrograph).

3.6.4. Chemical Compositional Analysis

The elemental composition of the thin films in this research study was first determined using EDS spectroscopy. (EDS/EDX) is a chemical microanalysis technique used in conjunction with scanning electron microscopy (SEM) (see section 3.6.6 for SEM description).

As elaborated in the SEM discussion, when a sample is bombarded by electron beam from the SEM, the incident beam of electrons interacts with core electrons of the sample's atoms transferring sufficient energy to it, thereby ejecting electrons from the surface creating electron vacancies which are filled by electrons from a higher state. In order to balance the energy difference between the electron states, an X-Ray is emitted as illustrated in figure 3-13. Such an x-ray usually possess an energy which is a characteristic of the element from which it was emitted [34]. Since various atomic energy levels have well-defined nature, the energies and related wavelengths of the set of x-rays emitted will have characteristic values for each of the atomic species present in a sample [35] as shown in figure 3-13 (a) and (b).

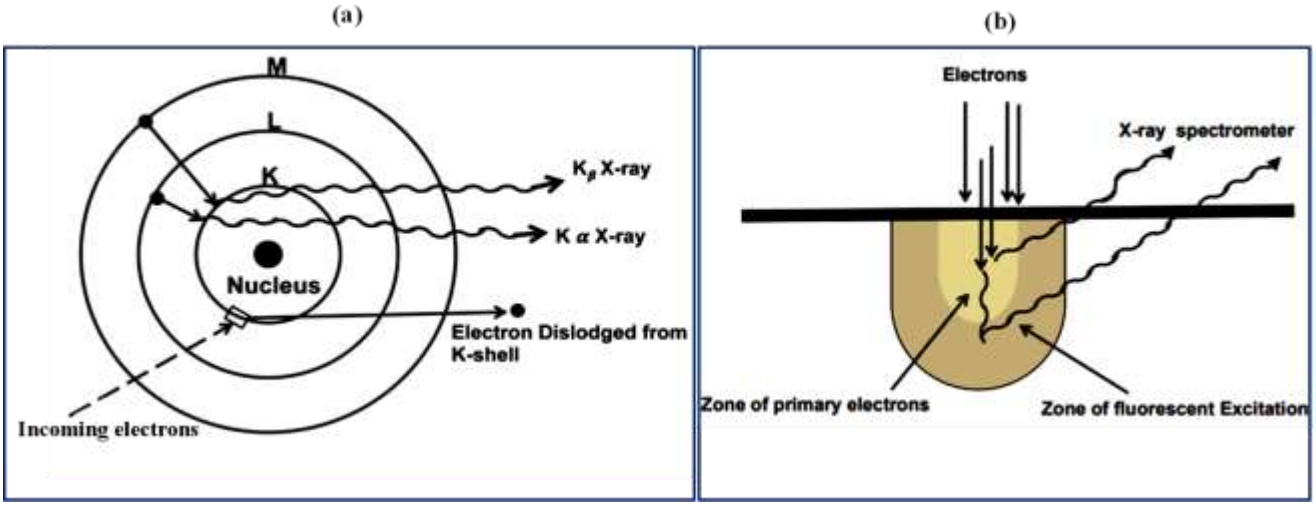


Figure 3-13: (a) and (b) Characteristic x-ray radiation

Once x-rays are emitted they are directed to an EDS x-ray detector used to measure the relative abundance of emitted x-rays versus their energy [36].

The spectrum normally plots the intensity of the peaks corresponding to the energy levels for which the most X-rays are collected. Each of these peaks corresponds to a particular atom, and therefore characteristic of a specific element. The intensity of a peak in the spectrum corresponds to the elemental concentration in the film [35]. Spectroscopy has the following limitations:

- Energy peak overlaps among different elements, particularly those corresponding to x-rays generated by emission from different energy-level shells (K, L and M) in different elements. This prohibited the separate detection of various rare earths elements which were all detected as RE as shown in figure 3-14.
- EDS cannot detect the lightest elements, typically below the atomic number of Na for detectors equipped with a Be window.
- Low peak-to-background ratio.
- Due to surface sensitivity, bulk analysis is complicated.

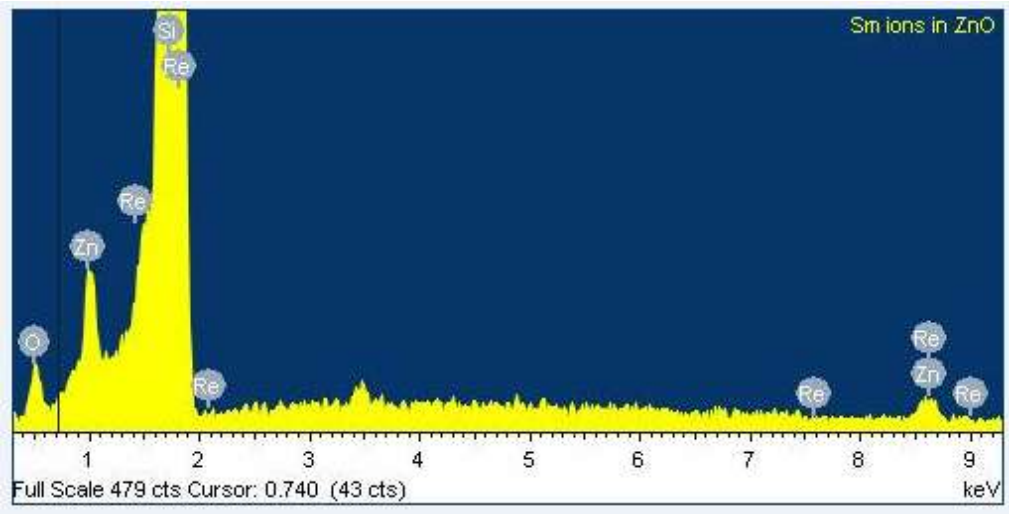


Figure 3-14: Example of an EDS spectrum of ZnO implanted with Sm rare earth.

As a result of the above limitations, the films were characterized using Rutherford backscattering spectroscopy (RBS) technique discussed in the subsequent section which was able to report the elemental composition at different depths below the film surface.

3.6.5. Rutherford backscattering spectroscopy (RBS)

Rutherford Backscattering Spectroscopy is a non-destructive technique that involves the irradiation of the sample being investigated using a monoenergetic MeV ion beams which are usually either $^{1}H^{+}$ or $^{4}He^{+}$ beams Upon hitting the target (sample), the ions penetrate to a particular depth where they are backscattered to the surface. The ions are then collected by a detector analysis system where their energies are measured. The yield and energy of the backscattered ions allow for quantitative analysis of atomic composition and depth-profiling. The total energy loss of the scattered ions can be categorized into three parts corresponding to the energy loss prior, during and after the scattering event. Theoretically RBS develops from the elastic scattering of the incident ions as a result of the Coulomb repulsion between the ions and the target atoms. An ion with initial energy E_0 and mass M_i is backscattered with an energy E_1 by the target atom of mass M_t (initially at rest). The expression for this interaction is given by Equation 3-15 and summarized to equation 3-16 [35].

$$E_1 = E_0 \left(\frac{M_i \cos\phi + \sqrt{M_t^2 - M_i^2 \sin^2\phi}}{M_i + M_t} \right)^2 \quad \ldots\ldots\ldots\ldots \text{3-15}$$

$$E_1 = E_0 K_{M_t}(\phi) \quad \ldots\ldots\ldots\ldots\ldots\ldots\ldots\ldots\ldots\ldots \text{3-16}$$

where ϕ is the scattering angle and $K_{M_t}(\phi)$ is the kinematic scattering factor. E_0 and E_1 represent incident and backscattered alpha particle energies respectively as elaborated in figure 3-15. The energy E_1 may be used to relate the depth at which the particle scattering took place as shown in section 3.6.5.1.

The Rutherford Backscattering Spectroscopy (RBS) measurements were carried out at the University of Pretoria – South Africa.

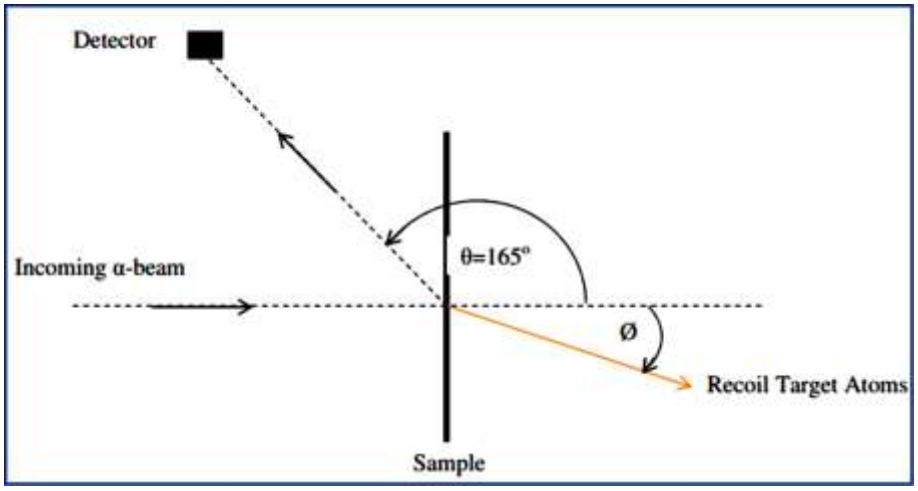


Figure 3-15: A schematic illustration of RBS experimental set-up used in this work.

3.6.5.1. Depth profiling

After scattering at a depth *x*, the particle loses energy as it traverses the sample, hence energy $E_1 < E$ as shown in figure 3-16.

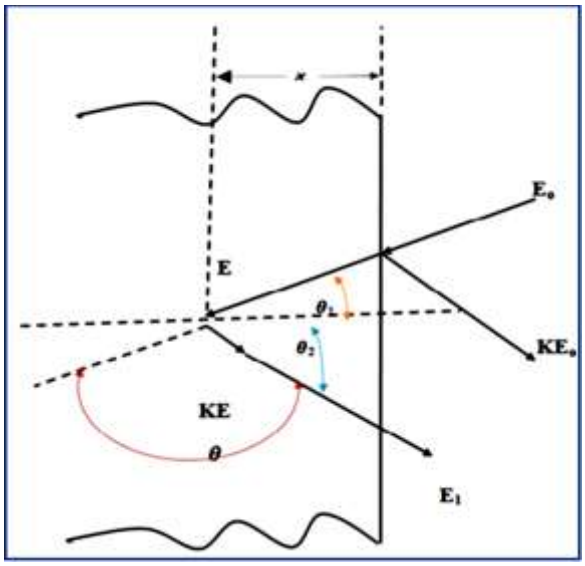


Figure 3-16: Schematic illustration of backscattered alpha particles and energy loss at a depth x.

From figure 3-16, the energy *E* immediately before scattering is related to the incident path length $x/\cos\theta_1$ of the incident path by equation 3-17.

$$\frac{x}{\cos\theta_1}\alpha - \int_{E_0}^{E} dE/(dE/dx) \quad \text{..... 3-17}$$

According Chu, W. K., *et al.* [37], the total energy loss of a particle scattered at a depth with assumption that the energy loss (dE/dx) stays constant along both the inward path (surface approximation) is given by equation 3-18.

$$\Delta E = KE_0 - E_1 = [S]x \quad \text{..... 3-18}$$

Where $[S]$ is the energy loss backscattering factor defined by equation 3-19.

$$[S] = \frac{K}{\cos\theta_1}\frac{dE}{dx}(in) + \frac{K}{\cos\theta_2}\frac{dE}{dx}(out) \quad \text{..... 3-19}$$

This energy loss factor has information relating the energy to the depth at which the scattering took place. It can be applied in converting the energy measured directly into a depth profile using numerically tabulated values of stopping powers [38, 39].

The energy difference equation 3-19 can be re-written in terms of the stopping cross-section as shown in equation 3-20.

$$\Delta E = [\psi]N_x \quad \text{..... 3-20}$$

Where N is the density of the atoms and $[\psi]$ is the stopping cross-section factor defined by equation 3-21.

$$[\psi] = \left[\frac{K}{\cos\theta_1}\psi_{in} + \frac{1}{\cos\theta_2}\psi_{out}\right] \quad \text{..... 3-21}$$

Where ψ_{in} and ψ_{out} are calculated at E_0 and KE_0

In this study we used $^4He^+$ ions of energy 1.6 MeV as projectiles for studying the elemental composition and penetration depth of rare earth doped ZnO. These charged particles were produced from an ion source then accelerated across the accelerator tube. The current was kept

low at 15 nA while the target chamber was kept at a pressure of 1×10^{-4} Pa. The backscattered particles in the target chamber were detected using silicon surface barrier detector where the output voltage from the detector is proportional to the backscattered projectiles energy. The amplified output voltage was then converted into a digital signal in the multi-channel analyzer (MCA) which reports an output of Yield (count) against channel number. The channel number and yield are proportional to the amount of backscattered energy and particles of the particles respectively. A typical RBS spectrum for the sample analyzed in this work is presented in Figure 3.17 below.

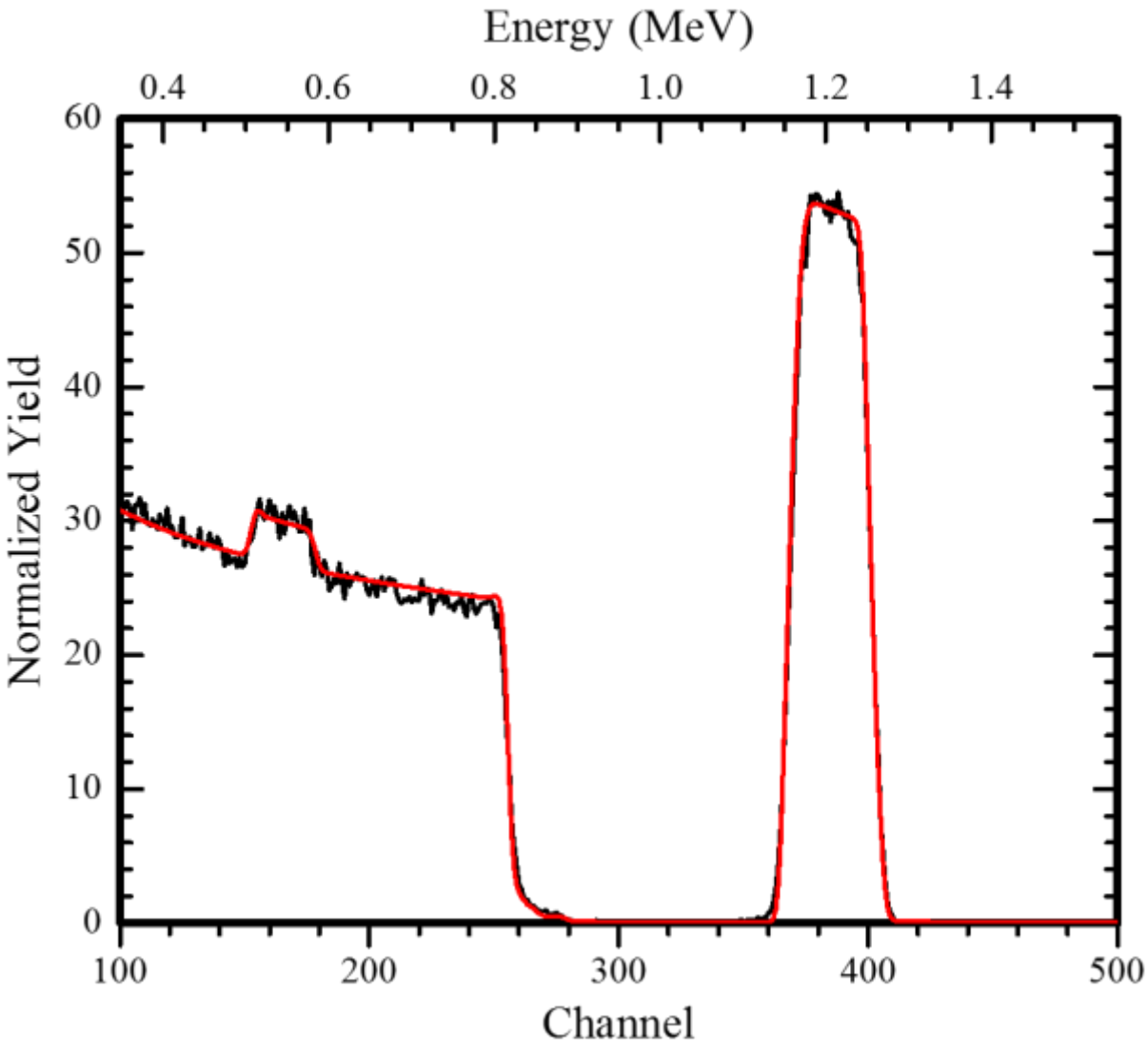


Figure 3-17: Typical RBS spectrum for ZnO thin film

#	Thickness		Sublayers	Composition . . .					
1	70.00	nm	auto	Zn	0.602	O	0.398		
2	33.00	nm	auto	Zn	0.632	O	0.418		
3	9.00	nm	auto	Zn	0.532	O	0.493	Si	0.413
4	2000.00	nm	auto	Si					

3.6.6. Morphological Studies using Scanning Electron Microscopy (SEM)

Scanning electron microscopy (SEM) is a high-resolution imaging procedure of surfaces where electrons are used to provide information on the sample morphology and structure at much higher magnification (>100,000X) and greater depth of field up to 100 times compared to the light microscopy .

.

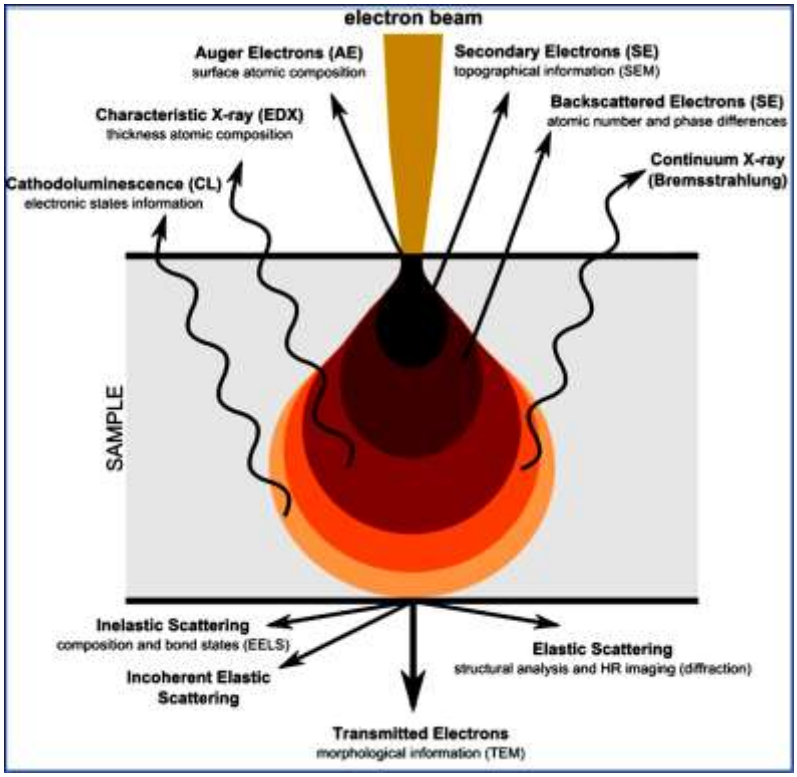


Figure 3-18: Schematic illustration of the phenomena resulting from the interaction of highly energetic electrons with matter.

It consists of an electron gun equipped with either a tungsten filament (requires heating) or a field emission cathode. The electrons beam upon emission is guided into the aperture using a series of electromagnetic lenses onto the sample surface stimulating emission of further electrons as a result of elastic and in-elastic scattering on the surface and near-surface [34] as shown in figure 3-18. Electrons (typically in the range 5-20 keV) are ejected via an elastic collision of an incident electron with the nucleus of the sample are called backscattered electrons. Their energies are usually comparable to that of the incident electrons. On the other side, electrons emitted with lower energy (typically 50 eV or less) produced by inelastic scattering are called secondary electrons. Usually they are formed by collisions with the nucleus accompanied by substantial energy loss or may result from the ejection of loosely bound electrons from the sample atoms. The secondary electrons are usually used to study surface topography. The impinging electrons may also be used to generate x-rays used to study chemical composition of the sample as discussed in section 3.6.4 [34].

Scanning electron microscopes vary in the resolution limit. This limit of resolution is defined as the minimum distance by which two structures can be separated but still appear as two distinct objects. According to Ernst Abbe [40], the limit of resolution depends on the illumination source wavelength and it can be described mathematically using Abbe's equation given represented by equation 3-22. At particular wavelength, the resolution exceeds the limit, the magnified image appear blurry.

$$d = 0.612\lambda / n\sin\alpha \quad \ldots\ldots\ldots\ldots\ldots\ldots\ldots\ldots \quad 3\text{-}22$$

Where d is the resolution, λ is the wavelength of the electrons (for an EM), n is the refractive index of medium (which is 1 for the vacuum in EM) between point source and lens relative to free space, α is half aperture angle in radians, while $\sin\alpha$ is often called the numerical aperture [41].

The current SEMs have the illumination source and condenser lens replaced with electron beam and electromagnetic coils.

To create a SEM image, the incident electron beam is scanned in a raster pattern across the surface of the sample. The emitted electrons are detected for each position in the scanned area by an electron detector. The emitted electron signal intensity is given as brightness on a cathode ray tube (CRT). When the CRT scan synchronized with the scan of the incident electron beam, then the CRT display will represents the morphology of the sample surface area scanned by the beam. Magnification of the CRT image is the ratio of the image display size to the sample area scanned by the electron beam [34]. Figure 3-18 shows a schematic illustration of the FEI Nova Nanolab 600 FEG-SEM/FIB set up found at Microscopy and Microanalysis Unit in Wits University.

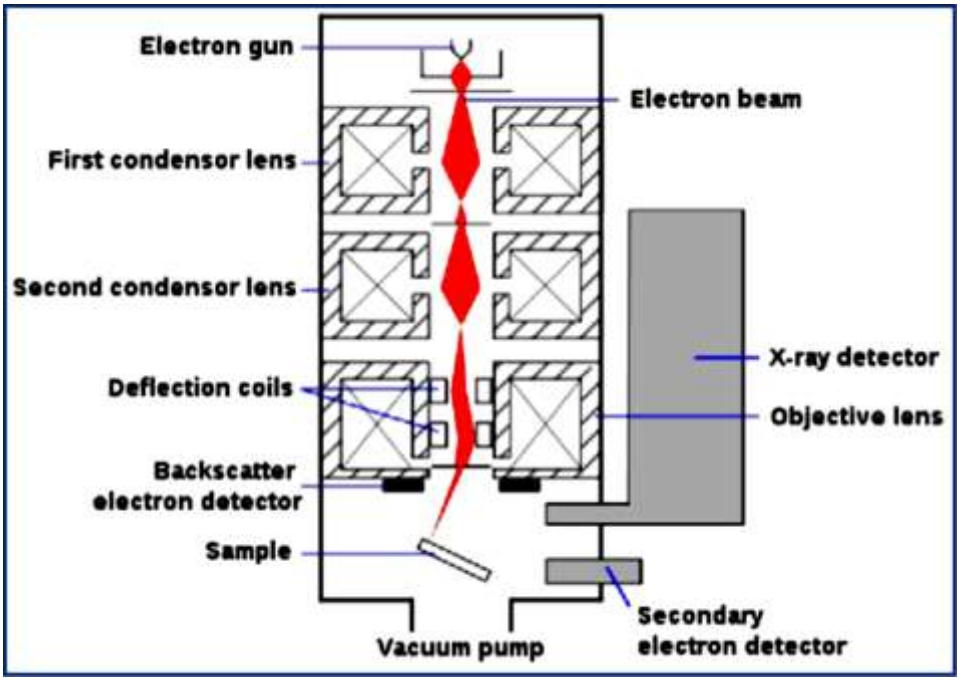


Figure 3-19: Schematic illustration of Scanning Electron Microscope.

3.6.7. Atomic Force Microscopy (AFM)

Atomic Force Microscopy (AFM) is a form of scanning probe microscopy (SPM) based on the interaction between the surface atoms and the tip of an elastic cantilever where a small probe is scanned across the sample to obtain information about the sample's surface. As a tip is swept over the sample surface, the forces between the tip and the surface lead to the cantilever bending. The deflections are then recorded by focusing a laser on the cantilever, which reflects the beam on to a position-sensitive photo detector. Any movement of the cantilever in either the normal- or lateral directions will be picked up by the detector, and an accurate description of the surface topography can be recorded. The distance between the photo diodes and the cantilever is about three orders of magnitude larger than the size of the cantilever, which magnifies the tip movements and hence gives extremely high sensitivity.

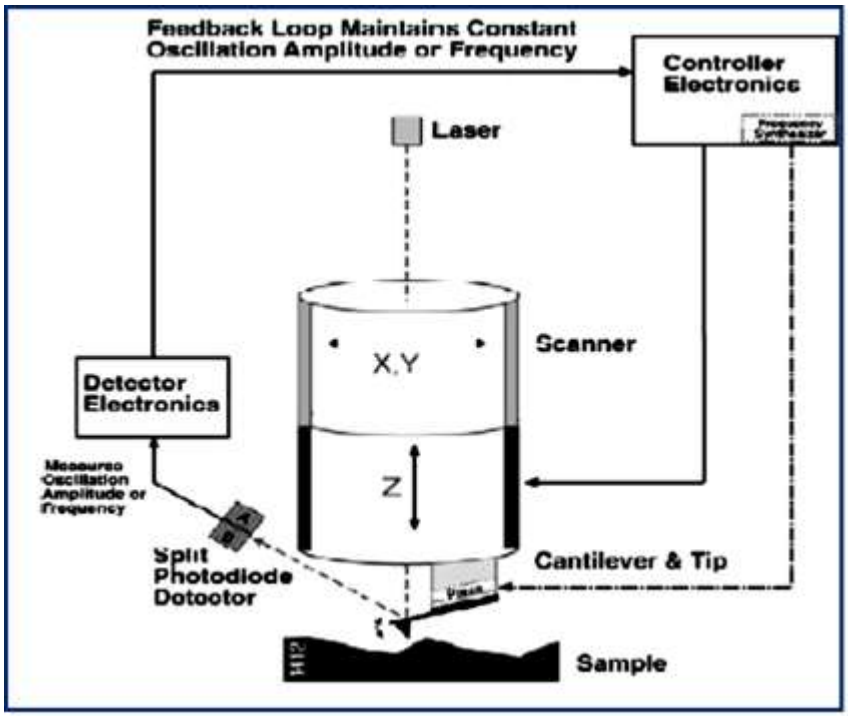


Figure 3-20: Schematic operation principle of atomic force microscopy.

To acquire the image resolution, AFMs can generally measure the vertical and lateral deflections of the cantilever by using the optical lever. The optical lever operates by reflecting a laser beam off the cantilever. The reflected laser beam strikes a position-sensitive photo-detector consisting of four-segment photo-detector. The differences between the segments of photo-detector of signals indicate the position of the laser spot on the detector and thus the angular deflections of the cantilever as illustrated in figure 3-20.

Atomic force microscope has two operational modes, namely static and dynamic mode. In the dynamic mode, the cantilever oscillates at a fixed frequency maintaining a particular amplitude during the scan. Dynamic mode also has different modes such as contact, non-contact and tapping mode. Among these, the tapping mode (semi-contact mode) is the most widely used. In this mode, the cantilever is oscillated at its resonant frequency with the tip lightly touching the surface during the lower part of the oscillation. During measurements the change in phase and amplitude is recorded. Normally the cantilever is maintained at a particular frequency and has less room to oscillate when the tip is scanned over an elevated surface hence reducing the amplitude while the reverse case is true when the tip is scanned over a depression. The phase change of the cantilever oscillations is quite sensitive to material composition (van der Waals interaction) and independent of large height differences making tapping mode the most appropriate for grain boundaries imaging. This is because it can be obscured by rough topography. Another merit of the use of tapping mode is that the tip is quite gentle on interacting with the surface hence preventing scratches and damage to the surface.

The accuracy of AFM topography measurements depends on the spatial resolution in both the vertical (*Z*) and lateral (*XY*) directions. In the *Z* direction, the resolution is limited mainly by the instrument noise. Factors such as mechanical vibrations and random electrical fluctuations create

variations in the height signal. Height features smaller than these variations cannot be meaningfully resolved [42].

The AFM image provides complex 3D information on the height correlations or fluctuations using roughness parameters. This surface roughness is most commonly described by amplitude parameters including the average deviation R_a, the root mean square R_{RMS}, and the standard deviation R_q where R_a and R_{RMS} describe the dispersion or spread in height variations. Other roughness parameters describing the spatial distribution of height variations is the dimensionless Skewness and kurtosis.

Skewness characterizes the symmetry of the height variation about its mean line, with $R_{sk} > 0$ for surfaces with high peaks or spikes and $R_{sk} < 0$ for those with deep valleys or pits. Kurtosis is a description of the uniformity of height variations, with $R_{ku} > 0$ for surfaces with many peaks and valleys and $R_{ku} < 0$ for those with fewer excursions. These parameters are described by equation 3-23 to 3-28.

Root mean square roughness

$$R_{RMS} = \sqrt{\frac{1}{N}\sum_{i=1}^{N} Z_i^2} \quad \text{..... 3-23}$$

Average deviation roughness

$$R_a = \frac{1}{N}\sum_{i=1}^{N}\left|Z_i - \bar{Z}\right| \quad \text{..... 3-24}$$

Skewness

$$R_{SK} = \frac{1}{N}\sum_{i=1}^{N}\left(\frac{Z_i - \bar{Z}}{\sigma}\right)^3 \quad \text{..... 3-25}$$

Kurtosis

$$R_{ku} = \frac{1}{N}\sum_{i=1}^{N}\left(\frac{Z_i - \bar{Z}}{\sigma}\right)^4 - 3 \quad \text{..... 3-26}$$

Where z_i is the height at a given pixel i, N is the total number of pixels in the image, and $\bar{Z}$ is the average height of the entire image.

3.6.8. Optical properties using UV-Vis-NIR Spectrophotometry

The UV-Vis spectrometer is used to identify the number of absorbing species in a sample for instance in analyzing compounds (molecules, ions and complexes) of organic, inorganic and biochemical in the ultraviolet (UV) and visible regions of the electromagnetic spectrum [43]. UV-vis spectroscopy is widely used owing to its simplicity, versatility, speed, accuracy and cost-effectiveness. The measured UV-Vis spectrum can be obtained as absorption, transmission and reflection spectrum [44].

It applies the concept of light interaction with matter that may lead to reflection, scattering, absorbance, fluorescence/phosphorescence and photochemical reaction [45]. Generally light absorption depends on the electronic structure of the species (molecules, ions and complexes). An interaction between a photon of particular energy with a species may cause a transition in the electronic energy level provided the relation in equation 3-27 is satisfied.

$$E_{photon} = E_1 - E_2 = h\nu \quad \text{..... 3-27}$$

Where E_1 and E_2 are the ground and excited state of the species respectively, h is Planck's constant and ν is the photon frequency.

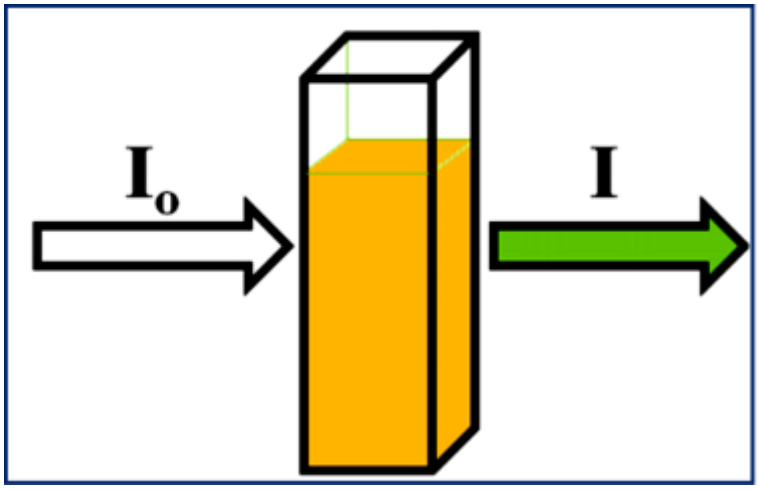


Figure 3-21: Illustration of absorption and transmitted light.

From figure 3-21 the amount of light absorbed by the sample may be described as the difference in the incident radiation (I_o) and the transmitted radiation (I). The amount of light absorbed is expressed as either transmittance (described by equation 3-28) or absorbance (described by equation 3-29).

$$T = \frac{I}{I_0} \quad \ldots\ldots\ldots\ldots\ldots\ldots\ldots\ldots \text{3-28}$$

$$A = -\log T \quad \ldots\ldots\ldots\ldots\ldots\ldots\ldots \text{3-29}$$

The UV-Vis measurements were carried out in the range 200-800 nm using a Cary 500 UV–visible spectrophotometer inside it are two light sources, a tungsten lamp responsible for giving the visible light and a deuterium lamp emitting the ultraviolet light and a set of mirrors. Mirror 1 directs light from the right light source through an entrance slit into a monochromator containing a diffraction grating meant for splitting the light into its constituent wavelengths. A monochromatic light passes through the filter in order to limit noise signal going into the modulator that contains a beam splitter (half-mirror) responsible for dividing the light into two beams. One beam is passed through the film (sample beam) to be measured while the other is passed through the reference cell. Both beams are then focused into the detectors by a set of lenses. These detectors then convey the signal to the

computer where their intensities are compared through the double beam method to calculate the ratio of their intensities. The logarithm of this ratio is referred to as absorbance, and it provides a measure of the amount of light is absorbed by the film at that particular wavelength. The schematic illustration of the UV-Vis spectrometer is as shown in figure 3-22 [46].

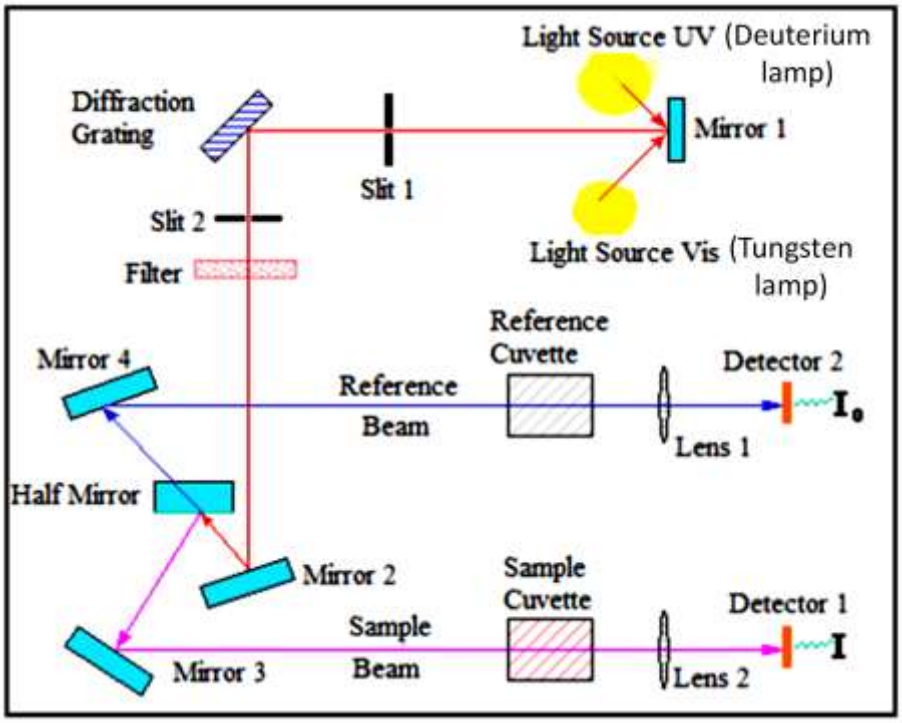


Figure 3-22: Schematic representation of a dual-beam UV-Vis spectrophotometer

From the absorption spectrum, the energy band gap can be estimated using Tauc law relation [47] given by equation 3-30.

$$\alpha h\nu = C_1\left(h\nu - E_g\right)^m \quad \ldots\ldots\ldots\ldots\ldots\ldots\ldots \text{3-30}$$

Where α is the absorption coefficient, $h\nu$ is the incident photon energy, C_1 is constant, E_g is the optical gap energy, and the exponent m is a parameter that vary depending on the type of electronic transition enabling absorption based on the Fermi Golden rules. For direct band gap, m takes the form

m = 1/2 for allowed transition,

m = 1/3 for forbidden transition,

On the other hand the indirect band gap materials provide for m values in the form;

m = 2 allowed transition

m = 3 for forbidden transition.

3.6.9. Photoluminescence Spectroscopy

Photoluminescence spectroscopy is a contactless, versatile, non-destructive, powerful optical method of studying the electronic structure of materials. Light is directed onto a sample, where it is absorbed and imparts excess energy into the material in a process called photo−excitation. Excess energy may be dissipated emitting light, process called luminescence. Photoluminescence is defined as the spontaneous emission of light from a material under optical excitation. This light may be collected and analyzed spectrally, spatially as well as temporally. The intensity and spectral content of this photoluminescence is a direct measure of various important material properties. The emission and excitation spectroscopy are performed in one setup thus imposing the requirement for a broadband excitation source. During a PL spectroscopy experiment, excitation is provided by laser light with energy much greater than the optical band gap of the material. The photo excited carriers consist of electrons and holes, which relax toward their respective band edges and recombine by emitting light at the energy of the band gap. Radiative transitions in semiconductors may also involve localized defects or impurity levels in the band gap hence the analysis of the PL spectrum may enhance identification of specific defects or impurities, and the magnitude of the PL signal gives their concentration [48].

The difference between a PL and an absorption spectrum is that the absorption spectrum measures transitions from the ground state to excited state, while photoluminescence analyses transitions from the excited state to the ground state as depicted in figure 3-23.

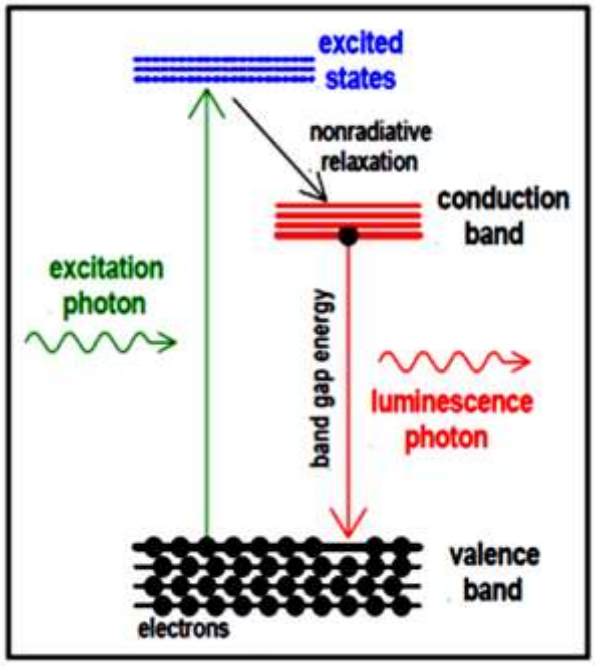


Figure 3-23: Principle of photoluminescence spectroscopy (PL).

During photoluminescence, the emission monochromator is set at a wavelength corresponding to a strong emission line and the excitation (the specific range of electromagnetic radiation where the emitters have a good absorption) light is scanned. On the other hand in emission spectroscopy, the excitation source is kept fixed while the emitted light is being scanned. Figure 3-24 gives a schematic illustration of a PL spectrophotometer with general basic equipment. In this instrument different excitation sources may be used such as lasers, photodiodes, and lamps. It is also fitted with two monochromators to enable selection of both the excitation and emission. The two monochromators are motorized to allow the automatic scanning of the wavelength. The output is

normally presented on a wavelength scale in graphical form which is recorded and stored with the computer.

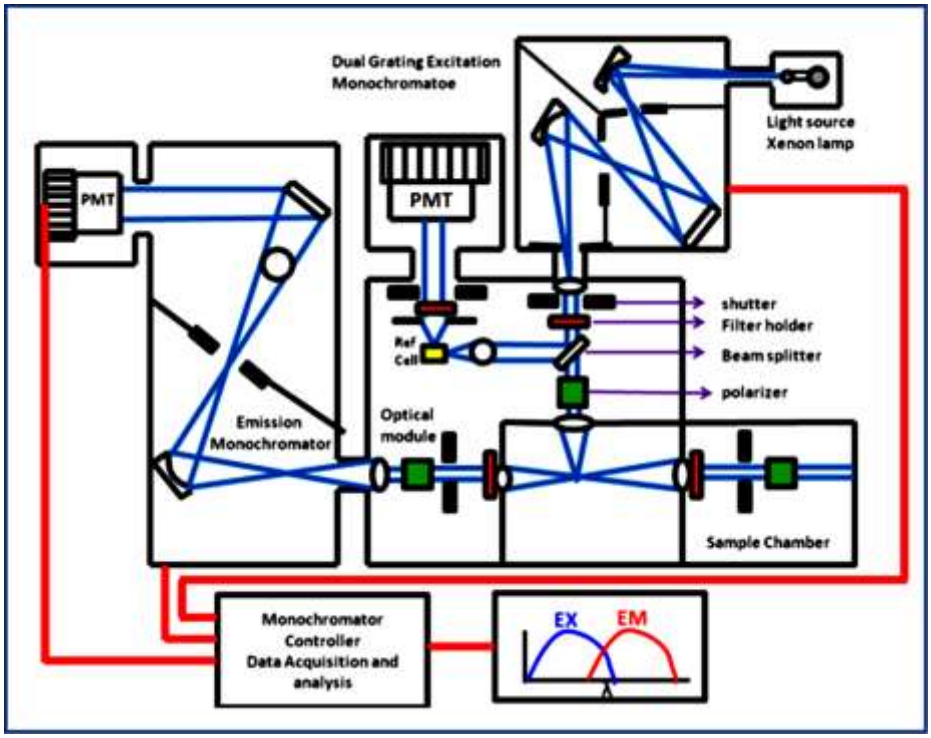


Figure 3-24: Schematic diagram of a fluorescence spectrometer

For ideal measurements, the spectrophotometer must have the following components:

(a) a light source with a constant photon output at all wavelengths.

(b) a monochromator to diffract photons of all wavelengths with equal efficiency.

(c) The efficiency of the monochromator must be independent of polarization.

(d) The detector must detect photons of all wavelengths with equal efficiency.

In this study, the PL measurements were carried out using a Horiba LabRAM HR spectrometer with a 150 lines/mm grating and an excitation wavelength of 244 nm from a frequency doubled Lexel argon ion laser.

3.7. References (for chapter 3)

[1] K. Ellmer, Magnetron sputtering of transparent conductive zinc oxide: relation between the sputtering parameters and the electronic properties, Journal of Physics D: Applied Physics, 33 (2000) R17.

[2] S. Schiller, U. Heisig, K. Goedicke, Electron-beam evaporation and high-rate sputtering with plasmatron-magnetron systems-comparison, Vakuum-Technik, 27 (1978) 51-55.

[3] S. Schiller, U. Heisig, K. Goedicke, electron-beam evaporation and high-rate sputtering with plasmatron-magnetron systems-comparison. 2, vakuum-technik, 27 (1978) 75-86.

[4] P. Sigmund, Theory of sputtering. I. Sputtering yield of amorphous and polycrystalline targets, Physical review, 184 (1969) 383.

[5] N. Laegreid, G. Wehner, Sputtering yields of metals for Ar+ and Ne+ ions with energies from 50 to 600 eV, Journal of Applied Physics, 32 (1961) 365-369.

[6] J.L. Vossen, W. Kern, Thin Film Processes II Academic Press, in, Inc, 1991.

[7] H.F. Winters, J.W. Coburn, Surface science aspects of etching reactions, Surface Science Reports, 14 (1992) 162-269.

[8] D.P. Smith, Scattering of Low-Energy Noble Gas Ions from Metal Surfaces, Journal of Applied Physics, 38 (1967) 340-347.

[9] B. Window, K.-H. Müller, Strain, ion bombardment and energetic neutrals in magnetron sputtering, Thin Solid Films, 171 (1989) 183-196.

[10] H.F. Winters, H. Coufal, W. Eckstein, Influence of energy reflected from the target on thin film characteristics, Journal of Vacuum Science & Technology A: Vacuum, Surfaces, and Films, 11 (1993) 657-663.

[11] R. Kukla, T. Krug, R. Ludwig, K. Wilmes, A highest rate self-sputtering magnetron source, Vacuum, 41 (1990) 1968-1970.

[12] J. Szczyrbowski, A. Dietrich, K. Hartig, Bendable silver-based low emissivity coating on glass, Solar Energy Materials, 19 (1989) 43-53.

[13] L.A. Giannuzzi, B.I. Prenitzer, B.W. Kempshall, Ion-solid interactions, in: Introduction to focused ion beams, Springer, 2005, pp. 13-52.

[14] S. Zhou, Transition metal implanted ZnO: a correlation between structure and magnetism, (2007).

[15] J. Lindhard, M. Scharff, Energy dissipation by ions in the keV region, Physical Review, 124 (1961) 128.

[16] G. Phelps, Dopant ion implantation simulations in 4H-Silicon Carbide, Modelling and Simulation in Materials Science and Engineering, 12 (2004) 1139.

[17] L.A. Giannuzzi, Introduction to focused ion beams: instrumentation, theory, techniques and practice, Springer Science & Business Media, 2004.

[18] J.F. Ziegler, J. Biersack, U. Littmark, The stopping and range of ions in matter, Vol. 1, 1, Pergamon Press, New York, (1985).

[19] M. Nastasi, J.W. Mayer, Surface Erosion During Implantation: Sputtering, Ion Implantation and Synthesis of Materials, (2006) 159-178.

[20] E. Aradi, S. Naidoo, R. Erasmus, B. Julies, T. Derry, Investigations on the characterization of ion implanted hexagonal boron nitride, Nuclear Instruments and Methods in Physics Research Section B: Beam Interactions with Materials and Atoms, 307 (2013) 214-217.

[21] H. Li, Structural and Optoelectronic Properties of Rare Earth Doped Silicon Photonic Materials, (2013).

[22] R. Minixhofer, Integrating technology simulation into the semiconductor manufacturing environment, na, 2006.

[23] C. Li, T. Kawaharamura, T. Matsuda, H. Furuta, T. Hiramatsu, M. Furuta, T. Hirao, Intense green cathodoluminescence from low-temperature-deposited ZnO film with fluted hexagonal cone nanostructures, Applied physics express, 2 (2009) 091601.

[24] Y. Lin, J. Xie, H. Wang, Y. Li, C. Chavez, S. Lee, S. Foltyn, S. Crooker, A. Burrell, T. McCleskey, Green luminescent zinc oxide films prepared by polymer-assisted deposition with rapid thermal process, Thin Solid Films, 492 (2005) 101-104.

[25] E. Johlin, N. Tabet, S. Castro-Galnares, A. Abdallah, M.I. Bertoni, T. Asafa, J.C. Grossman, S. Said, T. Buonassisi, Structural origins of intrinsic stress in amorphous silicon thin films, Physical Review B, 85 (2012) 075202.

[26] S. Sintonen, Superhilarakenteiden karakterisointi röntgendiffraktio-ja röntgenheijastusmenetelmillä, (2009).

[27] J. Huang, Zinc oxide thin film transistors by radio frequency magnetron sputtering, (2014).

[28] F.A. Settle, Handbook of instrumental techniques for analytical chemistry, Prentice Hall PTR, 1997.

[29] A. Braz, M. López-López, C. García-Ruiz, Raman spectroscopy for forensic analysis of inks in questioned documents, Forensic science international, 232 (2013) 206-212.

[30] M. López-López, C. García-Ruiz, Infrared and Raman spectroscopy techniques applied to identification of explosives, TrAC Trends in Analytical Chemistry, 54 (2014) 36-44.

[31] C.V. Raman, K.S. Krishnan, A new type of secondary radiation, Nature, 121 (1928) 501.

[32] D. Long, Introductory Raman Spectroscopy. John R. Ferraro, Kazuo Nakamoto and Chris W. Brown. Academic Press, Amsterdam, 2003. xiii+ 434, in, Wiley Online Library, 2005.

[33] S. Morel, F. Adar, Refined raman spectroscopy: Bringing new insight into industrial processes, Optics and photonics news, 16 (2005) 42-46.

[34] L.D. Hanke, Handbook of analytical methods for materials, Materials Evaluation and Engineering Inc., Plymouth, (2001) 35-38.

[35] B.G. Yacobi, L.L. Kazmerski, D. Holt, Microanalysis of solids, Springer Science & Business Media, 2013.

[36] J. Ungula, Growth and characterization of ZnO nanoparticles by sol-gel process, in, University of the Free State (Qwaqwa Campus), 2015.

[37] W. Chu, J. Mayer, M. Nicolet, T.M. Buck, G. Amsel, F. Eisen, Principles and applications of ion beam techniques for the analysis of solids and thin films, Thin Solid Films, 17 (1973) 1-41.

[38] J.F. Ziegler, The stopping and range of ions in solids, in: Ion Implantation Science and Technology (Second Edition), Elsevier, 1988, pp. 3-61.

[39] J. Ziegler, J. Manoyan, The stopping of ions in compounds, Nuclear Instruments and Methods in Physics Research Section B: Beam Interactions with Materials and Atoms, 35 (1988) 215-228.

[40] E. Abbe, XV.—The Relation of Aperture and Power in the Microscope (continued), Journal of Microscopy, 3 (1883) 790-812.

[41] W. Zhou, Z.L. Wang, Scanning microscopy for nanotechnology: techniques and applications, Springer science & business media, 2007.

[42] S. Bertolazzi, J. Brivio, A. Radenovic, A. Kis, H. Wilson, L. Prisbrey, E. Minot, A. Tselev, M. Philips, M. Viani, Exploring flatland: AFM of mechanical and electrical properties of graphene, MoS2 and other low-dimensional materials, Microsc. Anal, 27 (2013) 21-24.

[43] S. Skujins, A. Varian, Applications of UV-Visible Derivative Spectrophotometry, UV Instruments at work, Part, 1 (1986).

[44] H. Förster, UV/Vis spectroscopy, in: Characterization I, Springer, 2004, pp. 337-426.

[45] T. Owen, Fundamentals of Modern UV-Visible Spectroscopy: A Primer. edit, Agilent Technologie, German, (2000).

[46] O. Akiyama, Double-beam spectrophotometer, in, Google Patents, 1985.

[47] A.E. Morales, E.S. Mora, U. Pal, Use of diffuse reflectance spectroscopy for optical characterization of un-supported nanostructures, Revista mexicana de física, 53 (2007) 18-22.

[48] B.R. Masters, Principles of fluorescence spectroscopy, Journal of Biomedical Optics, 13 (2008) 029901.

Chapter 4: Structural and Optical characterization of ZnO thin films.

4.1. Introduction

Zinc oxide (ZnO) is a group II–VI semiconductor material whose ionicity resides at the borderline between a covalent and ionic semiconductor. The crystal structures shared by ZnO are wurtzite B4, zinc blende B3, and rocksalt B1[1]. It believed to have a lot of promising device application. Initially ZnO was considered as a substrate for GaN and other related alloys [2, 3]. At ambient conditions, ZnO possesses thermodynamically stable phase of a Wurtzite structure similar to GaN [1, 4], a factor that makes it widely applicable in high-performance optoelectronic devices. The increased research on zinc oxide as a semiconductor material is majorly driven by its prospective use as a wide band gap semiconductor for light emitting devices and for transparent or high temperature electronics [5]. It has a direct and wide band gap of 3.37 eV (at 300 K) in the near-UV spectral region, a large free-exciton binding energy (60 meV) such that excitonic emission processes can persist at or even above room temperature [6-8], a strong cohesive energy of 1.89 eV [9], with a high optical gain (300 cm^{-1}) [7], exhibits high mechanical strength, thermal stability, chemical stability, ambient insensibility, and negative electron affinity [10] as well as high radiation hardness [11]. These characteristics of ZnO as well as unique combination of its physical properties—optical, electrical, magnetic, piezoelectric, and ferroelectric properties make it a promising candidate material for advanced device applications. Different commercial applications have also been reported such as integrated optics, antireflection coatings, liquid crystal displays[1], light emitting, laser diodes [12, 13], *U-V* range detecting devices [14, 15], chemical sensors , solar cells [16-18], photodegradation and photocatalysis [19], superhydrophobic and self-cleaning surfaces. According to Chantal *et al.* [20] ZnO films possess superhydrophobic properties over a

wide pH range with excellent stability under high temperature and ambient long-term storage conditions making it a strong candidate for high temperature electronic devices that can reliably be operated in space and other harsh environments.

4.2. Growth conditions

ZnO films were deposited by R.F. magnetron sputtering system using a cylindrical metallic ZnO disc 76 mm diameter and 3–6 mm thick as the cathode (99.95% purity, Semiconductor Wafer). The substrates used were a p-type silicon with (100) orientation and quartz. The substrates were thoroughly cleaned with organic solvents and dried before loading in the vacuum chamber of the sputter system. The vacuum chamber was evacuated using a rotary roughing pump to a base pressure of 2×10^{-2} mbar before a further pumping using a turbomolecular pump to 1.8×10^{-5} mbar. The plasma generation chamber is surrounded by a hard magnet of 0.3T. Magnetron sputtering was carried out in an argon gas atmosphere supplied into the chamber through a precision leak valve at a flow rate of 13.0 sccm. The RF power supplied was varied from 100 W to 260 W. The time of deposition was also varied from 1-20 minutes to obtain films of different thicknesses and intrinsic stress. The target to substrate distance was 60 mm and was kept fixed for each deposition run. Prior to each deposition, the target was pre-sputtered for 30 minutes to remove any contamination adsorbed on its surface to make the system stable and reach optimum condition. The films were deposited on a [100] 380 μm thick silicon substrate. The substrate temperature was kept at room temperature. After deposition, the film were subjected to thermal treatment in a programmable furnace in air or Argon ambient to monitor the effect of temperature and heating environment on the morphological, optical and electrical properties of ZnO films. The films subsequently used as an electron transport layer to fabricate a perovskites solar cell

4.3. Characterization techniques

Rutherford backscattering spectrometry (RBS) and EDS measurements were performed to determine the composition and distribution profiles of Tb^{3+} ions in the ZnO matrix at room temperature using $^{4}He^{+}$ particles of energy 1.6 MeV at a backscattering angle of 165º. The EDS used was fitted on FEI Nova Nanolab 600 SEM. The surface morphology and the root-mean-square (rms) surface roughness of the films were characterized using a Di100 model atomic force microscope (AFM) in tapping mode and FEI Nova Nanolab 600 SEM. In order to investigate the crystallographic properties of the ZnO films, we carried out - high resolution GXRD using Bruker D8 Discover, set at 40kV, 40 mA to emit a CuKα X-ray radiation of wavelength 1.541 Å. The scanning range of 2θ was varied from 10º to 80º at a low scanning rate of 1.2º/minute. Photoluminescence measurements were carried out using a Horiba LabRAM HR spectrometer with a 150 lines/mm grating and an excitation wavelength of 244 nm from a frequency doubled Lexel argon ion laser. The Raman bands and the structural order of all the films were examined using a Horiba LabRAM HR Raman spectrometer equipped with an Ar ion laser (514.5 nm) and a laser power of <1 mW at the sample.Optical transmittance measurements were carried out in the wavelength range from 200 to 900 nm by using a CARY UV-visible spectrophotometer. The reflectance measurements obtained from FR-Basic-Vis/NIR spectroscopy over a wavelength range of 450-900 nm

4.4. Results and discussion

4.4.1. EDS and RBS measurements

The elemental composition of the films shows that there was no external impurity during the growth as well as at characterization stage as observed in the EDS in figure 4-1 below. This was also confirmed by the Rutherford Backscattering spectroscopy shown in figure 4-2.

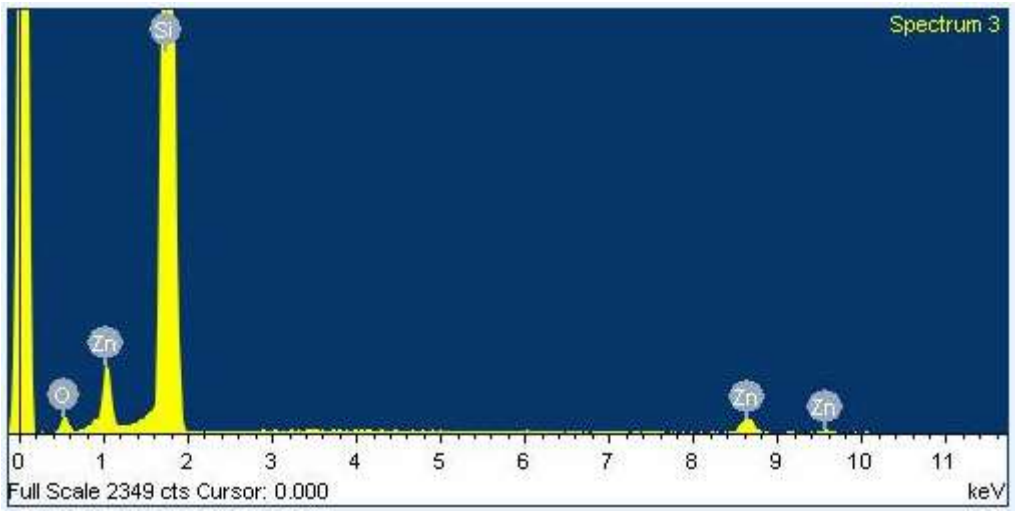


Figure 4-1: EDS analysis of the ZnO thin film grown using RF sputtering on Si wafer substrate.

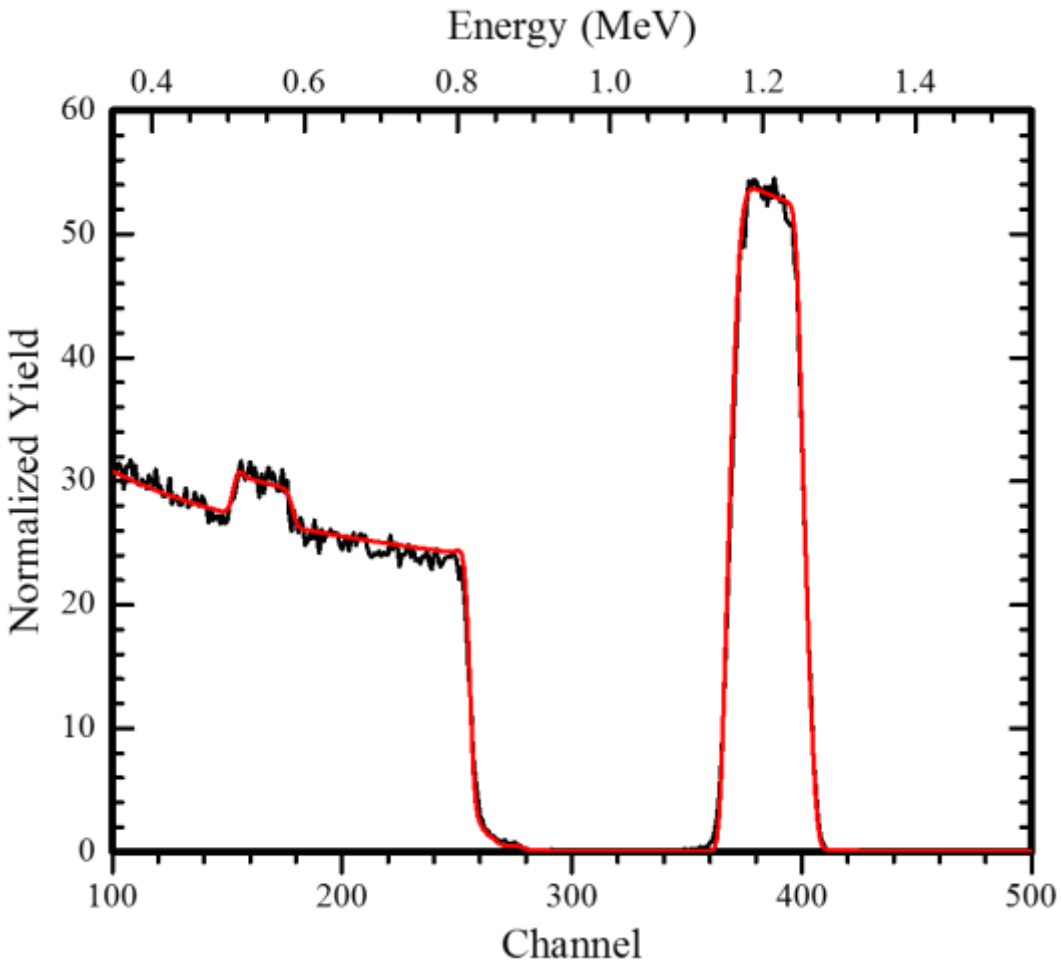


Figure 4-2: RBS image spectrum of ZnO layer on Si showing experimental curve (black) and simulated curve (red) using XRump code.

Table 4-1: XRump Simulation parameters of thickness and fractional elemental compositions.

#	Thickness		Sublayers	Composition . . .					
1	70.00	nm	auto	Zn	0.602	O	0.398		
2	33.00	nm	auto	Zn	0.632	O	0.418		
3	9.00	nm	auto	Zn	0.532	O	0.493	Si	0.413
4	2000.00	nm	auto	Si	1				

Analysis of the RBS data was carried out using XRump computer simulation to provide as described in chapter 7 the elemental composition at different layers of the film was as shown in

Table 4-1 which gives the depth profile distribution of Zn and O, a proof that the composition is homogeneous in depth. The composition is given in atomic fraction.

4.4.2. Atomic Force Microscopy & Scanning Electron Microscopy.

The influences of annealing temperature and deposition time on the surface topography and morphology of RF sputtered ZnO thin films were studied using Veeco Di100 model of atomic force microscopy (AFM) in the tapping mode. The annealing was carried out in an Ar filled furnace set to ramp at 10˚C/minute and at dwell time of 2 hours before cooling to room temperature. In order to estimate the AFM data specifically, the surface roughness of the samples was denoted by the average roughness Ra and root mean square (Rrms) value. The surface morphologies of the films were investigated over a scanned area of 5 µm × 5 µm and the results tabulated.

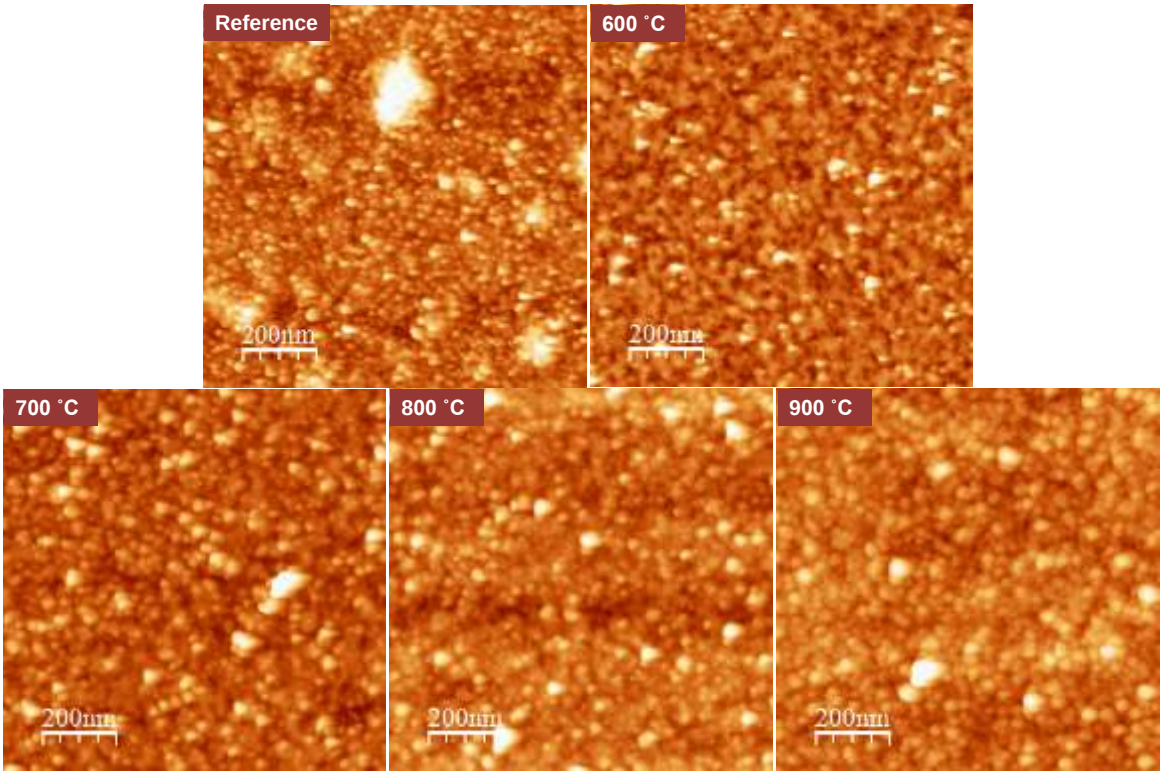


Figure 4-3: AFM images of ZnO thin film grown at 100 W, 1 minute and annealed at different temperatures (600-900 ˚C).

Figure 4-3 shows the effect of annealing at temperature range of 600-900 ˚C in Ar filled furnace. Table 4-2 shows a summary of the AFM analysis. The statistical analysis of AFM data was carried out using the height distribution histograms from the AFM analysis software WSxM 4.0.

The average roughness (*Ra*) is the mean height is usually calculated over the entire measured length/area. It is useful for detecting general variations in overall profile height characteristics and for monitoring an established manufacturing process while on the other side Root mean square (rms) roughness (R_{rms}) is described as the square root of the distribution of surface height and is usually considered to be more sensitive than the average roughness for large deviations from the mean line/plane. The rms may also be used in computing the skewness and kurtosis parameters [21].

The height asymmetry is described by the statistical parameters: the surface skewness and kurtosis. The surface skewness is a measure of heights distribution asymmetry. When it is a positive value then the measure shows above average height while a negative value is an indication of below average height. Kurtosis on the other side indicates the 'peakedness' of height value distribution. When the distribution has a high kurtosis value then this implies that there are small numbers of extreme heights as opposed to many moderate height features. For spiky surfaces, $R_{ku} > 3$; for bumpy surfaces, $R_{ku} < 3$; perfectly random surfaces have kurtosis of 3.

Table 4-2: Summary of tapping mode AFM analysis after annealing at 600-900 ˚C temperature range.

Annealing Temperature (˚C)	R_a (nm)	R_{rms} (nm)	Skewness (R_{sk})	Kurtosis (R_{ku})	Grain height (nm)
Reference	14.3	18.9	1.489	6.159	51.5
600	18.4	22.7	0.227	3.950	57.6
700	19.3	24.8	0.325	4.654	62.5
800	22.0	26.8	0.452	5.231	65.3
900	23.2	27.3	0.924	5.957	70.4

From table 4-2, the surface roughness of films was 18.9 nm while the average roughness was 11.3 nm. Upon annealing at high temperature, 600-900 ˚C range, the atoms acquire enough diffuse activation energy to enable them occupy the correct lattice sites in the crystal lattice enabling grains possessing low surface energy during growth to become larger [22]. When given sufficient energy the grain sizes are also observed to grow from 51.5 nm to 70.4 nm at 900 ˚C. This is attributed to coalescence of the grains at elevated temperatures. During the coalescence process some voids are created as a result of the grain boundary movement. As the surface roughness increases, it is more likely that negatively charged oxygen-related species are adsorbed on the surface of the crystallites which in turn act as electron traps [23]. This consequently leads to the gradual increase in surface roughness with increasing temperature. The statistical analysis of AFM data was done using the height distribution histograms within the WSxM 4.0 software. The film surface were found to possess positive skewness (larger than 0.2) and high kurtosis (larger than 3.0) values which imply that the surface height distribution does not follow a Gaussian distribution and there are relatively sharp surfaces which some authors have found to make ZnO favorable for tribological applications (e.g. low friction bearings). The smaller value of skewness (R_{sk}) for the film is attributed to more

symmetric surface. The results of Skewness and kurtosis show that the surfaces are generally spiky with dominant peaks.

The increasing grain size can be well illustrated using the scanning electroscope images as shown in Figure 4-4.

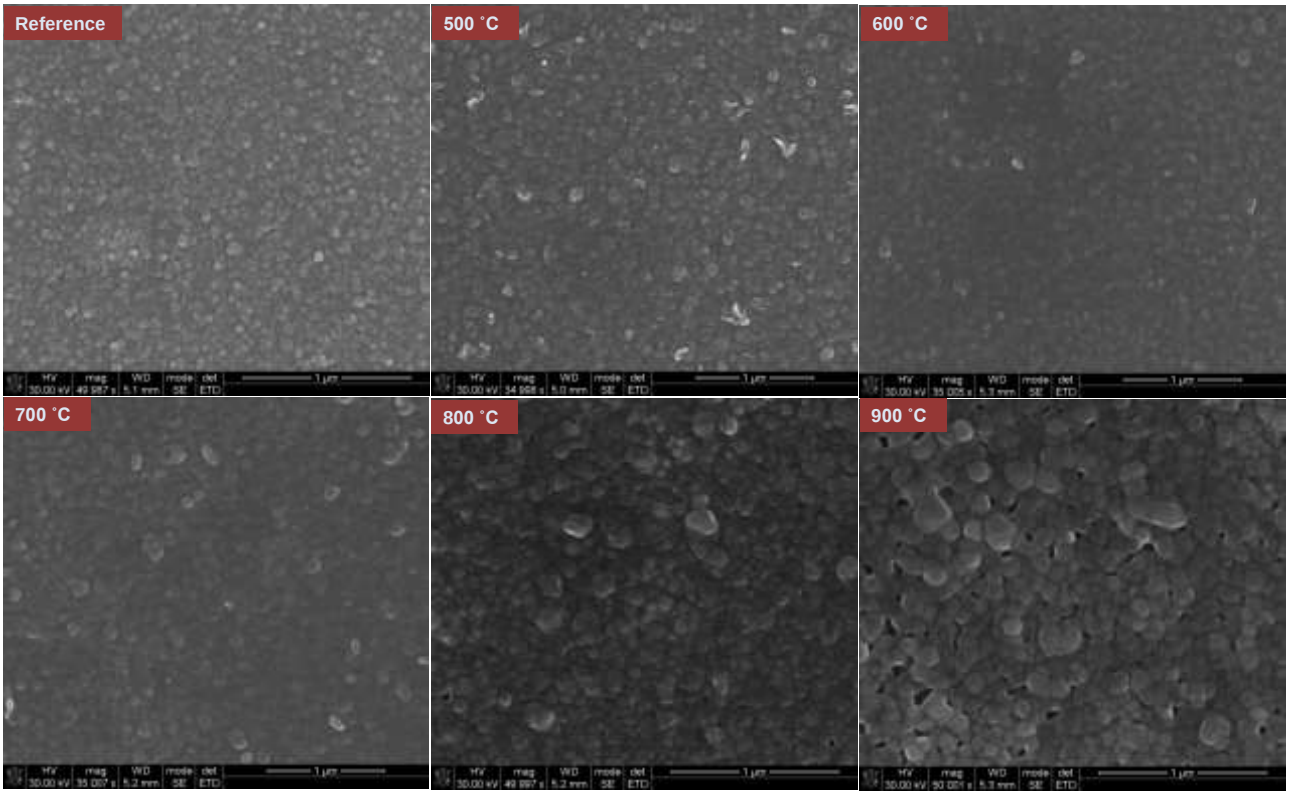


Figure 4-4: SEM images of ZnO thin film grown at 100 W, 1 minute and annealed at different temperatures (600-900 ˚C) using beam energy of 30000 in each case, working distance of 4.8mm, 5.0 mm, 5.2 mm, 4.8 mm and beam energy magnification of 36 000, 20 000, 20 000, 20 000 for 500 ˚C, 600 ˚C, 700 ˚C, 800 ˚C and 900 ˚C respectively.

Figure 4-4: shows the SEM images of the films with different film annealing temperature. As the annealing temperature increases from 600 ˚C to 900 ˚C, the density of microstructure was gradually decreased while the surface continuity of the film decreases due to the emergence of pores like structures on the surface. The increased size of the grain height is observed to be loosely formed on the surface.

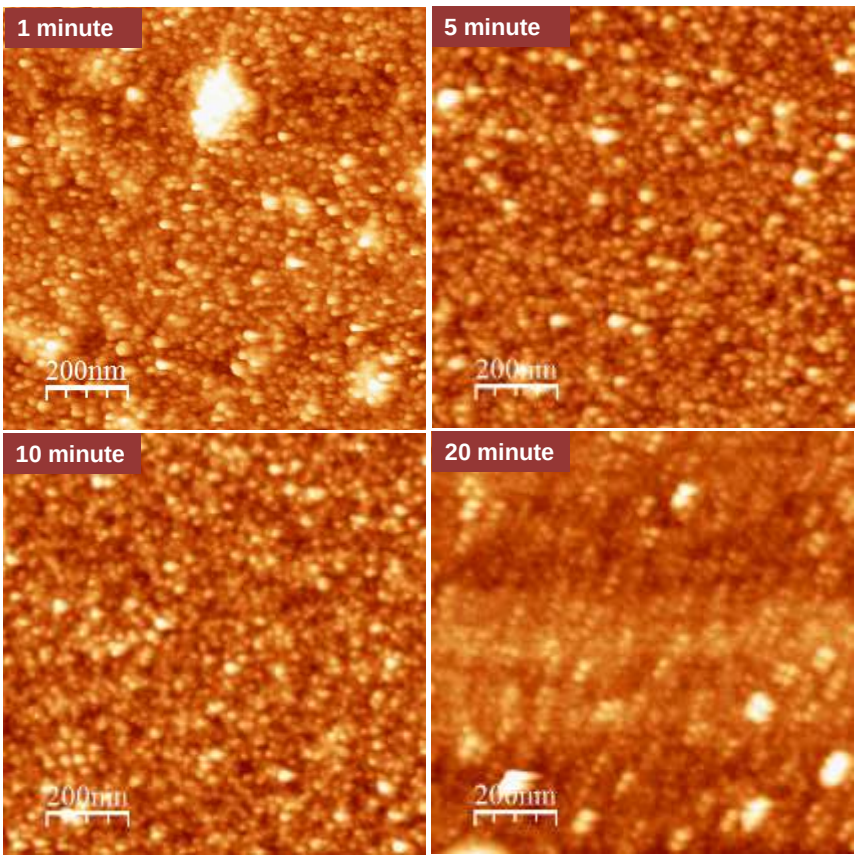


Figure 4-5: AFM images of ZnO thin film grown at 100 W at different deposition time ranging from 1-20 minutes.

Figure 4-5 shows the AFM images under the tapping mode for films deposited under varied deposition times (1-20 mins) using an RF power of 100 W. The summary of statistical data is as shown in table 4-3.

Table 4-3: Summary of tapping mode AFM analysis for films grown at different deposition time ranging from 1-20 minutes.

Deposition Time (minutes)	R_a (nm) ±0.2	R_{rms} (nm) ±0.2	Skewness (R_{sk}) ±0.01	Kurtosis (R_{ku}) ±0.01	Grain height (nm) ±0.1
1	14.3	18.9	1.489	6.159	51.5
5	13.0	17.8	1.005	6.079	56.7
10	12.2	16.1	1.174	5.687	64.2
20	11.7	13.2	1.314	7.041	71.5

From table 4-3 the films' roughness decreases with increasing deposition time from 18.9 nm at 1 minute deposition time to 13.2 nm at 20 minute deposition time. From the table 2-2 we can deduce that the film growth conditions such as deposition time play a vital role during the evolution of the film surface topography. For small thickness obtained using short deposition time, the AFM images present small nucleation sites as a result of the short incubation time. However, as we increase the deposition time, the grains coalescence and this leads to film thickness increase. The increase in grain size in the film under these conditions leads to a film morphology with uniformly large grains. According to Raoufi, D., & Hosseinpanahi, F. (2012), this trend has been observed and attributed to three processes, namely;

- the reflecting nucleation,
- coalescence and ultimately to
- continuous film growth processes,

This is the typical Volmer-Weber type initial growth [24]. From the fundamental structure forming phenomena of Volmer-Weber type, thin film growth evolves through island nucleation to islands

coalescence and ultimately to the growth of the continuous film. This leads to the formation of large grains due to the coalescence phenomena between grains [25].

This is further supported by the SEM images obtained from films with different deposition time as show in figure 4-6.

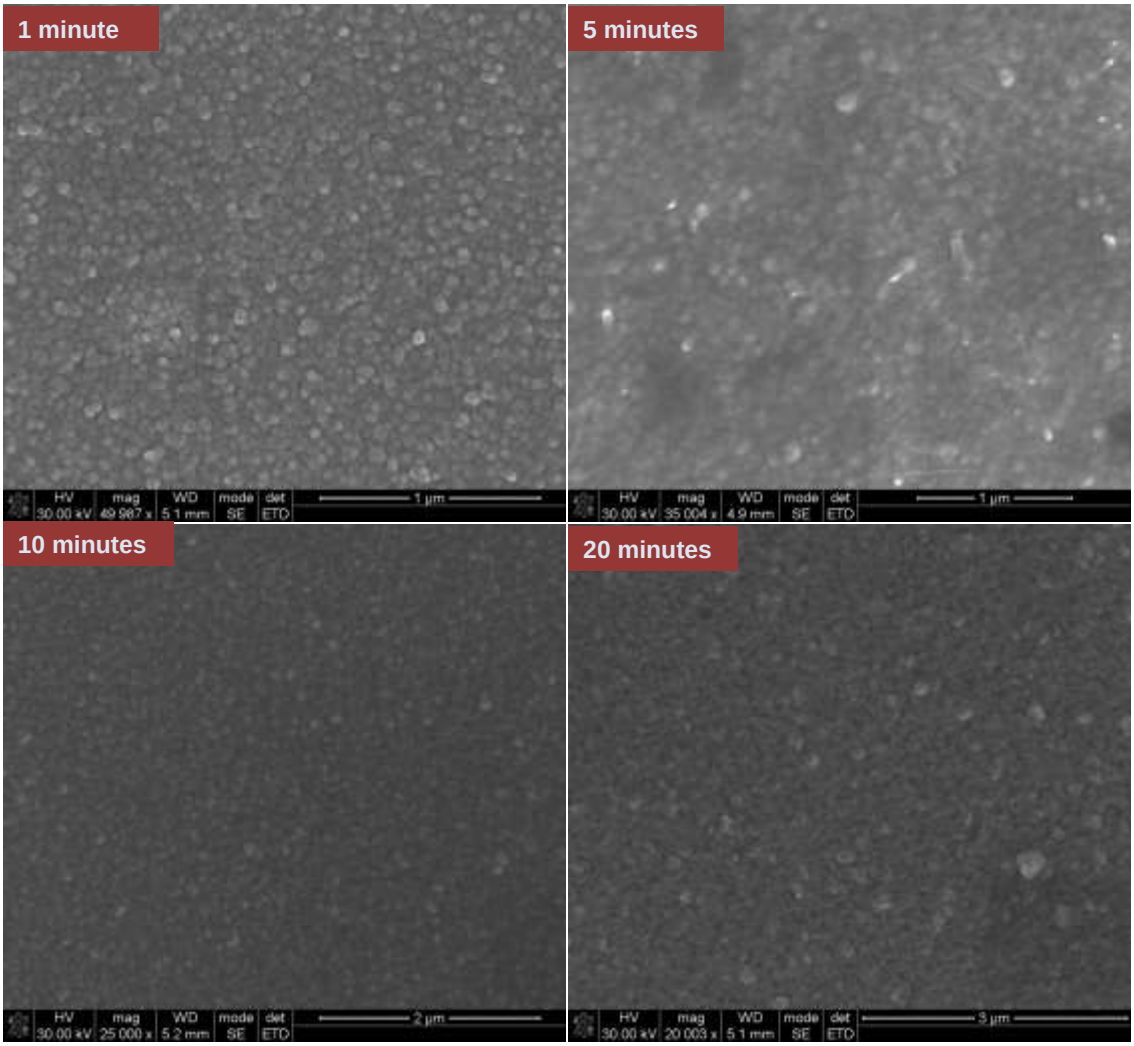


Figure 4-6: SEM images of ZnO thin film grown at 100 W at different deposition times, (1-20 minutes).

From Figure 4-6, the ZnO films present distinct separated particles due to its amorphous phase, as was later confirmed by the GIXRD measurements. As the deposition time increases (increasing film thickness), the pores between the grains decreased and densely packed ZnO films were

formed. The deposition time of 20 minutes formed denser films, whereas the film shows non homogeneous surface morphology. The above results have shown that the deposition time is a critical parameter that affects the physical properties of ZnO and the surface topography of the formed layers. Thus the deposition rate is essential in the determination of the arrival rate of the adatoms and the formation of the islands which subsequently determine the morphology of the films. It is important to note that the native oxide of the substrate was not removed and thus the formation of epitaxial layers is ruled out from surface energy considerations. Therefore the nature of the film thickness deposited by RF sputtering method is a significant parameter in determining the surface morphology. However ad atom mobility plays a crucial role on the surface morphology during deposition and this effect was further studied for ZnO thin films by varying the RF power. The variation in the RF power leads to the changes in the Ar accelerating voltage to the target and thus the ad atom energy and their subsequent thermalization energies on the substrates. This effect is presented in the AFM images of Figure 4-7.

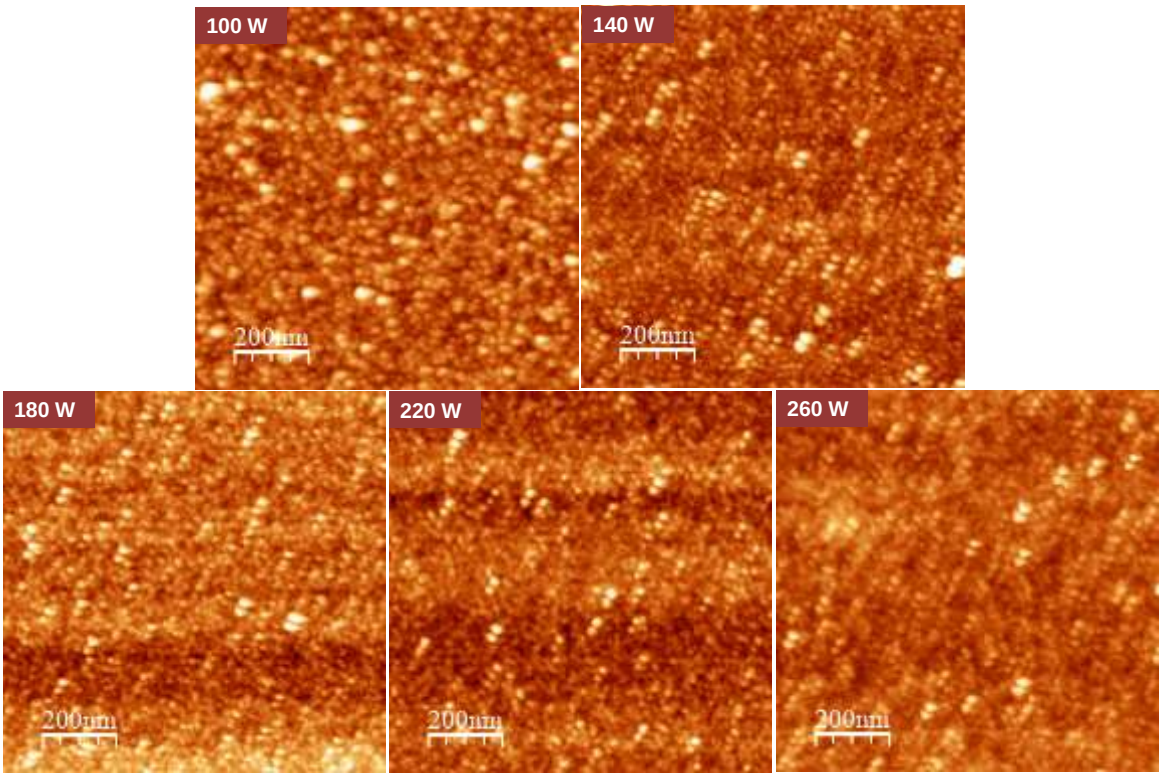


Figure 4-7: AFM images of ZnO thin film grown at a deposition time of 5 minutes at different RF sputtering power.

From the AFM images in Ffigure 4-7, the variation in the RF sputter power leads to an increase in the sputter rate and ad atom energies, thus resulting in changes in the grain size and surface roughness. Therefore, it seems that by choosing a suitable deposition power, the grain size and roughness can be controlled, this is particularly essential especially in grain boundary limited electron transport. A summary of the morphological results obtained at varied RF power is presented in table 4-4.

Table 4-4: Summary of tapping mode AFM analysis for films deposited at time of 5 minutes at different RF sputtering power.

RF sputtering Power (W)	R_a (nm)	R_{rms} (nm)	Skewness (R_{sk})	Kurtosis (R_{ku})	Grain height (nm)
100	13.0	17.8	1.005	6.079	56.7
140	15.7	19.9	0.470	4.019	62.9
180	23.9	28.3	0.558	2.463	66.4
220	20.6	25.1	0.512	2.623	68.2
260	21.0	26.2	0.724	3.318	70.1

From table 4-4, the values of the roughness of the films are seen to increase with RF power. This increase in surface roughness with increasing deposition rate may be due to the increasing energy of condensing particles and numbered atom flux leaving the target during the sputtering process [26]. The rms roughness and the grain size are increased as RF power increases then decreased beyond 180W. The increase in the grain size from 56.7 nm at 100 W to 70.1 nm at 260 W could be as a result of the increased ad atom fluence and the subsequent coalescence of neighboring grains at a much faster rate for higher RF powers. This is the source of the increase in the grains/particle size. According to Bordo, K. and Rubahn, H.G., 2012 [27] this trend can be explained by considering the simultaneous contribution of three independent processes, namely

- surface diffusion of adatoms
- nucleation of ad atom clusters and
- subsequent coalescence of the islands during deposition.

The atoms arriving onto the silicon substrate surface can diffuse along the surface and form clusters which can in turn contribute to the formation of crystallites (grains). At low RF sputter power the

surface diffusion of the atoms and formation of ZnO clusters is less prominent. Consequently, there is small density of clusters (nuclei) capable of coalescing to form grains, resulting in a small grain size. At higher RF power, the number of atoms arriving onto the surface per unit time is higher, therefore the number of nuclei formed on the surface is bigger resulting into to bigger grains formation.

At 100 W, smoother films are achieved. According to Guanghua, Wang, *et al*, the basic mechanism for the formation of large islands is the reduction of the surface energy, and the minimum surface energy is attained when all the islands are joined in one, single island [28]. For the case of the 100 W films, the combined effects of increased ripening and low surface mobility of the species on the surface resulted in the formation of comparatively smaller islands as well as increased island boundaries. Therefore, the coalescence of these smaller islands is energetically favorable even at a comparatively earlier stage. However, low surface mobility and ripening at a low deposition rate also essentially limits the areal density and height of these larger islands, both of which are comparatively lower. The growth rate is delayed by the extensive ripening as well as low surface mobility.

At an RF power of 220 W, the surface becomes completely covered by the film with significant amount of island boundaries. At this critical thickness for this regime, any further deposition leads to the formation of larger islands through coalescence. The complete covering of the surface leads to a decrease in surface roughness as seen in table 4-4 which then begin to rise as seen with the 260 W RF power. This can also be seen with visual inspection of the SEM image shown in Figure 4-8.

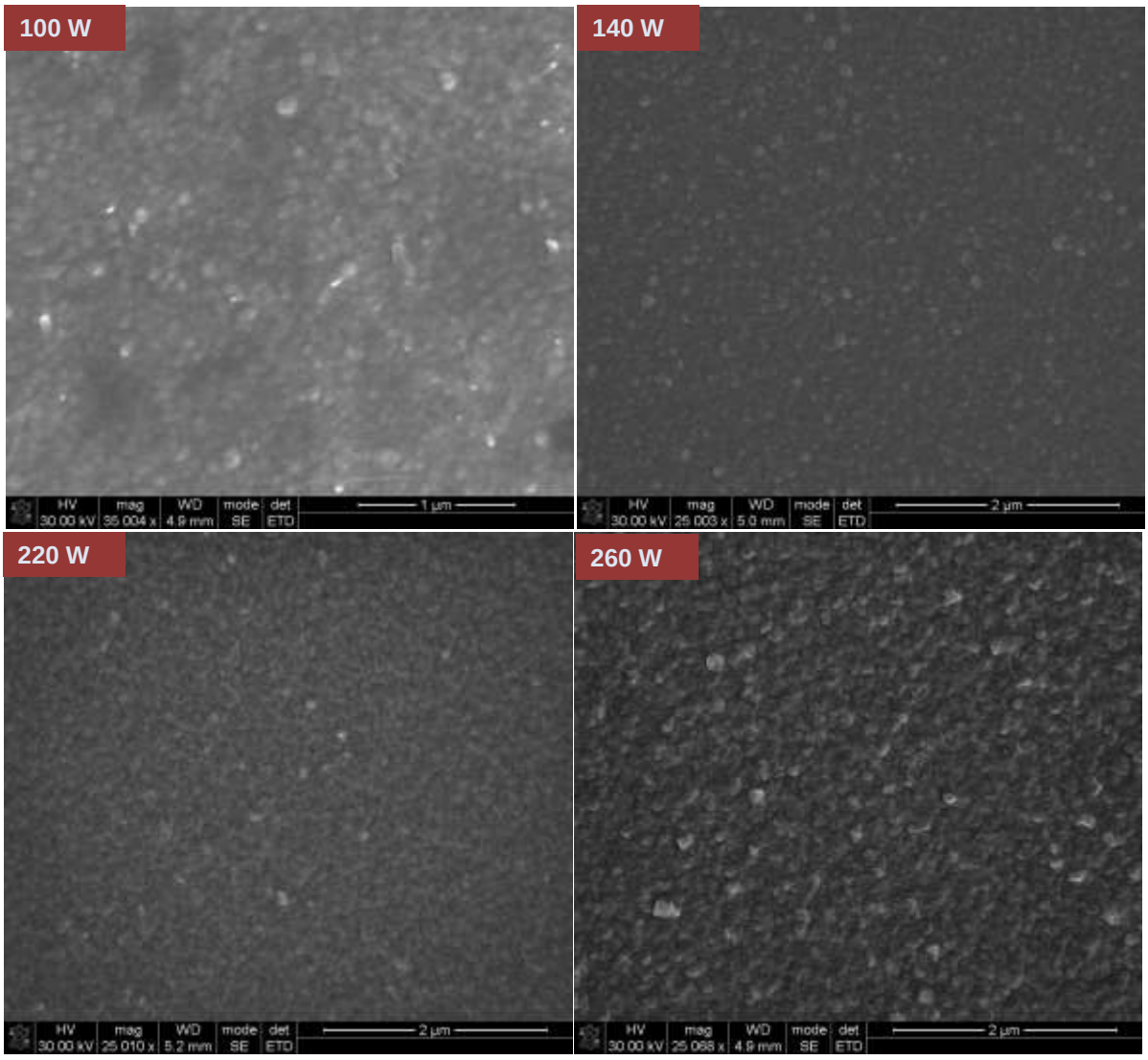


Figure 4-8: SEM image of ZnO thin film grown at a deposition time of 5 minutes at different RF sputtering power.

4.4.3. X-Ray Diffraction analysis

Figure 4-9 shows the XRD patterns of ZnO films deposited at a fixed deposition time and RF power of 1 minute and 100 W, respectively. The films were then annealed at a temperature range of 600 ˚C- 900 ˚C in Ar filled furnace. Representative XRD patterns of the annealed films are shown in the 2θ range of 20˚-80˚.

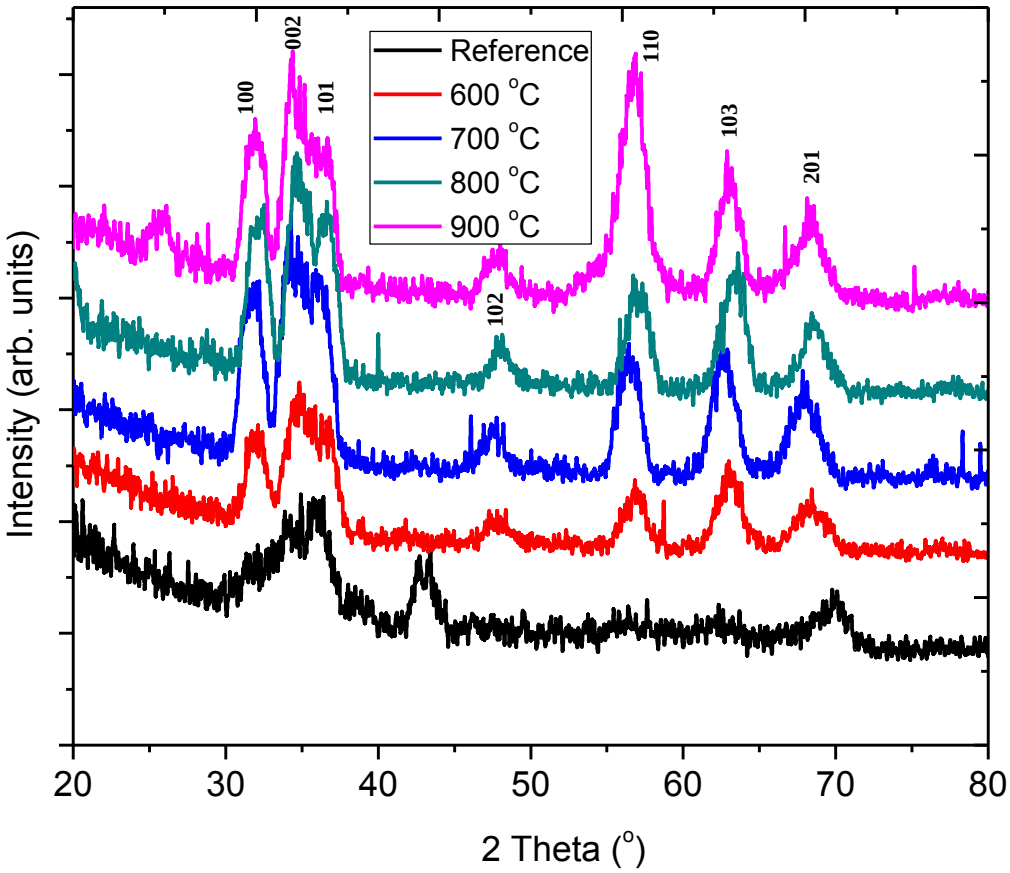


Figure 4-9: XRD patterns of ZnO thin film grown at 100 W, 1 minute unannealed and annealed at different temperatures (600-900 ˚C).

From figure 4-9, the characteristic peaks of the as-grown and annealed films as shown. The as-grown films peaks is observed at 2θ = 31.2˚, 34.6˚ and 47.5˚ which matches the reflection planes of (100), (002) and (102), respectively. All the diffraction peaks can be well indexed to the wurtzite structure of ZnO of the space group P63mc, which is consistent with the standard values reported

in JCPDS, card no. 03-0888. With an increase in annealing temperature, the diffraction peaks become more intense and sharper, this is an indication of grain growth and the improvement of crystallinity in the film. The increase in crystallite size with the annealing temperature also implies that the surface-to-volume ratio is decreased with the annealing temperature [29]. At one minute deposition time, although (002) is the preferred film orientation, the (100) and (110) can also be seen due to the formation of polycrystalline grains at low temperatures. From table 4-5, the FWHM of the (002) reduces with annealing temperature while the relative intensity of the (002) peak decreases with increasing temperature.

The lattice constants "*a*" and "*c*" for the ZnO thin films were obtained using the Bragg's law, equation 4-1:

$$n\lambda = 2d\sin\theta \quad \text{..... 4-1}$$

All the peaks are indexed to the JCP2 card number 003-0888 with hexagonal wurtzite structure of space group of P63mc and lattice constants, a = 3.24 Å and c = 5.21 Å.

Where n is the order of diffraction, λ is the X-ray wavelength and d is the spacing between planes of given Miller indices h, k, and l. The plane spacing was thereafter derived from the lattice constants "*a*" and "*c*" and the Miller indices by the following relation in equation 4-2:

$$\frac{1}{d^2_{(hkl)}} = \frac{(h^2+hk+k^2)}{a^2} + \frac{l^2}{c^2} \quad \text{..... 4-2}$$

The average crystalline size in ZnO films was then estimated using Scherrer's equation 4-3.

$$D = \frac{k\lambda}{\beta\cos\theta} \quad \text{..... 4-3}$$

Where D is crystal size, β the full width at half maxima FWHM (radians) and λ the wavelength of X-ray used (1·5409 Å) and k is a constant = 0.9.

From the crystallite size the dislocation density value which represents the amount of defects in the film was calculated by the expression:

$$\delta = \frac{1}{D^2} line / m^2 \quad \text{..... 4-4}$$

The tensile strain,ε was calculated using the formula:

$$\varepsilon = \frac{\beta \cos\theta}{4} \quad \text{..... 4-5}$$

Table 4-5: Summary of statistical values of ZnO thin film grown at 100 W, 1 minute and annealed at different temperatures (600-900 ˚C).

Annealing Temperature (˚C)	Crystallite size, D_{sh}/(Å)					
	(002) peak	FWHM peak	d-spacing a/(Å)	Crystallite size D (Å)	δ (10^{17})	ε (10^{-3})
Reference	38.6	5.71	2.33	14.8	4.60	23.5
600	37.8	3.56	2.38	23.6	1.79	14.7
700	35.4	2.88	2.54	28.9	1.19	12.0
800	35.1	2.81	2.56	29.6	1.14	11.7
900	35.1	2.70	3.57	30.7	1.06	11.2

From table 4-5, the strain on films decreased from 23.5×10^{-3} to $11{\cdot}2 \times 10^{-3}$ while the dislocation density decreased from 4.60×10^{17} to 1.06×10^{17}. As annealing temperature increased from 600 to 900 ˚C, the atoms gained sufficient kinetic energy and surface mobility to occupy stable positions inside ZnO crystals. This helped in enhancement of crystalline property of ZnO thin films.

At 5 minute deposition time, the annealed films showed a clear preferred orientation of developed *c*-axis (002) with high intensities compared to the 1 minute deposition time. Figure 4-10 shows the XRD patterns of films grown at RF power of 100 W before subjecting the films to annealing at a temperature range of (600-900 ˚C).

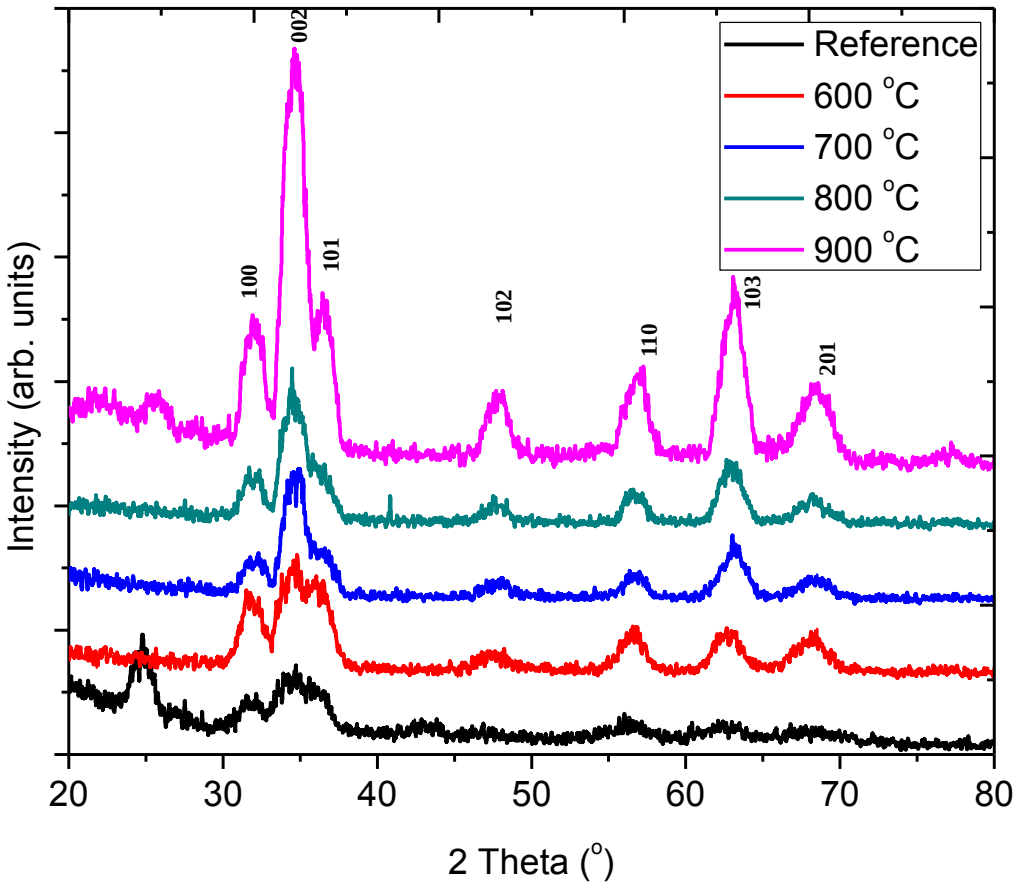


Figure 4-10: XRD patterns of ZnO thin film grown at 100 W, 5 minutes unannealed and annealed at different temperatures (600-900 ˚C).

Table 4-6: Summary of statistical values of ZnO thin film grown at 100 W, 5 minutes and annealed at different temperatures (600-900 ˚C).

Annealing Temperature (˚C)	Crystallite size, D_{sh}/(Å)					
	(002) peak	FWHM peak	d-spacing a/(Å)	Crystallite size D (Å)	δ (10^{17})	ε (10^{-3})
Reference	36.9	3.31	2.43	25.4	1.56	13.7
600	35.1	2.96	2.56	28.1	2.27	12.3
700	34.8	1.85	2.57	40.9	4.96	7.72
800	34.7	1.73	2.58	44.9	5.97	6.47
900	34.7	2.74	2.58	47.9	4.35	7.23

For the 5 minute deposition time, it was found that ZnO film annealed at 800 ˚C had a minimum value of 1.73˚ for the full width at half maximum (FWHM). The results also showed that ZnO crystallite size steadily increased with annealing temperature from a minimum value of 25.4 Å for the as-deposited film to a maximum value of 47.9 Å after at an annealing temperature of 900 ˚C. As observed, stress on films decreased from 13.7×10^{-3} to 6.47×10^{-3} for an annealing temperature increased from 600 to 800 °C and further increased to 7.23×10^{-3} as the annealing temperature rose to 900 ˚C. Without annealing, surface atoms have less energy hence low surface mobility of atoms, resulting in generation of defects in ZnO films. On annealing at 600-900 ˚C the atoms gained sufficient kinetic energy and surface mobility to occupy stable positions inside ZnO crystals. This helped in enhancement of crystalline property of ZnO thin films [29] as observed from the FWHM values. Further increase in annealing temperature to 900 ˚C resulted in breaking of partially coordinated Zn-O bonds on the surface rather than enabling the atoms to move freely

to their corresponding stable sites, producing defects and stress in ZnO film hence the increase in strain and dislocation density.

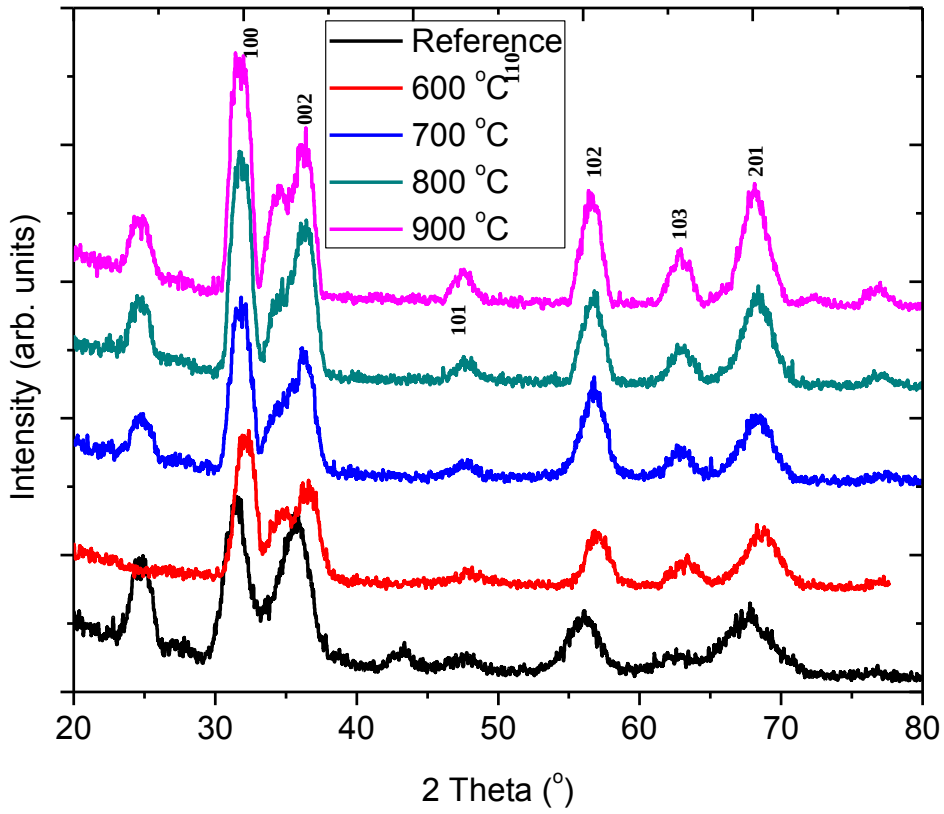


Figure 4-11: XRD patterns of ZnO thin film grown at 100 W, 20 minutes unannealed and annealed at different temperatures (600-900 ˚C).

Table 4-7: Summary of statistical values of ZnO thin film grown at 100 W, 20 minutes and annealed at different temperatures (600-900 ˚C).

Annealing Temperature (˚C)	Crystallite size, D_{sh}/(Å)					
	(002) peak	FWHM peak	d-spacing a/(Å)	Crystallite size D (Å)	δ (10^{16})	ε (10^{-3})
Reference	35.5	2.94	2.53	28.3	12.5	12.2
600	35.7	2.63	2.52	31.7	9.96	10.9
700	35.7	2.26	2.51	37.0	7.29	9.37
900	35.9	2.18	2.50	38.3	6.82	9.05
1000	35.5	2.41	3.52	38.9	8.35	10.01

At 20 minutes deposition time, a similar trend is observed, however a new peak at around 2θ=24˚ was observed. The decrease in the compressive stress with the annealing temperature may have led to the decrease in the tensile strain in the ZnO film as shown in table 4-7. From the annealing trends for different thickness annealed at different temperatures it worth noting that annealing, in general, is able to induce ductility, soften material, relieve internal stresses, refine the structure by making it homogeneous, and improve cold working properties. However, the relief of internal stresses in a material is a thermodynamically spontaneous process which is a very slow process at room temperatures. The annealing at high temperatures serves to accelerate the above process thereby improving the crystalline quality of the ZnO film as observed from the XRD analysis [29]. The data shows that increasing of annealing temperature results in larger crystal domains, and reduces the amount of pores in the films as witnessed by the general reduction in the dislocation density in the films.

A comparison of XRD analysis of films deposited with varied deposition time is shown in Figure 4-12, while table 4-8 presents a statistical analysis of XRD results.

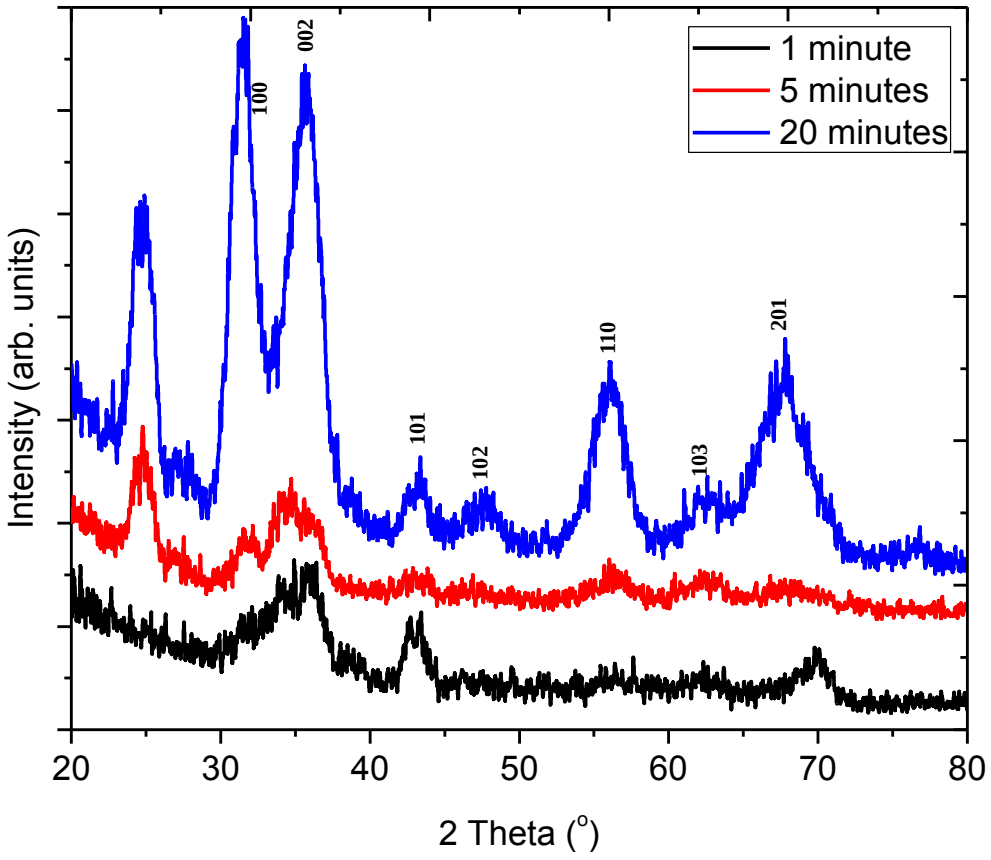


Figure 4-12: XRD patterns of ZnO thin film grown at 100 W with varied deposition time.

Table 4-8: Summary of statistical values of ZnO thin film grown at 100 W with varied deposition time.

Deposition Time (minutes)	Crystallite size, D_{sh}/(Å)					
	(002) peak	FWHM peak	d-spacing a/(Å)	Crystallite size D (Å)	δ (10^{17})	ε (10^{-3})
1	38.6	5.71	2.33	14.8	4.60	23.5
5	36.9	3.31	2.43	25.4	1.56	13.7
20	35.5	2.94	2.53	28.3	1.25	12.2

From figure 4-12 and table 4-8 analysis, the (002) peak centre is shifted to lower angle with increasing deposition time from 38.6˚ at 1 minute to 35.5˚ at 20 minutes. The crystallite size is also observed to increase from 14.8Å to 28.3Å. It is seen from the figure that as the film thickness increases, the intensity of the (002) peak increases and the width of the peak narrows. The peak intensity and crystallite size are usually associated with the crystallinity of the films. Poor crystallinity in thinner ZnO film could be due to the formation of nanocrystalline grains in an amorphous matrix [30].

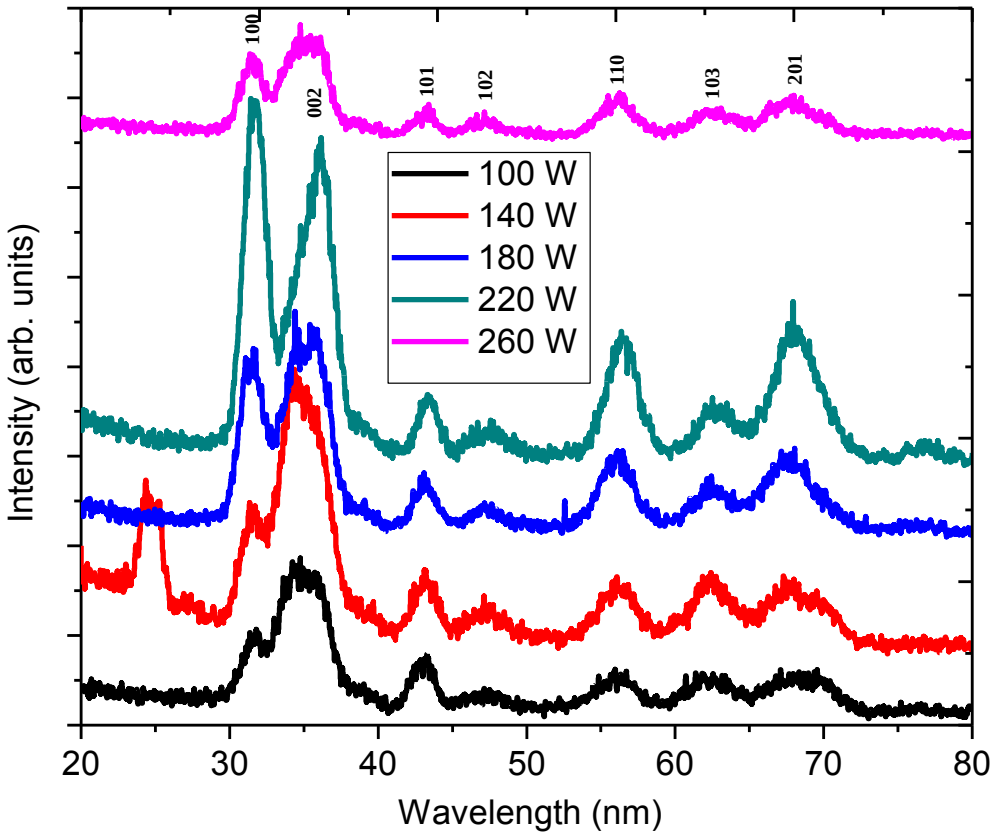


Figure 4-13: XRD patterns of ZnO thin film grown at deposition time of 5 minutes with varied RF power in the (100-260 W) range.

From figure 4-13, the RF power of 100 W, produces polycrystalline films with (002) as the preferred orientation. The peak intensities are seen to increase with increasing RF power. This

could be attributed to an increase in the crystallinity as the grain sizes increases with RF power. This similar to the trend obtained by Ref [31].

At 260 W, the (002) peak intensity is reduced considerably while the (100) intensity increases thus suggesting the prevalence of fibre texture in these films. This could be attributed to the fact that an increase of RF power induced faster reaction rate that caused insufficient time for the formation of the initially preferred film orientation [32]. As the RF power increases, the crystallite sizes became larger and it is attributed to the fact that increasing energy of the atoms arriving at the surface promotes grain growth [33]. The reduction in the peak intensity is also an indication of reduced film quality. Statistical analysis of the films grown using different RF power is shown below in table 4-9.

Table 4-9: Summary of statistical values of ZnO thin film grown at deposition time of 5 minutes with varied RF power in the (100-260 W) range.

	Crystallite size, D_{sh}/(Å)					
RF Power (W)	(002) peak	FWHM peak	d-spacing *a*/(Å)	Crystallite size *D* (Å)	δ (10^{16})	ε (10^{-3})
100	34.4	3.27	2.57	25.4	15.5	13.6
140	34.5	3.06	2.57	27.2	13.5	12.8
180	35.2	2.91	2.55	28.6	12.2	12.1
220	35.7	2.57	2.51	29.2	9.49	10.7
260	35.1	2.85	3.56	32.5	11.8	11.9

The (002) peak was used to estimate the crystallite size, since it is the most intense, and it appeared in all the samples. Table 4-9 shows the change in FWHM of (002) peaks and the crystallite size with the changing RF powers.

All deposited films exhibited significant tensile strain which tends to ease with an increase RF power. Increasing RF power also led to general shifting of (002) X-ray diffraction peaks to slightly larger 2θ angles which indicated a relief of intrinsic stress within the films. Stress in films is usually attributed to two reasons; one is the intrinsic stress due to impurities and defects in crystal and other is extrinsic stress due to lattice mismatch, growth conditions and mismatch in the thermal expansion coefficient of the film and substrate. It is worth noting that the nature of the stress in ZnO films is initially compressive, which becomes tensile with an increase in the film thickness as a result of increasing power.

The XRD peaks presented here are also be widened by internal stress and defects, so the mean grain size estimated here appears smaller than the actual value, and this discrepancy can be seen in scanning electron microscopy SEM/AFM Images in section 4.4.2 [34].

4.4.4. Raman spectroscopy

Raman scattering is the inelastic scattering of photons by phonons. For UV-Visible photons, the direct photon-phonon coupling is weak hence their interaction is aided by electrons via an electron-radiation. Finally the electron-hole pair recombines radiatively to emit scattered photon with a higher or lower energy but leaves the electronic state of the material unchanged [35, 36].

The wurtzite-type lattice structure of ZnO (space group $P6_3mc$) implies a base unit of four atoms in the primitive unit cell: two ZnO molecular units. This means 12 (3N) vibration eigenmodes. Using group theory, the eigenmodes are categorized following the irreducible representation: $\Gamma=2A_1+2B_1+2E_1+2E_2$ [37]. Three modes are attributed to acoustic phonons (i.e One A_1 mode and one E_1 mode, this are only two here). While the nine other modes are optical branches represented by $\Gamma_{optical}=A_1+2B_1+E_1+2E_2$. These modes have no counterpart in the centre of the ZB Brillouin zone.

The $A_{1,}$ E_1, and E_2 are first-order Raman-active mode [38]. The A_1 and E_1 polar modes split into the ion displacement vectors parallel to the propagation wave vector q called longitudinal optical (LO) and displacements and *q*-vector perpendicular to each other called transverse optical (TO) components, while the E_2 non-polar modes (low and high) are Raman active. Due to the frequency splitting of polar modes into LO and TO eigen frequency, more eigen frequency values may occur compared to the 12 modes predicted by group theory. The LO–TO splitting of both the A_1 and B_1 modes have their displacements directed along the *c*-axis. They are distinct i.e: The A_1 mode pattern arises from the oscillation of the rigid sub-lattices, Zn vs O. On the contrary, the B_1 modes have one of the sub-lattices essentially at rest, while the other possesses neighboring atoms moving opposite to each other. B1 (low) displacements usually occur in the heavier Zn sub-lattice (Zn) - while the B1 (high) excitations occur in the lighter O sub-lattice Since the displacements of the ions within each sub lattice sum up to zero, there is no net polarization induced by the B modes hence the three modes with displacement along the *c*-axis are categorized as one polar phonon mode A_1 and two non-polar modes B_1. The same scheme applies for the E modes with their atomic displacement directions being perpendicular to the *c*-axis. The E_1 mode is an oscillation of rigid sub lattices hence inducing an oscillating polarization contrary to the two E_2 modes which are non-polar due to the mutual compensation of the displacement vectors within each sub-lattice [39]. The eigenvectors (displacement patterns) of the optical phonon modes are shown in Figure 4-14.

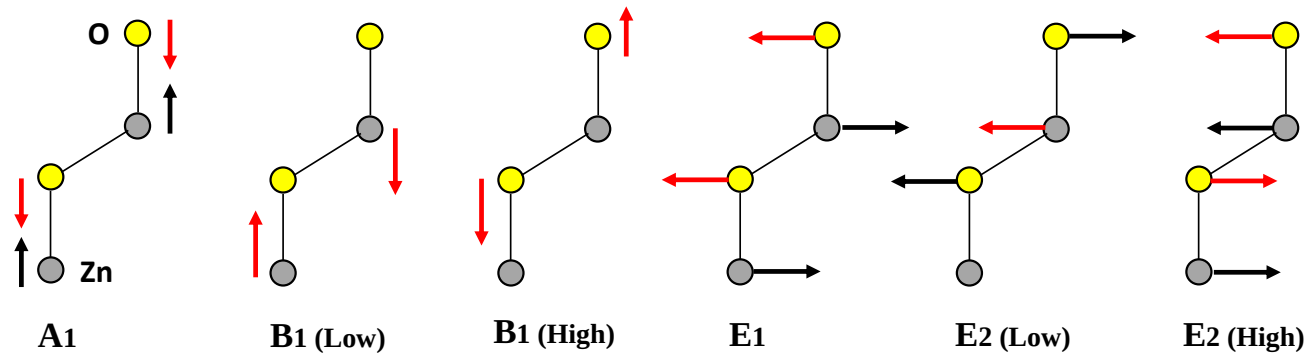


Figure 4-14: Eigenvectors of the ZnO optical phonon modes. For every mode, the red arrows represent the dominating displacement vectors. The A_1, B_1 (high), E_1, and E(high) modes are oxygen-dominated while B (low) and E_2 (low) modes are Zn-displacement dominated [39].

Figure 4-15 shows the Raman spectrum of bulk ZnO with 6 first-order peaks showing the active modes.

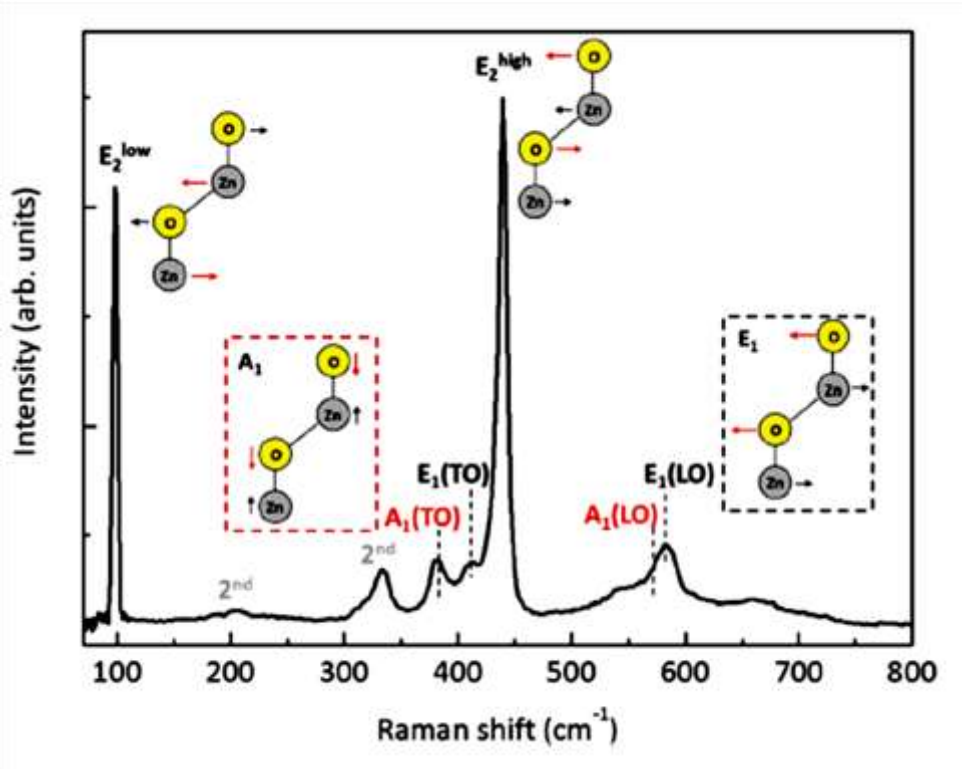


Figure 4-15: Unpolarized Raman spectrum of bulk ZnO showing Raman active modes with the corresponding vibrations of the ions. The red arrows specify the dominant ions displacements adopted from [40].

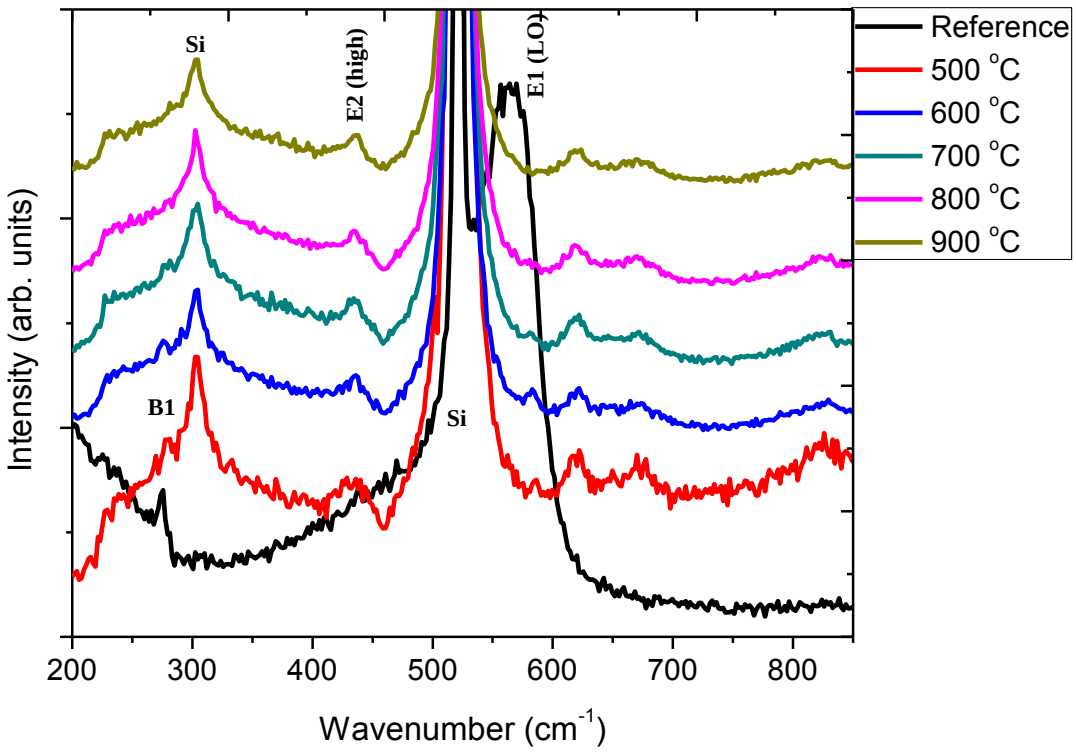


Figure 4-16: Raman spectra of ZnO thin film grown at 100 W for 1 minute before and after annealing at temperature 600-900 ˚C.

Figure 4-16 shows the ZnO thin film grown on Si(100) after deposition for 1 minute at 100 W using an Ar flow rate kept at 13 sccm. The films were then annealed in an Argon filled furnace for two hours. The peak at about 434.5 cm^{-1} for the reference corresponds to the non-polar optical phonons E_2 (high) modes of the ZnO film. The peaks at 522 and 303 cm^{-1} are attributed to the optical phonon modes of the silicon substrate, and the broad peak at about 565 cm^{-1} is attributed to the E_1 (LO) mode of ZnO. Upon annealing E_2 phonon frequency is blue shifted from 434.5 to 437 cm^{-1}. This shift of 2.5 cm^{-1} corresponds to the decrease in the tensile stress upon annealing. The intensity of the peaks did not change significantly. The broad modes at 630 and 680 cm^{-1} are attributed to A_1 (LO) and multiphonon processes mediated by intrinsic defects respectively.

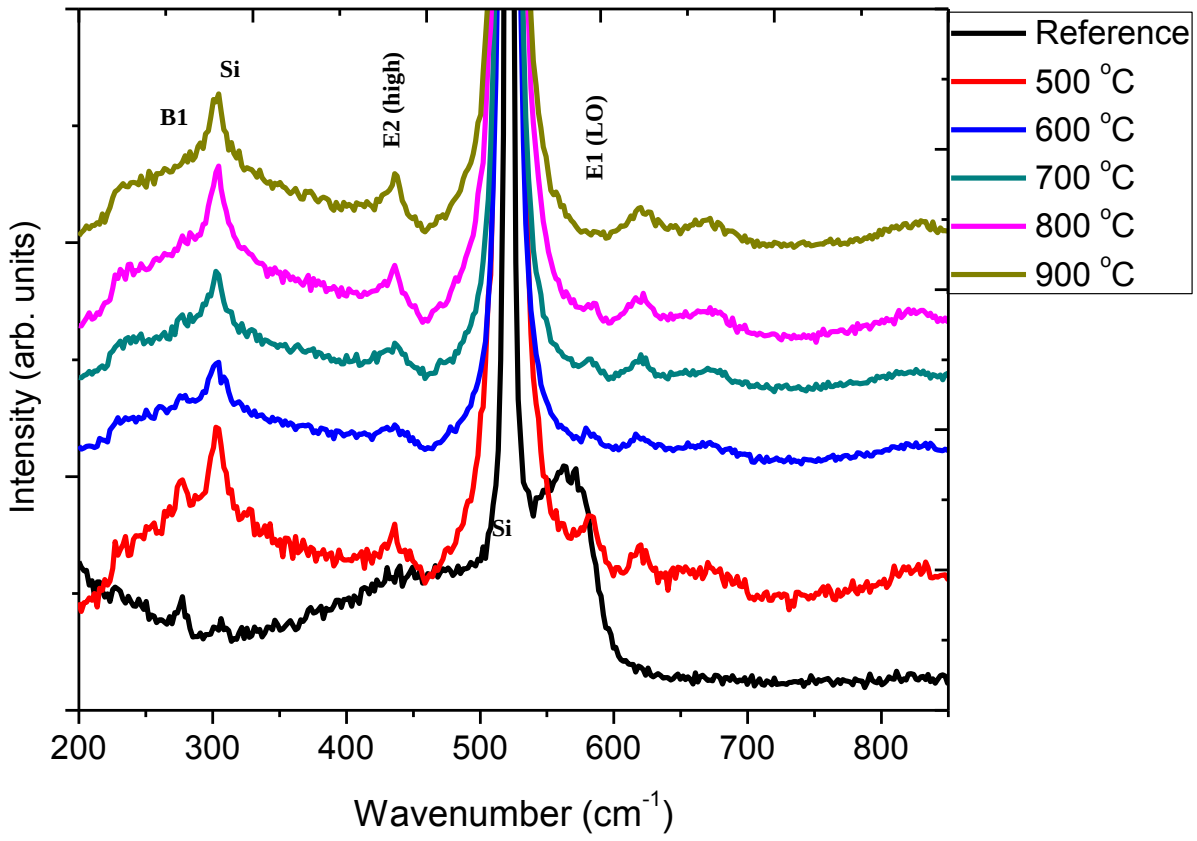


Figure 4-17: Raman spectra of ZnO thin film grown at 100 W for 5 minutes before and after annealing at temperature 600-900 ˚C.

When films deposited at 5 minutes are subjected to heat treatment, the resulting excitations are observed as shown in Figure 4-17. The E_2 (high) peak is observed at a lower wavenumber of 432 cm^{-1} compared to the film grown for 1 minute. This change indicates the presence of tensile stress in the deposited thin films. Probably the stress is due to the lattice mismatch or the mismatch of the thermal expansion coefficients of the films and the substrates. This is also experienced for films grown at 20 minutes (Figure 4-18). A comparison of variation with deposition time is shown in Figure 4-19. The E_2 (high) peak gradually increases in intensity for both film grown for 5 and 20 minutes.

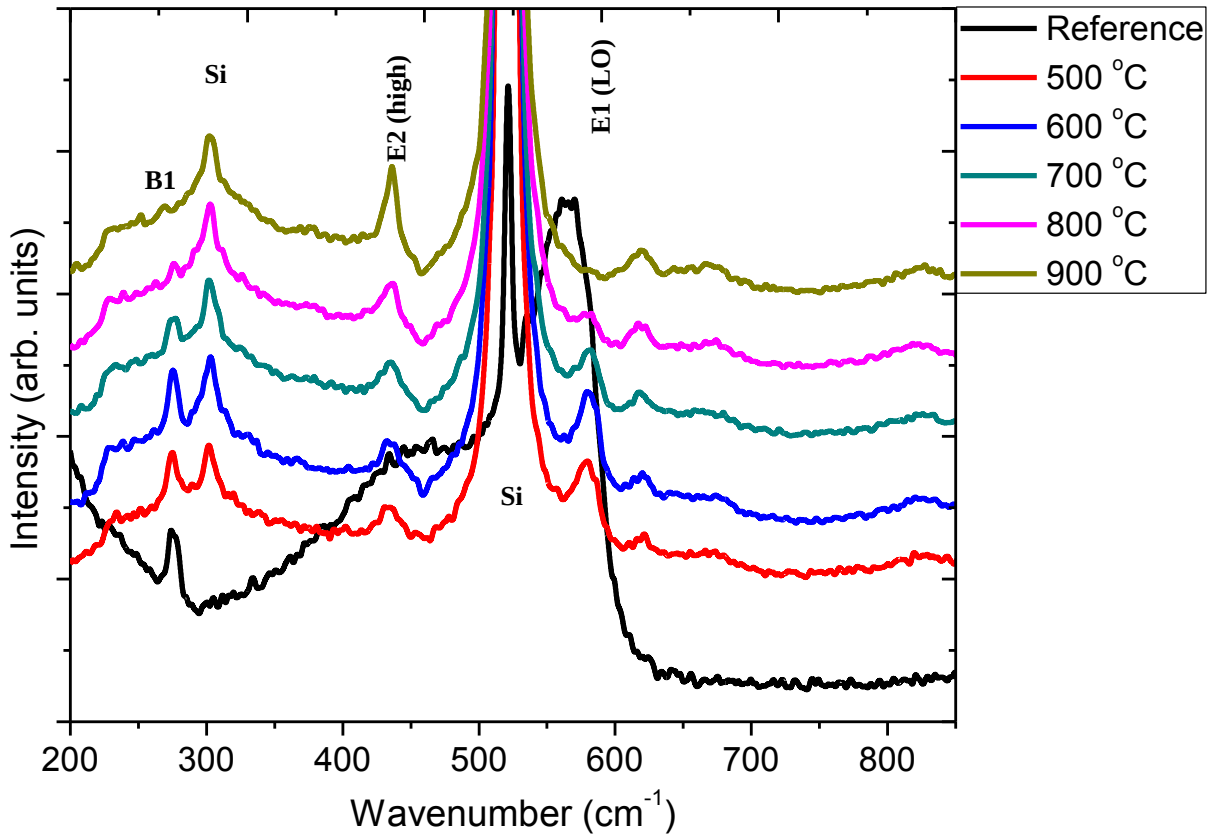


Figure 4-18: Raman spectra of ZnO thin film grown at 100 W for 20 minute before and after annealing at temperature 600-900 ˚C.

During this systematic annealing of films with different thicknesses, there is an appearance of a peak near 275 cm^{-1} attributed to the B1 silent inactive mode. This mode is observed at 277 cm^{-1} for films grown for 5 and 20 minutes. This peak gradually vanishes with increasing annealing temperature. According to Serrano, J., *et al* [41] DFT calculation, the B1 mode possibly originates from the breakdown of the translational crystal symmetry induced by defects and impurities or local electric field at grain boundaries [40, 42, 43]. The increase in the annealing temperature improves the crystallinity of the films the consequence of which is the annihilation of the B1 (high) excitation. This condition can however not be extrapolated to thicker film (20 minutes) since much

higher thermal energies are required to extinguish this mode as compared to thinner films (1 minute).

The additional mode observed in the vicinity of 580 cm^{-1} is attributed to the E1 (LO) branch and this confirms the deposition of wurtzite ZnO phases using RF magnetron sputtering. This mode has been a subject of discussion to many researchers. Some suggest it corresponds to silent modes [44], Nitrogen-related modes of vibration [45] and zinc interstitials, oxygen vacancies or their combination related defects [46] In our case, the peak may be as a result of two reasons:

(1) Due to the native defects of the films and the increase in particle size during annealing, the surface to volume ratio decreases resulting in decrease of the defect related states. Due to these changes, the scattering intensity of the respective phonon peak decreases [47].

(2) Oxygen-vacancy and its enhancement at growth before any annealing is an oxygen-deficient condition. Upon annealing, the mode gradually vanishes at 700 ˚C, 800 ˚C and 900 ˚C for the 1 minute, 5 minutes and 20 minutes deposition time respectively. This reduction in peak intensity could be attributed to the recombination with oxygen interstitials or migration into sinks [46]. According to Al Asmar, R., *et al*., the 580 cm^{-1} peak results from combination of the enhancement of electric field induced (EFI) via charge trapping at grain boundaries as well as presence of localized interface and/or surface phonon modes [48]. On annealing, the grain boundary density is gradually reduced with crystal growth. As a consequence, the charge trapping effect at grain boundaries vanishes as the annealing temperature increases. The EFI varies with deposition time and requires different temperature for different film thickness. This explains the reason behind the vanishing of the peak at 700 ˚C, 800 ˚C, and 900 ˚C for the corresponding deposition times of 1 minute, 5 minutes and 20 minutes, respectively.

On the contrary the peak intensity is enhanced with deposition time as shown is Figure 4-19.

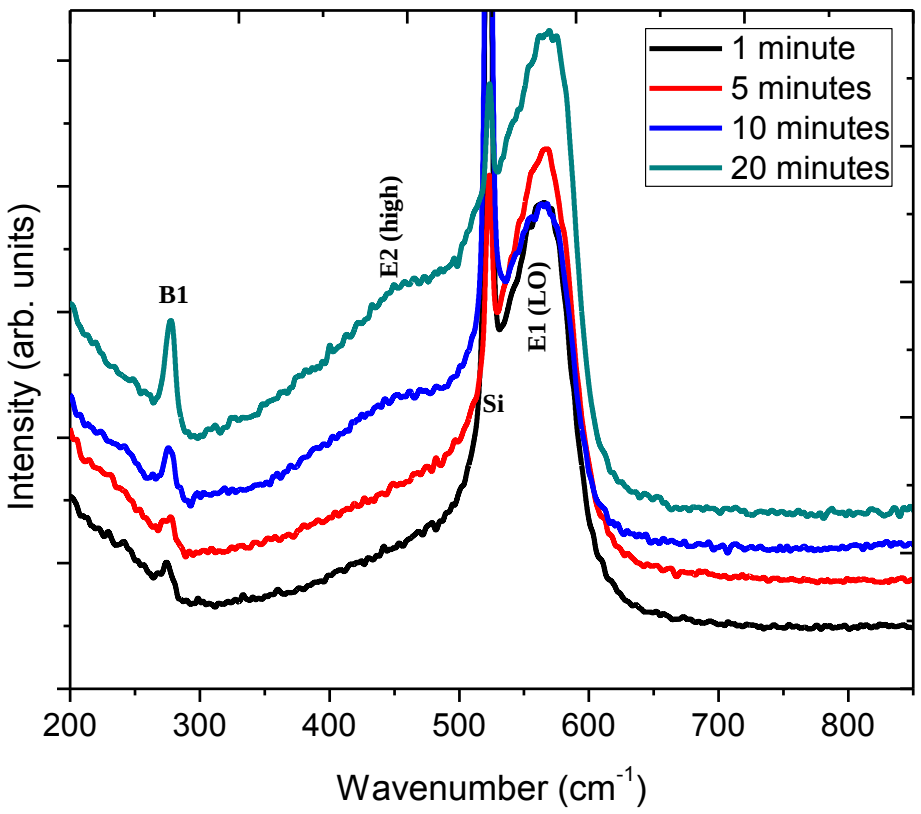


Figure 4-19: Raman spectra of ZnO thin film grown at 100 W for different time variation (1-20 minutes).

Upon increasing the deposition time the peak at 275 and 580 cm^{-1} both increases in intensity similar to an increase in RF sputtering power shown in Figure 4-20.

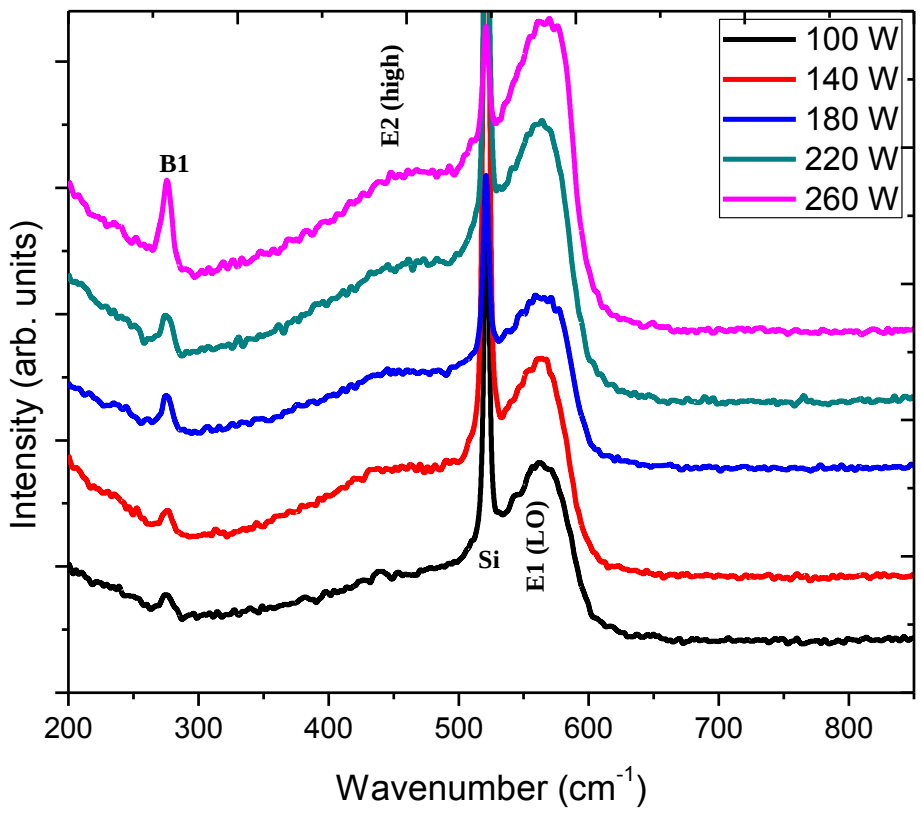


Figure 4-20: Raman spectra of ZnO thin film grown for 5 minutes at different RF power (100-260 W).

Figure 4-20 exhibits the distinct Raman peaks at 275 cm^{-1}, 522 cm^{-1} and 565 cm^{-1}. The sharp 522 cm^{-1} peak corresponds to the phonon of Si. The 275 cm^{-1} peak attributed to the B_1 silent inactive mode slightly shifts to 277 cm^{-1} and has increasing peak intensity as well with increasing deposition time. The shift of the peak position could be attributed to decrease in tensile strain. However the increase in defect level with 5 minutes time and RF power leads to increase in peak intensity. A similar trend is observed for the peak at 565 cm^{-1} which is gradually blue shift to 569 cm^{-1} for the film deposited for 20 minutes. This effect is also collaborated in the films fabricated at varying RF powers.

4.4.5. Photoluminescence studies

Photoluminescence studies were conducted at room temperature using a He-Cd (244 nm) laser as an excitation source on ZnO films deposited at room temperature and subsequently annealed in Ar filled furnace at different temperatures. In order to realize the optimum potential applications of the ZnO films, it is necessary to fabricated thin films with high-optical quality for strong UV luminescence. However, most of the as-grown films, irrespective of the growth conditions usually contain some type of native defects as well as structural defects. These defects may lower the UV emission efficiency and create luminescent centers in the visible range, thus limiting the applications of ZnO in optical device technologies [49]. In an effort to achieve an effective route towards enhancement of UV photoluminescence (PL), and gain further understanding of the defect dynamics involved in the process, this research focused on the effect of annealing on a wide range of the film's properties. Films of different thickness as determined by the deposition time were annealed between 600 – 900 ˚C.

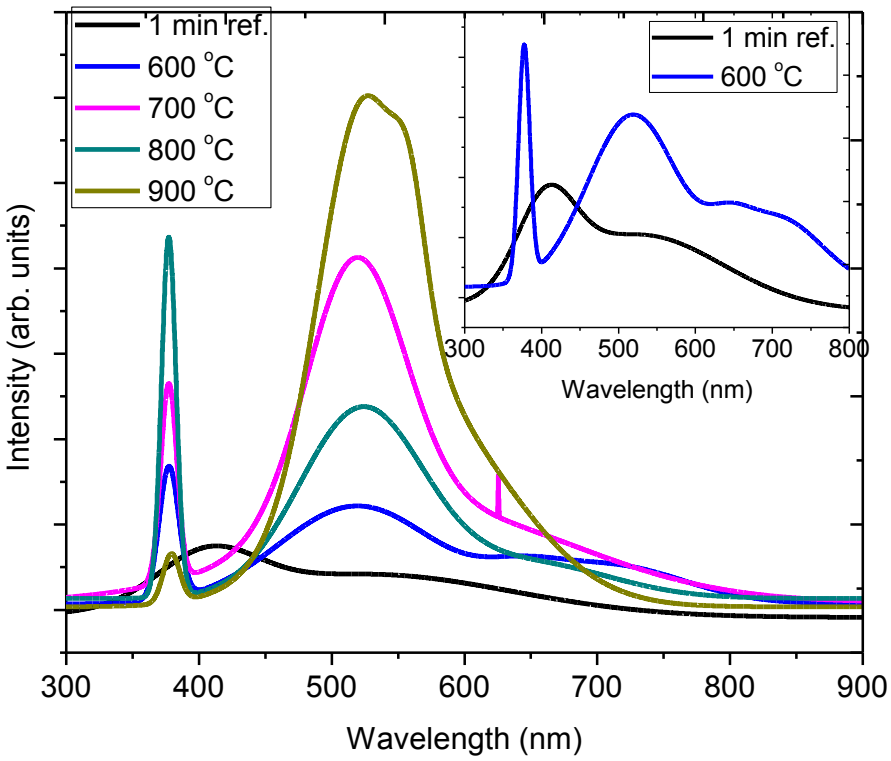


Figure 4-21: Room temperature photoluminescence study of ZnO films deposited on silicon substrate for 1 minute then annealed at 600-900 ˚C.

Typically, ZnO exhibit emissions in three optical ranges:

- near-UV (350–450 nm), associated mainly to the near band-edge (NBE),
- a broad deep-level (DL) visible emission (480–750 nm) associated to crystalline defects like vacancies and interstitial sites
- a near infrared (NIR) peak (750-800 nm). The NIR peak is usually as a result of the second-order grating diffraction of the UV emission band [50, 51].

At 1 minute deposition time, the NBE peak was observed at 412 nm while the deep level (DL) defect gave a yellow emission peak at 563 nm. On annealing at 600 ˚C, both peaks are blue shifted with the NBE peak appearing at 377 nm and the yellow DL peak emerging at 521 nm as a green emission. The blue shift is attributed to quantum size effects associated with the increase in the particle size as corroborated by the AFM and SEM results. This observation is in agreement with

the assertions due to A. van Dijken et al. [52], who established the dependence of the conduction band (CB_{edge}) and of the valence band (VB_{edge}) edges on the particle size. Essentially the absolute shifts of the band edges are expressed as a function of the particle radius *R* in the form:

$$CB_{edge} = E_g + \frac{h^2}{8m_e^* R^2} - \frac{0.9e^2}{4\pi\varepsilon_o\varepsilon_\infty R} \quad \text{..... 4-6}$$

$$VB_{edge} = \frac{h^2}{8m_h^* R^2} - \frac{0.9e^2}{4\pi\varepsilon_o\varepsilon_\infty R} \quad \text{..... 4-7}$$

Where *Eg* is the band gap, *h* is Planck's constant, m_e^* is the effective mass of electron which is 0.28 m_e, m_h^* is the effective mass of hole which is 0.50 m_e for ZnO. The difference in effective masses of the charge carriers results in variation in size-dependent shifts for both band edges.

The intensity of the DL peak increases while the peak narrows in width with increasing temperature. This is plausible as annealing in argon ambient for which more oxygen vacancies are formed. The NBE intensity also increases with an increase of annealing temperatures at temperature range of between 600-800 ˚C. According to Hsieh, P. T., et al., [53] the intensity of this NBE emission peak is also dependent on the grain and crystal orientation. As annealing temperature increases, there is a reduction in the grain boundaries and the number of particles on the surface of ZnO nanoparticles. Consequently, the number of non-radiative transitions and deep level defects may be both suppressed leading to an increase in the NBE emission intensity [54]. At 900 ˚C, there was a sudden drop in the intensity. Other researchers have reported that peaks at NBE are due to the existence of interstitial Zn^+ ions and the drop could be attributed to less existence of the interstitial Zn^+ ions [55]. Table 4-10 shows the peak position for thin films grown at different deposition times and annealed between 600-900 ˚C.

Table 4-10: Peak positions of the NBE and DL emission peaks.

Deposition time	Temperature	NBE (nm) Peak centre	DL (nm) Peak centre
1 minute	as deposited	412	563
	600 ˚C	377	521
	700 ˚C	377	521
	800 ˚C	377	523
	900 ˚C	378	528
5 minutes	as deposited	457	
	600 ˚C	383	430
	700 ˚C	380	437
	800 ˚C	377	466
	900 ˚C	380	507
20 minutes	as deposited	488	
	600 ˚C	381	544, 690
	700 ˚C	381	526, 664
	800 ˚C	381	426, 525,680
	900 ˚C	422	514, 556,614
Deposition Time variation	1 minute	378	521
	5 minutes	378	437
	10 minutes	376	449, 575
	20 minutes	381	415, 518, 662

The last 4 columns indicated the PL characteristics for thin films deposited over different duration without any annealing.

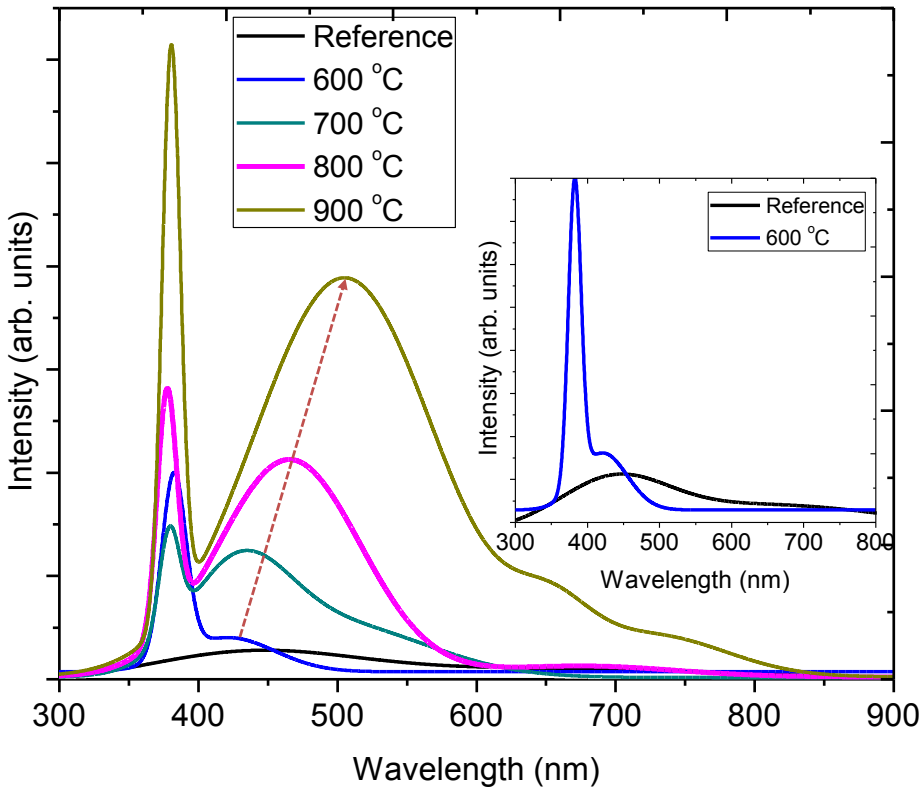


Figure 4-22: Room temperature photoluminescence study of ZnO films deposited on silicon substrate for 5 minutes then annealed at 600-900 ˚C.

For a 5 minute deposition time, the NBE emission of the as-deposited film was found to be at 457 nm with DL emission (expected at 430 nm) was barely visible. On annealing at 600 ˚C the NBE peak is blue shifted to 383 nm and further to 380 nm and 377 nm upon annealing at 700 ˚C and 800 ˚C respectively. At 900 ˚C, the peak relaxes back to 380 nm. Since the built-in strain in ZnO is tensile, it is expected that at 900 ˚C there is sufficient thermal activation to relax the tensile strain in the ZnO film. This causes a decrease in the band gap as evident from the shift in the near band edge emission peak. Moreover, the decrease in band-gap energy at 900 ˚C could also be possibly attributed to the removal of oxygen vacancies. This is holds true as the reduction in carrier density is removed by the annihilation of the oxygen vacancies in a manner related to the Burstein–Moss shift [56]. The peak intensity also shows a general increasing trend with temperature, an indication

of increased interstitial Zn^+. Compared to the film deposited at 1 minute, no drop in interstitial Zn^+ is observed at 900 ˚C. The centroid of the green emission peak is gradually red shifted with the annealing temperature range of interest (600-900 ˚C). This is indicated using an arrow in figure 4-13. This red shift can be partially explained by the shrinkage of the energy band gap with an increase in particle size as suggested by van Dijken et al. and by Wu et al [52, 57]. The shift to lower energies as the particle size increases as a result of quantum size effect related to the confinement of the charge carriers. The gradual increase in the green emission peak is consistent with literature reports showing that higher temperature results in a rapid increase in V_O^+ and O_i^- ion centers [34, 57].

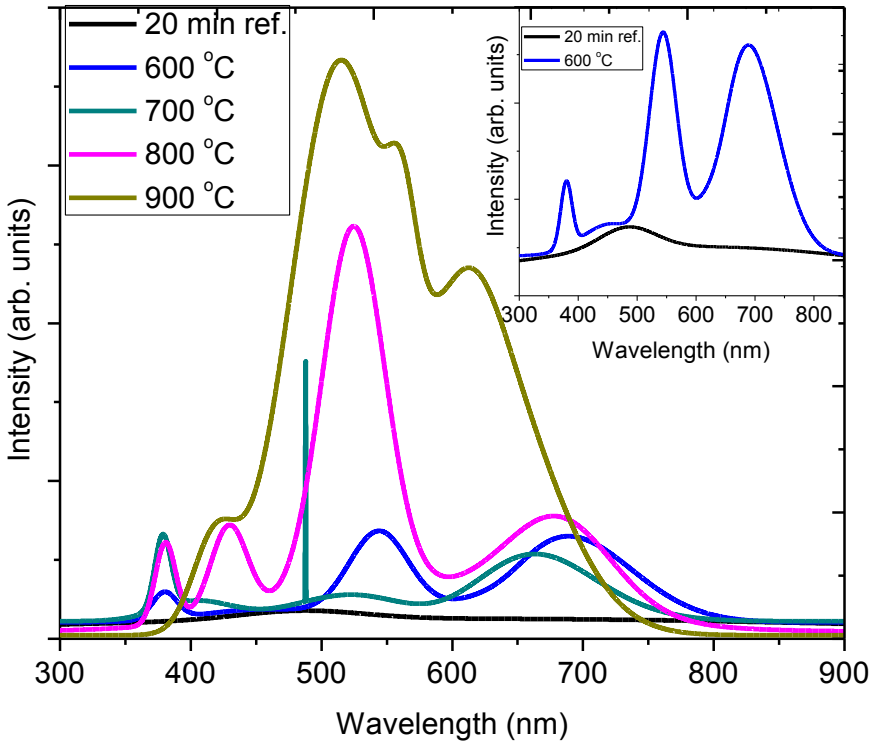


Figure 4-23: Room temperature photoluminescence study of ZnO films deposited on silicon substrate for 20 minutes then annealed at 600-900 ˚C.

At 20 minute deposition time, PL spectra of the ZnO films shown in figure 4-23 generally exhibited four peaks, namely;

- UV (NBE) emission peak around 488 nm,
- Green-yellow luminescence,
- Orange band luminescence and
- Red luminescence.

The as deposited ZnO films exhibit a low intensity NBE centered at 488 nm with broad DL emission peaks. The NBE emission is blue shifted from 488 nm to 381 nm and 378 nm, after annealing at 600 ˚C and 700 ˚C, respectively. At 900 ˚C, the additional orange band centered at 614 nm is observed. This may be attributed to either the presence of excess local oxygen or structural imperfections [58]. These lattice imperfections arise from the large lattice mismatch and compressive force between the film and the substrate. This is seen from the large variations in their thermal expansion coefficients. There are additional red emission bands centered at 690 nm, 664 nm, and 680 nm after annealing the films are annealed at 600 ˚C, 700 ˚C, and 800 ˚C, respectively. The sputtered ZnO films exhibit n-type conductivity, and hence the red and IR emission bands [59, 60]. According to Xu, Linhua, *et al*., this band has been associated with oxygen interstitial defects [61] while Koyano, M., *et al.*, suggest that it is due to the donor- to the acceptor-center transition (DA mechanism) a process rather similar to self-activated emission. Its broad bandwidth suggests that its related energy levels are of the nature of deep donor- and/or accepter centre that exhibits stronger electron-phonon interaction. [60]. Its intensity increased with the deposition temperature.

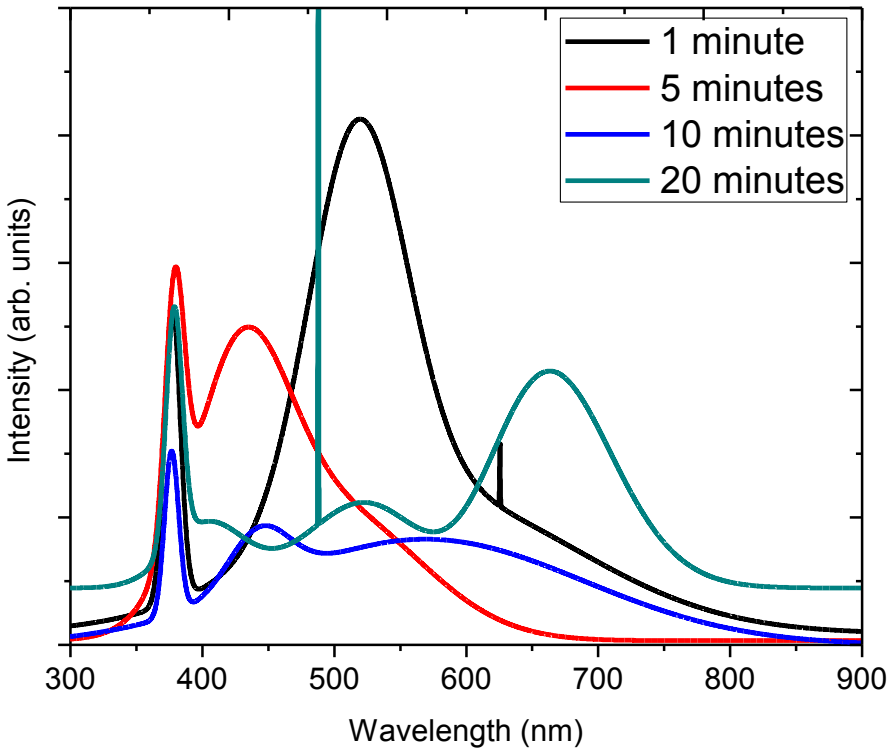


Figure 4-24: Room temperature photoluminescence study of ZnO films deposited on silicon substrate at different deposition time then annealed at 750 ˚C.

Figure 4-24 shows the room temperature PL of films with varied deposition time then annealed in Ar ambient at 750 ˚C. At 1 minute deposition time, the NBE band is centered at 378 nm while the DL is at 521 nm. For 5 minute deposition, the NBE remain unshifted while the DL is blue shifted to 437 nm, an indication of particle size growth. At 10 minutes deposition time there are two DL peaks centered at 449 nm and yellow peak at 575 nm while 20 minutes deposition time produced films with 4 PL peaks centered at 381 nm, shoulder at 415 nm, 518 nm and red band at 662 nm. The emergence of additional peaks may be attributed to lattice imperfection are as a result of the large lattice mismatch and compressive force on the film from the substrate due to differing thermal expansion coefficients which tend to increase with film thickness as deposition time increases.

4.5. The Effect of the Oxygen Concentration on the Zinc Oxide Films

In order to obtain stoichiometric ZnO film, it is necessary to optimize the concentration of O in the film through the introduction of oxygen gas at optimized flow rates in the argon plasma during sputtering. The ZnO thin films were later deposited in an oxygen and argon ambient, to compensate for the oxygen vacancies that annihilate hole concentrations. This was performed by varying the Oxygen partial pressure at constant Ar flow rate during deposition. The deposition rate have been observed to vary with the O_2 flow rate for ZnO. It has been reported that the addition of Oxygen during RF sputtering process is essential for obtaining n-type semiconducting ZnO film. The absence of oxygen or excess thereof can make the ZnO film either metallic or insulating [62]. An increase of the oxygen flow rate in the working gas reduces the number of incident Ar atoms which can transfer their high energy to the target. Therefore, the growth rate for ZnO films decreases with increasing oxygen concentration. In this work, instead of oxygen partial pressure, the oxygen flow rates are varied directly and their influence on photoluminescence properties of ZnO are discussed.

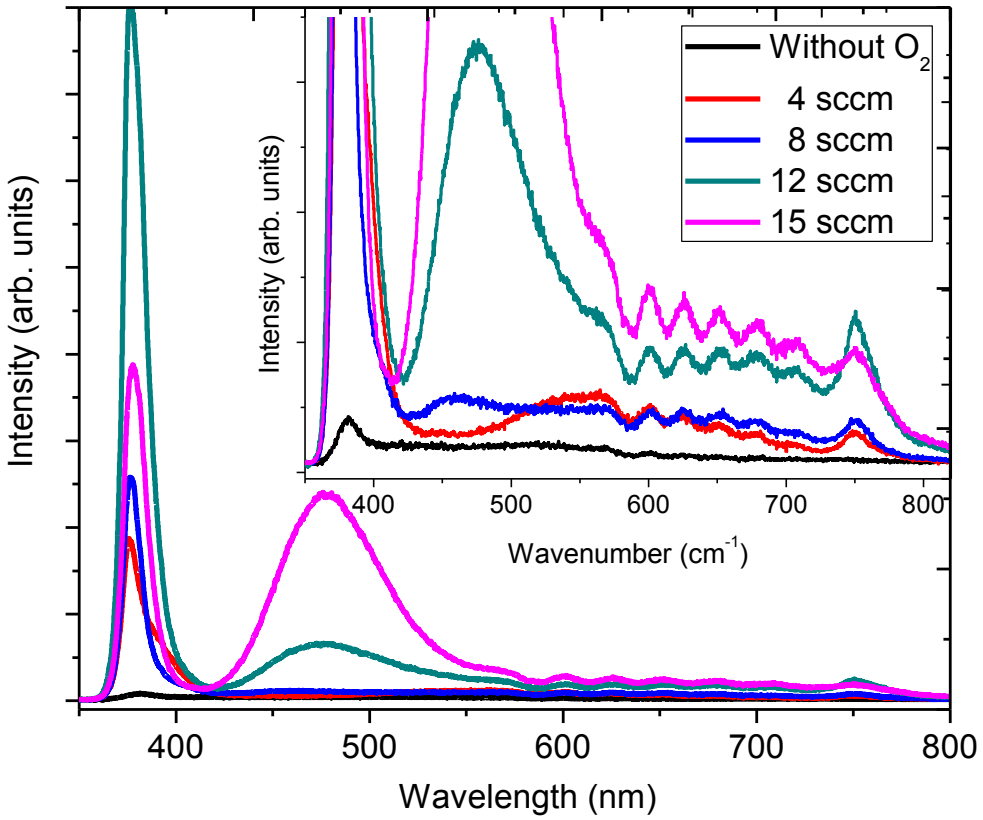


Figure 4-25: Room temperature photoluminescence study of ZnO films deposited on silicon substrate at constant Argon flow rate of 13 sccm but varied Oxygen flow rate (0-15 sccm) then annealed at 700 ˚C in Ar ambient.

Yang Bing-chu et al. [63] summarizes the dependence of the concentration of ZnO thin films' intrinsic defects on the variation of oxygen partial pressure in Table 4-11 below.

Table 4-11: Intrinsic defects concentration against oxygen concentration variation.

$n(O_2)$	$n(V_O)$	$n(Zn_i)$	$n(Zn_O)$	$n(V_{Zn})$	$n(O_i)$	$n(O_{Zn})$
↑	↓	↓	↓	↑	↑	↑

Where n denotes concentration; "↑" denotes increasing while "↓" denotes decreasing.

The films deposited in the presence of Argon only showed a NBE band at 381 nm and DL band at 522 nm. On introduction of Oxygen at 4 sccm into the chamber, the NBE band was blue shifted to 378 nm while the DL band was red-shifted to 548 nm. The NBE band gradually increases in

intensity with an increase in oxygen concentration to a maximum limit at 12 sccm. This is consistent with the findings of Abdallah, B *et al.* [64] who considered the UV intensity emission as an indicator to the nature of crystallinity of ZnO film, and hence the higher the crystallinity, the higher the UV (NBE) emission intensity [34, 65]. The green emission (DL) is observed to gradually increase in intensity with increasing Oxygen concentration. From table 4-11, It is noticeable that only the concentrations of zinc vacancy, interstitial oxygen and antisite oxygen increase with increasing oxygen partial pressure and therefore the increasing DL intensity may be attributed to increasing zinc vacancy, interstitial oxygen and antisite oxygen [63].

Several oscillations/band were also observed at 598 nm, 623 nm, 651 nm, 680 nm, 707 nm and the most intense at 752 nm. These bands/oscillations were also observed by Lauer, R. B [58] for films grown in oxygen rich environment and attributed them to either the presence of excess local oxygen or structural imperfections. On the other hand Alvi, N. H., *et al.*, suggest that the red emission in the range of 620 nm (1.99 eV) to 690 nm (1.79 eV) may be attributed to O_i while that in the range of 690 nm (1.79 eV) to 750 nm (1.65 eV) can be attributed to V_o [66].

Xu, Linhua, et al., classify Oxygen vacancies into three different charge states: the neutral oxygen vacancy (V_O^0), the singly ionized oxygen vacancy (V_O^+), and the doubly ionized oxygen vacancy (V_O^{++}) and that the red emissions in the 690-750 nm wavelength range are highly intense as a result of the transition of electrons from the conduction band to V_O^{++}. The suggested schematic diagram for red emission mechanism is shown in Figure 4-26.

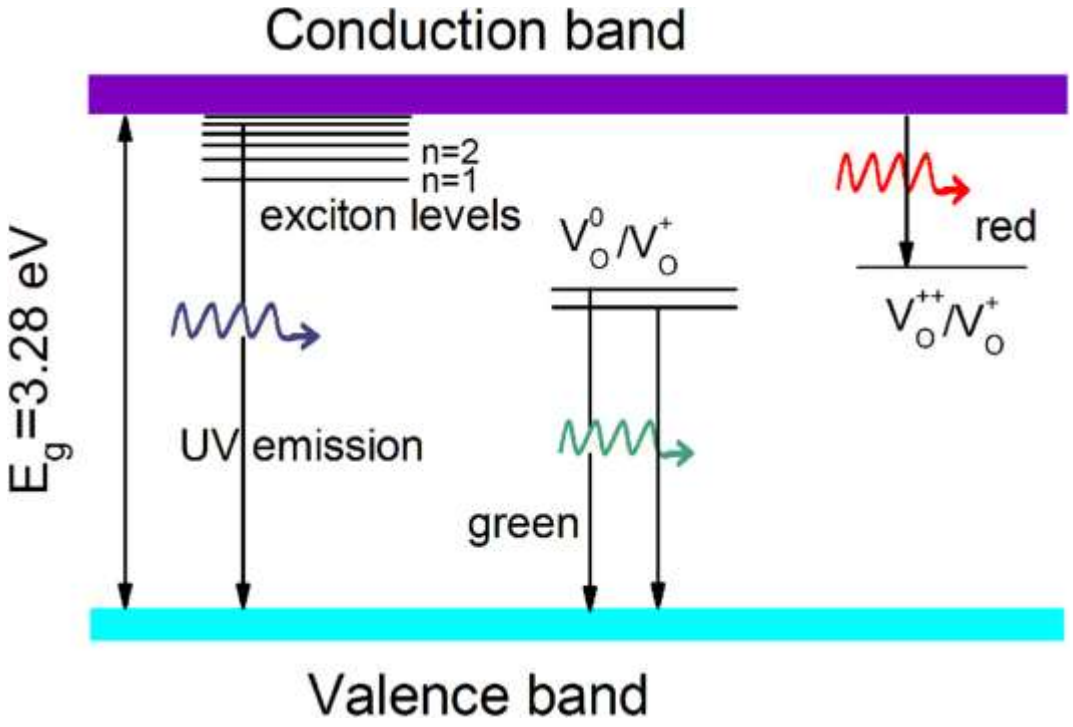


Figure 4-26: The schematic diagram of the suggested emission mechanisms of green and red light in ZnO thin films adapted from ref. [61].

The density of the V_O^{++} is affected by many factors in the film. Such factors include ZnO grain size, thickness of the thin film layer, grain boundary density and other defects around V_O^+. With the co-existence of numerous types of point defects in the ZnO thin films, the visible emissions originating from these different point defects may become competitive. As a result of the above factors the V_O^{++} may not necessarily be a light-emitting center or a dominant light-emitting center and this explains why the extra red emission seen here in oxygen rich environment is rarely observed in ZnO materials [61].

4.5.1. Raman studies on oxygen variation.

Figure 4-27 shows Raman measurements in the backscattering geometry that were used to identify the Raman active modes with variation in oxygen concentration at a constant Ar flow rate of 13 sccm. ZnO grown by RF sputtering exhibits a wurtzite structure with four atoms per unit cell giving rise to 12 phonons, 9 optical and 3 acoustic namely: longitudinal acoustic (LA), transverse-acoustic (TA), longitudinal-optical (LO), and transverse-optical (LO) branch. The A1 and a doubly degenerate E1 branch are Raman and infrared active, while the two double degenerate E2 branches (nonpolar) are Raman active only [67]. The E_2 low mode is associated with the vibrations of the Zn sub-lattice, while the E2 high mode is associated with phonon vibrations corresponding to the sub-lattice with oxygen atoms only [68]. The B branches are always inactive.

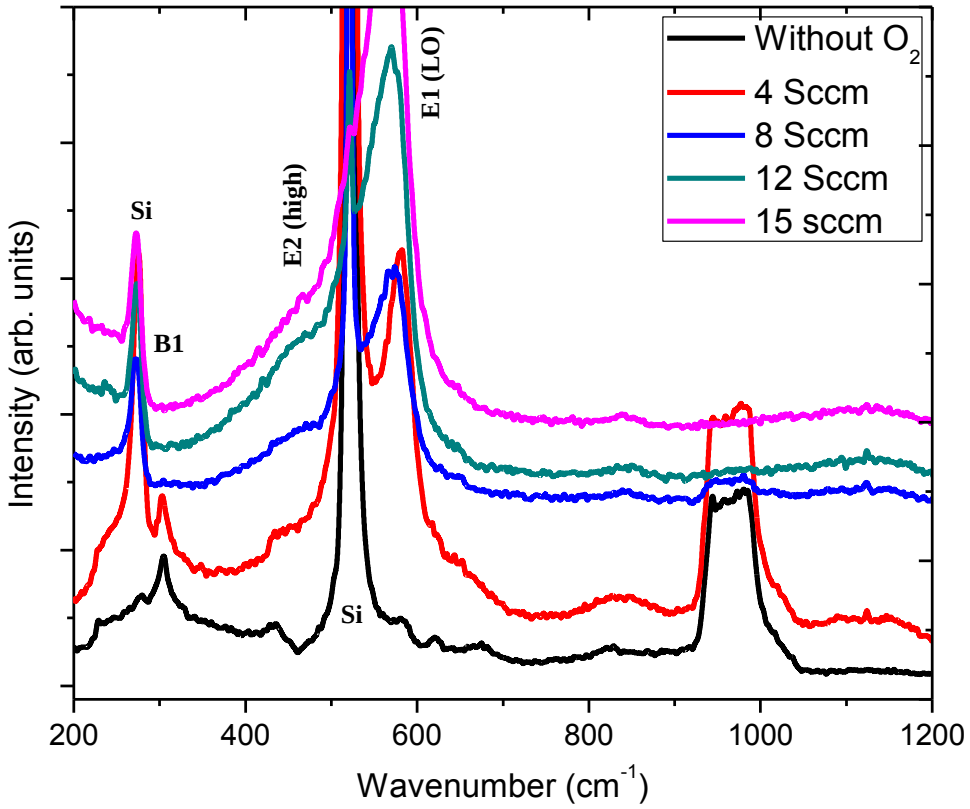


Figure 4-27: Raman spectroscopy of unannealed ZnO thin films grown at different O_2 concentration.

At 0 sccm O_2 flow, the Raman peaks were observed at 272 cm^{-1}, 303 cm^{-1}, 435 cm^{-1}, 522 cm^{-1}, 581 cm^{-1}, and a broad peak stretching from 941-1092 cm^{-1}.

The peak near 272 cm^{-1} could be attributed to the B1 silent inactive mode while that near to 435 cm^{-1} is the Raman active phonon mode E2 (TO). The additional mode observed around 581 cm^{-1} corresponds possibly to the E1 (LO) branch [47]. These optical phonon modes confirm that the RF magnetron sputtered polycrystalline thin films have the wurtzite hexagonal phase. Our results conform to the work of Tzolov, M., et al. [42] in which the bands near 272 and 581 cm^{-1} are common ascribed to ZnO thin films and not single crystal and sintered polycrystalline ZnO The absence of these modes in the latter materials is associated with the electric field formed in the depletion region which acts as a charge trap for free carriers. These traps can assume several formats such as defect interface states or as ionized adsorbates at the grain boundaries that leads to the enhancement of the intensity of the LO band and the silent mode. Additionally the enhancement of the peak intensity is further observed during the compensations of oxygen defects through increasing Oxygen flow rates [69, 70].

From the Raman spectra, the intensity of the 272 and 581 cm^{-1} Raman bands are seen to increase with increase in Oxygen concentration, an indication of enhanced charge trapping which is in agreement with equation 4-9. The increase in intensity is even more enhanced when the films are subjected to annealing in Ar ambient at 700 ˚C for two hours as shown in figure 4-26.

The Raman peaks at about 435 cm^{-1} is assigned to the non-polar optical phonons E_2 (high) modes of the ZnO thin films. This peak intensity reduces as Oxygen concentration increases and red shifted with annealing at 700 ˚C as shown in figure 4-28. The vanishing of this peak at 435 cm^{-1} at 8 sccm is an indication that the oxygen-rich environment plays a great role in reducing the defect states. On the other hand, the red shifting with annealing at 700 ˚C shows a change in stress within

the films. As temperature increases the compressive stress decreases while tensile stress increases causing oxygen out-diffusion and reduction in zinc interstitials by desorption [71].

The peaks at about 303, 522 and 960 cm^{-1} are attributed to the optical phonon modes of the silicon substrate. Silicon possesses the diamond structure O_h^7 (Fd3m) and therefore has only one first-order Raman-active phonon of symmetry Γ_{25} which is located at the Brillouin-zone center. The first order Raman (stokes) spectrum consists of one strong peak at 522 cm^{-1} arising from the creation of the triply degenerate, long wavelength transverse optical phonon (TO) [72]. The second order Raman (2TO mode) is observed around 941-1092 cm^{-1} and in our thin film material it is attributed to the convolution of the second order Raman bands of the ZnO thin films with the silicon substrate. This peak is not present with an increase in Oxygen concentration, an indication of the improvement in the film quality in comparison with that obtained under 100% Argon. The same is observed for the peak at 303 cm^{-1}.

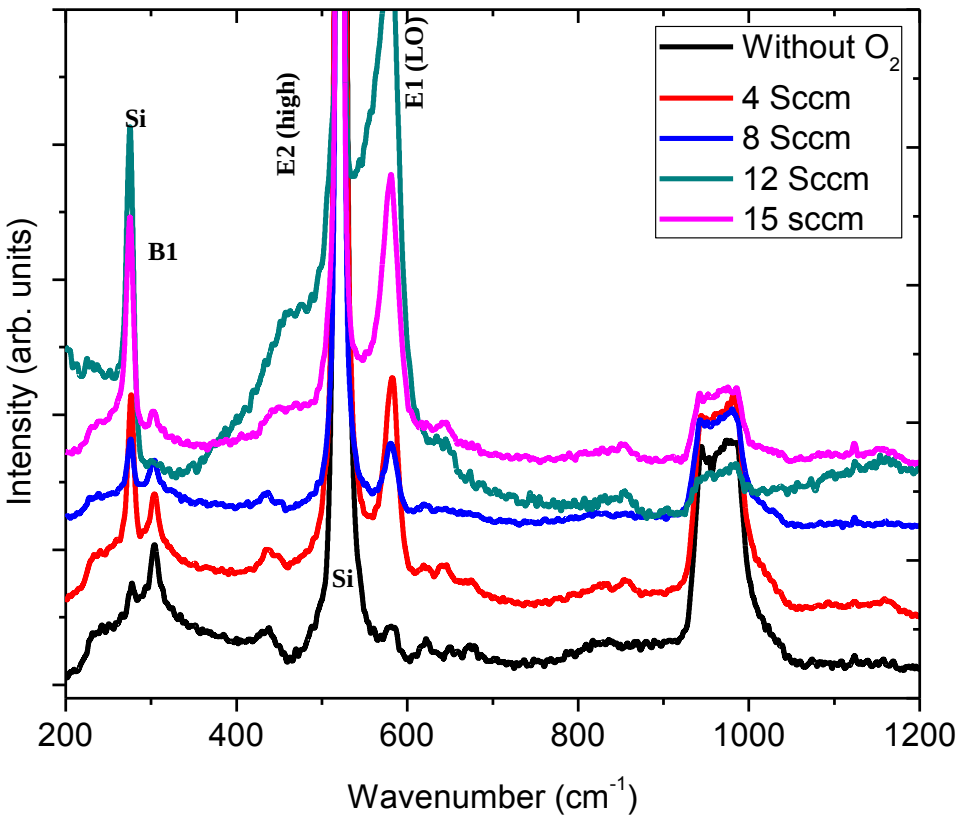


Figure 4-28: Raman spectroscopy of ZnO thin films grown at different O_2 concentration then annealed in Ar filled furnace at 700 ˚C.

Figure 4-28 shows the Raman spectra of ZnO thin films grown under different Oxygen concentrations (0-15 sccm) and subsequently annealed under Argon ambient at 700 ˚C. Upon annealing of the films at 700 ˚C, the Raman peaks at 303 cm^{-1} and 941-992 cm^{-1} re-emerge. The annealing usually leads to an increase of the resistance of the thin films and the decrease of the free carrier absorption due to the reduced band bending within the crystallites. The effect of the built-in field will subsequently reduce the Raman scattering. At high temperature we may find combinations of acoustic and optical branches [42].

4.5.2. VIS/NIR Analysis studies on oxygen variation

Figure 4-29 shows reflectance measurements obtained from FR-Basic-Vis/NIR spectroscopy over a wavelength range of 450-900 nm. Whenever electromagnetic wave crosses the interface between two different materials, fraction of light is reflected by the inner surface while some amount is refracted through the inner surface and finally transmitted [73].

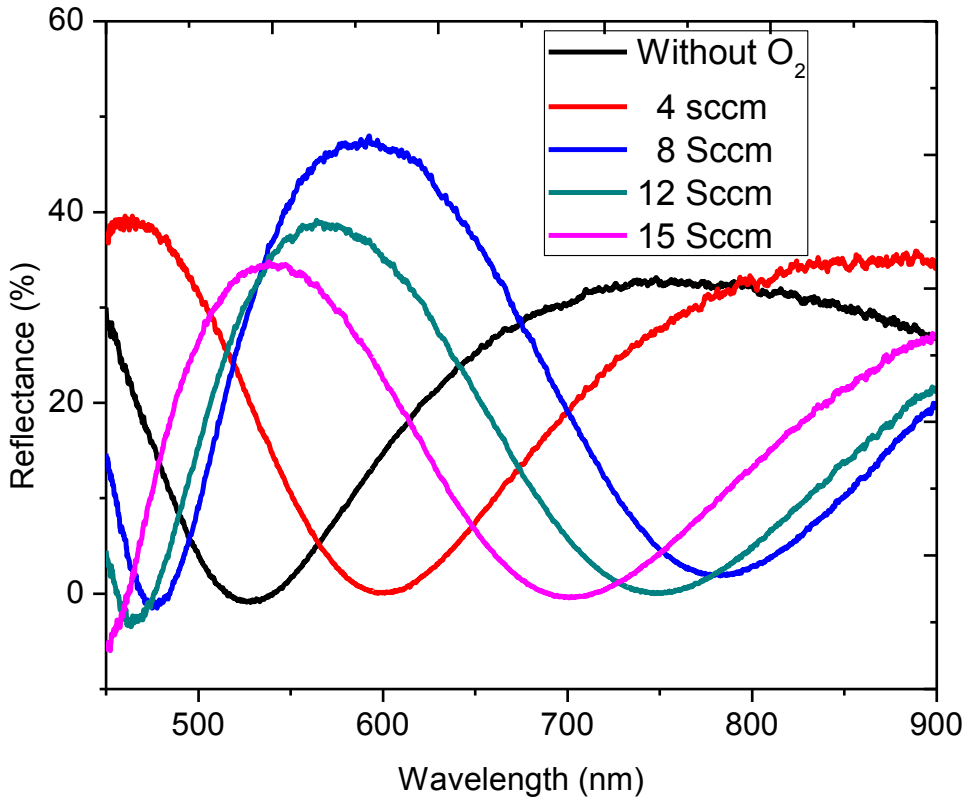


Figure 4-29 Optical reflectance spectrum of ZnO thin film deposited using different oxygen flow rates into the RF chamber.

Figure 4-29 shows the optical reflectance spectra of ZnO films grown with different oxygen flow rate into the RF chamber over spectral range 450–900 nm. The well-developed interference patterns are an indication that the films are specular to a great extent. Interference fringes with minima and maxima as a result of interference fringes brought about by multiple reflections of light occurring between the lower surface in contact with the substrate and the free surface of the

layer are reported. The shifting of these minima and maxima is indication of varying film thickness as reported by the peak fitting shown in figure 4-30. The fitting was carried out using FR tool software with high accuracy (<0.2% error).

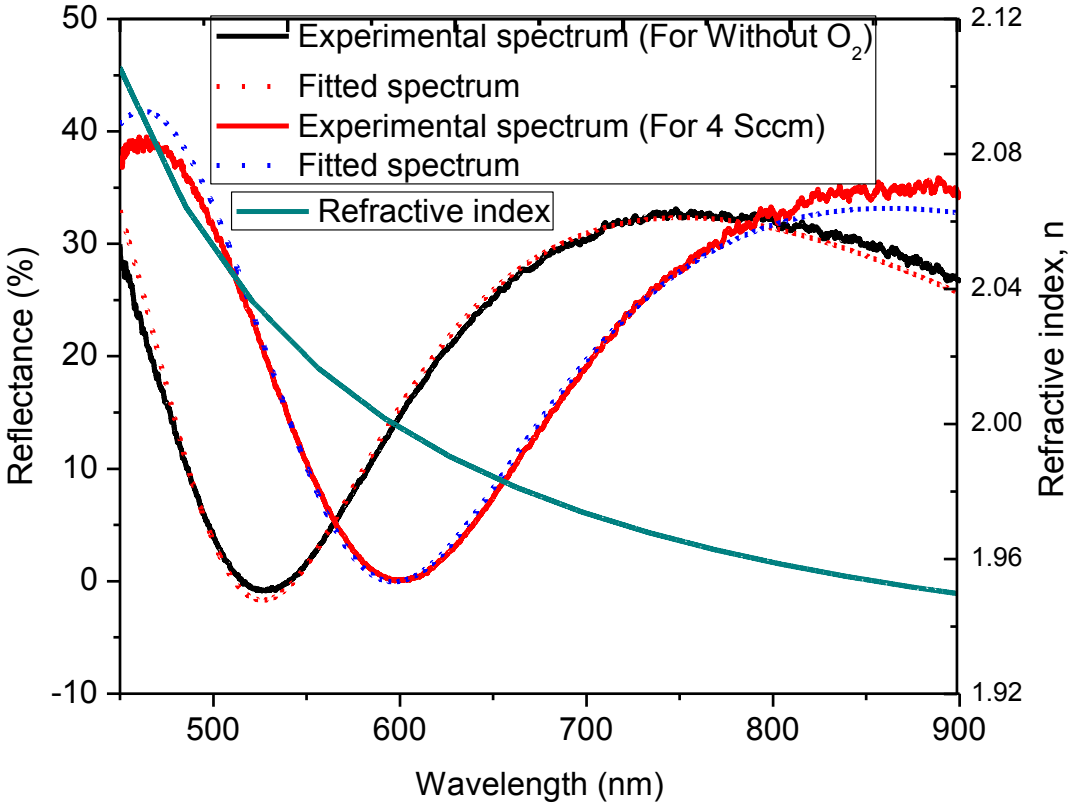


Figure 4-30: Spectrum fitting to derive thickness of the film and refractive index.

From the graph fitting shown in figure 4-30, the film thickness variation, an indication of varying deposition rate at different Oxygen flow rate into the chamber was calculated and results depicted in figure 4-31.

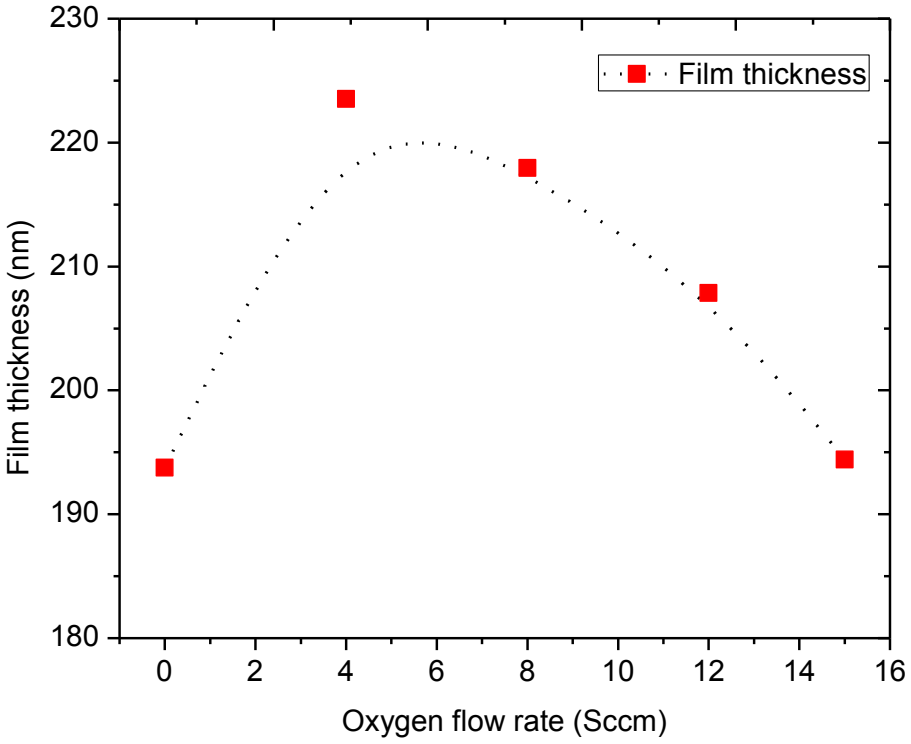


Figure 4-31: Film thickness variation with oxygen flow rate.

Thickness of the films deposited without Oxygen into the chamber was 193.8 nm. Upon introduction of oxygen at a rate of 4 sccm, the thickness first increased to 223.5 nm. This indication of increased deposition rate could be as a result of rapid oxidation of the target and since the oxides targets have a higher secondary electron yield compared to the metal targets, this could have resulted into more ionization of the sputtering gas hence an increase in the deposition rate [74]. The oxidation reaction likely to take place at the substrate surface as described by equation: $2Zn + O_2 = 2ZnO$ [75]. At this oxygen flow rate we observe highest peak intensity and minimum FWHM in the XRD analysis implying highest film crystallinity, this is because at this point the species deposited on the substrate are fully oxidized hence Zn:O ratio may be stoichiometric. At 8, 12 and 15 sccm there was a general decrease in film thickness to 217.9 nm, 207.8, and 194.4 nm respectively, an indication of declining rate of deposition. This reduction in the deposition rate can be explained in two aspects. The first scenario is that the further increase in the oxygen

concentration forms a surface layer of adsorbed oxygen, which prevents the sputtering of the atoms of the target used and thus reduces the deposition rate. The second as reported by Furuta, M. (2013) [76], as the oxygen concentration increases in the chamber, the concentration of the heavier Ar atoms decreases which could negatively affect the deposition rate. According to Tominaga, Kikuo, et al, [77] oxygen in the RF plasma exists as negative ion, which contributes to a neutralization of the plasma on the way to the anode [78]. This electron-negative species nature of oxygen may also lead to higher electron-temperature plasma [78]. The increase in the plasma neutralization with oxygen concentration results in decrease in the amount of Ar ions and hence a decrease in the deposition rate.

4.6. Application of ZnO thin films into perovskites solar cells

As a proof of concept, ZnO thin films were used as an electron transport layer to fabricate a perovskites solar cell whose working principle is described in section 2.9.8.2.

4.6.1. Preparation procedure

CH_3NH_3I was first prepared using equimolar CH_3NH_2 and HI. The HI was added drop-wise to a round bottom flask in an ice bath while stirring (orange solution); the sides of the flask were washed down with deionised water. The reaction was allowed 2 hours at 0 ˚C. Once complete, a rotary evaporator was utilised to supersaturate and crystallise the solution (controlled from 60 to 80 ˚C, 1 hour). The crystallites were dried at 80 ˚C for 1 hour, washed with diethyl either (20ml x 3) then dried overnight at 100 ˚C. For the deposition of the $CH_3NH_3PbI_3$ thin film, a precursor solution was prepared by dissolving 368.8 mg of PbI_2, 127.1 mg of CH_3NH_3I overnight in 1 ml of γ-butyrolactone while stirring at 40 ˚C. For each sample 80 µl of precursor was spin coated onto

clean ITO glass with RF sputtered ZnO (At room temperature using RF power of 100W) in a two stage process, 1000 rpm for 10 s then 5000 rpm for 40 s. During spinning 30 s into the second stage 80 µl of toluene was added as an antisolvent. The resulting film was then annealed at 100 ˚C for 10 min before spin coating hole transport layer (P3HT). The resulting film was then placed into a thermal evaporator for metallization with 200 nm Au film which was evaporated as the top electrode for device structure described in figure 4-32 as adapted from Ref [79]. The device was then annealed at 300 ˚C under Ar to improve the contact properties before characterization. The results of the device electrical characteristics are reported in the subsequent sections.

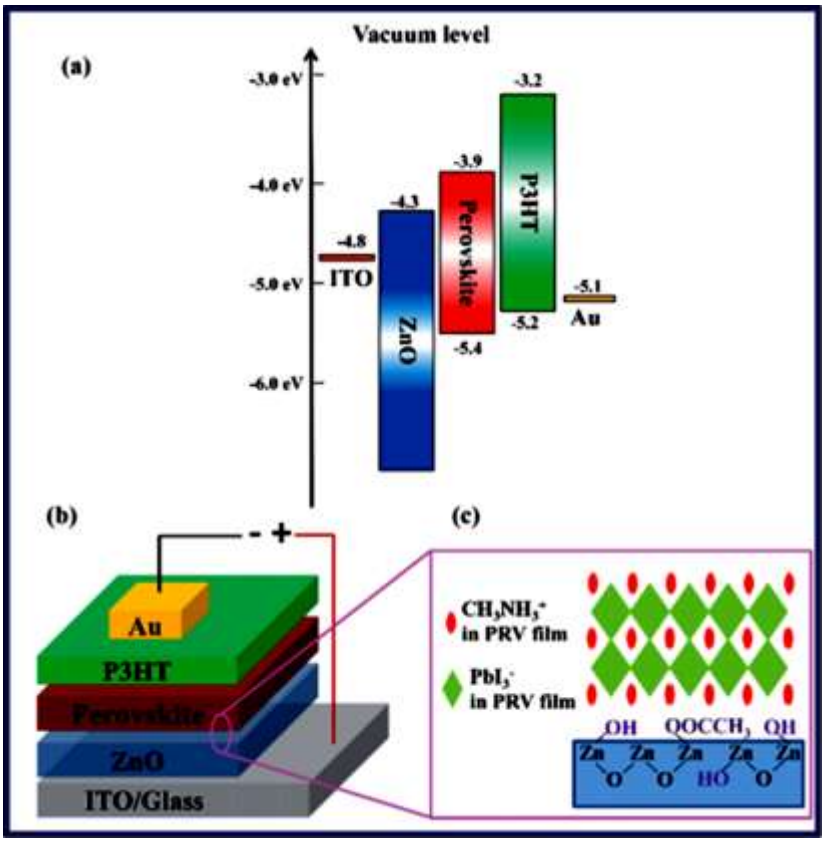


Figure 4-32: Energy level diagram and device structure of perovskite solar cells. (a) Energy diagram of individual layers used in perovskite devices. (b) Perovskite device structure. (c) Surface groups on the ZnO film and the crystalline structure of perovskite cry stalline structure of perovskite crystals.

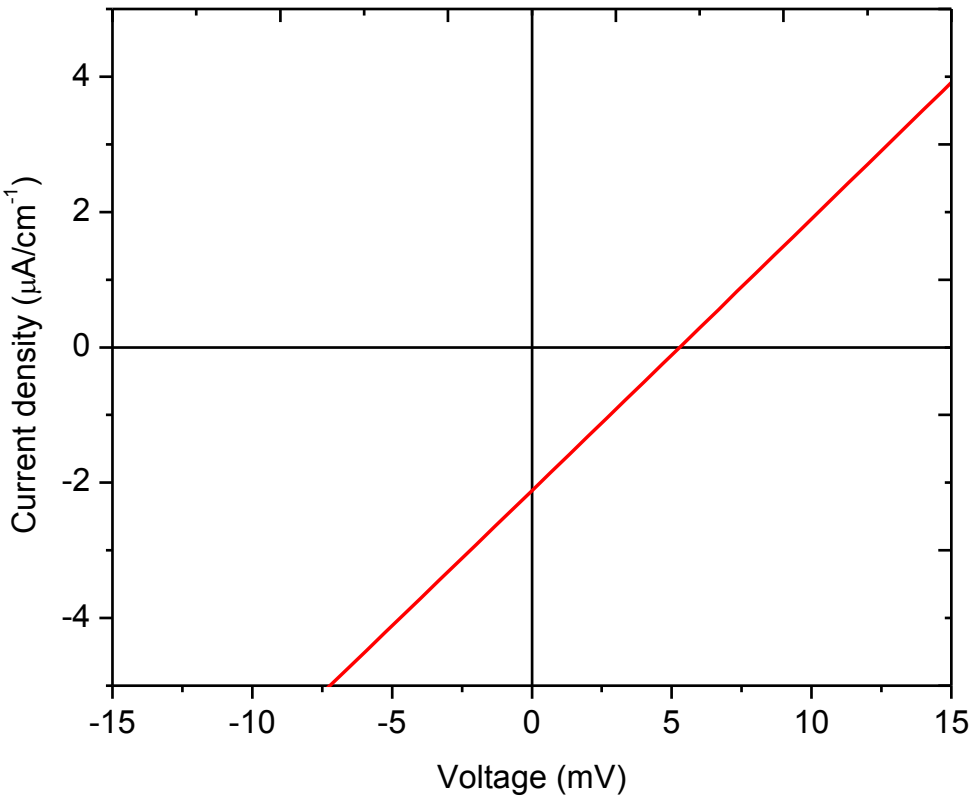


Figure 4-33: J-V characteristics of perovskites solar cell composed of ZnO as electron transport layer.

The perovskite solar cell device with ZnO as electron transport layer yielded low performance as shown in figure 4-33. The *Jsc* = 2.89 μA cm^{-2}, V_{oc} = 5.28 mV and *FF* = 23.3 %). These values are relatively low and could be as a result of exposure of the materials to air. These in some cases have been attributed to low conductivity and high resistance of the perovskites as well as its rapid degradation when exposed to the air.

4.7. Conclusion

In the present work, ZnO thin with varied thicknesses and annealed at different temperatures were prepared by RF magnetron sputtering technique on a silicon substrate. The pressure in the vacuum chamber during deposition was lower than $1 \cdot 10^{-5}$ Pa. The surface structure and morphology were investigated as a function of deposition rate and post-deposition annealing temperatures over a

wide range of temperature from 600-900 ˚C. SEM imaging of the as-prepared films reveals a grainy structure, with the grain size and overall roughness being strongly dependent on the deposition rate and annealing temperatures. Quantitative AFM characterization reveals a strong dependence of the surface roughness of the deposited films on the deposition rate and annealing temperature as well. The dependence of the grain size and surface roughness on the deposition rate and annealing temperature were attributed to three main factors: (1) the characteristic features of the island growth mode (surface diffusion of adatoms, nucleation and coalescence of Zn clusters); (2) influence of the residual gases (in particular oxygen), which can be incorporated into the film during deposition, on the grain growth; (3) the surface morphology of the corresponding bare substrates. Smaller values of skewness (R_{sk}) for the film was observed and was attributed to more symmetric surface while from both Skewness and kurtosis, the surfaces are generally spiky with dominant peaks.

Homoepitaxial growth of ZnO was achieved within individual *c*-axis oriented columnar grains using sputter deposition. Lower deposition time/power and low annealing temperatures gave higher crystal quality within the grains, but the crystallite sizes increased with increasing deposition time/power and annealing temperatures. XRD revealed a low magnitude of strains and stresses with high crystal quality. All the diffraction peaks can be well indexed to the wurtzite structure of ZnO of the space group P63mc, which is consistent with the standard values reported in JCPDS, card no. 003-0888. The PL results generally revealed a lower concentration of defects contributing to non-radiative recombinations in the near-band edge region, while an emerging peak related to deep level emissions pointed toward higher incorporation of deep level defects which varied with deposition time/power and annealing temperatures.

The residual stress in the as-grown ZnO film was evaluated from the position of the E_2 (high) Raman active mode. This stress was found to disappear upon annealing which was in agreement with the XRD findings. On the one hand the increase of grain size and the reduction of O vacancy and Zn interstitial lead the vanishing of the 574 cm^{-1} as seen in figure 4-18.

The structural and optical properties of as-deposited ZnO films were also found to depend on the strongly dependent on the Ar/O_2 ratio. The ZnO films had a hexagonal wurtzite structure and the crystallinity improved whereas the *c*-axis crystalline size increases with the increase of oxygen ratio. From optical analysis, the film thickness first increased as a result of the ZnO oxidization then assumes a decreasing trend. We have also shown that the growth conditions has a strongly influence on the emission characteristics of ZnO films grown by rf magnetron sputtering. Perovskite solar cell incorporating ZnO thin film was fabricated and tested in air, however it was a great challenge to obtain a working device and they showed a mere ohmic behavior. This could be attributed to exposure of the perovskites molecules to moisture making them readily oxidize.

4.8. References (for chapter 4)

[1] Ü. Özgür, Y.I. Alivov, C. Liu, A. Teke, M. Reshchikov, S. Doğan, V. Avrutin, S.-J. Cho, H. Morkoc, A comprehensive review of ZnO materials and devices, Journal of applied physics, 98 (2005) 11.

[2] A. Janotti, C.G. Van de Walle, Fundamentals of zinc oxide as a semiconductor, Reports on progress in physics, 72 (2009) 126501.

[3] O. Lupan, T. Pauporté, L. Chow, B. Viana, F. Pellé, L. Ono, B.R. Cuenya, H. Heinrich, Effects of annealing on properties of ZnO thin films prepared by electrochemical deposition in chloride medium, Applied Surface Science, 256 (2010) 1895-1907.

[4] V. Karpina, V. Lazorenko, C. Lashkarev, V. Dobrowolski, L. Kopylova, V. Baturin, S. Pustovoytov, A.J. Karpenko, S. Eremin, P. Lytvyn, Zinc oxide–analogue of GaN with new perspective possibilities, Crystal Research and Technology, 39 (2004) 980-992.

[5] K. Nomura, H. Ohta, K. Ueda, T. Kamiya, M. Hirano, H. Hosono, Thin-film transistor fabricated in single-crystalline transparent oxide semiconductor, Science, 300 (2003) 1269-1272.

[6] D. Thomas, The exciton spectrum of zinc oxide, Journal of Physics and Chemistry of Solids, 15 (1960) 86-96.

[7] Y. Chen, D. Bagnall, H.-j. Koh, K.-t. Park, K. Hiraga, Z. Zhu, T. Yao, Plasma assisted molecular beam epitaxy of ZnO on c-plane sapphire: growth and characterization, Journal of Applied Physics, 84 (1998) 3912-3918.

[8] D. Reynolds, D.C. Look, B. Jogai, C. Litton, G. Cantwell, W. Harsch, Valence-band ordering in ZnO, Physical Review B, 60 (1999) 2340.

[9] R.W. Chuang, R.-X. Wu, L.-W. Lai, C.-T. Lee, ZnO-on-GaN heterojunction light-emitting diode grown by vapor cooling condensation technique, Applied Physics Letters, 91 (2007) 231113.

[10] R. Wang, C. Liu, J.-L. Huang, S.-J. Chen, Y.-K. Tseng, S.-C. Kung, ZnO nanopencils: Efficient field emitters, Applied Physics Letters, 87 (2005) 013110.

[11] D.C. Look, D. Reynolds, J.W. Hemsky, R. Jones, J. Sizelove, Production and annealing of electron irradiation damage in ZnO, Applied Physics Letters, 75 (1999) 811-813.

[12] M. Willander, O. Nur, Q. Zhao, L. Yang, M. Lorenz, B. Cao, J.Z. Pérez, C. Czekalla, G. Zimmermann, M. Grundmann, Zinc oxide nanorod based photonic devices: recent progress in growth, light emitting diodes and lasers, Nanotechnology, 20 (2009) 332001.

[13] T. Pauporté, D. Lincot, B. Viana, F. Pellé, Toward laser emission of epitaxial nanorod arrays of ZnO grown by electrodeposition, Applied Physics Letters, 89 (2006) 233112.

[14] O. Lupan, L. Chow, G. Chai, A single ZnO tetrapod-based sensor, Sensors and Actuators B: Chemical, 141 (2009) 511-517.

[15] O. Lupan, L. Chow, G. Chai, L. Chernyak, O. Lopatiuk-Tirpak, H. Heinrich, Focused-ion-beam fabrication of ZnO nanorod-based UV photodetector using the in-situ lift-out technique, physica status solidi (a), 205 (2008) 2673-2678.

[16] O. Lupan, S. Shishiyanu, L. Chow, T. Shishiyanu, Nanostructured zinc oxide gas sensors by successive ionic layer adsorption and reaction method and rapid photothermal processing, Thin solid films, 516 (2008) 3338-3345.

[17] O. Lupan, S. Shishiyanu, V. Ursaki, H. Khallaf, L. Chow, T. Shishiyanu, V. Sontea, E. Monaico, S. Railean, Synthesis of nanostructured Al-doped zinc oxide films on Si for solar cells applications, Solar Energy Materials and Solar Cells, 93 (2009) 1417-1422.

[18] T. Yoshida, J. Zhang, D. Komatsu, S. Sawatani, H. Minoura, T. Pauporté, D. Lincot, T. Oekermann, D. Schlettwein, H. Tada, Electrodeposition of inorganic/organic hybrid thin films, Advanced Functional Materials, 19 (2009) 17-43.

[19] T. Pauporte, J. Rathouský, Electrodeposited mesoporous ZnO thin films as efficient photocatalysts for the degradation of dye pollutants, The Journal of Physical Chemistry C, 111 (2007) 7639-7644.

[20] C. Badre, T. Pauporté, M. Turmine, D. Lincot, A ZnO nanowire array film with stable highly water-repellent properties, Nanotechnology, 18 (2007) 365705.

[21] B.R. Kumar, T.S. Rao, AFM Studies on surface morphology, topography and texture of nanostructured zinc aluminum oxide thin films, Digest Journal of Nanomaterials and Biostructures, 7 (2012) 1881-1889.

[22] Z. Fang, Z. Yan, Y. Tan, X. Liu, Y. Wang, Influence of post-annealing treatment on the structure properties of ZnO films, Applied Surface Science, 241 (2005) 303-308.

[23] Z. Zulkifli, S. Sharma, S. Shinde, G. Kalita, M. Tanemura, Effect of annealing in hydrogen atmosphere on ZnO films for field emission display, in: IOP Conference Series: Materials Science and Engineering, IOP Publishing, 2015, pp. 012030.

[24] D. Raoufi, F. Hosseinpanahi, Surface morphology dynamics in ITO thin films, Journal of Modern Physics, 3 (2012) 645.

[25] P. Quintana, A. Oliva, O. Ceh, J. Corona, M. Aguilar, Thickness effects on aluminum thin films, Superficies y vacío, (1999).

[26] M. Mirzaee, A. Zendehnam, S. Miri, Surface statistical properties of ZnO thin films produced by magnetron sputtering at different rates, Scientia Iranica, 20 (2013) 1071-1075.

[27] K. Bordo, H.-G. RUBAHN, Effect of deposition rate on structure and surface morphology of thin evaporated Al films on dielectrics and semiconductors, Materials Science, 18 (2012) 313-317.

[28] W. Guanghua, K. Jincheng, L. Xiongjun, Q. Feng, L. Cong, Y. Lili, K. Lingde, J. Rongbin, Effect of power variation on microstructure and surface morphology of HgCdTe films deposited by RF magnetron sputtering, Journal of Semiconductors, 31 (2010) 053004.

[29] S.K. Pandey, S.K. Pandey, V. Awasthi, A. Kumar, U.P. Deshpande, M. Gupta, S. Mukherjee, Influence of annealing temperature on ZnO thin films grown by dual ion beam sputtering, Bulletin of Materials Science, 37 (2014) 983-989.

[30] V. Kumar, N. Singh, R. Mehra, A. Kapoor, L. Purohit, H. Swart, Role of film thickness on the properties of ZnO thin films grown by sol-gel method, Thin Solid Films, 539 (2013) 161-165.

[31] Z. Ghorannevis, E. Akbarnejad, M. Ghoranneviss, Effects of various deposition times and RF powers on CdTe thin film growth using magnetron sputtering, Journal of Theoretical and Applied Physics, 10 (2016) 225-231.

[32] A. Ismail, M. Abdullah, The structural and optical properties of ZnO thin films prepared at different RF sputtering power, Journal of King Saud University-Science, 25 (2013) 209-215.

[33] W. Dang, Y.Q. Fu, J. Luo, A. Flewitt, W. Milne, Deposition and characterization of sputtered ZnO films, Superlattices and Microstructures, 42 (2007) 89-93.

[34] Y. Wang, S. Lau, H. Lee, S. Yu, B. Tay, X. Zhang, H. Hng, Photoluminescence study of ZnO films prepared by thermal oxidation of Zn metallic films in air, Journal of Applied Physics, 94 (2003) 354-358.

[35] Y. Peter, M. Cardona, Fundamentals of semiconductors: physics and materials properties, Springer Science & Business Media, 2010.

[36] J.-H. Fan, P. Gao, A.-M. Zhang, B.-R. Zhu, H.-L. Zeng, X.-D. Cui, R. He, Q.-M. Zhang, Resonance Raman scattering in bulk 2H-MX2 (M= Mo, W; X= S, Se) and monolayer MoS2, Journal of Applied Physics, 115 (2014) 053527.

[37] R. Loudon, The Raman effect in crystals, Advances in Physics, 13 (1964) 423-482.

[38] A. Iqbal, M. Zakria, A. Mahmood, Structural and spectroscopic analysis of wurtzite (ZnO) 1− x (Sb 2 O 3) x composite semiconductor, Progress in Natural Science: Materials International, 25 (2015) 131-136.

[39] C. Klingshirn, ZnO: From basics towards applications, physica status solidi (b), 244 (2007) 3027-3073.

[40] J. Serrano, A. Romero, F. Manjon, R. Lauck, M. Cardona, A. Rubio, Pressure dependence of the lattice dynamics of ZnO: An ab initio approach, Physical Review B, 69 (2004) 094306.

[41] M. Tzolov, N. Tzenov, D. Dimova-Malinovska, M. Kalitzova, C. Pizzuto, G. Vitali, G. Zollo, I. Ivanov, Modification of the structure of ZnO: Al films by control of the plasma parameters, Thin Solid Films, 396 (2001) 276-281.

[42] J. Dong, X. Zhang, J. You, P. Cai, Z. Yin, Q. An, X. Ma, P. Jin, Z. Wang, P.K. Chu, Effects of hydrogen plasma treatment on the electrical and optical properties of ZnO films: identification of hydrogen donors in ZnO, ACS applied materials & interfaces, 2 (2010) 1780-1784.

[43] V. Russo, M. Ghidelli, P. Gondoni, C. Casari, A. Li Bassi, Multi-wavelength Raman scattering of nanostructured Al-doped zinc oxide, Journal of Applied Physics, 115 (2014) 073508.

[44] F. Manjón, B. Mari, J. Serrano, A. Romero, Silent Raman modes in zinc oxide and related nitrides, Journal of Applied Physics, 97 (2005) 053516.

[45] A. Kaschner, U. Haboeck, M. Strassburg, M. Strassburg, G. Kaczmarczyk, A. Hoffmann, C. Thomsen, A. Zeuner, H. Alves, D. Hofmann, Nitrogen-related local vibrational modes in ZnO: N, Applied Physics Letters, 80 (2002) 1909-1911.

[46] Z. Chen, A. Kawasuso, Y. Xu, H. Naramoto, X. Yuan, T. Sekiguchi, R. Suzuki, T. Ohdaira, Microvoid formation in hydrogen-implanted ZnO probed by a slow positron beam, Physical Review B, 71 (2005) 115213.

[47] K. Saravanakumar, C. Gopinathan, K. Mahalakshmi, V. Ganesan, V. Sathe, C. Sanjeeviraja, XPS and Raman studies on (002) oriented nanocrystalline zno films showing temperature dependent optical red shift, Adv Studies Theor Phys, 5 (2011) 155-170.

[48] R. Al Asmar, J. Atanas, M. Ajaka, Y. Zaatar, G. Ferblantier, J. Sauvajol, J. Jabbour, S. Juillaget, A. Foucaran, Characterization and Raman investigations on high-quality ZnO thin films fabricated by reactive electron beam evaporation technique, Journal of Crystal Growth, 279 (2005) 394-402.

[49] F. Shan, G. Liu, W. Lee, B. Shin, The role of oxygen vacancies in epitaxial-deposited ZnO thin films, Journal of Applied Physics, 101 (2007) 053106.

[50] M. Wang, E.J. Kim, E.W. Shin, J.S. Chung, S.H. Hahn, C. Park, Low-temperature solution growth of high-quality ZnO thin films and solvent-dependent film texture, The Journal of Physical Chemistry C, 112 (2008) 1920-1924.

[51] M. Wang, E.J. Kim, S.H. Hahn, Photoluminescence study of pure and Li-doped ZnO thin films grown by sol–gel technique, Journal of Luminescence, 131 (2011) 1428-1433.

[52] A. Van Dijken, E. Meulenkamp, D. Vanmaekelbergh, A. Meijerink, Identification of the transition responsible for the visible emission in ZnO using quantum size effects, Journal of Luminescence, 90 (2000) 123-128.

[53] P. Hsieh, Y. Chen, K. Kao, M. Lee, C. Cheng, The ultraviolet emission mechanism of ZnO thin film fabricated by sol–gel technology, Journal of the European ceramic Society, 27 (2007) 3815-3818.

[54] A. Mallika, A.R. Reddy, K.V. Reddy, Annealing effects on the structural and optical properties of ZnO nanoparticles with PVA and CA as chelating agents, Journal of Advanced Ceramics, 4 (2015) 123.

[55] R. Sakthivel, A.S. Ganesh, A. Geetha, B. Anandh, R. Kannusamy, K. Tamilselvan, Effect of Post Annealing on Antibacterial Activity of Zno thin films Prepared by Modified Silar Technique, Oriental Journal of Chemistry, 33 (2017) 355-362.

[56] S.-M. Lee, Y.-H. Joo, C.-I. Kim, Influences of film thickness and annealing temperature on properties of sol–gel derived ZnO–SnO 2 nanocomposite thin film, Applied Surface Science, 320 (2014) 494-501.

[57] X. Wu, G. Siu, C. Fu, H. Ong, Photoluminescence and cathodoluminescence studies of stoichiometric and oxygen-deficient ZnO films, Applied Physics Letters, 78 (2001) 2285-2287.

[58] R. Lauer, The IR photoluminescence emission band in ZnO, Journal of Physics and Chemistry of Solids, 34 (1973) 249-253.

[59] J.S. Kang, H.S. Kang, S.S. Pang, E.S. Shim, S.Y. Lee, Investigation on the origin of green luminescence from laser-ablated ZnO thin film, Thin Solid Films, 443 (2003) 5-8.

[60] M. Koyano, P. QuocBao, L. HongHa, N. NgocLong, S. Katayama, Photoluminescence and Raman spectra of ZnO thin films by charged liquid cluster beam technique, (2002).

[61] L. Xu, G. Zheng, J. Wang, F. Xian, Y. Liu, Stable co-emission of UV, green and red light in ZnO thin films with rapid annealing treatment, Optik-International Journal for Light and Electron Optics, 127 (2016) 5942-5949.

[62] C. Chiu, Z. Pei, S. Chang, S. Chang, S. Chang, Effect of oxygen partial pressure on electrical characteristics of amorphous indium gallium zinc oxide thin-film transistors fabricated by thermal annealing, Vacuum, 86 (2011) 246-249.

[63] B.-c. Yang, X.-y. Liu, F. Gao, X.-l. Ma, Photoluminescence properties of ZnO thin films prepared by DC magnetron sputtering, Journal of Central South University of Technology, 15 (2008) 449-453.

[64] B. Abdallah, A.K. Jazmati, R. Refaai, Oxygen Effect on Structural and Optical Properties of ZnO Thin Films Deposited by RF Magnetron Sputtering, Materials Research, (2017) 0-0.

[65] C.-C. Ting, Structure, Morphology, and Optical Properties of the Compact, Vertically-Aligned ZnO Nanorod Thin Films by the Solution-Growth Technique, in: Nanorods, InTech, 2012.

[66] N. Alvi, K. Ul Hasan, O. Nur, M. Willander, The origin of the red emission in n-ZnO nanotubes/p-GaN white light emitting diodes, Nanoscale research letters, 6 (2011) 130.

[67] Y.-P. Du, Y.-W. Zhang, L.-D. Sun, C.-H. Yan, Efficient energy transfer in monodisperse Eu-doped ZnO nanocrystals synthesized from metal acetylacetonates in high-boiling solvents, The Journal of Physical Chemistry C, 112 (2008) 12234-12241.

[68] S. Youssef, P. Combette, J. Podlecki, R.A. Asmar, A. Foucaran, Structural and optical characterization of ZnO thin films deposited by reactive rf magnetron sputtering, Crystal Growth and Design, 9 (2008) 1088-1094.

[69] J. Levinson, F. Shepherd, P. Scanlon, W. Westwood, G. Este, M. Rider, Conductivity behavior in polycrystalline semiconductor thin film transistors, Journal of Applied Physics, 53 (1982) 1193-1202.

[70] J. Huang, Zinc oxide thin film transistors by radio frequency magnetron sputtering, (2014).

[71] J.N. Zeng, J.K. Low, Z.M. Ren, T. Liew, Y.F. Lu, Effect of deposition conditions on optical and electrical properties of ZnO films prepared by pulsed laser deposition, Applied surface science, 197 (2002) 362-367.

[72] P. Spizzirri, J.-H. Fang, S. Rubanov, E. Gauja, S. Prawer, Nano-Raman spectroscopy of silicon surfaces, arXiv preprint arXiv:1002.2692, (2010).

[73] M. Sultan, N. Sultana, Analysis of reflectance and transmittance characteristics of optical thin film for various film materials, thicknesses and substrates, Journal of Electrical & Electronics, 4 (2015) 1.

[74] V. Valliyil Sasi, A. Iqbal, K. Chaik, A. Iacopi, F. Mohd-Yasin, RF sputtering, post-annealing treatment and characterizations of ZnO (002) thin films on 3C-SiC (111)/Si (111) substrates, Micromachines, 8 (2017) 148.

[75] J. Zhang, G. He, L. Zhu, M. Liu, S. Pan, L. Zhang, Effect of oxygen partial pressure on the structural and optical properties of ZnO film deposited by reactive sputtering, Applied surface science, 253 (2007) 9414-9421.

[76] M. Furuta, Stoichiometry control of ZnO thin film by adjusting working gas ratio during radio frequency magnetron sputtering, Journal of Materials, 2013 (2013).

[77] K. Tominaga, S. Iwamura, I. Fujita, Y. Shintani, O. Tada, Influence of bombardment by energetic atoms on c-axis orientation of zno films, Japanese Journal of Applied Physics, 21 (1982) 999.

[78] T. Nagata, A. Ashida, N. Fujimura, T. Ito, The effects of Xe on an rf plasma and growth of ZnO films by rf sputtering, Journal of applied physics, 95 (2004) 3923-3927.

[79] F. Yang, D.-W. Kang, Y.-S. Kim, Improved interface of ZnO/CH 3 NH 3 PbI 3 by a dynamic spin-coating process for efficient perovskite solar cells, RSC Advances, 7 (2017) 19030-19038.

Chapter 5: Structural and spectroscopic analysis of ex-situ annealed RF sputtered Al doped ZnO thin film.

5.1 Introduction

Environmental friendly ZnO has received much attention over the past decades as a result of its wide and direct band gap (3.27 eV) as well as large exciton binding energy (60 meV) [1]. This band gap can be engineered by alloying with MgO or CdO. This makes ZnO a promising candidate for various applications such as gas sensors, transparent conductors for thin films transistors, solar cell, light emitting diodes (LEDs) and laser diodes (LDs). Other important characteristics of ZnO include: strong luminescence in the green-white region of the spectrum making it a suitable material for phosphor application [2]; availability of large area single crystals and epi-ready substrates that can be easily fabricated by a versatile of CVD and PVD suites [3-5]. ZnO crystallizes in the wurtzite structure (Fig 5-7) almost always as n-type, the cause of which has been a subject of intense debate. The low symmetry of the wurtzite crystal structure combined with the large electromechanical coupling in ZnO also gives rise to strong piezoelectric and pyroelectric properties [6]. Various research groups have reported that the electrical and optical properties can be significantly changed using relatively small concentrations of native point defects and impurities [7, 8].

Recently Aluminium doped ZnO thin films have shown high potential as a low cost alternative to indium tin oxide (ITO) especially as a transparent electrode in solar cells. The drive force for Al: ZnO applications as alternative electrodes are attributed to the abundance and non-toxicity of the constituent elements in the films. Additionally the have been found to also exhibit high electrical conductivity, high optical transparency in the visible wavelength region (400-800 nm) as well as good chemical, mechanical and thermal stability [9].

Among the various growth techniques for Al doped ZnO, RF sputtering has its advantages such as ability to produce good quality films with high surface area and low electrical resistivity. This deposition can be carried out at room temperature yet still remain stable even at high temperature [1].

In this chapter, we studied the effect of deposition time and post-growth annealing of RF sputtered Al doped ZnO thin film at a temperature range of of 600-1000 ˚C in air. High temperature annealing appears to enhance optical properties such as photoluminescence, improved crystallinity as well provide mechanisms for the substitution of zinc doping in the presence of Al impurities. Aluminum doped zinc oxide (AZO) thin films have been prepared by Radio Frequency (RF) sputtering system in pure argon atmosphere with a power of 100 W. The structural results reveal a good adhesive nature of the thin film on quartz and (001) silicon substrates (100). The thin films were then subjected to heat treatment in a furnace under ambient air. The structural, morphological and optical properties of the thin films as a function of deposition time and annealing temperatures have been investigated using X-Ray Diffraction (XRD), Atomic Force Microscopy (AFM) and Scanning Electronic Microscopy (SEM). Photoluminescence (PL) properties of annealed films showed significant changes in the optical properties providing proof of defect formation. Annealing leads to an increase in the crystallite size as well as the roughness of the film. The crystallinity of the films also improved as evident from the Raman and XRD studies.

5.2. Experimental details

Aluminium doped ZnO thin films have been deposited using RF magnetron sputtering onto n-type (001) Silicon substrates of 1 cm square at room temperature. The substrates were initially cleaned with acetone and ethanol in an ultrasonic bath for 20 minutes and rinsed in deionized water before drying using a stream of nitrogen gas. The substrates were then mounted on a rotating substrate holder at a distance of 6 cm from the ZnO target. The target used was ZnO (98%): Al (2%) disk (99.99% purity) with a diameter of 76 mm and thickness 6 mm. This was bonded onto a circuit magnetron cathode in a vertical configuration. The sputtering chamber was evacuated to a base pressure of about 2×10^{-5} mbar while sputtering was performed under Argon with a working gas pressure of 2.3×10^{-3} mbar. The growth was undertaken under 13-sccm Ar flow, 100 W RF power with deposition time varied between 5-60 minutes. Post-growth annealing was carried out in air for films deposited for 40 minutes in a furnace at a temperature range of 600-1000 ˚C for 2 hours.

5.3. Characterization of the films.

The morphologies and structural analyses of the samples were characterized using Veeco Di-3100 atomic force microscopy (AFM) in tapping mode and FEI Nova Nanolab 600 SEM. The elemental composition of the films were analysed through an energy dispersive X-ray spectroscopy (EDX) attached to the SEM. The Raman bands and the structural order of all the films were examined using a Horiba LabRAM HR Raman spectrometer equipped with an Ar ion laser (514.5 nm). The laser power on the all the sample was set to <1 mW. The effect of deposition time and post growth annealing temperature on the crystallinity and phase were studied using AXS Bruker D8 Discover, 40kV, 40 mA using CuKα radiation in the Seeman-Bohlin geometry. The scanning range of 2θ was varied from 10° to 80° at a low scanning rate of 1.2^{o}/minute. The X-ray reflectivity (XRR) and diffraction spectrum of the sample were recorded before XRR curve fitting using Diffrac-Leptos

software. Photoluminescence measurements are carried out using a Horiba LabRAM HR spectrometer with a 150 lines/mm grating and an excitation wavelength of 229 nm from a frequency doubled Lexel argon ion laser.

5.4. Results and discussion

5.4.1. Morphology studies by AFM and SEM

The surface morphology of the films was characterized using Veeco Di3100 AFM under tapping mode and the results are shown in figure 5-1.

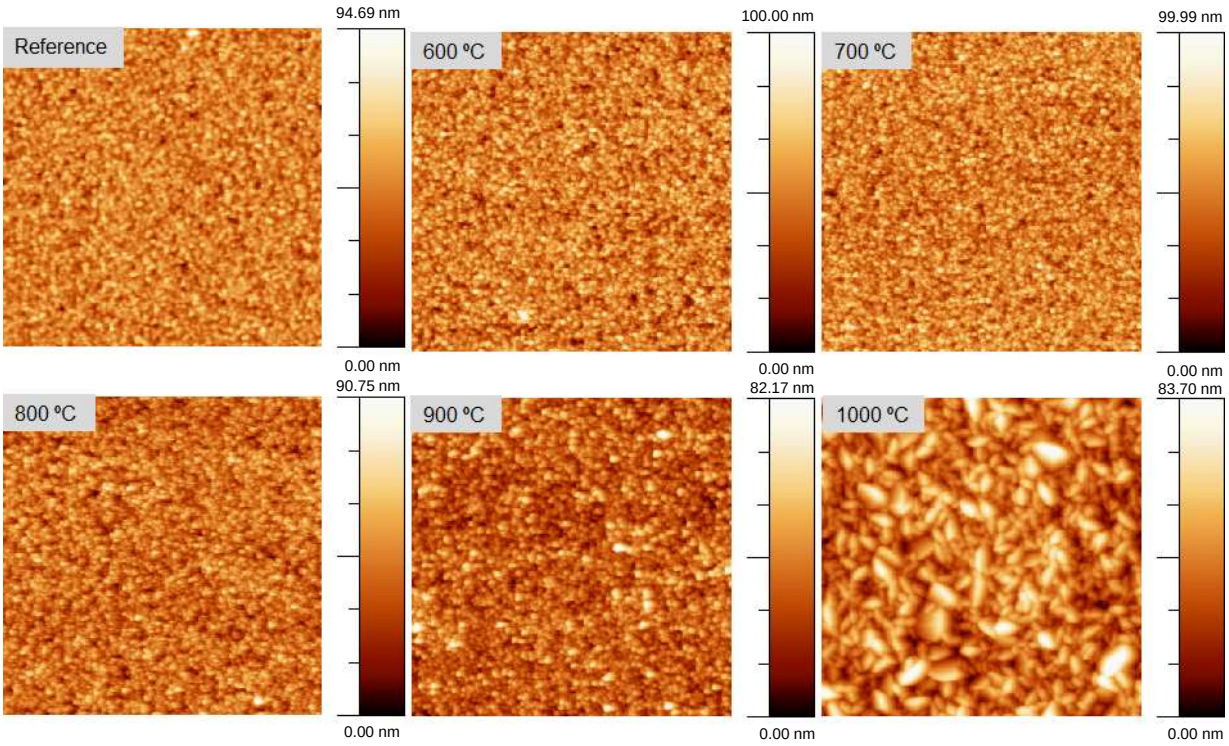


Figure 5-1: AFM images of the Al doped ZnO before and after annealing at temperature range of 600-1000 ˚C in air.

According to ref [6], the surface reconstruction as a result of formation of native defects can vary over a wide range (given by the formation enthalpy of ZnO, i.e. 3.6 eV) due to the variations of their chemical potentials.

From table 5-1, the average roughness of the film surface increases with annealing temperature showing that the degree of uniformity of the surface decreases as temperature increases. We further tabulated the skewness (R_{sk}) and the kurtosis (R_{ku}) parameters to provide information on the asymmetry and the sharpness of the surface topography respectively. The skewness (R_{sk}) was used to establish the profile symmetry about the mean line. The positive values attained indicate that the height distribution is asymmetrical with more peaks than valleys [9]. Annealing enhances the surface diffusion of particles leading to shape and size reconstruction as shown by the increase the skewness. Kurtosis (R_{ku}) on the other hand gives the measure of surface sharpness of the films surface. Since the kurtosis (R_{ku}) is higher than 3, this indicate spiky surface.

Table 5-1: Summary of tapping mode AFM analysis.

Annealing Temperature ($^{\circ}$C)	R_a (nm)	R_{rms} (nm)	Skewness (R_{sk})	Kurtosis (R_{ku})	Grain height (nm)
Reference	3.43	4.317	0.002	3.162	16.64
600	4.567	5.747	0.016	3.076	22.56
700	4.310	5.414	0.087	3.045	22.683
800	4.608	5.775	0.042	3.035	21.065
900	5.777	7.428	0.654	4.222	27.244
1000	28.563	35.883	0.653	4.132	94.149

The grain height is observed to increase with temperature due to coalescence. This is consistent with the XRD result, however the values are seemingly larger than those obtained from XRD analysis due to the fact that AFM gives the particle size while XRD derives the grain size. When annealed at high temperature, the atoms acquire enough activation energy to possibly occupy the

correct site in the crystal lattice and grains with the lower surface energy will become larger [10]. At 1000 ˚C there is sharp increase in both roughness and grain height due to major grain growth. On the account of vacancies reduction, larger grains are formed in a process similar to sintering.

Zinc has greater volume diffusion than oxygen [11]. Zn self-diffusion may be mediated by Zn vacancies which have a higher migration barrier of 1.40 eV, but with much lower formation energy in n-type ZnO [12]. Tomlins *et al* reported an activation energy of Zn in ZnO of 3.86 eV for self-diffusion compared to Oxygen in ZnO, and appropriately suggested that Zn self-diffusion is controlled by a vacancy mechanism [6].

Figure 5-2 shows the AFM image of films deposited at an RF power of 100 W at varied deposition time. At low deposition time, meso-flat islands, often with highly dendritic shapes are formed following Volmer-Weber growth mode. An increase in deposition time leads to formation of "spherical" like thicker films. This is confirmed by the increase in grain height with time as well as film thickness increase measured using thickness profilometer. From table 5-2, the roughness first increases with deposition time as larger porous particles are formed. At 40 minutes deposition time, the film appears more compact with a reduced roughness. This is also observed at a deposition time of 1 hour.

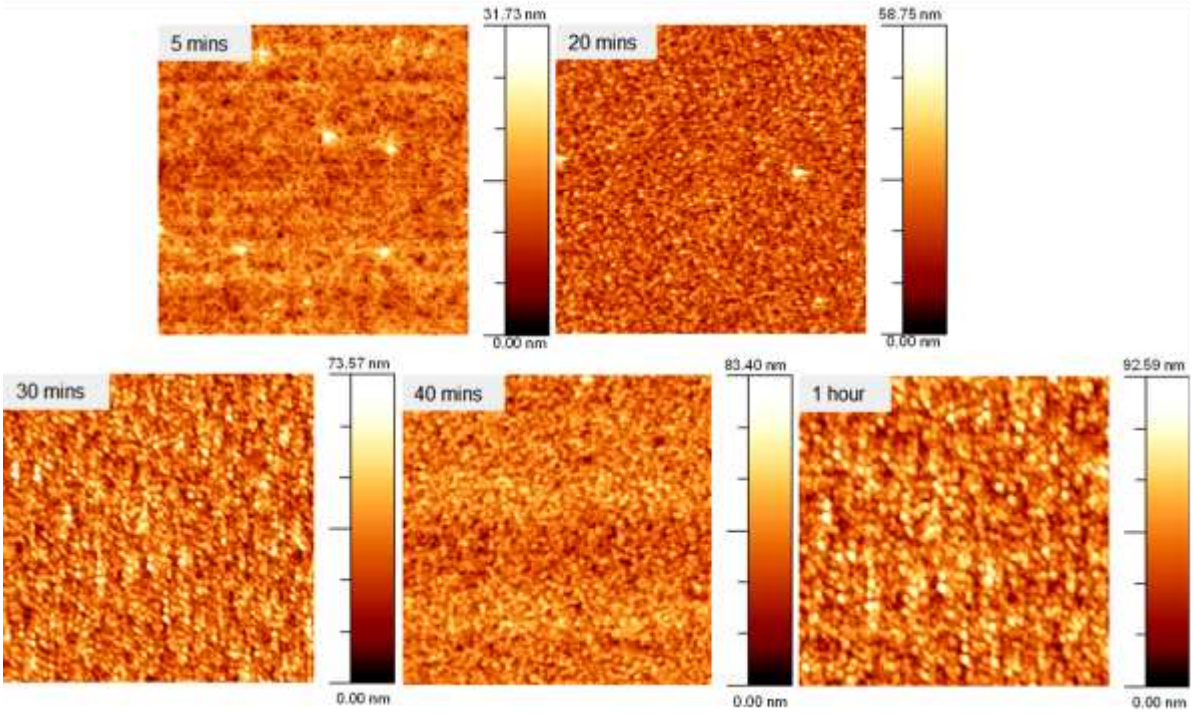


Figure 5-2: AFM images of the Al doped ZnO grown an RF power of 100 W over different deposition time ranging from 5 minutes to 1 hour.

Table 5-2: Summary of tapping mode AFM analysis for AZnO deposited at varied time.

Annealing Temperature (°C)	R_a (nm)	R_{rms} (nm)	Skewness (R_{sk})	Kurtosis (R_{ku})	Grain height (nm)
Reference	3.43	4.317	0.002	3.162	16.64
600	4.567	5.747	0.016	3.076	22.56
700	4.310	5.414	0.087	3.045	22.683
800	4.608	5.775	0.042	3.035	21.065
900	5.777	7.428	0.654	4.222	27.244
1000	28.563	35.883	0.653	4.132	94.149

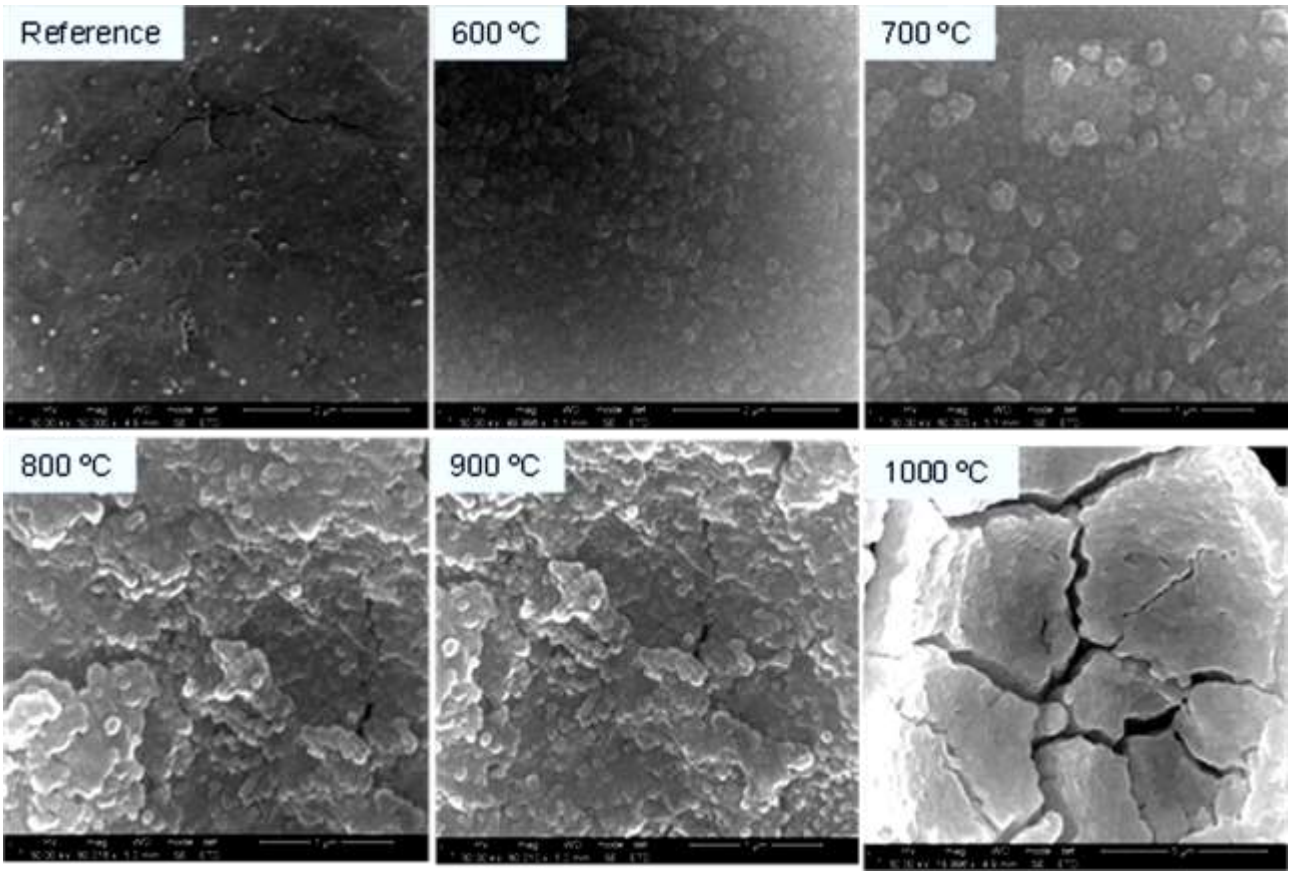


Figure 5-3: SEM images of the Al doped ZnO before and after annealing at temperature range of 600-1000 ˚C in air and EDS spectra.

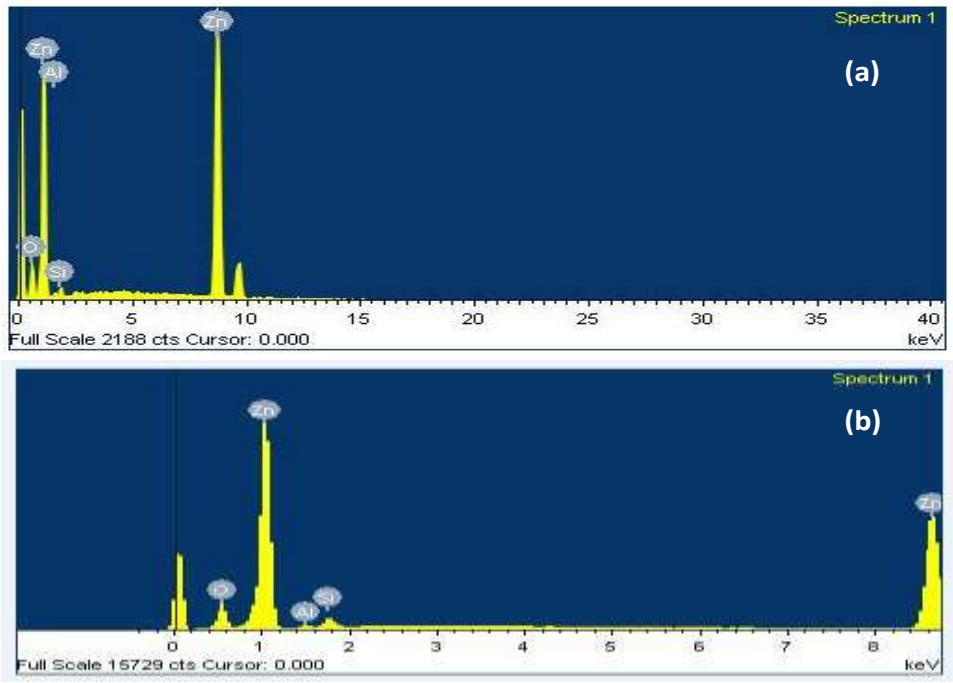


Figure 5-4: Energy Dispersive Spectroscopy (EDS) spectra of the pristine and annealed ZnO thin film (1000 ˚C).

The SEM micrographs of Al doped ZnO grown at an RF power of 100 W for 40 minutes shows that the films exhibit smother and uniform texture upon growth. The particles assume an almost spherical shape indicating a homogenous nucleation process involved in the RF sputtering. The emergence of small crack in the as-grown film is a clear indication of the competition between compressive elastic strain and film-substrate adhesion in the as-deposited films. With the increase of the annealing temperature, the strain relaxation occurs as the smaller strained grains are aggregated into larger grain sizes which are less strained. This is corroborated from the change in lattice parameters and the c/a ratio. At 1000 ˚C, the surface is smooth but with huge gaps between the blocks resulting from thermal stress due to mismatch of thermal expansion between the Al doped ZnO and the Silicon substrate. For instance ZnO has a thermal expansion coefficient of $4.75\times10^{-6}K^{-1}$ while silicon substrate has a mean thermal expansion of $2.69\times10^{-6}K^{-1}$ at room temperature [13, 14]. A mismatch in thermal expansion and anisotropic contraction during

annealing induces tensile stress on the ZnO film as the substrate cools from high temperature to room temperature such as stress relaxations lead to cracking of films [15]. The EDS spectrum measurements in figure 5-4 shows that there is no impurity from other materials or losses in the volatile Zn due to elevated temperatures. The peak on Si is due to the (001) Si substrate.

5.4.2. Raman Spectroscopy

Raman spectroscopy is the inelastic scattering of photons by phonons. This technique is predominantly used for estimating the crystallinity of materials. The finite optical phonons within the grains of ZnO nanostructures results in an interesting change in its vibrational spectra compared to that of their bulk counterparts. Some shifting of peaks as wells as broadenings in the Raman spectra may occur for crystals with reduced dimensionality. The Raman spectra of ZnO nanostructures always exhibit such shift and broadening from the bulk phonon frequencies. According to Khan *et al*, the phonon peak shifts in Raman spectra of nanostructures is attributed to spatial confinement within the quantum dot nanocrystal boundaries as well as phonon localization by defects [16]. ZnO is a semiconductor with wurtzite crystal structure. The wurtzite structure of ZnO crystal has C_{6v} symmetry with 4 atoms in the hexagonal unit cell leading to 12 phonon branches, of which 9 are optical and 3 are acoustic branches. This classification is based on the following irreducible representations:

$$\Gamma = 2A_1 + 2B_1 + 2E_1 + 2E_2 \quad \text{5-1}$$

where *A* and *B* modes have one-fold degeneracy and *E* modes are two-fold. One A_1 mode and one E_1 pair are the acoustic phonons [16, 17].

Figure 5-5 shows the various Raman modes obtained using the green excitation wavelength (514 nm, 2.41 eV) in the 100-800 cm^{-1} range. Raman peaks are observed at 278, 305,437,584 and 619 cm^{-1} in the as-synthesized sample.

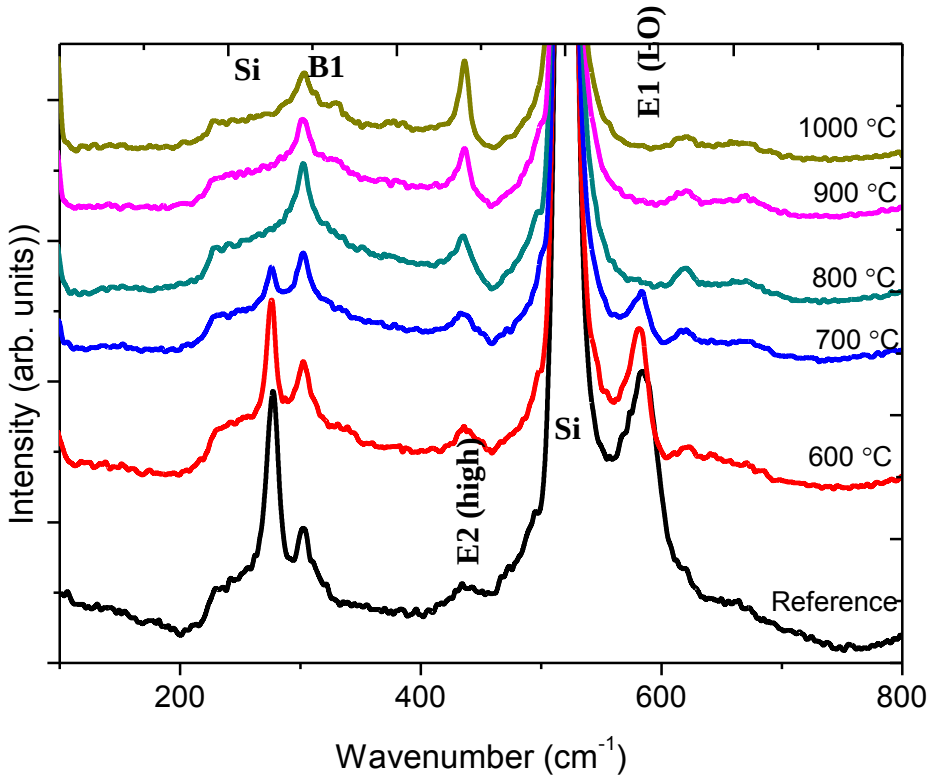


Figure 5-5: Raman spectra of Aluminium doped ZnO thin film before and after annealing at 600-1000 ˚C. The spectra were collected at normal incidence (at 90 ˚ to the surface).

The peak intensity at 278 cm^{-1} gradually reduces with annealing temperature and finally disappears at 800 ˚C. This peak is attributed to Raman inactive B_2 mode resulting from the presence of a built-in electric field within the separate grains that lowers the lattice symmetry [9]. As a result of increase in the A_1 (LO) vibrations, another peak due to the existence of a built-in electric field in the crystallites is seen at 584 cm^{-1}. The grain boundaries typically contain a relatively high interfacial density that captures the free carriers from most of the grains. This interface charge gives rise to band-bending in the bulk of the grain and thus leading to the formation of an interface

barrier. This confirms the substitution of Al in the ZnO. The depletion layer is located near the grain boundary due to the high carrier concentration resulting from Al doping, and the bulk density of the carrier density in most grains is constant. Lowering of the doping level, for example by addition of oxygen during annealing process, leads to nearly flat bands throughout each grain. This is evident by the peak at 278 cm^{-1} and in the high Raman shift regime, at 584 cm^{-1} which suddenly disappear at annealing temperature of 800 $^{\circ}C$. At this temperature there is formation of more insulating films and hence the value of the built-in electric field decreases and disappears [18].

A notable peak observed at 437 cm^{-1} in all samples is assigned E_2 (high) mode. Usually, this is the strongest mode in wurtzite crystal structure and is as a result of the vibrations of the oxygen atoms in the ZnO lattice [19]. The position of E_2 (high) mode shows no obvious change with increasing annealing temperature. The intense peaks at 305 and 525 cm^{-1} are associated with Silicon substrate. When the time of deposition is varied the Raman peaks obtained are as shown in figure 5-6.

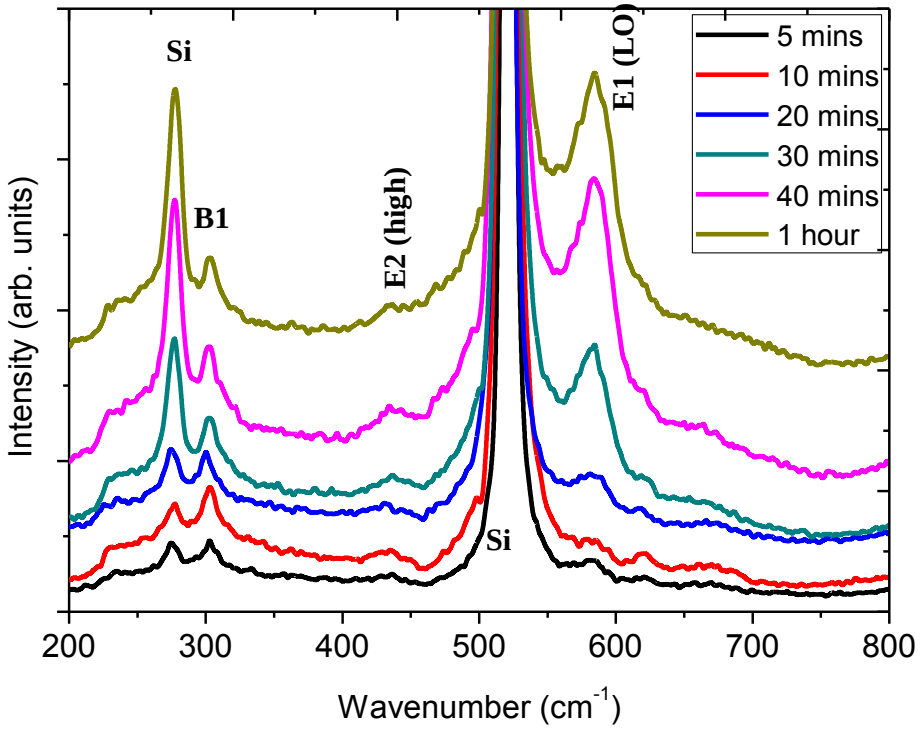


Figure 5-6: Raman spectra of Al doped ZnO thin film deposited at 100 W at different deposition time.

Figure 5-6 shows the Raman spectra of the prepared Al doped ZnO thin films with varied deposition time. The Raman lines around 278 cm^{-1}, 437 cm^{-1} and 584 cm^{-1} were observed for all the samples. These lines are assigned to ZnO B_2 mode, E_2 (high) and A_1 longitudinal optical (LO) mode respectively. The blue shift of the B_2 mode peak from 274.1 cm^{-1} to 277.6 cm^{-1} was caused by the tensile strain in the films which was in good agreement with the GIXRD results. The peaks at 278 cm^{-1}, and 584 cm^{-1} become intense with narrow FWHM as deposition time increases. This could be attributed to more scatter volume and thermalisation of the substrate for long deposition times. The A1 (LO) mode was caused by the defects of O-vacancy and Zn interstitial. The increase of the B_2 and A_1 (LO) mode intensity for Al doped ZnO thin film with increasing deposition time implied the increase of defects (O- vacancy and Zn interstitial) in this film which is consistent with the PL result [20]. The addition of oxygen through annealing in air or sputtering in Ar/O mixture affects the Oxygen vacancies in ZnO and this is seen in the high frequency E2 mode whose sensitivity to the oxygen composition is seen by the changes in the peak position of the mode. This provides an avenue to evaluate oxygen vacancies and also confirm the prospects of re-oxidation upon annealing in air. The Raman shift of E2 (high) with annealing time or temperature illustrate the contributions of the oxygen vacancy.

5.4.3. XRD measurements

The GIXRD patterns of the aluminum doped Zinc Oxide films annealed at different temperatures are shown in Figure 5-8. All the peaks are indexed to the JCP2 card number 003-0888 with hexagonal wurtzite structure having two lattice parameters, *a* and *c*, in the ratio of *c/a*= 5.21/3.24 = 1.63 and belongs to the space group of P63mc. A schematic representation of the wurtzitic ZnO structure is shown in Figure 5-7. The structure is composed of two interpenetrating hexagonal-

close-packed hcp sub lattices, each of which consists of one type of atom displaced with respect to each other along the threefold *c*-axis by the amount of *u* =0.379 defined as the length of the bond parallel to the c axis, in units of c and is given by equation 5-2 [21].

$$u = \frac{1}{3}\left(\frac{a^2}{c^2}\right) + \frac{1}{4} \quad \text{..... 5-2}$$

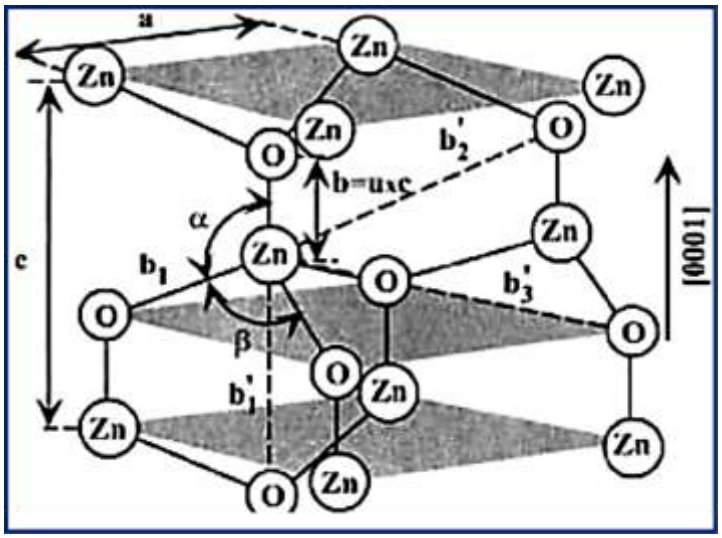


Figure 5-7: Schematic representation of a wurtzitic ZnO structure having lattice constants a in the basal plane and c in the basal direction; u parameter is expressed as the bond length [21]..

From the XRD patterns the films are polycrystalline in nature with a preferred orientation along the *c*-axis. Three distinct peaks are observed at (100), (002) and (112) planes. The (100) and (002) peak intensity increases with increasing annealing temperature up to a temperature of 900 ˚C while the full width at half maximum (FWHM) reduces. This is a clear indication of enhanced crystallinity of the films with increasing annealing temperature. The increase in peak intensity with annealing temperature between 600-900 ˚C may be attributed to thermally activated mobility of the atoms in the films that lead to the possible decrease in the structural or native defects in the ZnO films. This reduces the porosity and quality of films [10]. This effects is also plausible for thermal treatment beyond 900 ˚C as corroborated in the sharp decrease of the peak intensity. [22].

In ZnO, the most intense peak is usually along (002) plane, however, this is contrary to our observation in which a higher intensity peak corresponding to (100) plane is reported. This is fibre texture and it is attributed to disturbance of the charge neutrality induced by Al^{3+}substitution of Zn^{2+} [23]. Furthermore, the presence of Al changes the diffusion rate of Zn and O on the Si substrate during deposition and annealing. This may alter the energetic balance between (100) and (002) orientations hence making the usually preferred (002) orientation in the wurtzite structure [24] to be unfavorable. This peak intensity increases with temperature as a result of more substitution.

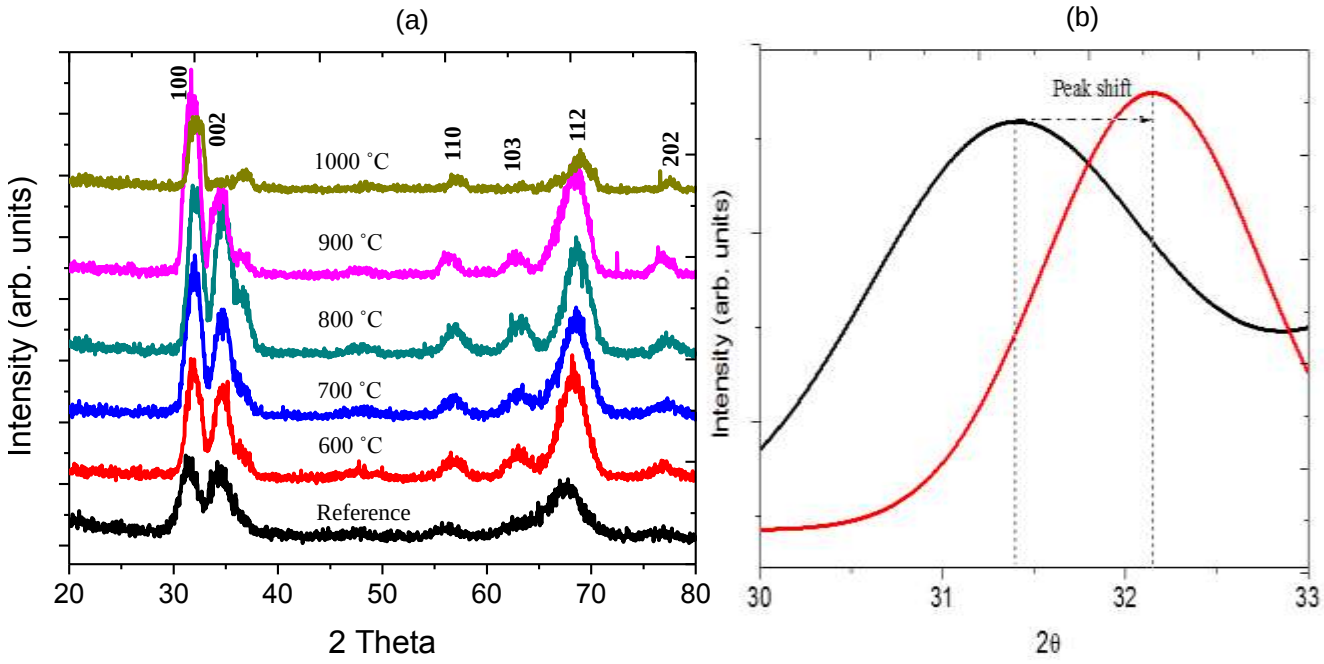


Figure 5-8: X-ray diffraction (XRD) pattern of (a) the Al doped ZnO thin film before and after annealing at temperature between 600-1000 ˚C in air, (b) curve fit of the (100) peak before and after annealing at 1000 ˚C.

At temperatures between 600-900 ˚C, the FWHM of the peaks decreases relative to the strong increase of their intensities (table 5-3). This observation can be explained using the Scherrer's theory that the full width of a peak at half maximum in a polycrystalline sample is correlated with

the extension d of the crystalline domains[25]. The peak positions are shifted to lower wavelength in this temperature regime as a result of compressive stress induced by annealing effects. This may also be due to the fact that more Al ions occupy the lattice position of Zn ions and less stress remains in films after annealing [26]. At 900 ˚C the shift in peak position is towards that of pristine film. Annealing also reduces the concentration of structural defects/pinhole and thus decreases the intrinsic stress. During annealing, atoms of ZnO films acquire energy to arrange leading to reduction in the tensile stress. There is higher chances of Zn self-diffusion mediated by Zn vacancies which have a higher migration barrier of 1.40 eV, but with a much lower formation energy. Indeed, Tomlins *et al* reported an activation energy of 3.86 eV for self-diffusion of Zn in ZnO, and appropriately suggested that Zn self-diffusion is controlled by a vacancy mechanism [27]. However, ZnO has a higher thermal expansion coefficient compared to the substrate (Si) hence a compressive stress will be generated by Si when the substrate cools to room temperature. This difference causes the shift in the peaks position [10].

Table 5-3: Characteristics of Al doped ZnO annealed at 600-1000 ˚C in air as estimated from XRD patterns

Annealing Temperature (˚C)	**fwhm** (100)	2θ	**fwhm** (002)	2θ	**fwhm** (112)	2θ
Reference	1.53822	31.35932	2.45638	34.46864	3.54359	67.34772
600	1.32936	31.91696	1.79432	34.78054	2.64725	68.40601
700	1.29202	31.91529	1.73682	34.70507	2.45601	68.20376
800	1.17732	32.02756	1.42188	34.93952	2.26733	68.63416
900	1.28508	31.7629	1.52375r	34.48858	2.40098	68.29923
1000	1.19040	32.15058	1.29611	36.65045	1.91422	68.91316

The associated stress and strain are evident in the changing lattice constants *a* and *c* values as shown in table 5-4. From the multi-peak fitting carried out using Origin, the peak center positions were obtained as recorded in table 3 and used to derive the lattice spacing for all the samples using Bragg's relation:

$$\lambda = 2d_{hkl}\sin\theta_{hkl} \quad \text{..... 5-3}$$

Where θ is the Bragg's angle (angle between normal to the diffracting plane and incident X-ray), λ is the X-ray wavelength which in our case was CuKα radiation with a wavelength of 1.541 Å. The lattice parameters *a* and *c* were obtained for the three major peaks using the expression for hexagonal system [19].

$$\frac{1}{d^2} = \frac{4}{3}\left(\frac{h^2+hk+l^2}{a^2}\right) + \frac{l^2}{c^2} \quad \text{..... 5-4}$$

The lattice parameters *a* and *c* calculated at different annealing temperatures as well as the reference film are nearly equal to the lattice constants given in the standard data (JCP2 card number 003-0888). The slight increase in the lattice parameters with increasing annealing temperature is attributed to strain in the lattice or stresses induced by Al dopant which have a higher valence states than Zn. The change in the lattice parameters of the ZnO host material depend on the ionic radii of the impurity that substitute the Zn ions at the lattice sites. In our case, since the ionic radius of Al^{3+} (0.053 nm) used as a dopant is less than that of Zn^{3+} (0.074 nm), Al^{3+} substituting Zn^{2+} will lead to compression of the lattice hence a decrease in the lattice parameters observed in table 4. It is plausible that the increase in temperature provides sufficient energy to thermally activate Zn/Al atoms into the sites in the ZnO film, this increases the probability of atomic substitution. Site substitutions for atoms with different charge states than host could lead to a reduction in the lattice parameters [19].

Table 5-4 shows calculated crystallite sizes for the three peaks with the highest peaks as well as an average size derived using Scherrer's formula shown in equation 5-5.

$$D = \frac{k\lambda}{\beta \cos\theta} \quad \ldots\ldots\ldots\ldots\ldots\ldots\ldots\ldots \quad 5\text{-}5$$

Where k is the crystallite shape factor usually 0.9, λ is the X-ray wavelength used which is our case was 1.541 Å, β is the FWHM which are tabulated in table 5-4 while θ is the Bragg's angle in radians.

From table 5-4, the average crystallite size becomes larger as annealing temperature increases and this is in agreement with AFM and SEM analysis. This increase could be attributed to the fact that at high temperature, the atoms have enough diffusion activation energy to occupy the correct site in the crystal lattice and thus grains with the lower surface energy will become larger at high temperature. As a result the growth orientation develops into one crystallographic direction of the low surface energy, leading to the improvement of the film crystallinity [22].

$$D = D_o e^{-E_A/kT} \quad \ldots\ldots\ldots\ldots\ldots\ldots\ldots\ldots\ldots\ldots\ldots\ldots\ldots\ldots\ldots\ldots \quad (6)$$

where D_o is the diffusion coefficient at reference temperature T.

Table 5-4: Estimated crystallite size, lattice parameters, dislocation density and strain from XRD data.

Annealing Temperature (°C)	Crystallite size, D_{sh}/(nm)							
	(100) peak	(002) peak	(112) peak	Average size	a/(Å)	c/(Å)	δ (10^{15})	ε (10^{-3})
Reference	10.73	6.79	5.39	7.63	3.29	5.20	8.69	3.23
600	12.43	9.28	7.26	9.65	3.24	5.16	6.47	2.79
700	12.79	9.58	7.81	10.06	3.24	5.17	6.11	2.71
800	14.04	9.51	8.48	10.67	3.23	5.13	6.07	2.70
900	12.86	12.04	7.99	10.96	3.25	5.19	6.05	2.69
1000	13.89	12.92	10.06	12.29	3.21	4.90	5.18	2.49

The dislocation density δ, defined as the length of dislocation lines per unit volume of the crystal (Williamson and Smallman) and the strain present in thin film were investigated using equations 5-7 and 5-8 respectively.

$$\delta = \frac{1}{D_{sh}^{2}} \quad \text{..... 5-7}$$

$$\varepsilon = \frac{\beta \cos\theta}{4} \quad \text{..... 5-8}$$

The strain in the films gets released as temperature increases as a result of the removal of defects in the lattice with increase in temperature as indicated in table 5-4. Such a release in strain reduces the variation of interplanar spacing d, leading to the decrease in dislocation density. The reducing strain and dislocation density together enhances the stoichiometry of the films, which in turn causes the volumetric expansion of thin films hence and improvement of crystallinity [28].

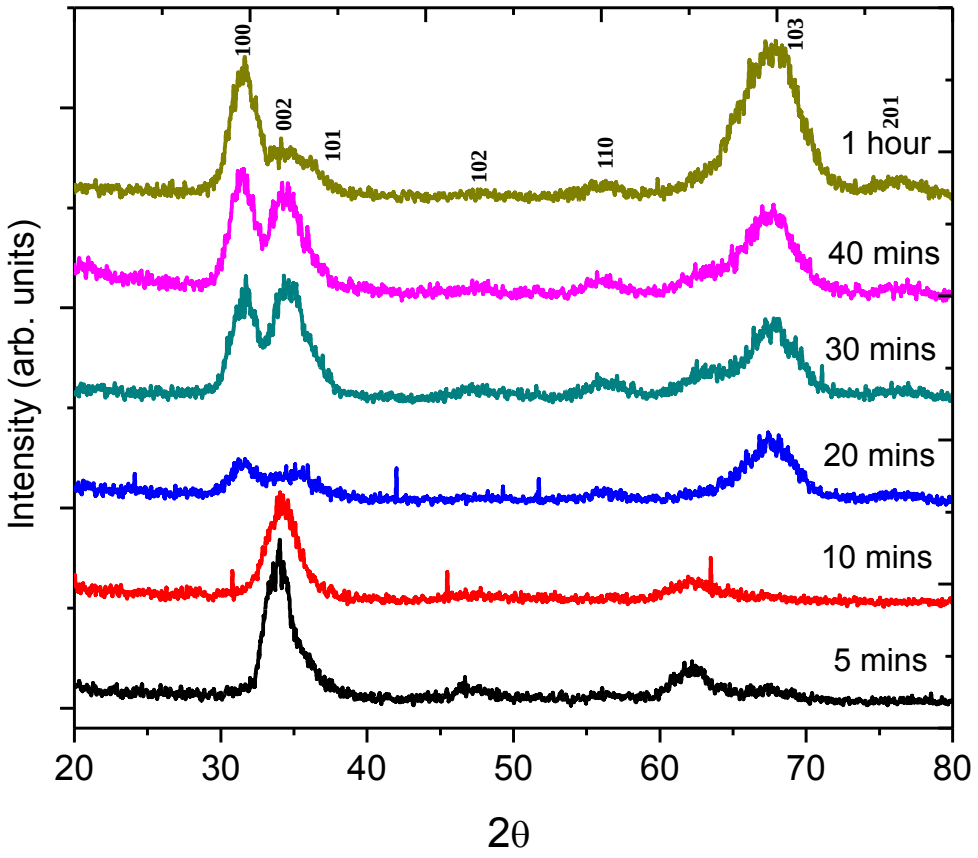


Figure 5-9: X-ray diffraction (XRD) pattern of the Al doped ZnO thin film grown using varied deposition time.

Figure 5-9 shows the effect of varied deposition time on the XRD patterns. The films grown at 5 and 10 minutes shows that the film is polycrystalline in nature with a preferred orientation along *c*-axis *i.e.* (002) plane and certain fraction along (103) plane. Increasing the deposition time shows a decrease in (002) plane intensity and emergence of the (100) and (112) planes as the preferred orientations. In addition a shift to higher Bragg's angle is observed. This change in the preferred crystal orientation is attributed availability of more Al ions substituting Zn ions.

5.4.4. XRR measurements.

The surface and interface sensitivity of X-ray reflectivity (XRR) has also been exploited to determine the film density, interfacial roughness and thickness of Al doped ZnO films. The presence of smooth interfaces is responsible for the Kiessig oscillations in the XRR spectrum for a film deposited for 5 minutes. Figure 5-10 represents the simulation of the XRR data in which precise information of the layer thickness, film density, surface and interfacial roughness have been extracted for the layer.

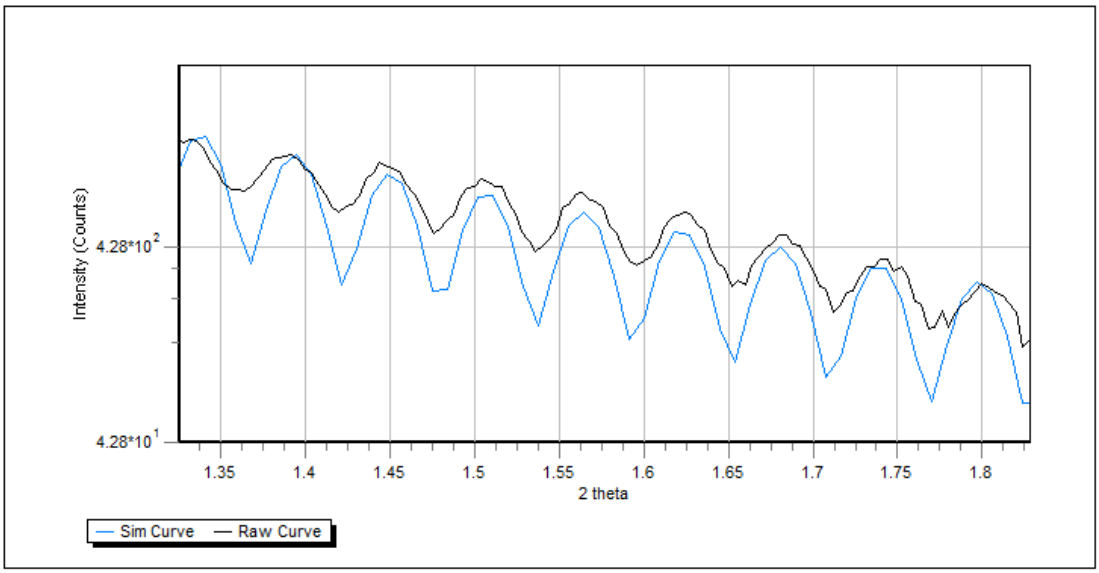


Figure 5-10: Experimental (black) and simulated (blue) XRR spectra of as-deposited Al doped thin film deposited at 100 W for 5 minutes.

From the simulation of the specular reflectivity, the thickness and rms roughness of the film deposited at 5 minutes was found to be 139.49 ±0.05nm and 0.51±0.05 nm, respectively. This implies a deposition rate of 278.98 Å/min. The density was found to be 5.56±0.1 gcm^{-3} which is in agreement with the literature value of 5.61gcm^{-3}. The value of the film thickness for film grown for 5 minutes is in agreement with that obtained from Surface profilometer as shown table 2. Further measurements of films grown at different deposition times reveal that films deposited on silicon substrates at room temperature show a greater dispersion as deposition time increases. This

is in agreement with the findings of Camacho-Espinosa, E., *et al* [29]. This could also be attributed to variation in the chamber pressure which was not easy to keep constant.

5.4.5. Photoluminescence measurements

5.4.5.1. Introduction.

The band-to-band excitation of ZnO promotes electrons from the valence band to the conduction band, leaving holes in the valence band. The holes migrate from the valence band to deep levels. Recombination between electrons and holes occurs through several pathways namely;

- electronic transitions from the conduction band
- electron transitions from shallow donor levels
- electron transitions to the trapped holes on the deep levels.

Basically, the Photoluminescence (PL) of ZnO is related to the presence of holes in the valence band [30]. Thus upon photoexcitation in a semiconductor, the photogenerated charge carriers are trapped almost instantaneously. This can take place in either shallow levels or in deep traps. Shallowly trapped charge carriers are still spatially delocalized. Due to this delocalization the energetic position of these shallow traps is related to the band structure of the material. An emission process may involve recombination of charge carriers to yield photons whose energy is close to the energy band gap of the semiconductor (nanoparticle etc). Such an emission is normally referred to as exciton emission. Localized states with energy deep in the band gap can be found either in the bulk or at the surface of a semiconductor particle. Their position of the emission energy is more or less independent of particle size and it is determined by the chemical nature of the trap and the surroundings of the trapped charge carrier. When trapping of a charge carrier occurs via a radiative process this is referred to as trap emission [31].

At room temperature ZnO films are usually known to exhibit an intense near band-edge UV emission peak centered around 380 nm. In addition to the strong UV emission, the films also show a broad emission peaks in violet, green and blue-green spectral regions. The enhanced PL peaks can be attributed to improved crystallinity of the deposited films which reduces the recombination centers in the films and consequently, decreases the non-radiative recombination processes. The reduction of the non-radiative recombination channels leads to an increase in the radiative recombination for non-equibrium photogenerated carriers [32].

[33]. The UV band emission is commonly referred to as the excitonic band emission and it is related to exciton recombination across the band gap at a specific temperature. On the other hand the wide visible band on the PL spectrum is as a result of the localized defect states in the band gap. Thus the nature of these emissions, their shapes and positions in the spectrum, is determined by the type of defect state and its populations [34]. To date the origin of visible emission remains consistently controversial.

As discussed in chapter 2 and 4, five species (oxygen vacancy (V_O), zinc vacancies (V_{Zn}), zinc interstitials (Zn_i), substitution of Zn at O position (O_{Zn}) and oxygen interstitials (O_i)) have been identified to contribute to the photoluminescence process in ZnO. The emission due to excitonic recombination processes and that due to the defect centers (visible emission) compete with each other through the quality of the ZnO produced and the lifetimes of the transitions. The visible emission involves a step in which a photogenerated hole is effectively trapped on the surface in the particle. For a ZnO nanoparticle the visible emission is expected to occur on the surface due to large surface to volume ratio. A probable candidate for the trapping of holes is O^{2-} ion at the surface.

Although the origin of the green emission is still controversial, it is generally accepted that it is associated with the deep-level oxygen vacancy. Furthermore, the fundamental carrier recombination dynamics of the green emission is still not well understood. The fundamental properties of the ZnO have been studied over several decades. Despite many years of extensive studies some of the fundamental properties of the luminescence in ZnO are still not fully understood. One of the poorly understood concept is the origin of the room temperature photoluminescence (PL) structure [35]. Usually the green luminescence is centered between 2.3 and 2.5 eV and reported to be produced by various sources, in some instances it has been attributed to the zinc vacancies, oxygen antisites, singly ionized oxygen vacancies and surface defects etc. [6]. According to Reynolds et al [36] and Kohan et al [37], this luminescence can be as a result of Zn vacancy. This is justified by calculated transition level between -1 and -2 charge states that occurs at 0.9 eV above the VBM and hence a transition between the conduction band (or a shallow donor) and the V_{Zn} acceptor level would give rise to luminescence around 2.4 eV [6] which is also in agreement with the experimental data both under 229 and 514.5 nm excitation line.

The room temperature emissions for two different excitation wavelengths are explored. The use of different excitation wavelengths is useful in examining the luminescence spectra of materials containing multiple defect levels, since these defect centres exhibit different optical response to multi- excitation wavelengths. Thus the sub-band excitations of ZnO can be used probe directly the radiative relaxations of these defect levels.

5.4.5.1. Photoluminescence of Al:ZnO (AZnO) films using 514.5nm excitation line.

Room-temperature PL spectra of AZnO films deposited a varied times and later annealed at various temperatures are shown in Figure 5-11. The PL spectra of AZnO thin films exhibit two

emissions: a strong green emission located at ~518nm and a weak broad emission band in the orange-red visible range.

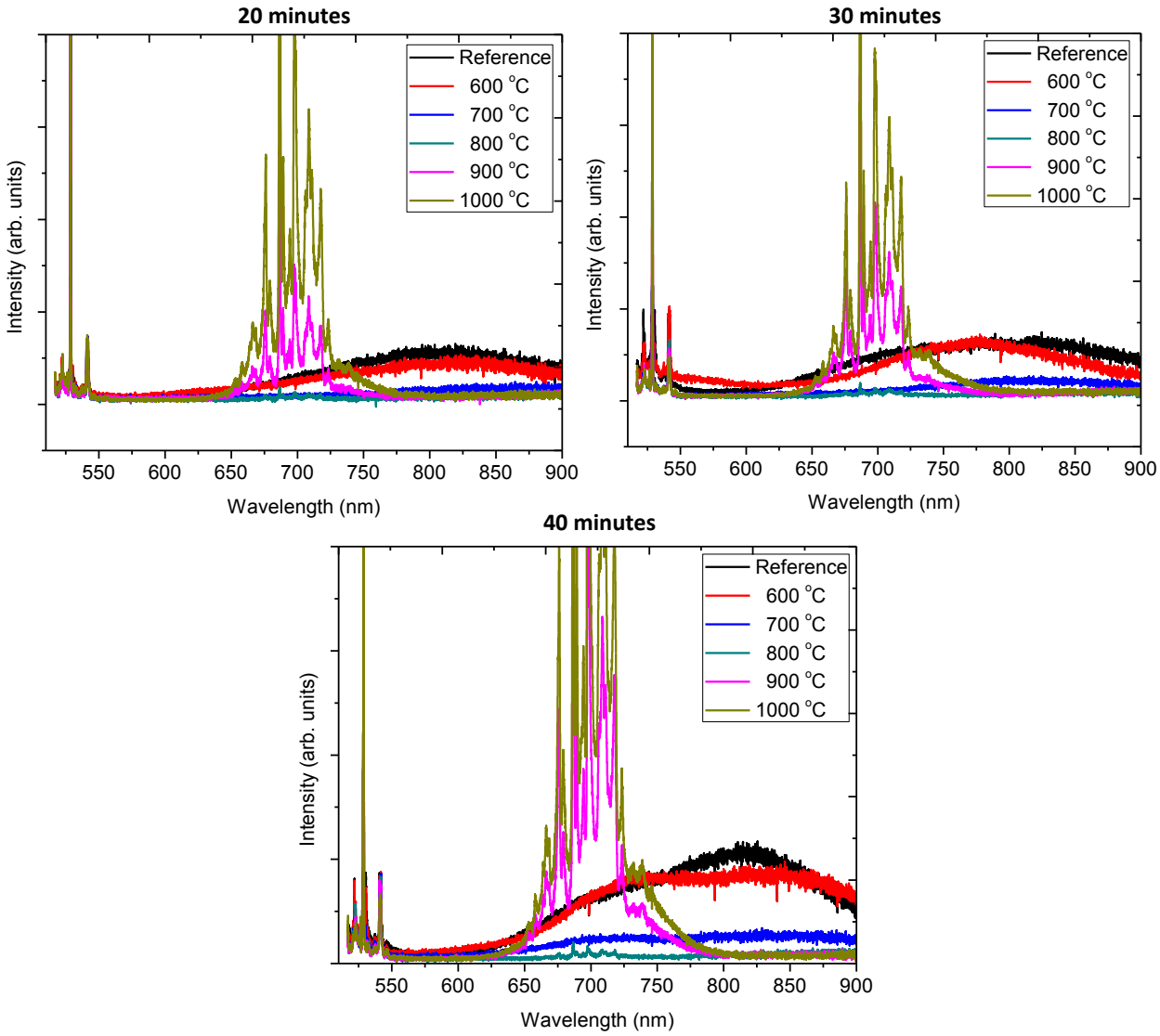


Figure 5-11: Room temperature photoluminescence spectra of Al doped ZnO thin film grown for 20, 30 and 40 minutes before and after annealing at temperature between 600-1000 ˚C in air.

From figure 5-11, the as-deposited film shows a green and a broad orange-red emission. It can be observed that the green defect emission from the films did not exhibit significant changes with annealing in air, while orange-red emission intensity reduces with annealing. Green emission has been previously attributed to surface defects [40], as well as the defects just below the crystallite

surface[41]. Such defects include singly ionized oxygen vacancy V_o^+, V_o^{2+} center, oxygen antisite as well as zinc vacancy V_{Zn} [42].

The importance of band bending at grain boundaries has also been cited [40]. Band bending will result in creation of a depletion region at the grain boundaries, which will affect the ionization state of the defects within the depletion region. Since the films have a large surface area and lots of grain boundaries, the green emission likely originates from donor– acceptor defect transitions, where donor and/or acceptor defects are located at surfaces or grain boundaries. The exact chemical nature of those defects, however, is difficult to establish since no significant changes with annealing are observed.

The orange-red emission has been associated with excess oxygen [42] as well as to the interstitial zinc Zn_i. This reduction can be ascribed to excessive oxidized layers formed on the surface and at the grain boundary of ZnO thin films upon annealing in air. Generally the intensity of emission is temperature dependent and it is usually described in the form of equation 5-2

$$I(T) = \frac{I_0}{1 + \alpha \exp(-E_T / kT)} \quad \ldots\ldots\ldots\ldots\ldots\ldots\ldots\ldots \text{5-2}$$

$$I(T) = \frac{I_0}{1 + \alpha_1 \exp(-E_{T1} / kT) + \alpha_2 \exp(-E_{T2} / kT)} \quad \ldots\ldots \text{5-3}$$

where α is the process rate parameter, E_T is the activation energy, k is the Boltzmann constant, and T is temperature [42]. Equation 5-3 gives a description of two competitive non-radiative channels (activation energies) or the description of different responses in low and high temperature regimes. At low temperatures, the emission intensity is dominated by the low activation energy which may be as a consequence of T^{-2} temperature dependence of the capture section for carriers at recombination centers [43].

Annealing at temperatures above 900 ˚C, several emission peaks appear in the region between 650-750 nm as shown in figure 5-11. This could be attributed to heavy inter-diffusion of the Si from the substrate and Al into the substrate.

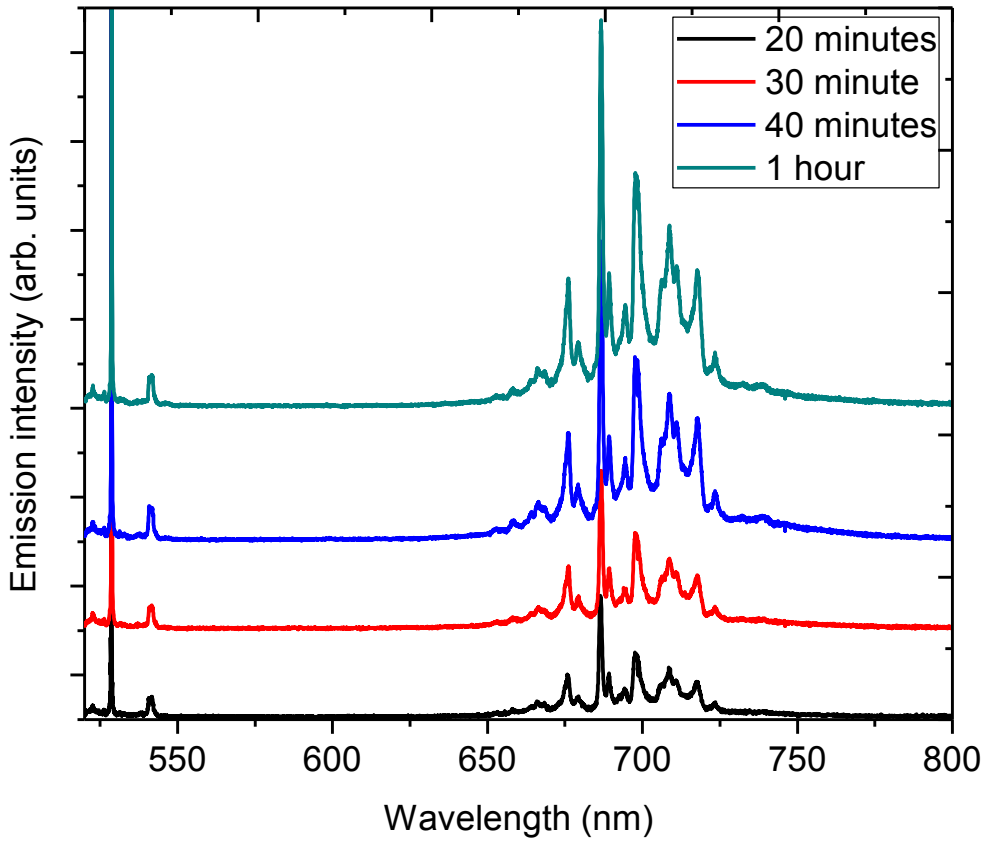


Figure 5-12: Room temperature photoluminescence spectra of Al doped ZnO thin film grown for 20,30 and 40 minutes before and after annealing at 900 ˚C

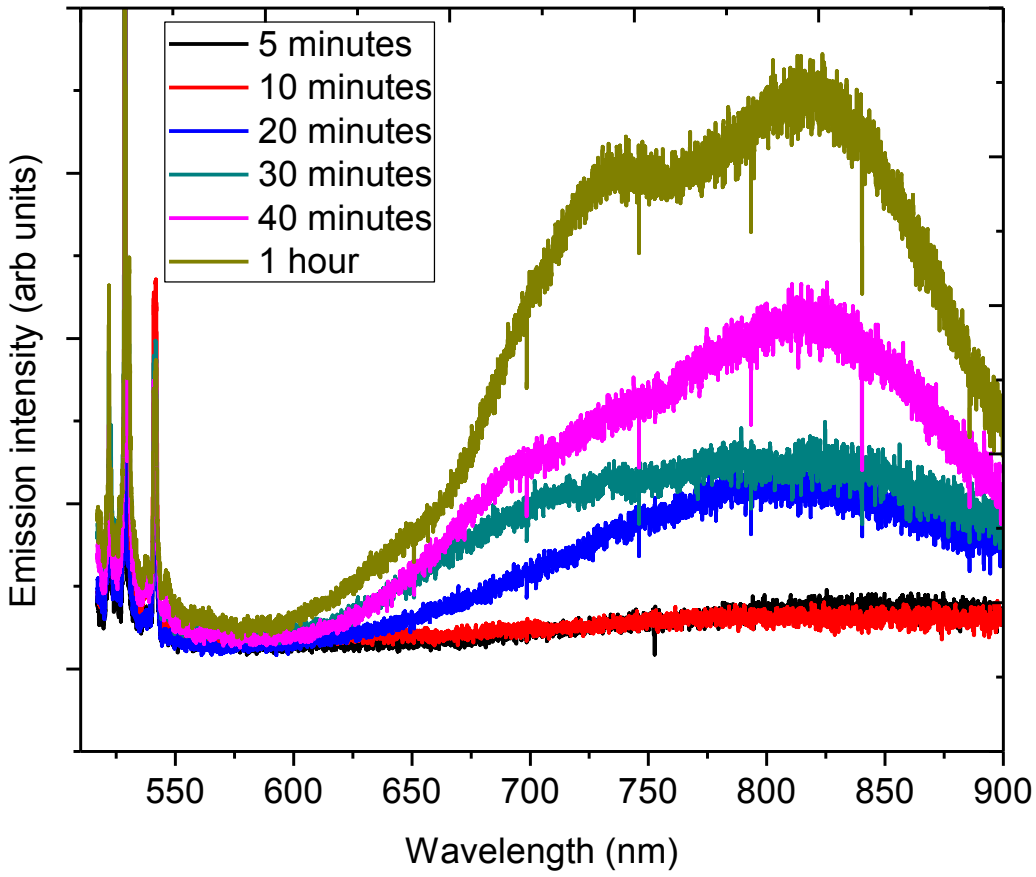


Figure 5-13: PL spectrum showing the effect of variation of deposition time on the emission spectrum.

From the room temperature PL spectra of the AZO film deposited at different deposition times shown in figure 5-12, it can be clearly seen that the PL spectra intensity increased markedly with the deposition time. This could be related to the sampled volume of the material which scales with the film thickness. The enhanced PL peaks can be attributed to improved crystallinity of the deposited films. The improved crystallinity reduces the recombination centers in the films and consequently, decreases the probability of non-radiative recombination. This leads to an increase in the radiative recombination for non-equibrium photogenerated carriers [32].

It should be noted herein that although an extrinsic donor such as substitutional aluminum (Al^{3+}) is one of the major type of defect responsible for the increase in the defect state emission, this is not discernible from the PL spectra taken at RT since this level is formed very close to the

conduction band. Furthermore its low ionization energy in ZnO (i.e., 0.053 eV) enables it to be easily donated to this band at room temperature. Similar observations have also been reported in the literature, wherein the identification of defect states formed due to Al doping in ZnO was not possible [44].

5.4.5.2. Photoluminescence of ZnO using 244 nm excitation line

The use of 229 nm excitation line with a higher energy (5.41 eV) relative to the band gap of Al doped ZnO (3.2-3.3 eV) allows for more emissions as shown in Figure 5-13. Figure 5-13 shows room temperature photoluminescence spectra of Al doped ZnO before and after annealing. The spectra were acquired using a 229 nm excitation line from a frequency-doubled argon ion laser. The spectrometer utilized a 150 lines/mm grating and a 20X UVB objective. The spectrum was acquired from 250nm to 900nm at 5 seconds acquisition time.

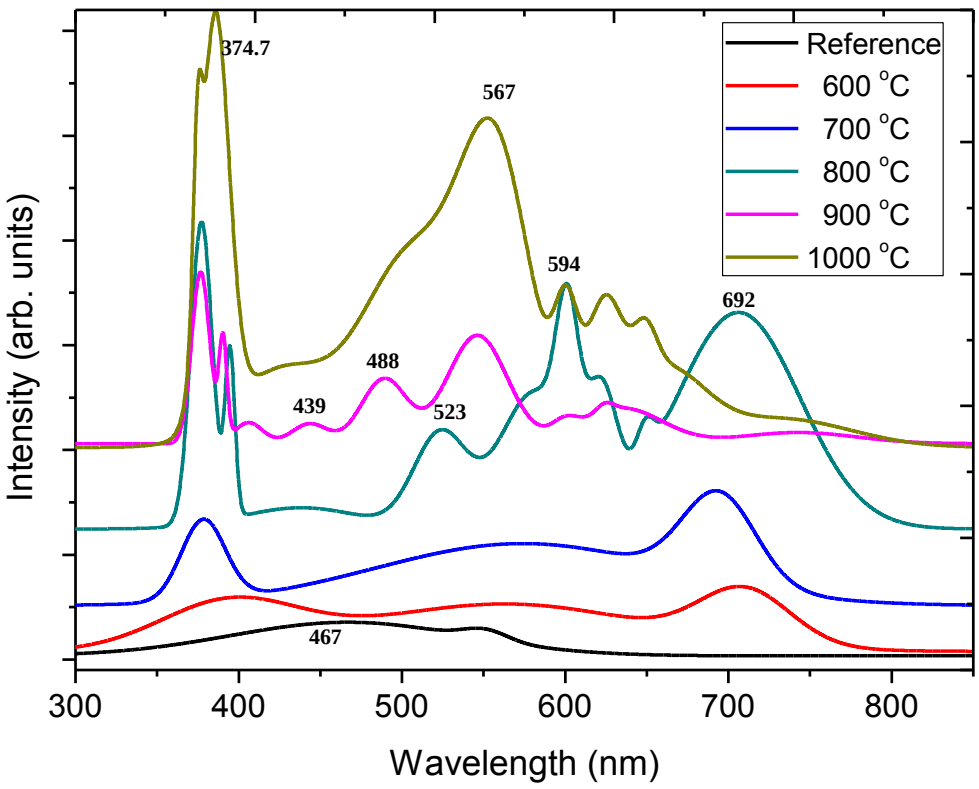


Figure 5-14: Room temperature photoluminescence spectra of Al doped ZnO thin film grown for 40 minutes before and after annealing at temperature between 600-1000 °C in air. The spectra have been stacked for clarity

The thin films grown at a duration of 40 minutes (Figure 5-14) show an emission band at 467 nm (2.7 eV). This band is attributed to the near band edge (NBE) emission corresponding to the exciton related transition from localized level below the conduction band to the valence band. The relatively high wavelength of this band could be as a result of substitution of Zn^{2+} that has a higher ionic radius, 0.074 nm with Al^{3+} of ionic radius 0.053 nm. This confirms the observation made in XRD analysis. Annealing of this film leads blue-shifting of this peak to around 374.7 nm (3.31 eV) when annealing temperature is 1000 ˚C. Several other bands are also formed as shown in figure 5-13. During annealing in air Zn interstitials could be reduced or removed since they are shallow donors hence separating the conduction band and other defect band leading to a wider optical band gap due to reduced overlapping of the defect and conduction bands.

The band at 439 nm (2.82 eV) emerges when annealing is carried out at 800 ˚C and increases in intensity with temperature. This could be attributed to O_i centers, which promotes the chemisorption of oxygen hence increasing the density of electronic state in the film [9]. Other bands also emerge upon annealing at 800 ˚C such as at 488 nm that may be associated to Zn_i^+ and 545 & 600 nm associated with $Zn_i^+ \rightarrow V_{Zn}^-$ transition. The band at 523 nm increases in intensity upon annealing at 800 ˚C. This response of the emission with temperature is a finger print of the increase in the concentration of O vacancies with increasing temperature.

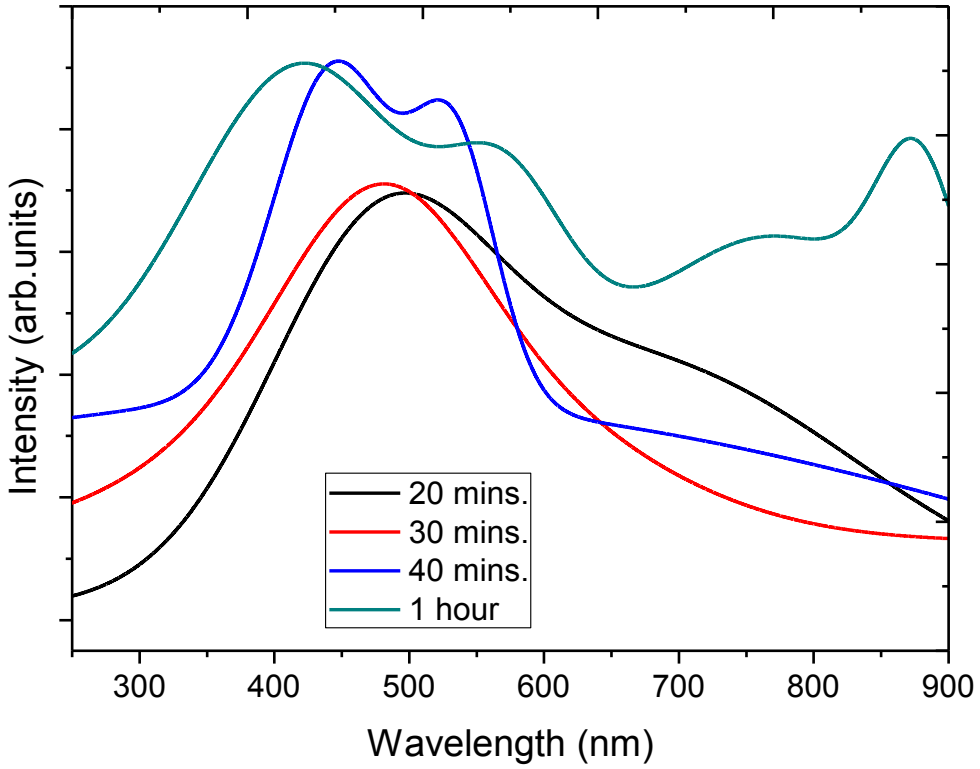


Figure 5-15: Room temperature photoluminescence spectra of Al doped ZnO thin film as-grown at an RF power of 100 W at different deposition time.

The thin films grown at 20 minutes (Figure 5-15) show a blue band near 474 nm (2.62 eV) and a broad shoulder near 720-730 nm due to defect level emission (DLE). This band (2.62 eV) is attributed to the near band edge (NBE) emission. Increasing the deposition time leads to blue-shifting of this peak to around 421 nm (2.95 eV) when deposition time is 1 hour. The infrared

emission at 830.0 nm when the film is grown for 1 hour could be attributable to an electronic transition from the O_i to the higher V_{Zn} – level.

5.5. Conclusion

The influences of thermal annealing and deposition time on the structural and optical features of radio frequency (RF) magnetron sputtered self-assembled aluminium doped Zinc Oxide on Si (100) are investigated. Preferentially oriented structures of Al doped ZnO along the (100), (002) and (112) directions together with peak shift and reduced strain due to post-annealing at between 600-1000 ◦C are discerned from x-ray diffraction (XRD) measurement. There was an evident increase in intensity with annealing temperature up to a temperature of 900 ˚C while the full wavelength at half maxima (FWHM) reduced. This was attributed to an enhancement of crystallinity of the films with increasing annealing temperature. The increase in peak intensity was also be as a result of thermally activated mobility of the atoms in the films leading to the possible decrease in the structural or native defects in the ZnO films. Atomic force microscopy (AFM) images showed increasing roughness and particle size. We observed meso-flat islands at low deposition time, an indication of highly dendritic shapes being formed in accordance to Volmer-Weber growth mode. An increase in deposition time led to formation of "spherical" like thicker films leading to the increase in grain height with time as well as film thickness as confirmed using thickness profilometer. The observed blue-shift and emerging of many photoluminescence peaks resulting from thermal annealing and increase in deposition time have been reported.

5.6. References (for chapter 5)

[1] G.-S. Kim, S. Ansari, H.-K. Seo, Y.-S. Kim, H.-S. Shin, Effect of annealing temperature on structural and bonded states of titanate nanotube films, Journal of applied physics, 101 (2007) 24314-24314.

[2] W.M. Yen, H. Yamamoto, Phosphor handbook, CRC press, 2006.

[3] S. Heinze, A. Krtschil, J. Bläsing, T. Hempel, P. Veit, A. Dadgar, J. Christen, A. Krost, Homoepitaxial growth of ZnO by metalorganic vapor phase epitaxy in two-dimensional growth mode, Journal of Crystal Growth, 308 (2007) 170-175.

[4] T. Ive, T. Ben-Yaacov, C. Van de Walle, U. Mishra, S. DenBaars, J. Speck, Step-flow growth of ZnO (0001) on GaN (0001) by metalorganic chemical vapor epitaxy, Journal of Crystal Growth, 310 (2008) 3407-3412.

[5] F. Quaranta, A. Valentini, F.R. Rizzi, G. Casamassima, Dual-ion-beam sputter deposition of ZnO films, Journal of applied physics, 74 (1993) 244-248.

[6] A. Janotti, C.G. Van de Walle, Fundamentals of zinc oxide as a semiconductor, Reports on Progress in Physics, 72 (2009) 126501.

[7] S. Pandelides, Deep Centers in Semiconductors: A State-of-the-Art Approach, in, Gordon and Breach Science, Yverdon, 1992.

[8] R.K. Willardson, E.R. Weber, M. Stavola, Identification of defects in semiconductors, Academic Press, 1998.

[9] S.-Y. Kuo, K.-C. Liu, F.-I. Lai, J.-F. Yang, W.-C. Chen, M.-Y. Hsieh, H.-I. Lin, W.-T. Lin, Effects of RF power on the structural, optical and electrical properties of Al-doped zinc oxide films, Microelectronics Reliability, 50 (2010) 730-733.

[10] Z. Fang, Z. Yan, Y. Tan, X. Liu, Y. Wang, Influence of post-annealing treatment on the structure properties of ZnO films, Applied Surface Science, 241 (2005) 303-308.

[11] A.C.S. Sabioni, About the oxygen diffusion mechanism in ZnO, Solid State Ionics, 170 (2004) 145-148.

[12] A. Janotti, C.G. Van de Walle, Oxygen vacancies in ZnO, Applied Physics Letters, 87 (2005) 122102.

[13] J.-P. Colinge, Silicon-on-Insulator Technology: Materials to VLSI: Materials to Vlsi, Springer Science & Business Media, 2004.

[14] C.-m. Lai, K.-m. Lin, S. Rosmaidah, Effect of annealing temperature on the quality of Al-doped ZnO thin films prepared by sol–gel method, Journal of sol-gel science and technology, 61 (2012) 249-257.

[15] Z. Tang, P.C. Chan, R.K. Sharma, G. Yan, I.-M. Hsing, J.K. Sin, Investigation and control of microcracks in tin oxide gas sensing thin-films, Sensors and Actuators B: Chemical, 79 (2001) 39-47.

[16] K.A. Alim, V.A. Fonoberov, M. Shamsa, A.A. Balandin, Micro-Raman investigation of optical phonons in ZnO nanocrystals, Journal of Applied Physics, 97 (2005) 124313-124313.

[17] V. Russo, M. Ghidelli, P. Gondoni, C. Casari, A.L. Bassi, Multi-wavelength Raman scattering of nanostructured Al-doped zinc oxide, Journal of Applied Physics, 115 (2014) 073508.

[18] M. Tzolov, N. Tzenov, D. Dimova-Malinovska, M. Kalitzova, C. Pizzuto, G. Vitali, G. Zollo, I. Ivanov, Vibrational properties and structure of undoped and Al-doped ZnO films deposited by RF magnetron sputtering, Thin Solid Films, 379 (2000) 28-36.

[19] A. Iqbal, M. Zakria, A. Mahmood, Structural and spectroscopic analysis of wurtzite (ZnO) 1− x (Sb 2 O 3) x composite semiconductor, Progress in Natural Science: Materials International, 25 (2015) 131-136.

[20] A. Ismail, M. Abdullah, The structural and optical properties of ZnO thin films prepared at different RF sputtering power, Journal of King Saud University-Science, 25 (2013) 209-215.

[21] Ü. Özgür, Y.I. Alivov, C. Liu, A. Teke, M. Reshchikov, S. Doğan, V. Avrutin, S.-J. Cho, H. Morkoç, A comprehensive review of ZnO materials and devices, Journal of Applied Physics, 98 (2005).

[22] K.S. Kim, H.W. Kim, N.H. Kim, Structural characterization of ZnO films grown on SiO 2 by the RF magnetron sputtering, Physica B: Condensed Matter, 334 (2003) 343-346.

[23] M. Najafi, H. Haratizadeh, The effects of Al doping and post-annealing via intrinsic defects on photoluminescence properties of ZnO: Eu nanosheets, Materials Science in Semiconductor Processing, 31 (2015) 76-83.

[24] T.M.K. Thandavan, S.M.A. Gani, C. San Wong, R.M. Nor, Enhanced Photoluminescence and raman properties of Al-Doped ZnO nanostructures prepared using thermal chemical vapor deposition of methanol assisted with heated brass, PloS one, 10 (2015) e0121756.

[25] V. Noack, A. Eychmüller, Annealing of nanometer-sized zinc oxide particles, Chemistry of materials, 14 (2002) 1411-1417.

[26] F. Wang, M. Wu, Y. Wang, Y. Yu, X. Wu, L. Zhuge, Influence of thickness and annealing temperature on the electrical, optical and structural properties of AZO thin films, Vacuum, 89 (2013) 127-131.

[27] G.W. Tomlins, J.L. Routbort, T.O. Mason, Zinc self-diffusion, electrical properties, and defect structure of undoped, single crystal zinc oxide, Journal of Applied Physics, 87 (2000) 117-123.

[28] S. Thanikaikarasan, T. Mahalingam, K. Sundaram, A. Kathalingam, Y.D. Kim, T. Kim, Growth and characterization of electrosynthesized iron selenide thin films, Vacuum, 83 (2009) 1066-1072.

[29] E. Camacho-Espinosa, E. Rosendo, T. Díaz, A. Oliva, V. Rejon, J. Peña, Effects of temperature and deposition time on the RF-sputtered CdTe films preparation, Superficies y vacío, 27 (2014) 15-19.

[30] K. Bouzid, A. Djelloul, N. Bouzid, J. Bougdira, Electrical resistivity and photoluminescence of zinc oxide films prepared by ultrasonic spray pyrolysis, physica status solidi (a), 206 (2009) 106-115.

[31] A. Van Dijken, E. Meulenkamp, D. Vanmaekelbergh, A. Meijerink, Identification of the transition responsible for the visible emission in ZnO using quantum size effects, Journal of Luminescence, 90 (2000) 123-128.

[32] K. Prabakar, C. Kim, C. Lee, UV, violet and blue-green luminescence from RF sputter deposited ZnO: Al thin films, Crystal Research and Technology, 40 (2005) 1150-1154.

[33] B. Cao, W. Cai, H. Zeng, G. Duan, Morphology evolution and photoluminescence properties of ZnO films electrochemically deposited on conductive glass substrates, Journal of applied physics, 99 (2006) 073516.

[34] M. Balestrieri, G. Ferblantier, S. Colis, G. Schmerber, C. Ulhaq-Bouillet, D. Muller, A. Slaoui, A. Dinia, Structural and optical properties of Yb-doped ZnO films deposited by magnetron reactive sputtering for photon conversion, Solar Energy Materials and Solar Cells, 117 (2013) 363-371.

[35] W. Shan, W. Walukiewicz, J. Ager III, K. Yu, H. Yuan, H. Xin, G. Cantwell, J. Song, Nature of room-temperature photoluminescence in ZnO, Lawrence Berkeley National Laboratory, (2004).

[36] D.C. Reynolds, D.C. Look, B. Jogai, H. Morkoc, Similarities in the bandedge and deep-centre photoluminescence mechanisms of ZnO and GaN, Solid State Communications, 101 (1997) 643-646.

[37] A. Kohan, G. Ceder, D. Morgan, C.G. Van de Walle, First-principles study of native point defects in ZnO, Physical Review B, 61 (2000) 15019.

[38] B. Lin, Z. Fu, Y. Jia, Green luminescent center in undoped zinc oxide films deposited on silicon substrates, Applied Physics Letters, 79 (2001) 943-945.

[39] A.K. Srivastava, J. Kumar, Effect of zinc addition and vacuum annealing time on the properties of spin-coated low-cost transparent conducting 1 at% Ga–ZnO thin films, Science and Technology of Advanced Materials, (2016).

[40] A.B. Djurišić, Y.H. Leung, Optical properties of ZnO nanostructures, small, 2 (2006) 944-961.

[41] S. Studenikin, N. Golego, M. Cocivera, Fabrication of green and orange photoluminescent, undoped ZnO films using spray pyrolysis, Journal of Applied Physics, 84 (1998) 2287-2294.

[42] K. Tam, C. Cheung, Y. Leung, A. Djurišic, C. Ling, C. Beling, S. Fung, W. Kwok, W. Chan, D. Phillips, Defects in ZnO nanorods prepared by a hydrothermal method, The Journal of Physical Chemistry B, 110 (2006) 20865-20871.

[43] J. Krustok, H. Collan, K. Hjelt, Does the low-temperature Arrhenius plot of the photoluminescence intensity in CdTe point towards an erroneous activation energy?, Journal of applied physics, 81 (1997) 1442-1445.

[44] C. Singh, E. Panda, Variation of electrical properties in thickening Al-doped ZnO films: role of defect chemistry, RSC Advances, 6 (2016) 48910-48918.

Chapter 6: Structural and optical study of annealed ZnO:Tb^{3+} and Zn:Eu^{3+} nano-polycrystalline thin films and their application for down conversion in solar cells.

6.1 Introduction

Rare-earth (RE)-doped semiconductors have attracted extensive interest for possible applications in high power lasers, optical manipulation as visible emitting phosphors in display devices, and other optoelectronic products [1, 2]. This enormous interest for their application potential is attributed to the stable intra-4f shell transitions of the rare earth ions which favor the energy transfer from host semiconductors to dopant RE ions [3]. These transitions are shielded from their local environments by the completely filled $5s^2$ and $5p^6$ outer orbitals.

Zinc oxide (ZnO) thin film technology has continued to attract widespread research interest as a transparent conducting oxide (TCOs) due to its high electrical conductivity (2×10^{-6} to 2×10^{-4} S/cm) [4] and optical transmission (> 80% in the UV-Visible range). This has been evidenced mainly in n-type ZnO due to the favorable formation energies of the Zn^{2+}/O^{2-} defects. Besides ZnO is a wide and direct band gap (about 3.3 eV at room temperature) with large exciton binding energy (60 meV), excellent chemical and thermal stability and can be cost effectively and easily fabricated [5]. These properties enable it to be considered as a favorable candidate for use as transparent electrode in solar cells. Zinc oxide thin films can be grown using several methods such as magnetron sputtering, sol gel technique, spray pyrolysis, CVD, and PECVD [6, 7]. RF sputtering is usually preferred mainly due to its reproducibility, high deposition rate, low substrate temperature and ability to give films with tunable preferred orientation [8, 9].

When doped with a rare earth metal, ZnO can be used as sensitizer to excite rare-earth(RE) ions such as Ce^{3+}, Er^{3+}, Ho^{3+}, Nd^{3+}, Tm^{3+}, Dy^{3+}, Eu^{3+} and Tb^{3+}. This is made possible due to its large absorption cross-section and broad excitation spectrum [10]. This way, the REs are able to absorb

the UV-blue emission from ZnO and emit in the visible or infra-red range thus enabling this material to serve as an excellent doping host for rare earth ions with an optimal spectrum modifying matrix for diverse solar cells.

The optical properties of RE doped ZnO usually depend on the dopant concentrations, fabrication process as well as the host structure which is sensitive to the crystal field energy and spin-orbit coupling. The emission characteristics of the rare earth ion in ZnO are sensitive to the nature of the fabrication process, the size of the ZnO nano-crystals and their morphology. The morphology and structure of thin films can be tuned by changing the ad-atom energies and mobility through thermal treatment. Enhancing film crystallinity during growth due to lattice strains and thermal stresses between the ZnO film and the substrate presents one approach to spectrum modification in these films [1].

In organic solar cells, ZnO is widely used as a buffer layer since it has a low work function, excellent optical transparency, high electron mobility, and ease of fabrication [11]. Combining the positive attributes of ZnO and RE in organic solar cell would therefore be a good spectrum modifying matrix with dual functionality as an electron transporting layer and as a photon-conversion layer as well. In addition, the implementation of the buffer layer requires a simple architecture with no losses induced by the space gap between the down converting layer and active layers, a feature that is consistently persistent in externally stacked phosphor based photovoltaic devices.

In this chapter, the effect of annealing on the structure, morphology and optical properties of room temperature Tb^{3+} and Eu^{3+} doped ZnO thin films for photovoltaic applications through spectrum modification is reported. All films have been deposited using RF magnetron sputtering. As a proof of concept, pristine and doped ZnO thin films deposited on ITO glass have been

incorporated as separate bi-functional layers in inverted organic solar devices. In these devices the P3HT:$PC_{61}BM$ blend was used as the active layer of the bulk heterojunction (BHJ) in the following device architectures; Glass/ITO/ZnO/P3HT:PCBM/PEDOT:PSS/Al and Glass/ITO/ZnO:Tb^{3+}/P3HT:PCBM/PEDOT:PSS/Al, respectively. The donor and acceptors in the bulk heterojunction were mixed in the mass ratio of 1:1. We report an increase in efficiency of 17.2 %. This enhanced device performance may be attributed to the ZnO $\rightarrow$ Tb^{3+} energy transfer through the down-conversion process. All devices were fabricated and characterized at room temperature with exposure to air.

6.2. Experimental procedure

6.2.1. Materials

ZnO (97%): Tb (3%) (99.99% purity), ZnO (97%): Eu (3%) (99.99% purity and ZnO disks targets of diameter 76 mm and thickness 6 mm sourced from Semiconductor Wafer, Inc. (SWI) have been used for thin film deposition. The Si wafer (001) and quartz substrate were also purchased from Semiconductor Wafer, Inc. (SWI). ITO (surface resistivity: 30-60 Ω/sq.), PEDOT:PSS (1.3 wt% dispersion in H_2O), P3HT (purity: 99.995%) and PCBM (purity: 99.5%) were purchased from Sigma Aldrich.

6.2.2. The growth of ZnO:Tb^{3+} and ZnO:Eu^{3+} thin films.

Tb^{3+} and Eu^{3+} doped ZnO thin films have been deposited at room temperature using RF magnetron sputtering onto n-type (001) Silicon-, ITO- and quartz- substrates. The substrates were initially cleaned with acetone and ethanol in an ultrasonic bath for 20 minutes and rinsed in deionized water before drying using a stream of dried nitrogen gas. They were then mounted on a rotating substrate holder at a distance of 6 cm from the target. The sputtering chamber was evacuated to a base

pressure of about 2.5×10^{-5} mbar while sputtering was performed under Argon with a working gas pressure of 3.1×10^{-3} mbar. The growth was undertaken under 13-sccm Ar flow, and 2.20 Wcm^{-2} RF power density. Post-growth annealing was carried out in Ar filled furnace at a heating rate of 10˚C/min over a temperature range of 600 - 900 ˚C for 2 hours.

6.2.3. Characterization

The film morphologies and structural analyses were characterized using Veeco Di-3100 atomic force microscopy (AFM) in tapping mode. Grazing incidence x-ray diffraction (XRD) measurement of the ZnO:Tb^{3+} and ZnO:Eu^{3+} thin film was taken using AXS Bruker D8 Discover, (40kV, 40 mA) using Cu Kα radiation in the Seeman-Bohlin geometry at a low scanning rate of 1.2^{o}/minute and glancing angle of 1˚. The transmittance spectra of the films deposited onto the quartz substrates were measured using a Cary 500 UV–visible spectrophotometer. Photoluminescence measurements were carried out using a Horiba LabRAM HR spectrometer with a 150 lines/mm grating and an excitation wavelength of 244 nm from a frequency doubled Lexel argon ion laser. Rutherford backscattering spectrometry (RBS) measurements were performed to determine the composition and distribution profiles of Tb^{3+} ions in the ZnO matrix at room temperature using $^{4}He^{+}$ particles of energy 1.6 MeV at a backscattering angle of 165º (IBM geometry). The beam current was kept between 10 and 15 nA during measurements.

6.3 Results and discussion of ZnO:Tb^{3+} thin films

6.3.1 Morphology Studies

Figure 6-1 shows the surface topography of the ZnO:Tb^{3+} films characterized using Veeco Di3100 AFM in tapping mode.

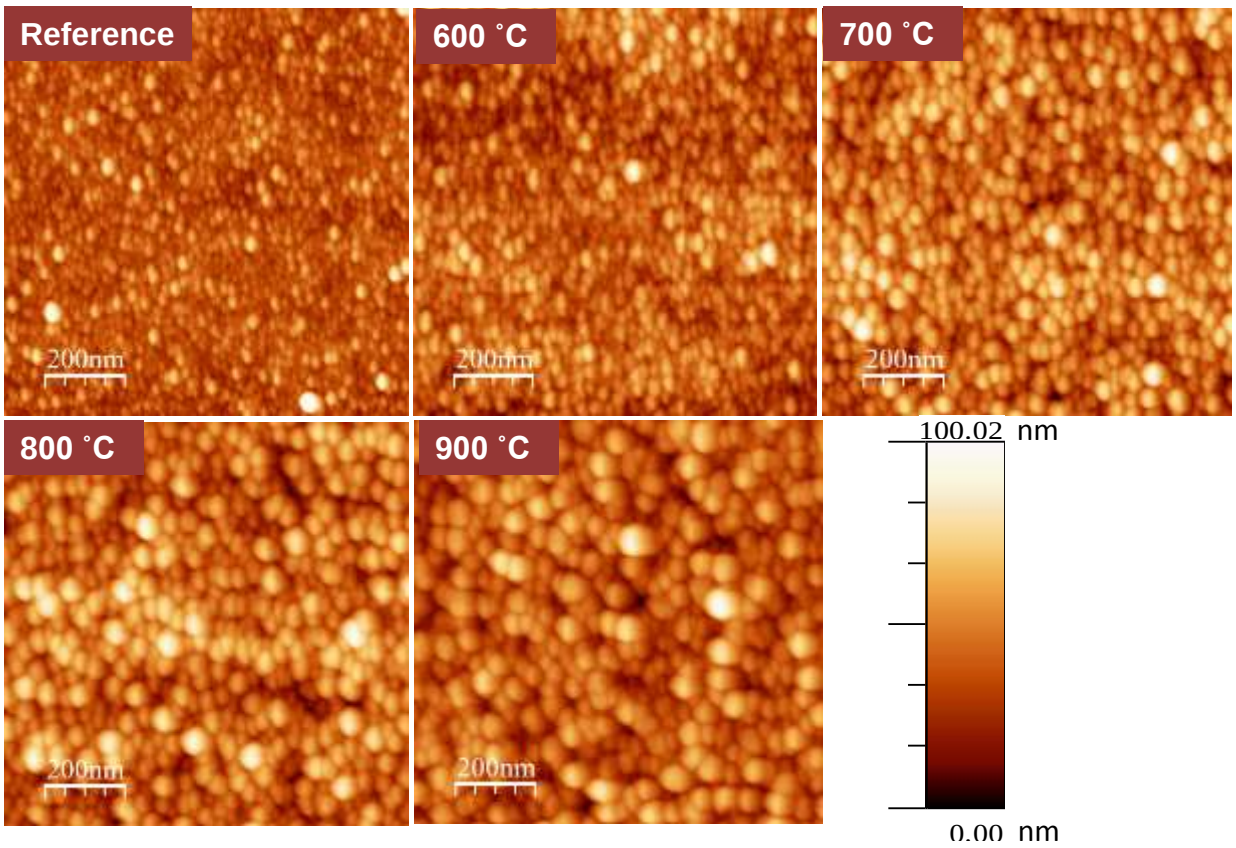


Figure 6-1: AFM images of pristine ZnO:Tb3+ films (room temperature) and after annealing in Ar filled furnace for 2 hours in the range between 600 and 900 ˚C.

The average roughness of the ZnO:Tb^{3+} film surface is shown in table 6-1 for all temperature ranges of interest. As the annealing temperature increases, the surface roughness of the film increases dramatically (from 4.9 nm for as-deposited ZnO:Tb^{3+} film to 36.9 nm at 900°C).

Table 6-1: Summary of Rms and grain height from taping mode AFM

Annealing Temperature (°C)	Roughness Rms (nm)	Grain height (nm)
RT	4.9	12.2
600	11.8	49.3
700	17.2	54.0
800	27.8	68.8
900	36.9	81.4

It is noted that the surface corrugations of ZnO:Tb^{3+} films analyzed from AFM represent possibly the particle size and could thus be larger than the grain size determined from GIXRD shown in Table 6-1. This is plausible since the particle size measured from AFM is the surface morphology of coalesced grains [12]. Furthermore the geometry of the XRD measurement of the grain size is normal to the surface of the film and not in plane. Diffusion with annealing also enables the atoms to occupy the lattice sites in the lattice thereby enhancing film quality as seen in the XRD data. The increase in grain height with annealing temperature is an indication of thermally activated diffusion of atoms that coalesce to larger grains in regions with lower activation barriers for self-diffusion [13, 14]. The major grain growth also results in an increase in the surface roughness as evident by the rms values.

6.3.2 Rutherford Backscattering Spectroscopy Measurements

A RBS spectrum of ZnO:Tb^{3+} thin film on Si substrate annealed at 700 ˚C is shown in Figure 6-2 together with - the simulation profile obtained using the XRump code. The experimental spectrum is well reproduced. The structure in the Si spectrum around channel 180, 260, 410 and 470 is due to the non-Rutherford scattering cross-section from O, Si, Zn and Tb respectively and the surface energy positions in channels of the elements have been shown using arrows. All other samples annealed at different temperatures showed insignificant change in surface energy position and concentration.

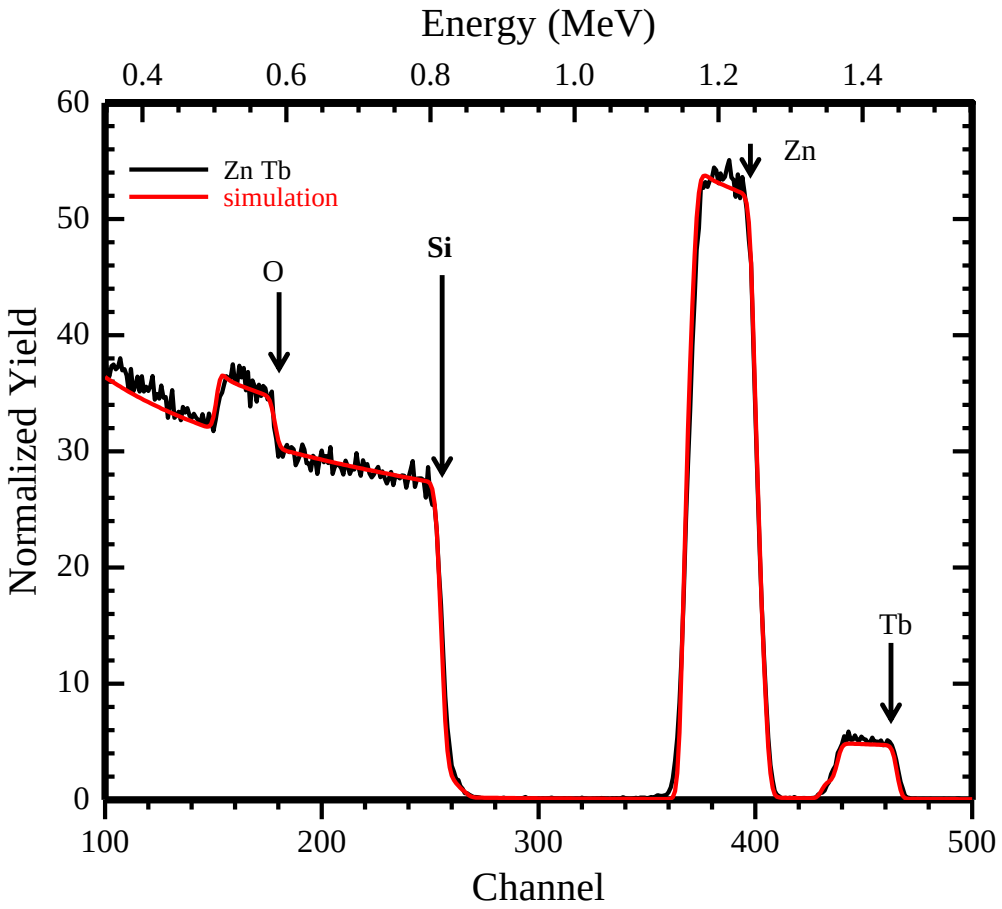


Figure 6-2: RBS spectrum of an 190 nm ZnO:Tb^{3+} layer on Si showing experimental data and computer simulation using XRump code. The sample structure and the thicknesses of the layers were derived.

The presence of Tb^{3+} in the films is very prominent and the global atomic concentrations of the different species contained in the film can be deduced. From the XRump simulation, stoichiometry of the matrix of 48.1, 49.2 and 2.7% for Zn, O and Tb, respectively was derived. The Tb^{3+} in channel 470 has a nearly flat yield suggesting a homogeneous distribution of the Tb^{3+} along the growth direction, which is independent of the annealing temperature.

6.3.3 Grazing incidence XRD measurements

Figure 6-3 shows the grazing incidence XRD patterns of pristine ZnO:Tb^{3+} and after annealing in the temperature range 600-900 ˚C in Ar filled furnace. The pristine ZnO:Tb^{3+} film appears as partially crystalline with low intensity of the (hkl) reflex. Annealing leads to preferred orientation of the ZnO reflexes. The typical strong diffraction peaks ascribed to hexagonal wurtzite ZnO (JCP2) card number 003-0888 were observed without any extra peaks from other oxide phases at elevated temperatures. This is an indication that the films were of high phase purity and that no diffraction peaks corresponding to Tb^{3+} based compounds or any other impurities were present. The diffraction peaks become gradually stronger up to 800°C, an indication of increasing crystallinity. The appearance of reduced peak intensity and dislocation density after annealing at 900 ˚C may be attributed to the presence of porosity [15]. The dislocation density d, defined as the length of dislocation lines per unit volume of the crystal (Williamson and Smallman) and the strain present in the thin film were also investigated and presented in Table 6-2.

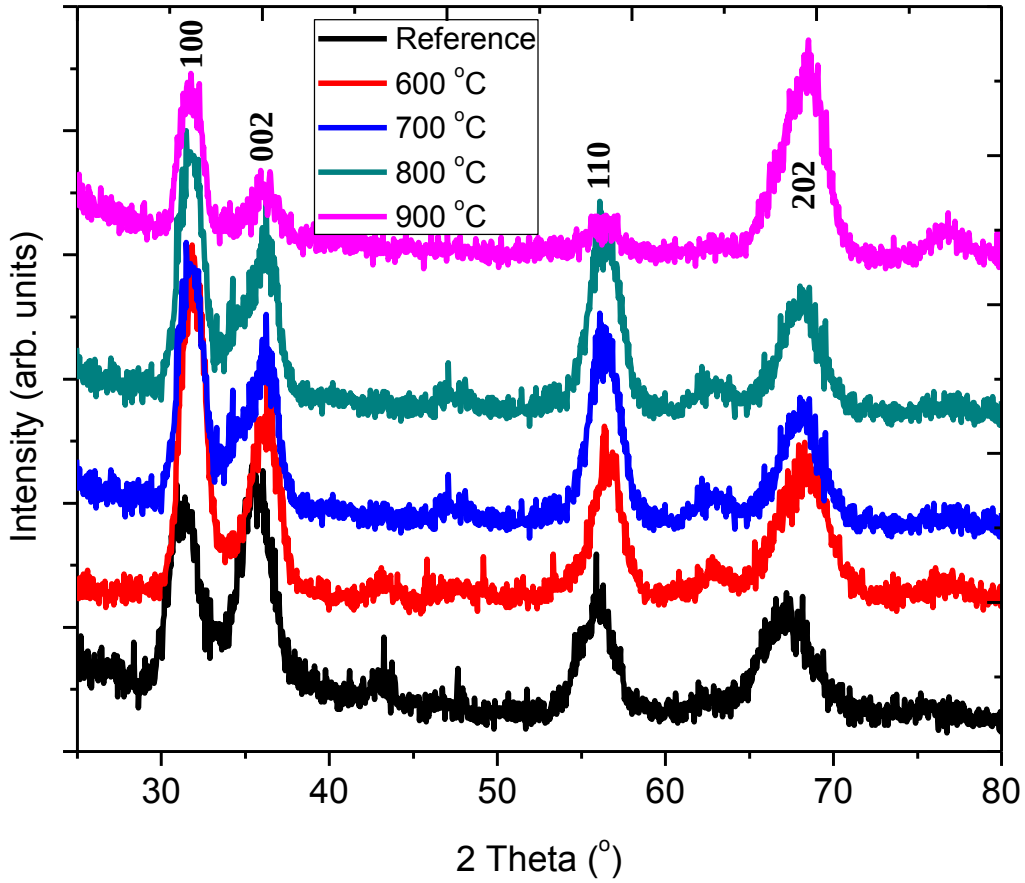


Figure 6-3: Grazing incidence X-ray diffraction of ZnO:Tb^{3+} thin films deposited by RF sputtering at room temperature then annealed different temperatures (600-900 ˚C).

Table 6-2: Characteristics of Tb^{3+} doped ZnO estimated from XRD measurements.

Temperature (˚C)	FWHM (100)	2 theta	Size, D (nm)	a/(Å)	c/(Å)	δ (10^{16})	ε (10^{-3})
Reference	1.620	31.397	5.09	3.28	5.69	3.86	6.81
600	1.473	31.901	5.61	3.23	5.61	3.18	6.18
700	1.332	31.784	6.19	3.24	5.63	2.63	5.59
800	1.332	31.764	6.20	3.25	5.63	2.60	5.57
900	1.207	31.820	6.84	3.25	5.64	2.14	5.07

6.3.4 Optical properties

Figure 6-4 shows the optical transmittance of pristine (183 nm) and annealed (190 nm) ZnO:Tb^{3+} films on quartz substrate in the wavelengths range of 250–800 nm. The sharp optical transmission edge observed around 380 nm corresponds to the inter-band transitions of the valence electrons consistent with the laser excitation energy used in the PL measurements. The contributions of the substrate have been de-convoluted from the transmission spectra through calibration using the substrates as the reference.

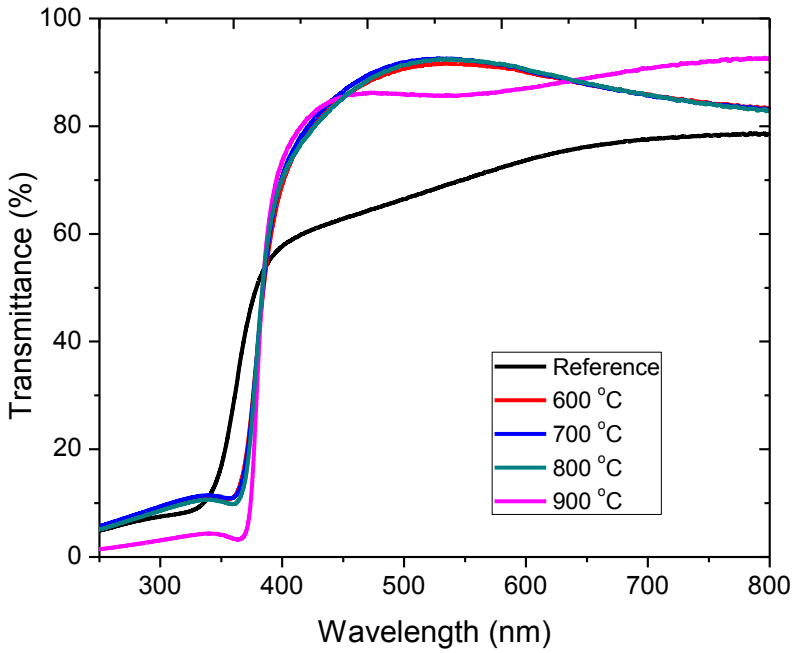


Figure 6-4: Transmission spectra of pristine ZnO:Tb^{3+} thin films and upon annealing at different temperatures, 600-900 ˚C in Ar filled furnace.

The average transmittance for all the deposited films is in the range between 71% and 92% within the visible region. Thus enabling the use of these ZnO:Tb^{3+} films in thin films solar cell applications [16]. At short wavelengths, a steep decrease in the transmittance around the absorption edge is evident. The enhanced absorption at 900 ˚C is attributed to increased crystallinity leading to decrease in the extinction coefficient as the structural defects are minimized with increasing

temperature thus increasing the absorption coefficient [17]. To correlate the effect of temperature and grain size with the optical properties of ZnO:Tb^{3+} thin films, the absorption coefficient (α) and the band gap (*Eg*) were determined from Tauc's formalism for direct and indirect transition in the form given in equation 6-1;

$$(\alpha hv) = A(hv - Eg)^{p} \quad \text{..... 6-1}$$

Where *A* is a constant, *h* is the Plank's constant and *P* is an exponent that dependent on the nature of the allowed or forbidden electronic transitions. Thus for an allowed direct transition $p = 1/2$. However $p = 3/2$ describes the case for forbidden direct transition, $p = 2$ for indirect allowed transition and $p = 3$ for indirect forbidden transitions. Since ZnO:Tb^{3+} is a direct band gap semiconductor with a hexagonal wurtzite crystal structure as confirmed in the GIXRD measurements, $p = 1/2$ was used in the analysis [18-20]. $h\upsilon$ is the photon energy expressed in eV while α is the absorption coefficient calculated using the relation in equation 6-2:

$$T = \exp(-\alpha d) \quad \text{..... 6-2}$$

where *T* is the optical transmittance and *d* is the thickness of ZnO:Tb^{3+} films.

The optical band gap of the films annealed at various temperatures was obtained by plotting $(\alpha hv)^2$ as a function of photon energy (*hv*). The values of the direct energy gap *Eg* were derived from the intercept after extrapolation to zero absorption with photon energy axis as shown in Figure 6-5. The non-zero absorbance below the energy cut-off for the pristine film is attributed to the phonon contributions associated with structural defects or trap states arising from a partially crystalline pristine ZnO:Tb^{3+} film.

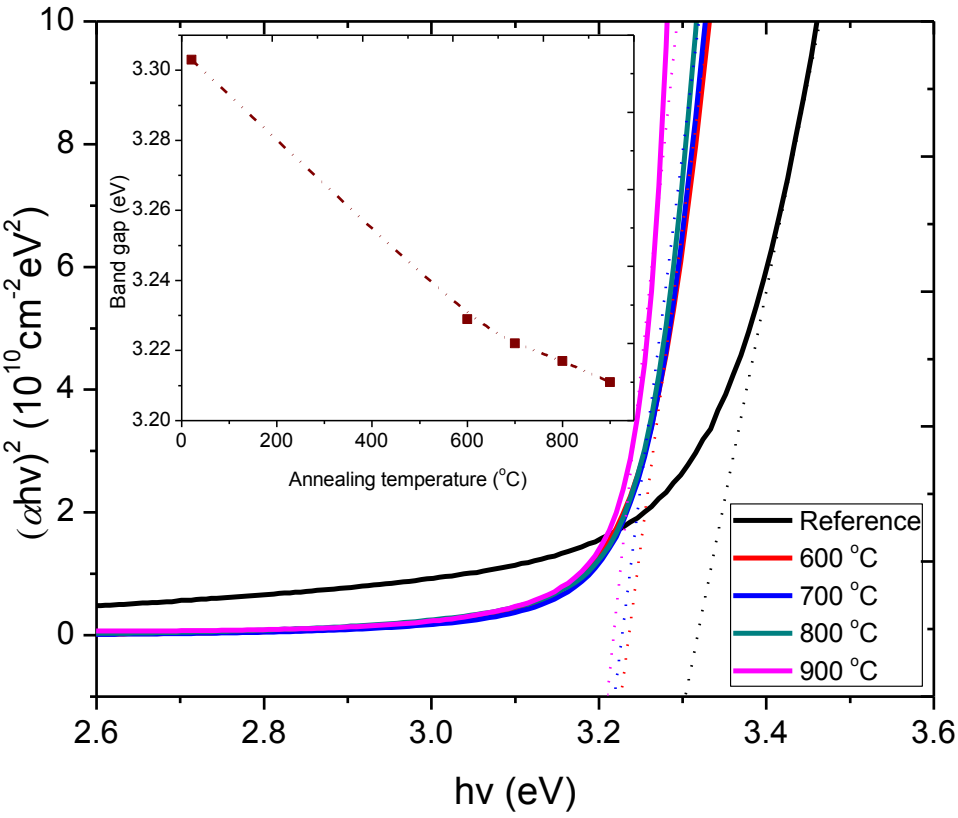


Figure 6-5: Plot of $(\alpha hv)^2$ versus hv for the pristine ZnO:Tb^{3+} thin film and after annealing at 600-900 ˚C. The inset shows the variation of optical band gap as a function of annealing temperature.

The sharpness of the absorption edge is found to be maximum at 800 ˚C annealing temperature, beyond which it broadens. The change in the optical band gap is comparatively small but a minimum is shown at 900 ˚C. The estimated values of the band gap for all the samples are summarized in the inset figure in Figure 5. These values are within the range reported for films and single crystal [21-23] and are also in agreement with band gap approximation from the PL results obtained.

6.3.5 Photoluminescence studies

Figure 6-6 shows the PL emission spectrum of ZnO:Tb^{3+} thin film excited at 244 nm wavelength. The spectra show emissions at 378 nm corresponding to a band to band emission of ZnO. This

emission is attributed to the recombination of the excitons of granular ZnO through an exciton-exciton collision process corresponding to near band edge (NBE) emission of ZnO [24]. Its intensity increased with increasing annealing temperature, an indication of enhanced film crystallinity necessary for effective charge transfer (grain size commensurate to the mean free path of the electrons) in solar cell application. This is due to the decrease of the non-radiative defects and the increase of ZnO grain size [1]. At 900 ˚C, this peak showed reduced peak intensity. A plausible reason is that the decrease in the length of *c*-axis of ZnO films annealed at higher temperature may induce an acute lattice distortion, which would significantly increase the polarizability in the ZnO:Tb^{3+} matrix and thus affect the optical properties of ZnO:Tb^{3+} films and quench the PL efficiency [25]. This is in agreement with XRD findings. This decrease in the emission of ZnO or the inter-band transitions could also be attributed to some of the excited electrons to the energy levels associated with oxygen vacancies while others are transferred to the energy levels of Tb^3. The broad emissions between 400-500 nm are attributed to deep level defects emission arising from the recombination between the Zn_i and the valence band level [26]. ZnO has six kinds of defects classified as vacancies, interstitials and antisites and their emission intensities can be influenced by the defect concentration and defect-defect interactions which varies with annealing temperature.

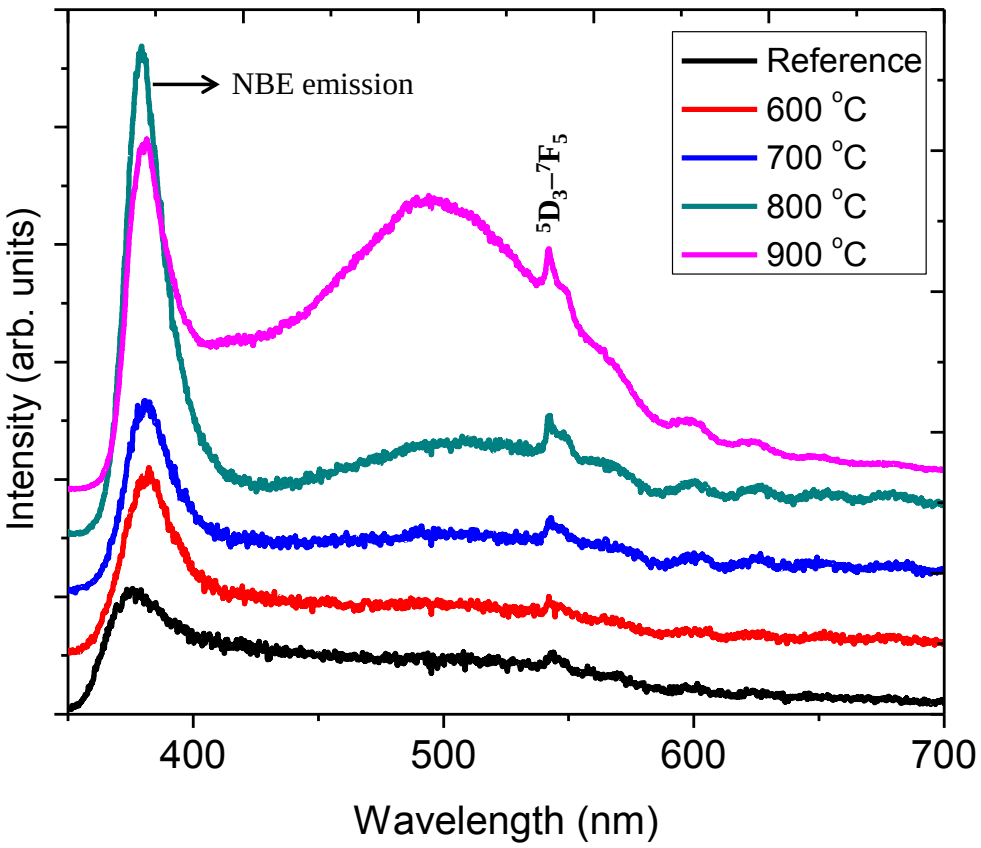


Figure 6-6: PL spectra of the ZnO:Tb^{3+} thin films annealed at different temperatures excited at 244 nm together with that of the ZnO:Tb^{3+} thin film annealed at temperature range of 600-900 ˚C.

Table 6-3: Summary of peak center position and FWHM for the NBE PL peak.

Annealing Temperature (˚C)	Peak Centre (nm)	FWHM (nm)
Reference	477	21.9
600	381	19.1
700	382	16.6
800	384	12.2
900	398	26.3

The sharp emission peak at 543 nm is related to Tb^{3+} ions emission. Here, the electric dipole (ED) transitions between the 4f states in the free Tb^{3+} ions are parity forbidden. However the ED are transitions are partially allowed but with weak intensity when the Tb^{3+} ions are occupying interstitials or lattice sites in ZnO with a large absorption transition probability arising from its direct band gap nature [26, 27]. Hence according to Bylander *et al*. [28], majority of excited charge carriers trapped at Tb^{3+} centers originate from band gap absorption in the ZnO matrix and a marginal fraction of these electrons are contributed from the 4f-4f absorption transition within the Tb^{3+} ions.

Table 6-3 shows the peak centroid and the corresponding full width at half maximum (FWHM) for the near band edge peak as well as the broad band peak while figure 6-7 gives an elaborate schematic band diagram for these proposed emissions. The shifting of the peak center with annealing temperature could attributed to by the relaxation of built-in strain in ZnO:Tb^{3+} thin films. The efficiency of the energy transfer from the host ZnO to rare earth ions such as Tb^{3+} are usually lower due to the large mismatch in the ionic radii and the valence state of the Zn^{2+} (74 pm) and rare earth ions, Tb^{3+} (118 pm). Furthermore the location of the rare earth in the host also determines the efficiency of the energy transfer, thus generally, rare earth ions can occupy two different sites in the hosts, namely: (i) in the substitution sites of Zn^{2+} in the ZnO lattice, (ii) or at the ZnO grain boundaries. The location of Tb^{3+} on the surface or grain boundaries can be rule out for RBS data which consistently show a relatively homogeneous distribution of Tb^{3+} in the ZnO thin film. The distinction of surface and bulk emissions can thus be resolved qualitatively using the RBS profiles of the RE and the film constituent atoms. Figure 6-7 shows a schematic diagram of the energy level the ZnO:Tb^{3+} thin films [29].

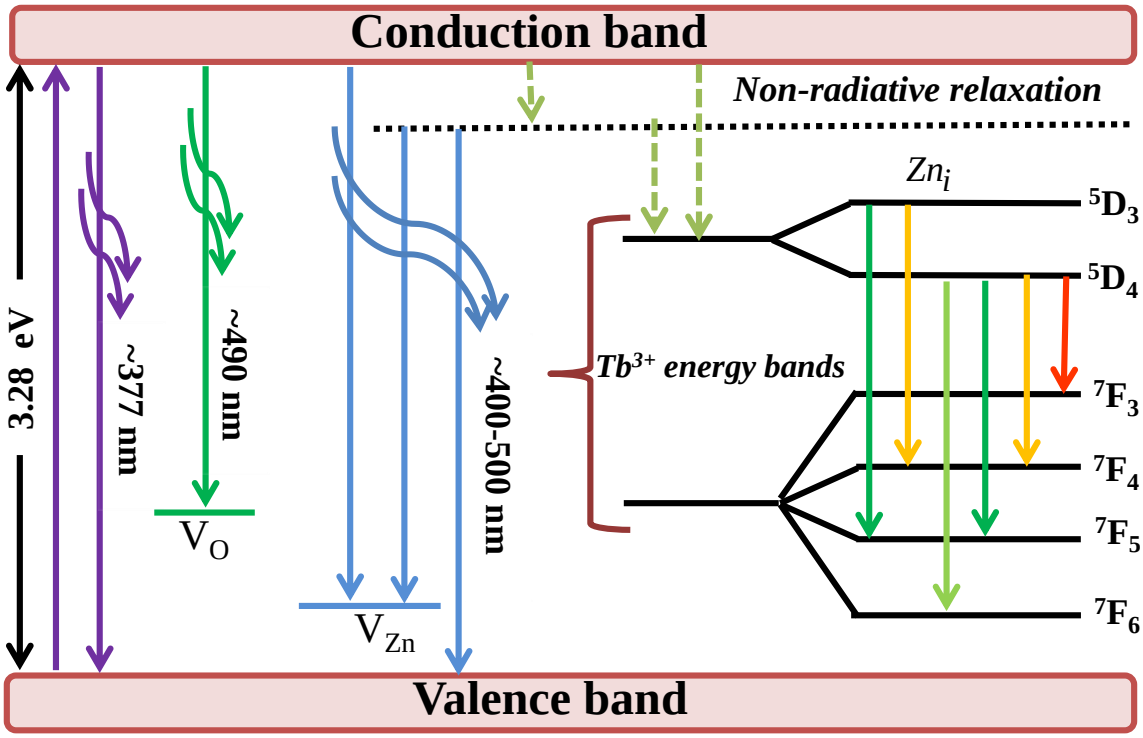


Figure 6-7: schematic of the energy level diagram of the ZnO:Tb^{3+} thin films.

All samples show the defect related emission with a major green emission peak at 543 nm and a few oscillations attributed to the emissions of Tb^{3+}. These occur at 492, 543, 595, 624, 543 and 563 nm. These peaks represent the $^5D_4$–$^7F_6$, $^5D_4$–$^7F_5$, $^5D_4$–$^7F_4$, $^5D_4$–$^7F_3$, $^5D_3$–$^7F_5$ and $^5D_3$–$^7F_4$ transitions of Tb^{3+}, respectively. The excitations are assigned to direct excitation of the Tb^{3+} through the f $\rightarrow$ d transitions [29, 30]. A band gap value of 3.28 eV was obtained from the NBE peak. The theoretical position of the Zn_i level is at 0.22 eV below the conduction band [28]. When excitation is done at 244 nm, charge carriers are pumped from the valence band to the conduction band leaving a hole in the VB and an electron in the CB can radiatively recombine to give UV emission, which is generally assigned to near band edge emission (377 nm) from ZnO shown in Figure 6-7.

6.4. Application of ZnO:Tb^{3+} thin films into organic solar cells

6.4.1. Device fabrication and characterization

The photovoltaic devices applying ZnO:Tb^{3+} thin films into organic solar cell were fabricated on glass coated with indium tin oxide (ITO), which had been cleaned by sonication using the procedure described in ref [31, 32]. Thin ZnO or ZnO:Tb^{3+} (about 35 nm) films were grown on the cleaned ITO by RF sputtering using procedure described in section 2.2 and then annealed at 300 ˚C in Ar filled furnace for 1 hour. Active layers composed of P3HT:PCBM blended at a ratio of 1:1 chlorobenzene with a total concentration of 20 mg ml^{-1} , were then spin coated at 2000 rpm for 1 minute. The active layers were subsequently annealed at 80 °C for 10 min in Ar filled furnace before spin coating of the hole transport layer (PEDOT:PSS). Finally, the Al electrode was thermally evaporated at a pressure of 2×10^{-5} Pa. The current density–voltage (*J*–*V*) characteristics were obtained using a HP 4141B source measure unit under 100 mW/cm^2 illumination (AM 1.5G). All the measurements were carried out at room temperature under standard conditions. More than 20 devices of pristine ZnO and ZnO:Tb^{3+} based inverted solar cell each of area 8.4 ± 0.1 mm^2 were fabricated, characterized and the results obtained exhibited a high degree of repeatability to within 2.5%.

6.4.2. Current –Voltage (*I-V)* Characteristics

Figure 6-8 shows *J-V* characteristics curve used as a proof of concept of the influence of Tb^{3+} doping on photoactive performance in an organic solar cells with an inverted structure of ITO/ZnO:$Tb^{3+/}$P3HT:PCBM/PEDOT:PSS/Al. The Inset in the figure represents the UV-Visible absorption spectra of active layer (P3HT:PCBM), ZnO/ P3HT:PCBM and ZnO:Tb^{3+}/ P3HT:PCBM films used in device fabrication. The films were annealed at 300 ˚C to avoid softening of the glass as well as deterioration of electrical properties of ITO film.

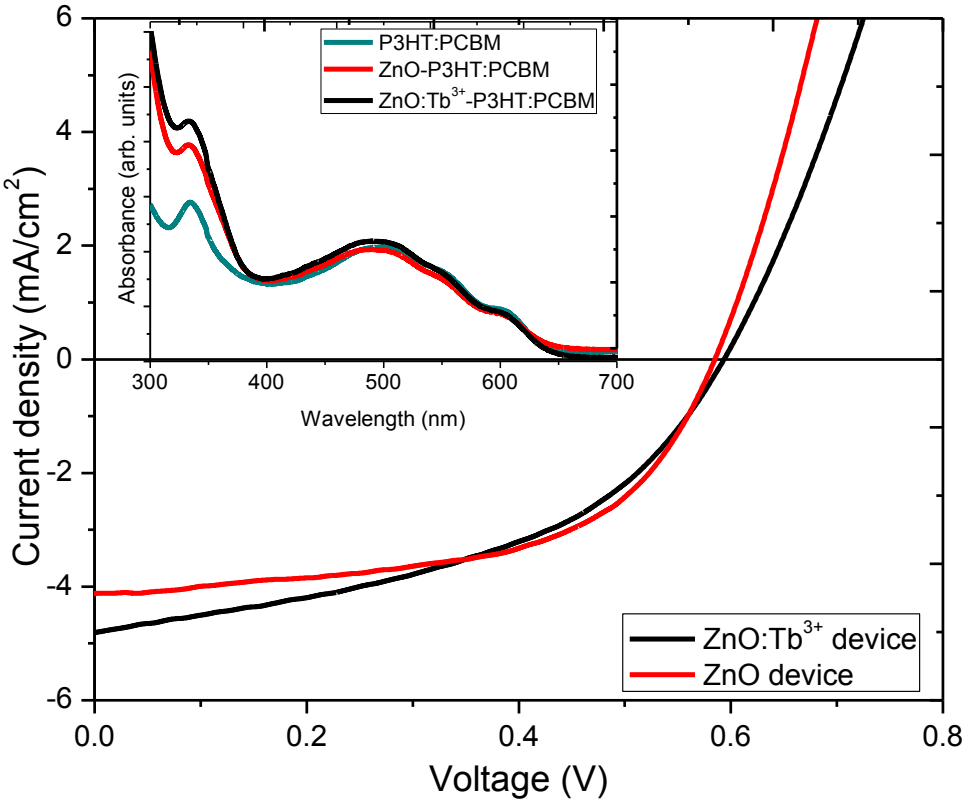


Figure 6-8: J–V characteristics (a) under illumination of devices formed from pristine and heat treated P3HT:PCBM blends.

ZnO and ZnO:Tb^{3+} thin films grown by RF sputtering on ITO coated glass substrate were both used as electron transport and spectra conversion layers. Table 6-4 shows the performance parameters. The two devices showed almost similar fill factor (FF) and open circuit voltage (V_{OC}) values, an indication that the electronic properties of ZnO thin films were not altered by the Tb^{3+} doping. This is also supported by the nearly constant value of the shunt resistance of the device. However, there was a slight increase in J_{SC} from 4.11 to 4.82 mA cm^{-2}. This could be attributed to spectrum down-conversion as a result of Tb^{3+} doping. According to the absorption measurements shown in the inset in Figure 6-8, there is an increased absorption in the ultraviolet region from 300–400 nm with introduction of ZnO thin film as a layer before P3HT:PCBM blend thin film which is further enhanced upon doping with Tb^{3+} leading to an increase in the number of photo-

generated photons in the visible region converted from the UV region. The down-conversion process altered the UV properties of the solar cell under the solar emission spectrum enabling absorption of photons in the UV range and re-emitting light at a longer wavelength in visible region, where the organic solar cell has a considerably better response. The increase in light absorption with ZnO thin film compared to the film with P3HT:PCBM blend alone may be an indication the emission being in resonance with the P3HT electronic structure since exciton generation occurs through the $\pi \rightarrow \pi^*$ interaction in the P3HT.

Table 6-4: Summary of the performance of the P3HT:PCBM bulk heterojunction solar cells device with pure ZnO and ZnO: Tb^{3+} as the cathode buffer layer.

Device	***Jsc*** (mA/cm^2)	***V_{oc}*** (V)	***R_s*** (Ω cm^2)	***R_{sh}*** (kΩ cm^2)	***FF*** (%)	***PCE*** (%)
ZnO	4.11±0.10	0.59± 0.02	51.8 ± 1.2	232 ± 3	47.8±1.0	1.16 ± 0.08
ZnO:Tb^{3+}	4.82 ±0.12	0.60 ± 0.01	52.3 ± 1.0	235 ± 2	46.9 ±1.1	1.36 ±0.06

6.5. Results and discussion of ZnO: Eu^{3+} thin films

6.5.1. Morphological studies

Figure 6-9 shows the SEM image of ZnO:Eu^{3+} annealed at different temperatures ranging between 500-900 ˚C.

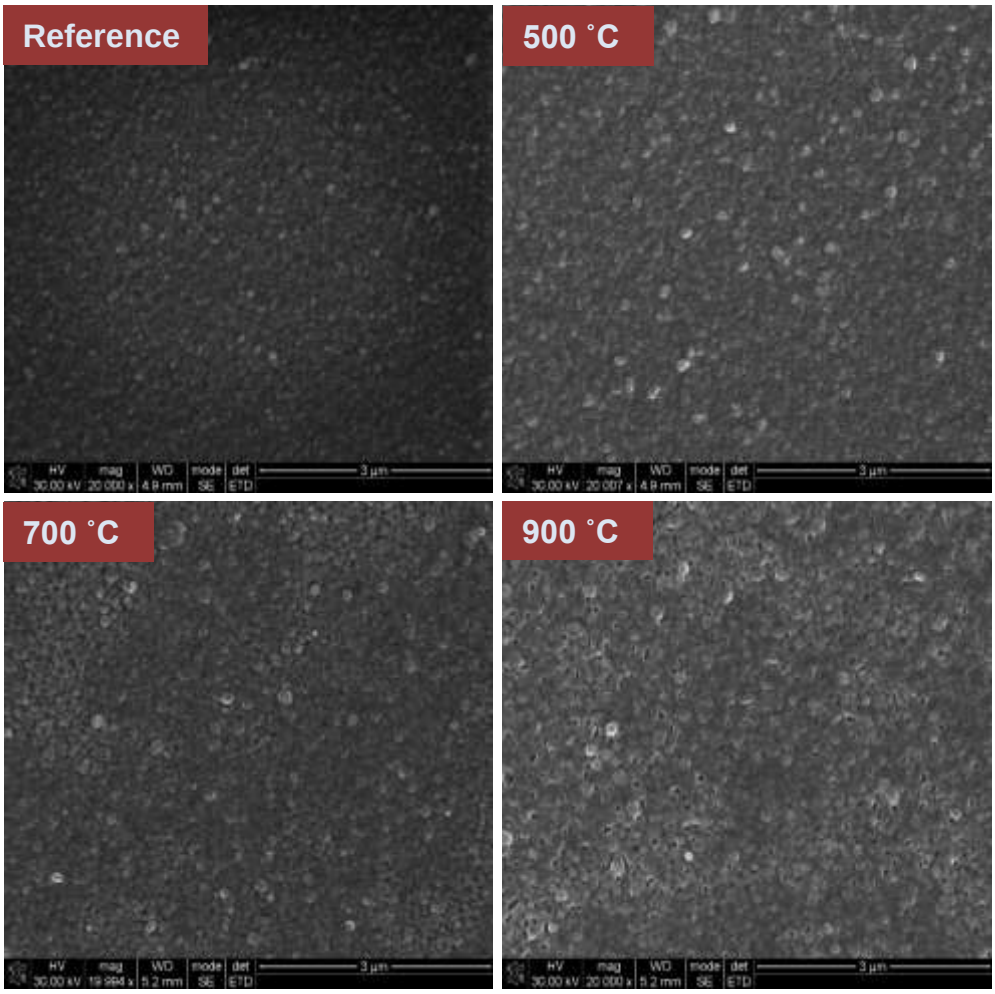


Figure 6-9: Scanning Electron Microscopy micrographs of Eu doped ZnO films annealed at temperature range of 500-900 ˚C.

The micrographs both pristine and annealed thin films are shown in Figure 6-9 which show a uniform deposition and compact columnar growth of ZnO:Eu^{3+} spherical particles. As the temperature increases the size and of the particles forming the surface appears to change. This change can be attributed to the stress in the thin films and as a result of which columnar growth is disturbed.

6.5.2. Rutherford Backscattering Spectroscopy Measurements

The elemental and percentage composition and distribution of the Eu^{3+} ions in the ZnO thin film was established using Rutherford Backscattering Spectroscopy as shown in figure 6-10.

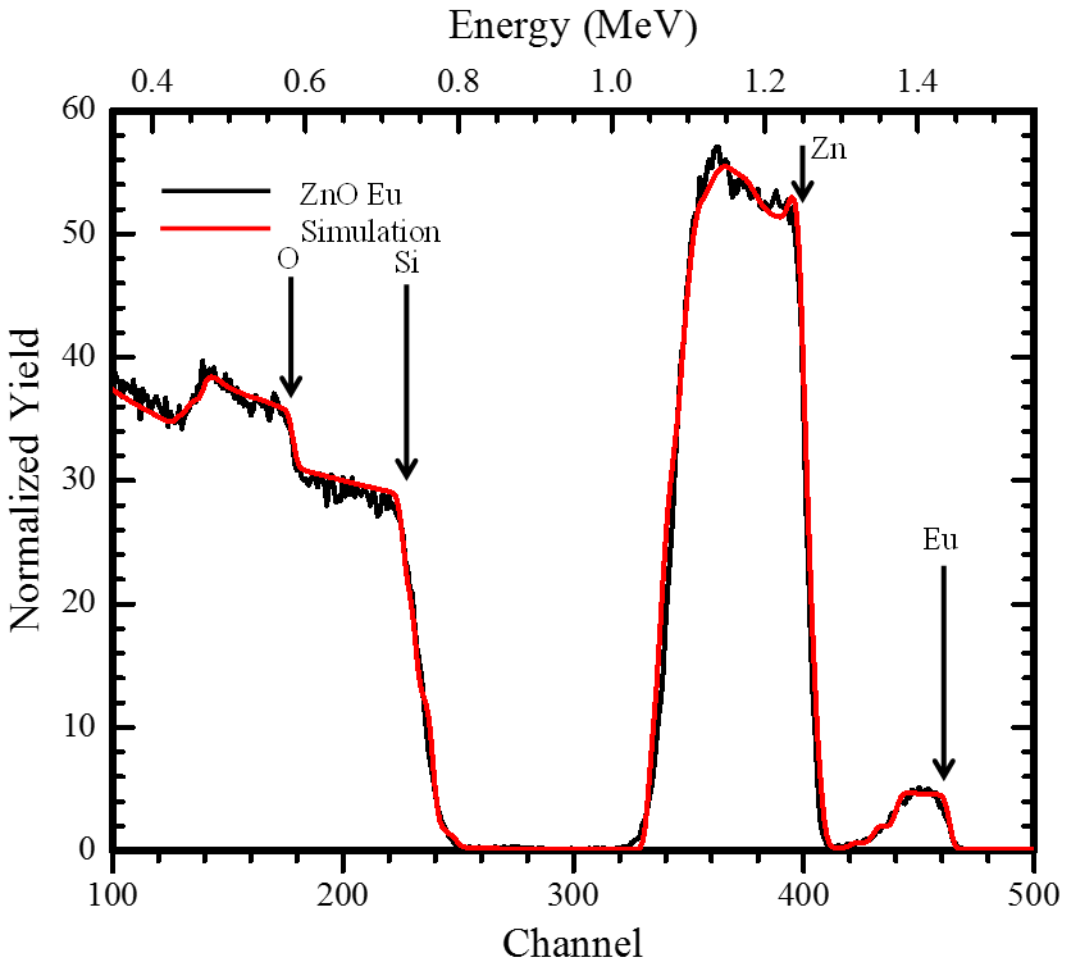


Figure 6-10: Random and simulated RBS spectra from the ZnO:Eu^{3+} thin film annealed at 900 ˚C.

Figure 6-10 shows the RBS spectra of pristine ZnO:Eu^{3+} thin film. The simulation of the experimental spectra was carried out using the XRump code using concepts outlined in Ref [33]. Vertical arrows indicate the scattering energies of the different chemical elements at the surface. The black line indicates the experimental data while the red represent the simulated using XRump

code. Table 6-5 shows the summary of Eu^{3+} distribution in the ZnO thin film as calculated from the XRump code.

Table 6-5: Derived atomic composition at various film depth from XRump code

#	Thickness	Sublayers	Composition . . .					
1	118.00 nm	auto	Zn	0.480	O 0.515	Eu	0.010	
2	50.00 nm	auto	Zn	0.500	O 0.500	Eu	0.004	
3	50.00 nm	auto	Zn	0.500	O 0.500	Eu	0.001	
4	60.00 nm	auto	Zn	0.500	O 0.567	Si	0.030	
5	46.00 nm	auto	Zn	0.261	O 0.250	Eu	0.010	Si 0.360
6	33.00 nm	auto	Zn	0.150	O 0.125	Eu	0.005	Si 0.700
7	2000.00 nm	auto	Si	1.000				

From the XRump code simulation, the film thickness was derived as 357 nm which was in agreement with profilometer values. A small amount of Si is observed to diffuse into ZnO thin films as a result of the annealing effect giving the atoms adequate energy to move, this could be the source of the shoulder on the Eu^{3+} channel. The total average Eu composition is ~1% with majority being found at a depth of 278 nm.

6.5.3. X-Ray Diffraction Analysis

The room temperature XRD of ZnO:Eu^{3+} thin film annealed at various temperatures are depicted in figure 6-11. It can be seen that the XRD pattern of the films mainly consists of hexagonal ZnO (JCPDS database No: 00-003-0888.

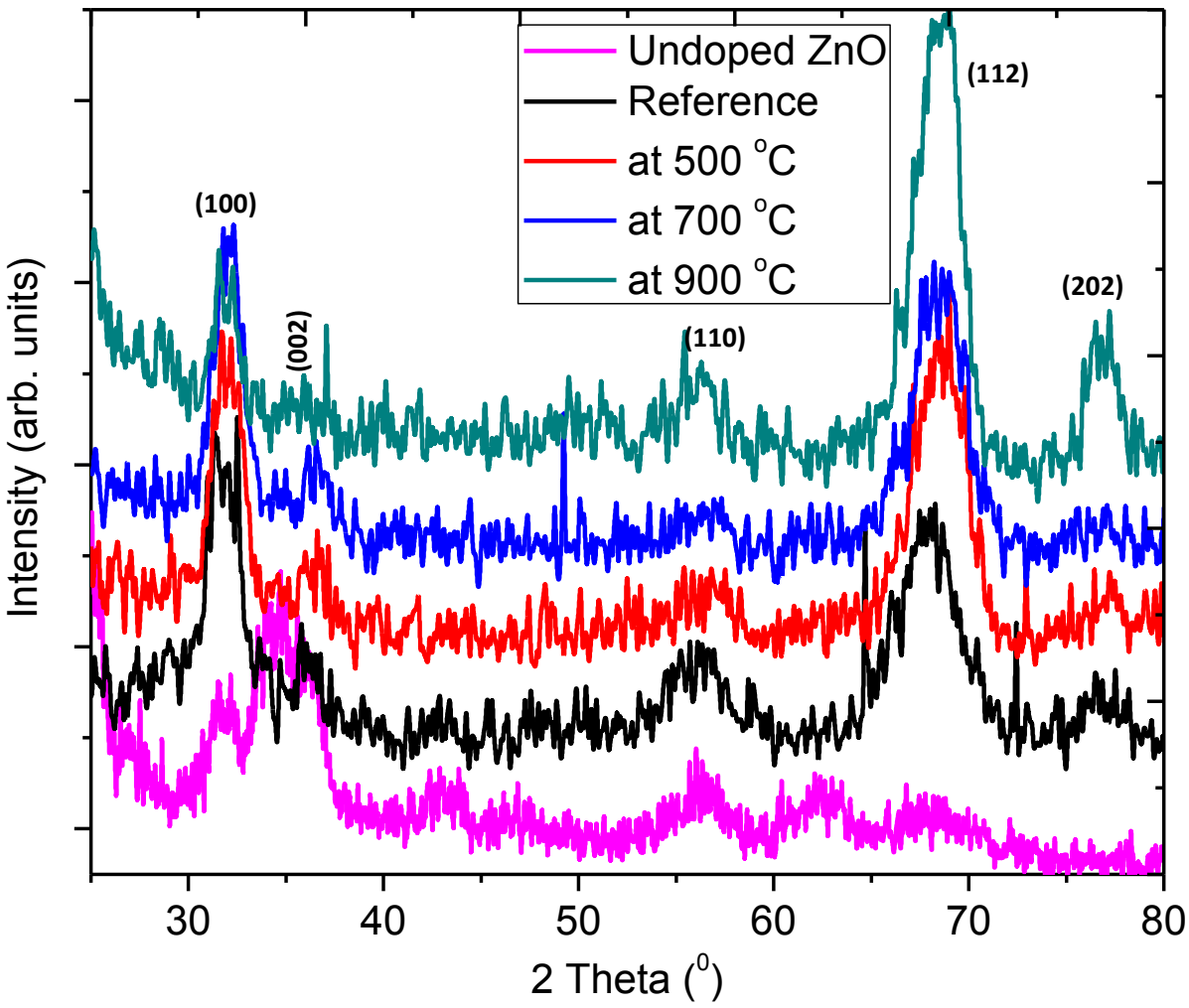


Figure 6-11: Room temperature XRD pattern of pristine and annealed ZnO:Eu^{3+} thin films compared to the undoped ZnO.

From the XRD pattern shown in figure 6-11, no diffraction peaks from europium oxides or other impurities were detected, indicating that the Eu^{3+} ions were incorporated into the ZnO lattice or . All peaks in the XRD pattern are of ZnO and can be readily indexed as the hexagonal wurtzite ZnO phase with cell constants (a) 3.248 Å and (c) 5.206 Å, which are in good agreement with literature [34]. Compared to the undoped ZnO thin film, the diffraction peaks of Eu^{3+} doped ZnO samples shift about 0.5 (2θ) to a lower angle due to the larger ionic radius of Eu^{3+} (0.95 Å) compared to that of Zn^{2+} (0.74 Å) [34].

Upon annealing ZnO:Eu^{3+} thin films, the (100) peak which is the more pronounced compared to the (002) gradually shifted to higher 2θ from 31.74˚ to 32.04˚ while its FWHM gradually decreases from 2.155° to 0.999°, an indication of enhanced crystallinity with annealing.

6.5.4. Optical studies

Figure 6-11 represents transmittance (%) of the thin films as a function of wavelength. All the four films show a dip near 372 nm which is due to the band edge absorption.

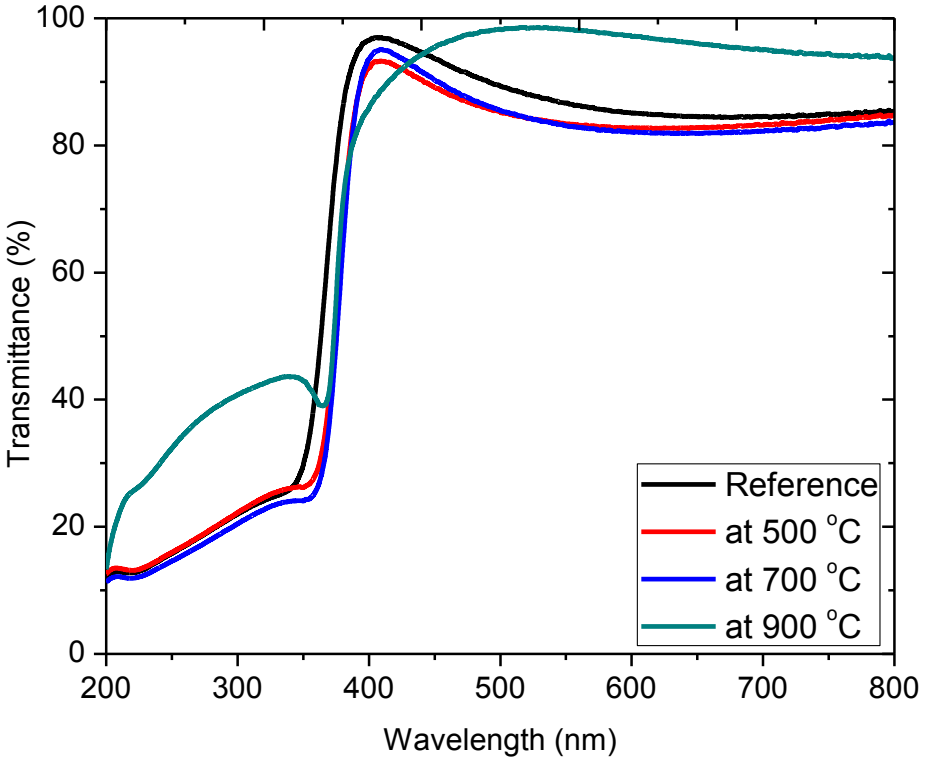


Figure 6-12: Optical transmittance of pristine and ZnO:Eu^{3+} annealed at 500-900 ˚C.

The transmittance of Eu doped ZnO thin films in the wavelength range of 200-800 nm are shown in Figure 6-12. All films are highly transparent (95%) in the visible wavelength range and sharp ultraviolet absorption edge is observed at approximately 372 nm in the UV region. The high transmittance becomes more pronounced with annealing at 900 ˚C as a result of optical forward scattering caused by rough surface of the film. This is a very vital result since the project was

aimed at acquiring highly transparent and conductive electrodes for device application. In addition, a shift towards the lower energies of the absorption edge with increasing annealing temperature is noticed. The incorporation of Eu^{3+} is accompanied by a systematic low-energy shift of the band gap indicating the narrowing of the optical band gap [35]. The UV-Vis transmittance spectra was used to derive the optical band gap variation with annealing temperature as shown in figure 6-13 using Tauc method.

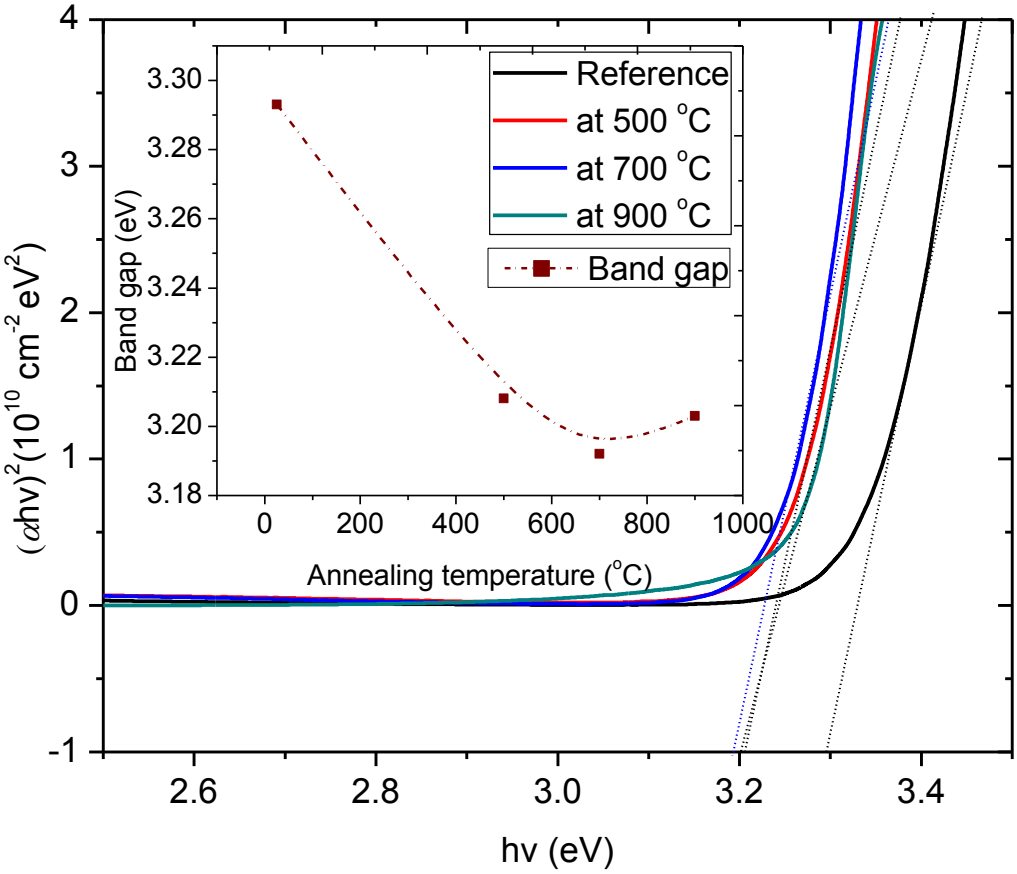


Figure 6-13: Plot of $(\alpha hv)^2$ versus hv for the pristine ZnO:Eu^{3+} thin film and after annealing at 500-900 ˚C. The inset shows the variation of optical band gap as a function of annealing temperature.

When the films are annealed from 500-800 ˚C, the optical bandgap is observed to decreases from 3.29 to 3.19 eV before slightly increasing upon annealing at 900 ˚C as shown in figure 6-13. The

tailoring of the bandgap of semiconductors could be attributed to the introduction of new energy levels in the band gap near conduction edge such as shallow level donor impurities [36].

6.5.5. Photoluminescence properties

The structural and compositional changes in the films at the nanoscale level can strongly influence the luminescence properties. The correlation between the structure and the emission behavior of ZnO:Eu^{3+} thin films as a function of the annealing temperature was investigated by PL. Figure 6-15 shows the photoluminescence spectra of Eu-doped ZnO films in the 350-800 nm range, in which several bands associated with transitions from the excited $^5D_0$ level to the ^7F_J (J = 0, 1, 2, 3, 4) levels of the Eu^{3+} $4f^6$ configuration [37] are observed. The spectra which is mainly showing the $^5D_0$ - $^7F_2$ transitions, indicates that ZnO:Eu^{3+} films experience severe modifications on increasing the treatment temperature, an indication of presence of structural re-arrangements around the Eu^{3+} centers. This is in agreement with the suggested transitions as indicated in figure 6-14

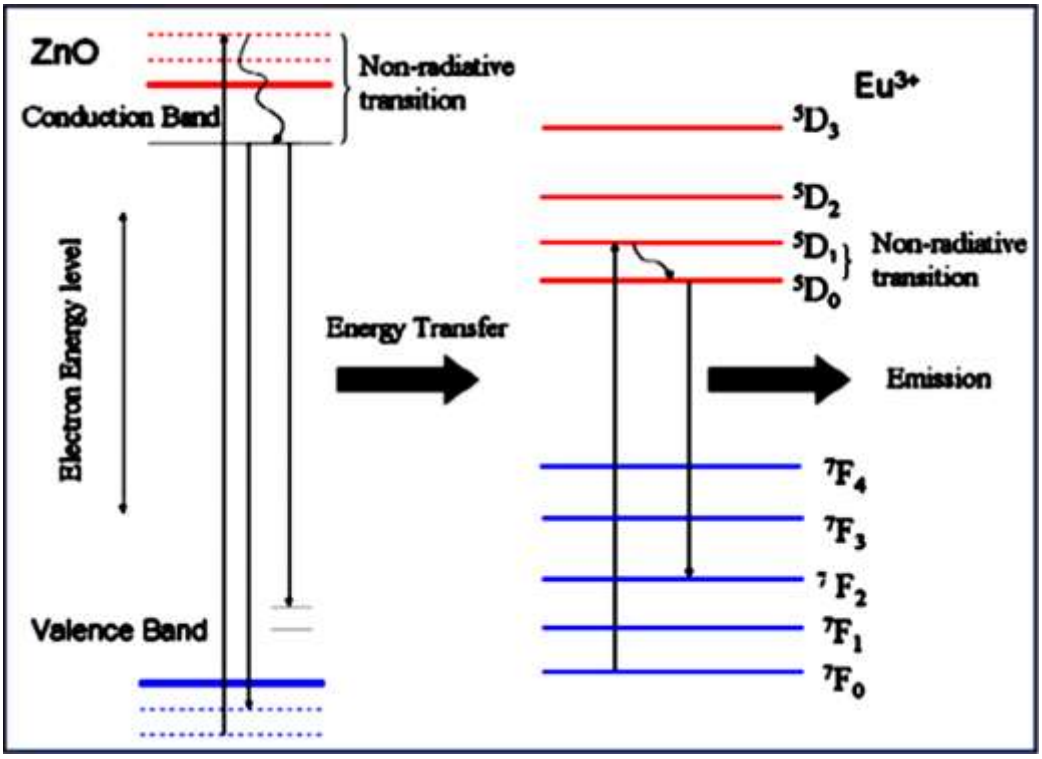


Figure 6-14: Schematic illustration of the proposed mechanism of energy transfer from the ZnO host to the Eu^{3+} ions.

From figure 6-15&16, the UV emission attributed to near-band-edge (NBE) exciton recombination and a broad deep level emission is depicted as discussed in detail in chapter 4. The sharp red emission peaks exhibited at 590-705 nm are attributed to Eu^{3+} ions. Figure 6-15 shows the PL spectra of films annealed at between 500-700 ˚C while Figure 6-16 includes films annealed at 900 ˚C.

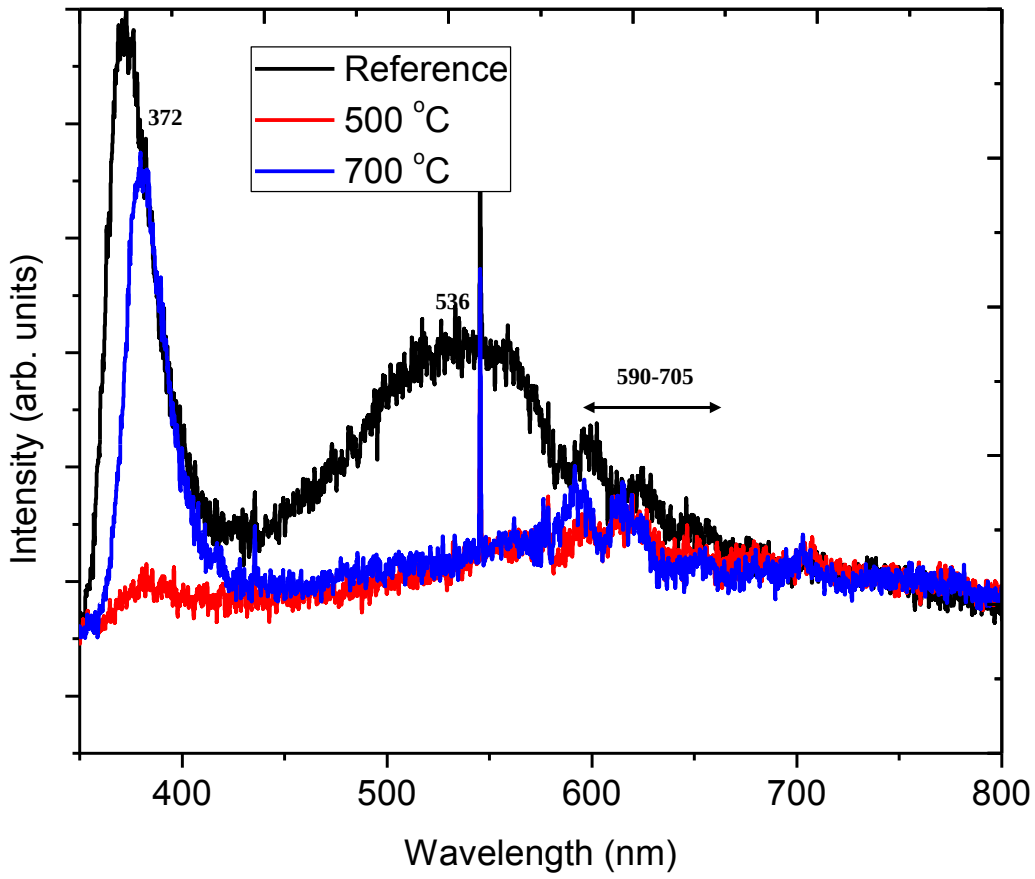


Figure 6-15: Room temperature PL spectrum of ZnO:Eu^{3+} annealed at 500-700 ˚C measured at 244 nm excitation wavelength.

From figure 6-15, the decrease in intensity of both the near-band-edge emission and deep level defects emission at 372 nm and 536 nm respectively while increasing emission of the $^5D_0$ - $^7F_2$ transition at 613 nm confirm the energy transfer from ZnO to Eu^{3+} ions [38-40].

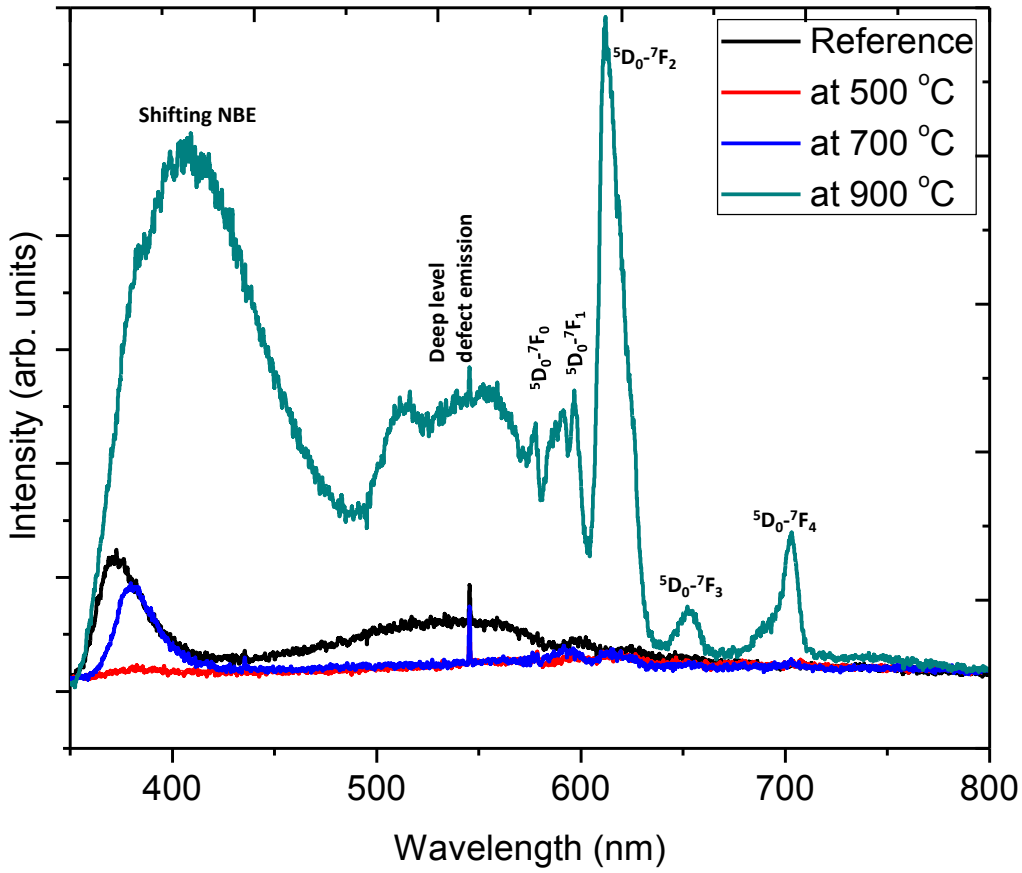


Figure 6-16: Room temperature PL spectrum of ZnO:Eu^{3+} annealed at 500-700 ˚C using 244 nm excitation wavelength.

From figure 6-16, sharp peaks are observed upon annealing at 900 ˚C at 576 nm, 594 nm, 613 nm, 651 nm, 703 nm that correspond to the intrinsic 4f → 4f transitions of Eu^{3+} in the ZnO host. The resulting intrinsic 4f → 4f transitions of Eu^{3+} were assigned to $^5D_0$ - $^7F_0$, $^5D_0$ - $^7F_1$, $^5D_0$ - $^7F_2$, $^5D_0$ - $^7F_3$, and $^5D_0$ - $^7F_4$ transitions of Eu^{3+} ions, respectively [34, 41, 42]. The peak situated at 613 nm is observed to be stronger which is a clear indication that the Eu^{3+} ions are located at the inversion anti-symmetric sites of the ZnO host [34]. According to the Judd–Ofelt theory, the magnetic dipole transition is permitted. However, the electric dipole transition is only permitted when the Eu^{3+} ion occupies a non-inversion center site and the intensity is significantly affected by the symmetry in local environments [43]. If the Eu^{3+} ions occupied an inversion symmetry site in the crystal lattice,

the magnetic transition $^5D_0$ - $^7F_1$ (around 594 nm) would be the dominant transition. However the dominance of the $^5D_0$ - $^7F_2$ transition points to an electric dipole transition. The ratio of intensity ($^5D_0$- $^7F_2$)/($^5D_0$ - $^7F_1$) may be used to establish the degree of distortion from the inversion symmetry of the Eu^{3+} ion local environment 69]. A lower symmetry around Eu^{3+} ion is known to yield a large value of the intensity ratio, this value is also referred to as the asymmetric factor or asymmetric ratio [44]. The high intensity of the red peak at 613 nm, due to the $^5D_0$-$^7F_2$ transition upon annealing at 900 ˚C is a confirmation of the fact that the Eu^{3+} emission is parity forbidden and observed only when the lattice environment is distorted and has non-inversion symmetry [43]. Because this is a forced electric-dipole transition, this transition is hypersensitive to the annealing temperature. Eu^{3+} ions are known to likely to occupy two sites that is the inner and surface lattice sites of the ZnO materials [40, 45, 46]. Theoretically, the Eu^{3+} ions are incorporated into the inner lattice site of the ZnO, or Eu^{3+} ions are at the substitutional Zn site with C_{3v} symmetry, the *J=0, J=1* transition would split into two crystal-field levels ($J=0 \rightarrow D=0$, $J=0 \rightarrow F=1$), however from figure 6-16, there are five peaks at $^5D_0$-^7F_j, an indication that the Eu^{3+} ions have been incorporated into a lower symmetry site than C_{3v} [47].

6.6. Application of ZnO:Eu^{3+} thin layer into Dye sensitized solar cells

6.6.1. Fabrication procedure.

The application of ZnO:Eu^{3+} thin to dye sensitized solar cell was done using the following procedure:

Cleaned FTO was used as an electrode onto which ZnO and Eu doped ZnO were deposited and the films were subsequently annealed at 350 °C for 30 min. Heat treatment was performed to improve the electrical contact between the film and the adsorbing dye molecules. The thickness and the active area of the film used as active area was approximated to 150 nm and 0.25 cm^2,

respectively. For sensitization, the ZnO films were quickly immersed in a dye solution (3.0×10^{-4} M mixture of the ruthenizer 535-bisTBA (N-719) in methanol) then left to dry for 12h at room temperature. The counter electrode was composed of a thin of layer of Pt (50 nm) sputter coated on a clean FTO substrate.

The electrode with ZnO thin film photoanode was placed face up on a flat surface, and the counter electrode placed on top of it. These two opposing glass plates were offset from one another so that the entire photoanode was covered by the counter electrode. The redox electrolyte solution (I^-/I_3^-), composed of 0.6 M methylhexylimidazolium iodide, 0.1 M iodine, 0.5 M tert-butylpyridine, and 0.1 M lithium iodide in 3-methoxypropionitrile, was placed at the edges of the plates, and the liquid was drawn into the space between the electrodes via capillary action. An epoxy adhesive was utilized to hold/seal the electrodes together and the results of the I-V characteristics were obtained as shown in figure 6-17.

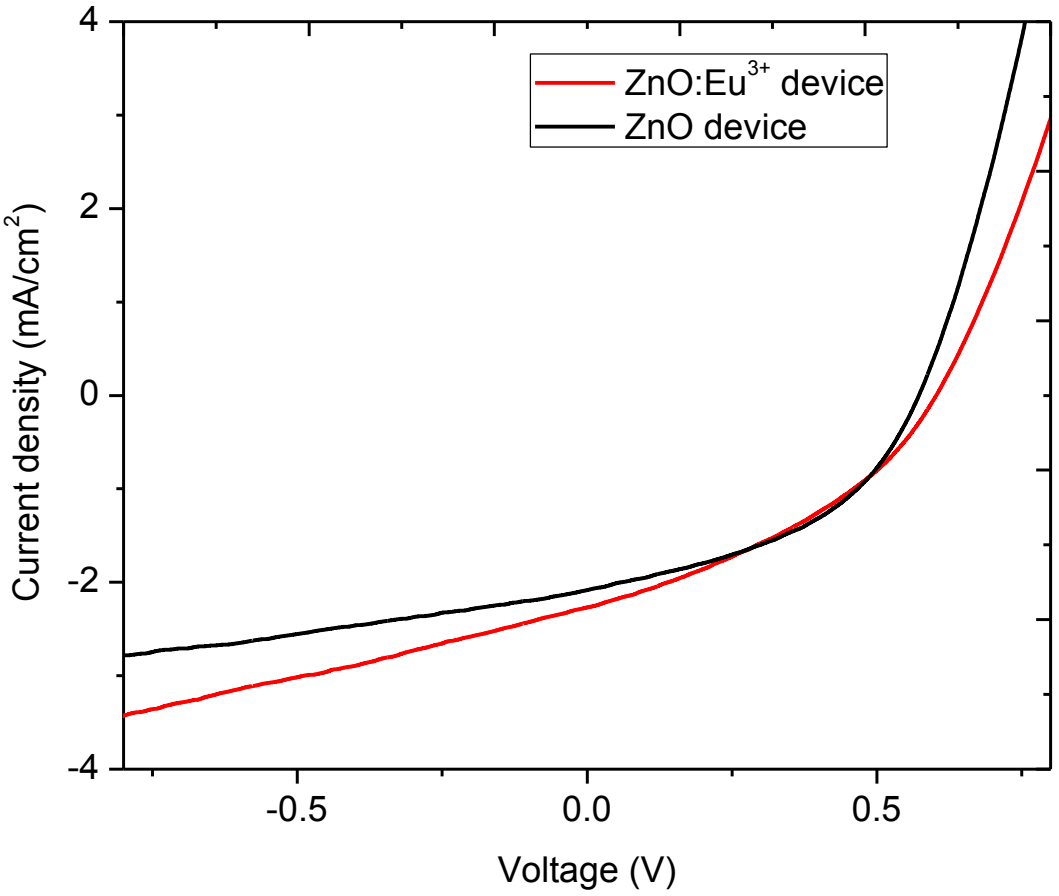


Figure 6-17 J-V characteristics curves of pristine and Eu^{3+} doped ZnO used in dye sensitized solar as a photoanode.

6.6.2. Results and discussion.

The DSSC with Eu doped ZnO yielded a PCE of 0.56 % (Jsc = 2.28 mA cm^{-2}, V_{oc} = 0.59 mV and FF = 42.3 %), while the DSSC with pristine ZnO without Eu produced a PCE of 0.52 % (Jsc = 2.07 mA cm^{-2}, Voc = 0.57 V, FF = 43.6 %) indicating 7.7 % efficiency enhancement which could be attributed to spectral conversion by the Eu doped ZnO. The values are relatively low and could be as a result of exposure of the materials to air.

6.7. Conclusion

Polycrystalline ZnO:Tb^{3+} thin films were deposited on Si, quartz and ITO coated glass substrate by RF magnetron sputtering technique. The films showed excellent transparency and conductivity required for solar cell applications. X-ray diffraction (XRD), atomic force microscope (AFM) and the Photoluminescence (PL) were employed to analyze the influence of the post-deposition annealing treatment on the structural properties of the ZnO:Tb^{3+} thin films. The films showed an increasing roughness and grain size of ZnO:Tb^{3+} with annealing temperature between 600-900 ˚C and a shift of the diffraction peak position. As a proof of concept, hybrid OPV devices based on P3HT:PCBM blend were fabricated. Incorporation of ZnO and ZnO:Tb^{3+} thin films showed an increase in absorption within 300-400 nm wavelength range. The high absorption when ZnO:Tb^{3+} was used to show that the films can be effectively used as a buffer layer and down-conversion layer with enhancement of OPV device performance.

Down conversion has been applied to minimize thermalization losses in photovoltaic devices. In this work, Terbium doped ZnO (ZnO:Tb^{3+}) thin films were deposited on ITO coated glass, quartz and silicon substrate using RF magnetron sputtering technique fitted with a high purity (99.99%) Tb^{3+} doped ZnO target (97% ZnO, 3% Tb) for use in organic solar cell as a bi-functional layer. A systematic study on the film crystallization dynamics is carried out through elevated temperature annealing in Ar ambient. The films were characterized using grazing incidence (XRD), Rutherford backscattering spectrometry (RBS), Atomic force microscopy, UV-Visible transmittance, Photoluminescence measurements using an excitation wavelength of 244 nm.

The tunability of the size and bandgap of ZnO:Tb^{3+} nanocrystals with annealing has exhibited quantum confinement effects which enable the control of emission characteristics in ZnO:Tb^{3+}. The energy transfer of ZnO $\rightarrow$ Tb^{3+} ($^5D_3 - {}^7F_5$) is also observed from the photoluminescence

(PL) spectra. At an inter-band resonance excitation of around 300–400 nm, a typical emission band from the Tb^{3+} is obtained. The ZnO:Tb^{3+} grown on ITO coated glass were then used as a bi-functional layer in an organic solar cell based on P3HT:PCBM blend as an active layer in an inverted device structure. The energy transfer through down conversion between ZnO and Tb^{3+} leads to enhanced absorption in P3HT:PCBM in the 300-400 nm range, and subsequently augments the J_{sc} of Tb^{3+} based device by 17 %.

Eu-doped ZnO thin films were also deposited using RF sputtering and the role of annealing on the modification of red photoluminescence was studied. From the PL spectra analysis, there is a correlation between the annealing temperature and the characteristics of the red photoluminescence, which suggests that the intrinsic defects can assist efficient energy transfer from the ZnO host to the Eu^{3+} ions. Five peaks in the region of $^5D0$ - ^7F_J were observed, which indicate that the Eu^{3+} is located in the surface lattice sites of the ZnO materials. The DSSC with Eu doped ZnO yielded a PCE of 0.56 % compared to 0.52 % obtained from DSSC with pristine ZnO without Eu produced indicating 7.7 % efficiency enhancement which could be attributed to spectral conversion by the Eu doped ZnO.

6.8. References (for chapter 6)

[1] X. Teng, H. Fan, S. Pan, C. Ye, G. Li, Influence of annealing on the structural and optical properties of ZnO: Tb thin films, Journal of applied physics, 100 (2006) 053507.

[2] T. Matsumoto, H. Kato, K. Miyamoto, M. Sano, E.A. Zhukov, T. Yao, Correlation between grain size and optical properties in zinc oxide thin films, Applied physics letters, 81 (2002) 1231-1233.

[3] J. Lang, J. Wang, Q. Zhang, Q. Han, J. Yang, S. Xu, D. Wang, M. Wei, X. Li, Y. Sui, Tunable bandgap and optical properties of (Eu, Sm) codoped ZnO nanoparticles, Journal of Materials Science: Materials in Electronics, 27 (2016) 11034-11040.

[4] M. Caglar, S. Ilican, Y. Caglar, F. Yakuphanoglu, Electrical conductivity and optical properties of ZnO nanostructured thin film, Applied surface science, 255 (2009) 4491-4496.

[5] G.A. Kumar, M.R. Reddy, K.N. Reddy, Structural, optical and electrical characteristics of nanostructured ZnO thin films with various thicknesses deposited by RF magnetron sputtering, Res. J. Phys. Sci., 1 (2013) 17-23.

[6] H.-p. XIE, S.-r. ZHANG, C.-t. YANG, H.-w. ZHANG, Y. YANG, Influence of Postdeposition Annealing on the Properties of ZnO Films Prepared by RF Magnetron Sputtering, Piezoelectrics & Acoustooptics, 1 (2008) 031.

[7] A. Mosbah, A. Moustaghfir, S. Abed, N. Bouhssira, M. Aida, E. Tomasella, M. Jacquet, Comparison of the structural and optical properties of zinc oxide thin films deposited by dc and rf sputtering and spray pyrolysis, Surface and Coatings Technology, 200 (2005) 293-296.

[8] W. Water, S.-Y. Chu, Physical and structural properties of ZnO sputtered films, Materials Letters, 55 (2002) 67-72.

[9] T. Shimomura, D. Kim, M. Nakayama, Optical properties of high-quality ZnO thin films grown by a sputtering method, Journal of luminescence, 112 (2005) 191-195.

[10] J. Muth, R. Kolbas, A. Sharma, S. Oktyabrsky, J. Narayan, Excitonic structure and absorption coefficient measurements of ZnO single crystal epitaxial films deposited by pulsed laser deposition, Journal of Applied Physics, 85 (1999) 7884-7887.

[11] N. Wu, Q. Luo, X. Qiao, C.-Q. Ma, The preparation of a Eu3+-doped ZnO bi-functional layer and its application in organic photovoltaics, Materials Research Express, 2 (2015) 125901.

[12] Z. Fang, Z. Yan, Y. Tan, X. Liu, Y. Wang, Influence of post-annealing treatment on the structure properties of ZnO films, Applied Surface Science, 241 (2005) 303-308.

[13] W.-C. Shih, M.-S. Wu, Growth of ZnO films on GaAs substrates with a SiO 2 buffer layer by RF planar magnetron sputtering for surface acoustic wave applications, Journal of Crystal Growth, 137 (1994) 319-325.

[14] M. Puchert, P. Timbrell, R. Lamb, Postdeposition annealing of radio frequency magnetron sputtered ZnO films, Journal of Vacuum Science & Technology A: Vacuum, Surfaces, and Films, 14 (1996) 2220-2230.

[15] F. Otieno, M. Airo, R.M. Erasmus, D.G. Billing, A. Quandt, D. Wamwangi, Structural and spectroscopic analysis of ex-situ annealed RF sputtered aluminium doped zinc oxide thin films, Journal of Applied Physics, 122 (2017) 075303.

[16] B.-Y. Oh, M.-C. Jeong, W. Lee, J.-M. Myoung, Properties of transparent conductive ZnO: Al films prepared by co-sputtering, Journal of Crystal Growth, 274 (2005) 453-457.

[17] V. Gupta, A. Mansingh, Influence of postdeposition annealing on the structural and optical properties of sputtered zinc oxide film, Journal of Applied Physics, 80 (1996) 1063-1073.

[18] H. Wahab, A. Salama, A. El-Saeid, O. Nur, M. Willander, I. Battisha, Optical, structural and morphological studies of (ZnO) nano-rod thin films for biosensor applications using sol gel technique, Results in Physics, 3 (2013) 46-51.

[19] J. Chen, J. Chen, D. Chen, Y. Zhou, W. Li, Y. Ren, L. Hu, Electrochemical deposition of Al-doped ZnO transparent conducting nanowire arrays for thin-film solar cell electrodes, Materials Letters, 117 (2014) 162-164.

[20] B. Kang, F. Ren, Y. Heo, L. Tien, D. Norton, S. Pearton, p H measurements with single ZnO nanorods integrated with a microchannel, Applied physics letters, 86 (2005) 112105.

[21] H. Yoshikawa, S. Adachi, Optical constants of ZnO, Japanese Journal of Applied Physics, 36 (1997) 6237.

[22] T. Tansley, D. Neely, C. Foley, Optical dispersion in zinc oxide, physica status solidi (a), 77 (1983) 491-496.

[23] G. Heiland, E. Mollwo, F. Stöckmann, Electronic processes in zinc oxide, Solid state physics, 8 (1959) 191-323.

[24] Y. Kong, D. Yu, B. Zhang, W. Fang, S. Feng, Ultraviolet-emitting ZnO nanowires synthesized by a physical vapor deposition approach, Applied Physics Letters, 78 (2001) 407-409.

[25] Y.-C. Lee, S.-Y. Hu, W. Water, K.-K. Tiong, Z.-C. Feng, Y.-T. Chen, J.-C. Huang, J.-W. Lee, C.-C. Huang, J.-L. Shen, Rapid thermal annealing effects on the structural and optical properties of ZnO films deposited on Si substrates, Journal of luminescence, 129 (2009) 148-152.

[26] V. Kumar, O.M. Ntwaeaborwa, H.C. Swart, Deep level defect correlated emission and Si diffusion in ZnO: Tb 3+ thin films prepared by pulsed laser deposition, Journal of colloid and interface science, 465 (2016) 295-303.

[27] S.-M. Liu, F.-Q. Liu, Z.-G. Wang, Relaxation of carriers in terbium-doped ZnO nanoparticles, Chemical physics letters, 343 (2001) 489-492.

[28] E. Bylander, Surface effects on the low-energy cathodoluminescence of zinc oxide, Journal of Applied Physics, 49 (1978) 1188-1195.

[29] D. Wang, P. Yang, Z. Cheng, W. Wang, Z. Hou, Y. Dai, C. Li, J. Lin, Patterning of Gd 2 (WO 4) 3: Ln 3+(Ln= Eu, Tb) luminescent films by microcontact printing route, Journal of colloid and interface science, 365 (2012) 320-325.

[30] V. Kumar, O. Ntwaeaborwa, E. Coetsee, H. Swart, Role of deposition time on the properties of ZnO: Tb 3+ thin films prepared by pulsed laser deposition, Journal of colloid and interface science, 474 (2016) 129-136.

[31] F. Otieno, B.K. Mutuma, M. Airo, K. Ranganathan, R. Erasmus, N. Coville, D. Wamwangi, Enhancement of organic photovoltaic device performance via P3HT: PCBM solution heat treatment, Thin Solid Films, 625 (2017) 62-69.

[32] F. Otieno, M. Airo, K. Ranganathan, D. Wamwangi, Annealed silver-islands for enhanced optical absorption in organic solar cell, Thin Solid Films, 598 (2016) 177-183.

[33] E. Kótai, Computer methods for analysis and simulation of RBS and ERDA spectra, Nuclear Instruments and Methods in Physics Research Section B: Beam Interactions with Materials and Atoms, 85 (1994) 588-596.

[34] P.P. Pal, J. Manam, Structural and photoluminescence studies of Eu3+ doped zinc oxide nanorods prepared by precipitation method, Journal of Rare Earths, 31 (2013) 37-43.

[35] R. Swapna, T. SrinivasaReddy, K. Venkateswarlu, M.S. Kumar, Effect of Post-Annealing on the Properties of Eu Doped ZnO Nano Thin Films, Procedia Materials Science, 10 (2015) 723-729.

[36] V. Kumar, S. Som, V. Kumar, V. Kumar, O. Ntwaeaborwa, E. Coetsee, H. Swart, Tunable and white emission from ZnO: Tb3+ nanophosphors for solid state lighting applications, Chemical Engineering Journal, 255 (2014) 541-552.

[37] L. Armelao, F. Heigl, S. Brunet, R. Sammynaiken, T. Regier, R.I. Blyth, L. Zuin, R. Sankari, J. Vogt, T.K. Sham, The Origin and Dynamics of Soft X-Ray-Excited Optical Luminescence of ZnO, ChemPhysChem, 11 (2010) 3625-3631.

[38] M. Wang, C. Huang, Z. Huang, W. Guo, J. Huang, H. He, H. Wang, Y. Cao, Q. Liu, J. Liang, Synthesis and photoluminescence of Eu-doped ZnO microrods prepared by hydrothermal method, Optical Materials, 31 (2009) 1502-1505.

[39] X. Zeng, J. Yuan, Z. Wang, L.-d. Zhang, Nanosheet-Based Microspheres of Eu3+-doped ZnO with Efficient Energy Transfer from ZnO to Eu3+ at Room Temperature, Advanced Materials, 19 (2007) 4510-4514.

[40] Y. Liu, W. Luo, R. Li, G. Liu, M.R. Antonio, X. Chen, Optical spectroscopy of Eu3+ doped ZnO nanocrystals, The Journal of Physical Chemistry C, 112 (2008) 686-694.

[41] Y.-K. Park, J.-I. Han, M.-G. Kwak, H. Yang, S.-H. Ju, W.-S. Cho, Time-resolved spectroscopic study of energy transfer in ZnO: EuCl3 phosphors, Journal of luminescence, 78 (1998) 87-90.

[42] T.-H. Fang, Y.-S. Chang, L.-W. Ji, S.D. Prior, W. Water, K.-J. Chen, C.-F. Fang, C.-N. Fang, S.-T. Shen, Photoluminescence characteristics of ZnO doped with Eu3+ powders, Journal of physics and chemistry of solids, 70 (2009) 1015-1018.

[43] V. Natarajan, M. Bhide, A. Dhobale, S. Godbole, T. Seshagiri, A. Page, C.-H. Lu, Photoluminescence, thermally stimulated luminescence and electron paramagnetic resonance of europium-ion doped strontium pyrophosphate, Materials research bulletin, 39 (2004) 2065-2075.

[44] P. Dorenbos, L. Pierron, L. Dinca, C. Van Eijk, A. Kahn-Harari, B. Viana, 4f–5d spectroscopy of Ce3+ in CaBPO5, LiCaPO4 and Li2CaSiO4, Journal of Physics: Condensed Matter, 15 (2003) 511.

[45] S. Lima, F. Sigoli, M.R. Davolos, M. Jafelicci Jr, Europium (III)-containing zinc oxide from Pechini method, Journal of Alloys and Compounds, 344 (2002) 280-284.

[46] Y. Liu, W. Luo, R. Li, X. Chen, Spectroscopic evidence of the multiple-site structure of Eu 3+ ions incorporated in ZnO nanocrystals, Optics letters, 32 (2007) 566-568.

[47] H. Shahroosvand, M. Ghorbani-asl, Solution-based synthetic strategies for Eu doped ZnO nanoparticle with enhanced red photoluminescence, Journal of Luminescence, 144 (2013) 223-229.

Chapter 7: Implantation of Sm^+ ions into ZnO matrix for spectral conversion.

7.1. Introduction

Zinc oxide (ZnO) thin film has emerged as a promising candidate for transparent electronic device applications such as bottom electrode layer in solar cells, ultraviolet laser emission, photodetectors, piezoelectricity and biosensors [1]. The widespread application has been prompted by its wide direct band gap (3.3 eV), a large exciton binding energy of ~60 meV at room temperature [2-4]. These excellent properties enable its application as a light-emitter due to its efficient excitonic emission at room temperature. In addition, ZnO is also a well-known green light-emitting phosphor when excited at wavelengths below 385 nm [5]. Energy absorption occurs due to the interband transition by valence electrons to the conduction band. Recombination usually occurs close to or in the electronic defects [6]. Such defects are usually dependent on the morphology, structure, particle size, composition and crystallinity of ZnO [7].

Doping of ZnO nanostructures with selective elements has been explored to tune its opto-electrical properties [3] through band gap engineering [8]. Among the promising materials for incorporation to the active layer in electroluminescent materials are rare earth ions [9] which provide intermediate emission pathways through electronic transitions to the associated energy levels. The addition of the Rare earth can be accomplished by either ion implantation in a doping process or via physical vapor deposition technique. Hence there is need to investigate suitable doping element that enables efficient excitation of RE ions through energy transfer between the host semiconductors and the RE ions.

The 4f levels of triply charged rare-earth ions have a wide range of applications such as lasers, phosphors and luminophors [10]. The use of electron impact to excite ions when incorporated into

a semiconducting matrix has attracted much interest because of these numerous applications owing to the stability of the semiconducting oxides. However, the doping has had its own share of challenges such as the low saturated concentration of rare earth ions in ZnO lattice due to the following reasons:

- the large differences in ionic size, the ionic radii of most rare earth elements are larger than those of Zn^{2+}
- mismatch in the charge state as the rare earth used carry mainly the 3+ charge state
- the inappropriate energy level position of rare earth ion relative to the valence band and conduction band of ZnO host [11].

There is still need to evaluate the composition, structure and optical properties of ZnO thin films after RE addition. Additionally the choice of the RE atom and its crystalline environment in these doped metal oxides must satisfy the optimum requirements for the diverse photonic applications. Herein, we report the structural and optical behavior of Sm^{+}-doped ZnO thin films for potential application as a bi-functional smart window layer in solar cells. These films were grown by RF magnetron sputtering on (001) Si substrates and subsequently annealed in Ar filled furnace at 700 ˚C at a ramping rate of 10 ˚C/minute. The ZnO films were subsequently implanted with Sm^{+} ions using a Varian 200-20A2F ion implanter located at iThemba LABS (Gauteng) operated at an energy of 80 keV with different fluences of $\approx$1-10x10^{15} ions/cm^2 in order to yield ion concentration as tabulated in Figure 7-2. The concentration of the Sm^{+} was calculated from Stopping and Range of Ions in Matter (SRIM) computer software and confirmed by Rutherford backscattering spectroscopy. The morphology and structure of Sm^{+} implanted ZnO films were investigated and correlated to their corresponding optical properties.

7.2. Experimental procedure

ZnO disk (99.99% purity) targets of diameter 76 mm and thickness 6 mm sourced from Semiconductor Wafer, Inc. (SWI) have been used for thin film deposition. The Si wafer (001) substrate were also purchased from Semiconductor Wafer, Inc. (SWI). The Sm^{+} ions were produced from a cut piece of a Sm_2O_3 sputter target (99.99% purity, sourced from SWI) and extracted as incident ions for implantation into pristine ZnO thin film through selection of the corresponding charge to mass ratio.

A Varian 200-20A2F ion implanter located at iThemba LABS (Gauteng), Johannesburg, was used for the implantation experiments. All implants were done at room temperature at high vacuum using Sm, ions at energy of 80 keV at different fluence ranging from $\approx 10^{14}$ -10^{16} ions/cm^2. The Sm^{+} ions were obtained from a chip of Sm_2O_3 sputter target. Stopping and Range of Ions in Matter (SRIM) programme was first used before ion implantation to project distribution profiles of the Sm^{+} in ZnO matrix. This showed an estimated projected range of ≈ 20 nm and an average Sm^{+} ion concentration of 2.37% as shown in Figure 7-1.

The film morphologies and structural analyses were characterized using Veeco Di-3100 atomic force microscopy (AFM) in tapping mode. Grazing incidence x-ray diffraction (XRD) measurements were taken using AXS Bruker D8 Discover, with the generator set at 40kVand 40 mA to produce a highly collimated and high resolution8.0 keV Cu Kα radiation after projecting the beam through the Gobbel Mirror and 004 Ge crystal as monochromator. The GIXRD measurements were performed in the Seeman-Bohlin geometry at a low scanning rate of 1.2°/minute and fixed incident angle of 1°.

Photoluminescence measurements were carried out using a Horiba LabRAM HR spectrometer with a 150 lines/mm grating and an excitation wavelength of 244 nm from a frequency doubled Lexel argon ion laser. Rutherford backscattering spectrometry (RBS) measurements were

performed to determine the thickness and distribution profiles of Sm^+ ions in the ZnO matrix at room temperature using $4He^+$ particles of energy 1.6 MeV at a backscattering angle of 165° (IBM geometry). The beam current was kept between 10 and 15 nA during measurements and the implantation was carried out of the channeling direction of ZnO on Si substrate hence restricting the implantation to required damage depth.

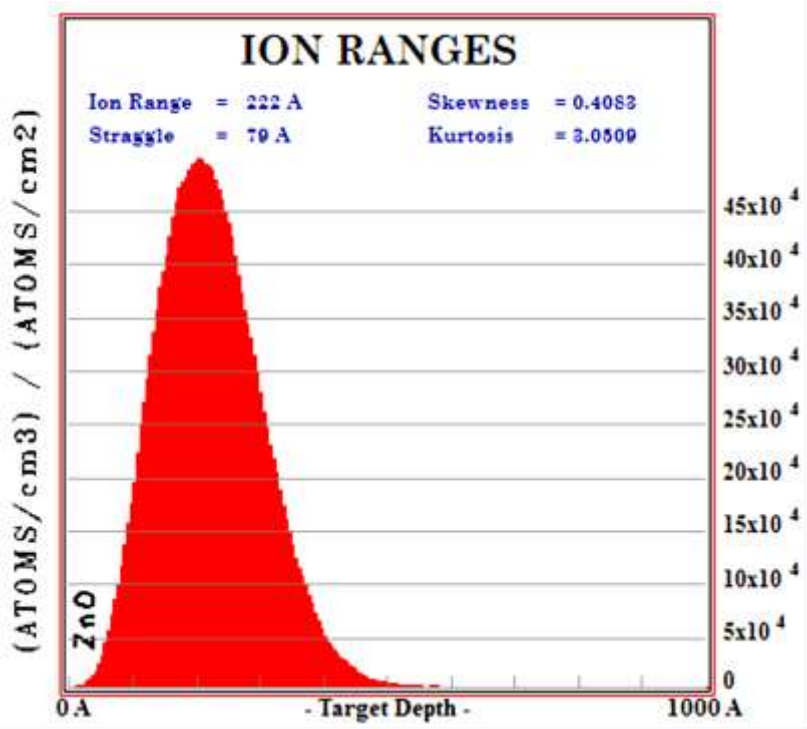


Figure 7-1: SRIM profile illustrating the estimated ion distribution with penetration depth for Sm+ ions of energy 80 keV.

7.2. Stopping and Range of Ions in Matter (SRIM) calculation

7.2.1. Introduction to SRIM and analysis of Sm based implantations in ZnO

SRIM is a software package used to investigate the Stopping and Range of Ions in Matter. It has been continuously upgraded since its introduction in 1985 [12]. As at 2010, it had received more than 700 scientific citations on average annually [13]. This tremendous increase makes SRIM an extremely popular program in the radiation effects on materials community. SRIM is based on a

Monte Carlo simulation method, namely the binary collision approximation with a random selection of the impact parameter of the next colliding ion. It is capable of producing quick calculations of tabulated data for the stopping powers, range and straggling distributions of any ion at any energy (in the range 10 eV–2 GeV) and in any elemental target [14]. Additionally SRIM calculates the backscattered and sputtered particle distribution functions resulting from positive atomic - ion bombardment of any amorphous surface. When energetic ions bombard a solid surface, the target material's surface is eroded by the cascade of collisions. This erosion rate is quantified as the sputter yield, and it is defined as the average number of atoms leaving the surface of a solid per incident ion / particle. It has been shown that the penetration depth can be expressed in terms of parameters characterizing the target material and the incoming ion energy [15].

From these SRIM calculations, it is observed that the implant depth is localized to depths just below the surface (at the sub-surface) and as the energy increases the implanted region is buried more into the sub-surface regions of the substrate. The depth distribution also depends on the ion mass, with the lighter ions penetrating more below the surface than the heavier ones at the same energies.

7.3 Results and discussion.

7.3.1 Morphology Studies using Atomic force microscopy

Figure 7-2 shows the surface topography of ZnO layer before and after Sm^{+} implantation characterized by the Veeco Di3100 AFM in tapping mode.

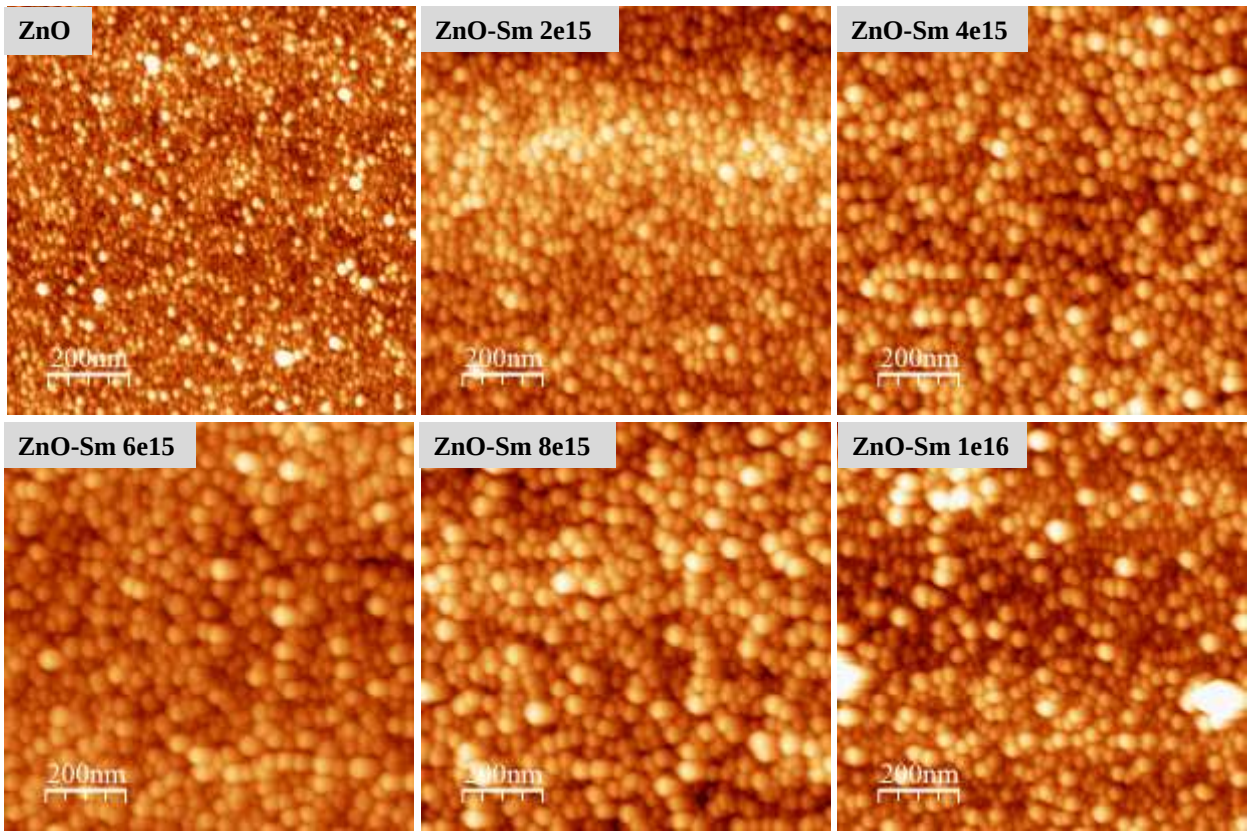


Figure 7-2: Tapping mode AFM images of ZnO and ZnO:Sm^{+} thin films.

The roughness, rms of the pristine ZnO film surface was 5.29 nm with an average grain size of 22.4 nm. Upon ion implantation of Sm^{+} at a fluence of 2×10^{15} ions/cm^2, the rms increases to 17.5 nm with an average grain size of 61.1 nm. The increase in the surface roughness is attributed to the competition between ad atom diffusion/mobility and energy dissipation on the film. As the implanted dose of Sm increases, the surface roughness increases steadily as a result of formation of microvoid structures or amorphization of the surface [17]. Statistical analysis of the film is as shown in table 7-1.

Table 7-1: Summary of tapping mode AFM analysis with varied fluence

Samarium fluence (ions/cm^2)	R_a (nm)	R_{rms} (nm)	Skewness (R_{sk})	Grain height (nm)
0	3.92	5.29	1.454	22.4
2×10^{15}	13.9	17.5	0.253	61.1
4×10^{15}	20.7	25.8	0.308	70.9
6×10^{15}	21.9	27.8	0.463	84.5
8×10^{15}	26.7	33.3	0.304	87.0
10×10^{15}	20.8	26.2	0.752	62.7

During the early stages of ion implantation process, the rms roughness increases from 5.29 nm for the virgin sample to 33.3 nm after implanting with a fluence of 8×10^{15} ions/cm^2. However, at a fluence of 10×10^{15} ions/cm^2 , the roughness decreases to about 26.2 nm. During low fluences, the coarsening of the particless makes the surface to become rougher whereas when the fragmentation and inverse-coarsening of the particles occurs at 10×10^{15} ions/cm^2, a slight smoothening in the surface is observed [18]. According to Paramanik, Dipak, et al., smoothening of surface beyond certain fluence may be associated with partial amorphization or localized melting on the surface. At high fluences, there is an increase in the density of electronic excitations hence the covalent bonds in the lattice weaken or get broken leading to relaxation causing the surface amorphization [19, 20] or reduced strain in the film [21].

It is also worth noting that the grains sizes appear larger than average particle size estimated using Debye-Sherrer relation on XRD Bragg reflexes which gave a particle size of 22.4 nm for the virgin ZnO and 61.1 nm for the ZnO implanted with Sm^+ at a fluence of 2×10^{15} ions/cm^2. As the fluence increased there is coarsening and the particles appear larger as seen from their increasing grain

height. At a fluence of 10×10^{15} ions/cm^2 there is a decrease in grain height suggesting that the inverse ripening occurs as a result of the fragmentation of particles [18].

Even though this indicates the polycrystalline nature of the ZnO films, the differences in the grain size are attributed to the nature of the GIXRD diffraction experiment which provides particle size measurement along the in plane direction. However it can also be postulated that majority of the Sm^+ implants occupy interstitial sites that are slightly displaced from the substitutional Zn site, with a (nearly) isotropic root mean square (rms) displacement of the order of 0.10–0.25 Å [22, 23] while the remainder of the ions are assumed to reside on a low symmetry sites with a more disordered surrounding. These could be the cause of increase in roughness. The roughness however reduces with annealing, an indication of better on-site incorporation of the RE upon annealing. The film thickness of the virgin ZnO was estimated at 152 ± 5 nm using a surface profilometer. The particles are generally smooth and well separated with a regular spherical shape covering the overall surfaces with a high packing density of the films.

7.3.2. Scanning Electron Microscopy (SEM).

Figure 7-3 presents the SEM images of the undoped ZnO and Sm^{+} implanted ZnO thin films.

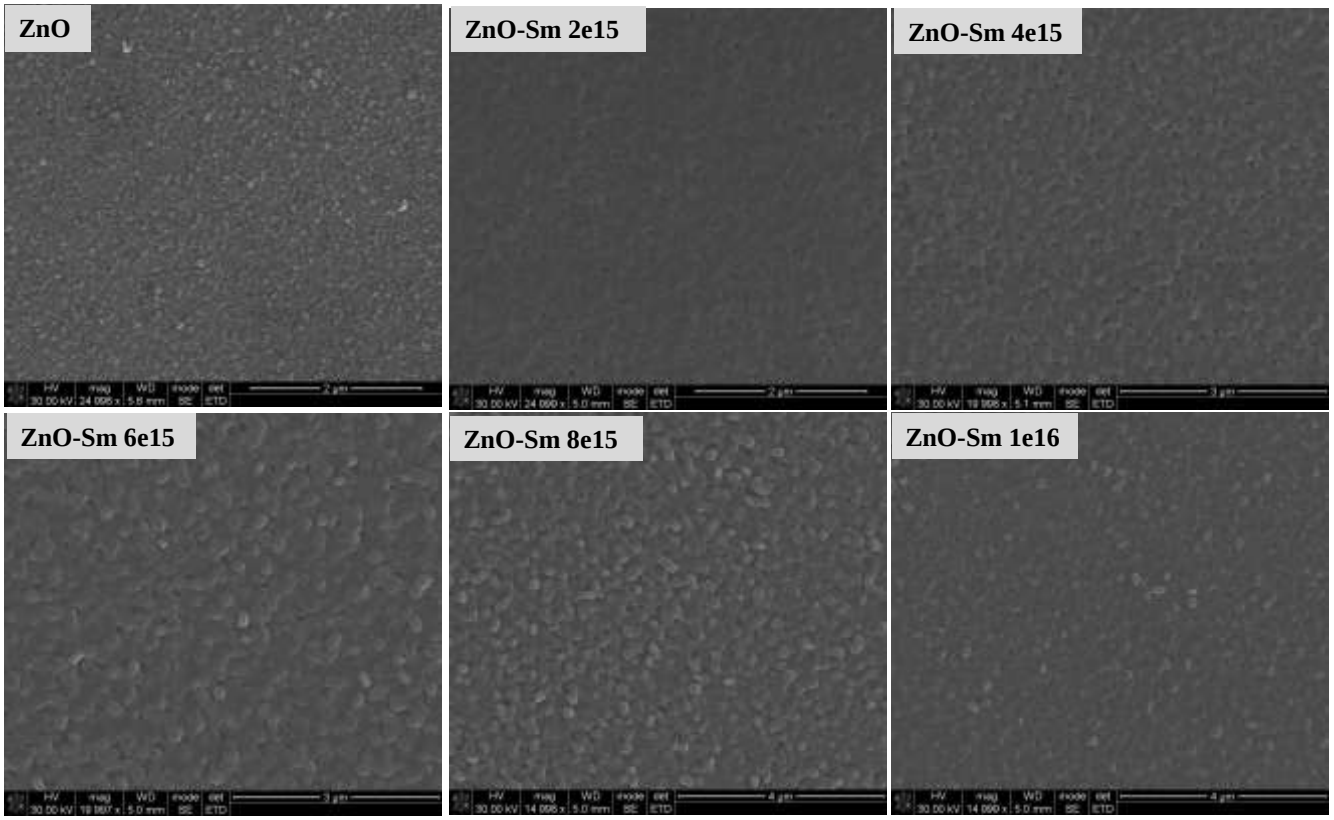


Figure 7-3: SEM micrographs of the undoped ZnO Sm^{+} - doped ZnO films implanted at different fluences.

One may note that all the thin films exhibit lateral homogeneity consistent with uniformly distributed particles across the substrate. The film thickness of the virgin ZnO was estimated at 152 ± 5 nm using a surface profilometer. The particles are generally smooth and well separated with a regular spherical shape covering the overall surfaces with a high packing density of the films.

The elemental compositions of the films were qualitatively determined using Energy-dispersive X-ray spectroscopy measurements as shown in figure 7-4. The EDS showed that pristine ZnO films had no impurity only until after the implantation of Sm. The presence of Sm upon implantation is marked as Re in the EDS spectrum. From this figure the peak convolution of the

Re and the elemental constituent in the EDS setup makes it difficult to distinguish the X-ray singnal due to rare earth ions from the constituent elements in the ZnO film. This is expected due to the limited resolution of the Si (Li) detector used in these measurements. We therefore studied the films using Rutherford Backscattering Spectroscopy measurements and the results of the measurements are discussed in the following section.

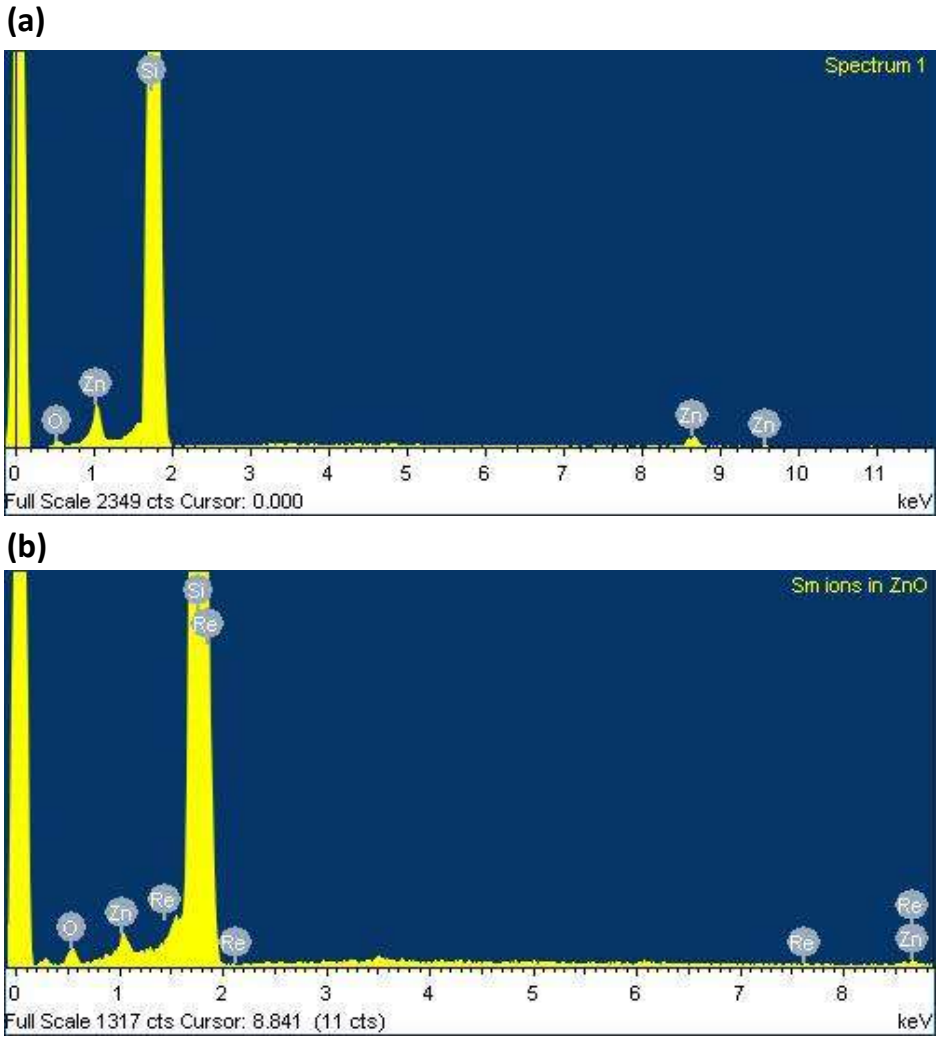


Figure 7-4: EDS of ZnO thin film before and after Sm ion implantation

7.3.3 Rutherford Backscattering Spectroscopy measurements

A RBS spectrum of virgin ZnO and Sm^+ - doped ZnO thin film at a fluence of 2×10^{15} ions/cm^2 on Si substrate is shown in Fig.7-5. Each experimental spectrum could well be reproduced together with a computer simulation using the XRump code shown in Figure 7-5. The structures in the RBS spectrum around channel 180, 260, 410 and 480 are attributed to the non-Rutherford scattering cross-section from O, Si, Zn and Sm respectively and the surface energy positions in channels of the elements have been shown using arrows.

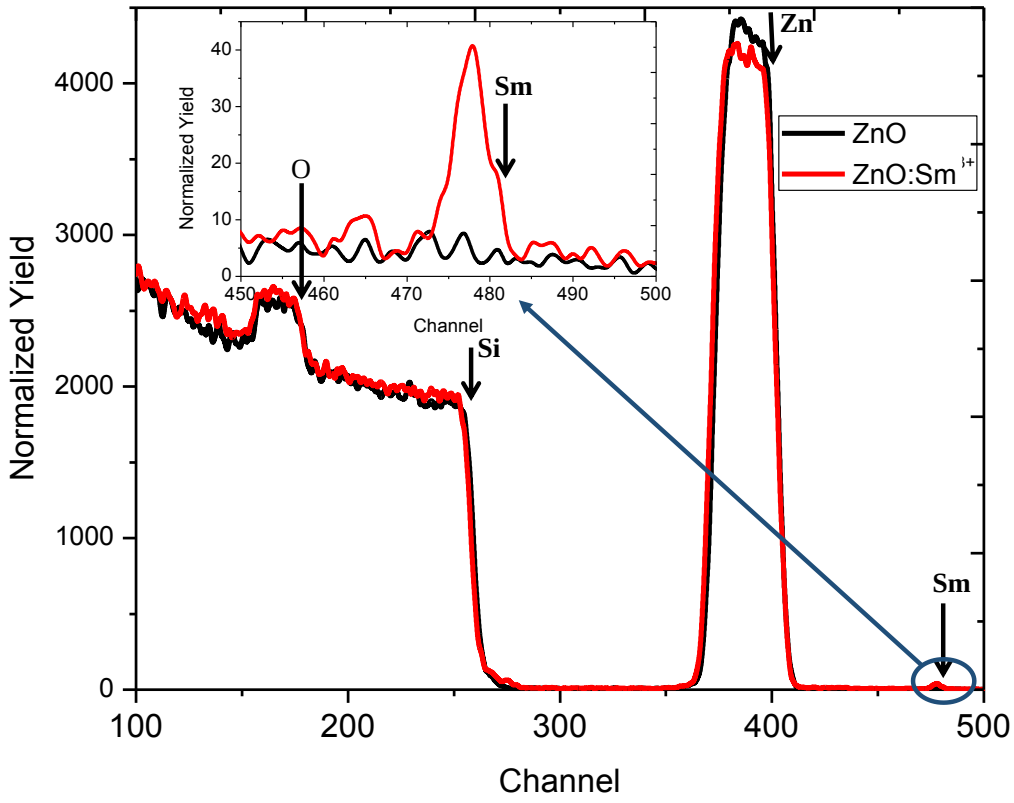


Figure 7-5: RBS spectrum of an 154 nm Sm implanted ZnO layer on Si showing experimental data at a fluence of 2 × 10^{15} ions/cm^2. Inset is a zoom plot of channel range 450-500.

Figure 7-5 shows RBS spectrum (raw data) of the as-deposited ZnO and Sm^+-implanted ZnO films on Si substrate with the constituent atoms at different energy channels to confirm the composition depth profile and thickness of the deposited films. The measured RBS has been simulated using

the XRUMP software to establish the composition profile throughout the films as shown in Figure 7-6. The simulated spectra yield an average thickness of the films 154 ± 2 nm in agreement with the thickness measurement by the surface profilometer (152 nm).

The presence of Sm^+ ions in the films is quite evident and the global atomic concentrations of the different species contained in the film can be deduced. From the XRump simulation for Sm^+ doped ZnO shown in Figure 7-6, stoichiometry of the matrix of 49.3, 48.3 and 2.37 % for Zn, O and Sm, respectively was derived.

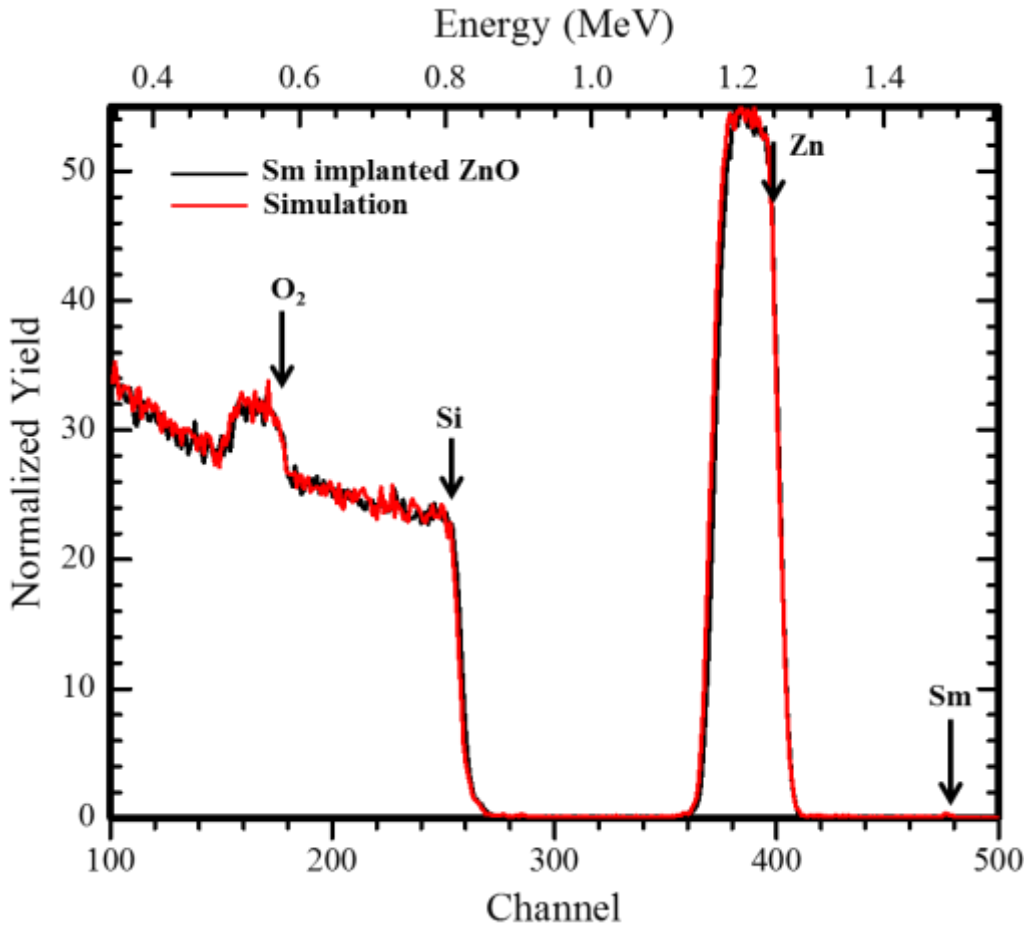


Figure 7-6: RBS spectrum of an 154 nm Sm implanted ZnO layer on Si showing experimental data and computer simulation using XRump code.

Figure 7-6 shows the raw data RBS spectrum of ZnO implanted with varying Sm fluence. The concentration of the Sm ions is seen to steadily increase with fluence as predicted from the SRIM simulation in table 7-2.

Table 7-2: Simulated Sm concentration using varied fluences.

Samarium fluence (ions/cm^2)	Mean depth (nm)	Max. concentration %	Average concentration %
10^{12}	20.01	6.12×10^{-4}	3.89×10^{-4}
10^{14}	20.01	6.12×10^{-2}	3.89×10^{-2}
2×10^{15}	20.01	1.22	0.77
3×10^{15}	20.01	1.84	1.17
4×10^{15}	20.01	2.45	1.55
5×10^{15}	20.01	3.06	1.94
6×10^{15}	20.01	3.67	2.33
8×10^{15}	20.01	4.90	3.11
1×10^{16}	20.01	6.12	3.89

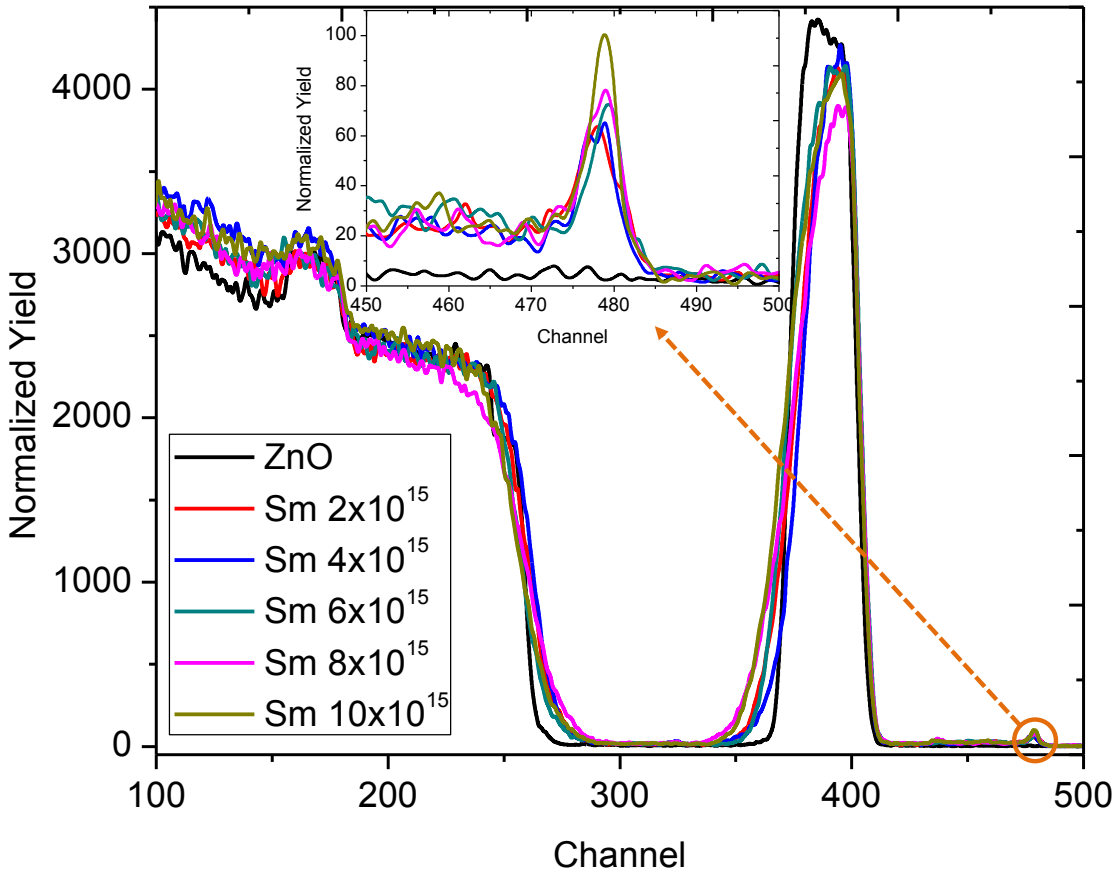


Figure 7-7: RBS spectra of Sm implanted ZnO layer at different fluences at energy of 80 keV. Inset is a zoom plot of channel range 450-500.

Figure 7-7 shows RBS spectra profile for Sm implanted ZnO thin film at varied fluences. The Sm profile was found to be almost Gaussian in shape with a maximum depth around 20 nm. This is in agreement with the projected range calculated for 80 keV Sm in ZnO using the SRIM simulation.

The simulated spectrum shown in Figure 7-6 for the 2×10^{15} ions/cm^2 implantation was generated by assuming a three layer structure with the Sm concentration in the layers progressively decreasing; viz. layer I with width 11 nm, layer II width 19 nm and layer III with width 124. The atomic surfaces were determined to be in channels: Zn = 401, Sm = 461, Si = 287, O = 180. The normalized yield is observed to gradually increase for all fluences, an indication that the implanted Sm ions were quite below saturation point.

7.3.4. Grazing incidence XRD measurements.

Figure 7-10 shows the Grazing incidence X-ray diffraction patterns of ZnO thin films deposited by RF sputtering at room temperature and post-annealed at 700 ˚C for 2 hours at a ramping rate of 10 ˚C/min and Sm^{+}-doped ZnO.

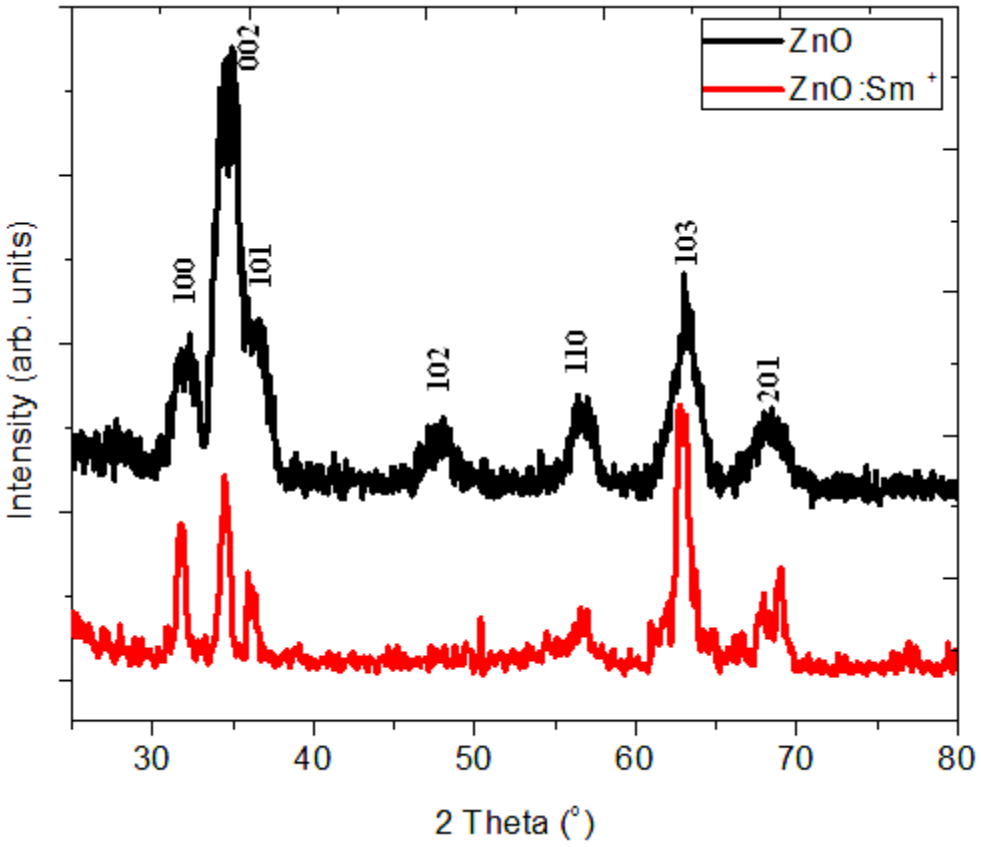


Figure 7-8: GIXRD patterns of pristine-, unannealed Sm implanted- - and annealed Sm implanted ZnO thin films. The dose used for Sm implantation is ions/cm².

The diffraction pattern of the pristine ZnO films confirms their polycrystalline nature with a preferentially *c*-axis-oriented for the wurtzite structure. All the peaks have been indexed to the JCP2 card number 003-0888 corresponding to wurtzite structure of space group P63mc and lattice constants, a = 3.2489Å and c = 5.2062Å. The first three peaks are (100), (002) and (101). The diffraction pattern of the Sm^{+} implanted ZnO thin film (red) in figure 7-9 depicts the shift in the

peak positions of the strongest peaks and preferential orientation (103) associated with texture. The peak positions of the ZnO (100) and (002) planes shift to a lower angle side, indicating an increment in both the *c*-axis and *a*-axis lattice constants. Since the ionic radius of the Sm^{+} ions (0.096 nm) is larger than that of Zn^{2+} (0.074 nm), implantation of Sm^{+} ions into ZnO lattice leads to an increase in the lattice constants hence the diffraction peaks shifting toward a lower diffraction angle. However the prevalence of tensile macro stresses in the lattice cannot be ruled out. The evidence of texture is further supported by the suppression in the intensity of the (002) peak in Sm^{+}-doped ZnO patterns and this could possibly indicate preferred formations of crystallographic planes with higher surface energy due to the substitution of Zn site with mismatched Sm^{+} ions [24].

7.3.5. Raman Spectroscopy

Figure 7-9 shows the Raman spectra for pristine ZnO annealed at 700 ˚C and Sm^+ implanted ZnO thin films.

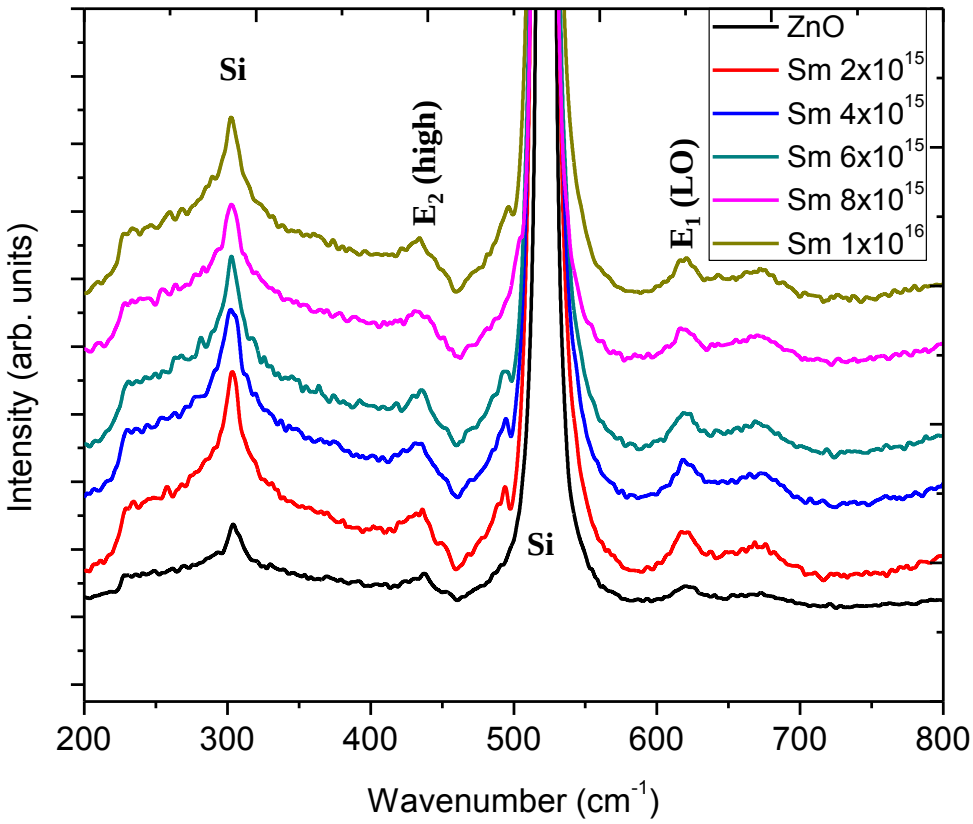


Figure 7-9: Raman spectra of RF sputtered ZnO films grown on Si (100), as grown and after ion implantation with Sm^+ to form ZnO:Sm^+.

The room temperature Raman spectra of ZnO and Sm^+-doped ZnO thin films at a wavenumber of 200 to 800 cm^{-1} are shown in Figure 7-9. The A1 and E1 modes are polar phonons which split into transverse optical (TO) and longitudinal optical (LO) phonons. The nonpolar E_2 modes have two frequencies, namely, E_2 (low) and E_2 (high) which corresponds to the Zn and O sublattice vibrations, respectively [25, 26, 27]. In our case since the measurement was carried out between 200 to 800 cm^{-1} only the E_2 (high) was observed for both undoped ZnO (at 435.3 cm^{-1}) and Sm^+-doped ZnO at (431.3 cm^{-1}) using a fluence of 2×10^{15} ions/cm^2. This E_2 (high) mode is known to

be sensitive to the stress within ZnO nanostructures [28]. This peak also appears broader (FWHM value is 14.2 $cm^{-1}$for illustration) upon implantation with Sm^{+} ions compared to FWHM value of 13.44 cm^{-1} for the undoped ZnO. The red shift may be attributed to the local lattice softening caused by the incorporation of highly mismatched (charge state imbalance and mass) Sm^{+} into Zn antisites. Softening of the lattice is caused by the large sized Sm^{+} ion sitting in a strongly electronegative environment as a result of the negatively charged surrounding oxygen ions [29, 30]. Since Zn has four nearest oxygen atoms neighbors, the mode softening for the E_2 (high) mode is most likely.

The intensity of the E_2 (high) mode denotes the crystallization of ZnO crystal structure [31], hence Sm^{+}-doped ZnO thin films is obviously having lower intensity compared to that of ZnO, revealing the restrained degree of crystallization along the *c*-axis. The possible emergence of the fiber texture along the (103) reflex in the implanted films could also lead to the suppression in the intensity of the Raman mode. The band at 580 cm^{-1} is usually defect related and is assigned to E_1(LO) mode and its presence in both films indicates the presence of oxygen vacancies or oxygen interstitials [24].

7.3.6. Photoluminescence studies

The photoluminescence properties of the ZnO and Sm^{+}-doped ZnO films are examined using room temperature photoluminescence (PL) spectroscopy fitted with an excitation source at 224 nm. Figure 7-10 shows explicitly distinct emissions UV emission (378.8 nm for pure ZnO thin films and 379.7 nm for Sm^{+}- doped ZnO) resulting from the free excitons recombination through an exciton-exciton collision process corresponding to the near-band edge (NBE) exciton emission of the wide band gap ZnO [32, 33]. The red-shift in the NBE emission upon implanting Sm^{+} into

ZnO could possibly indicate the narrowing of the band gap due to increased dopant states near the bottom of the conduction band [14] or the prevalence of vibronic states that act as exciton recombination pathways. The films were annealed before ion implantation but not after.

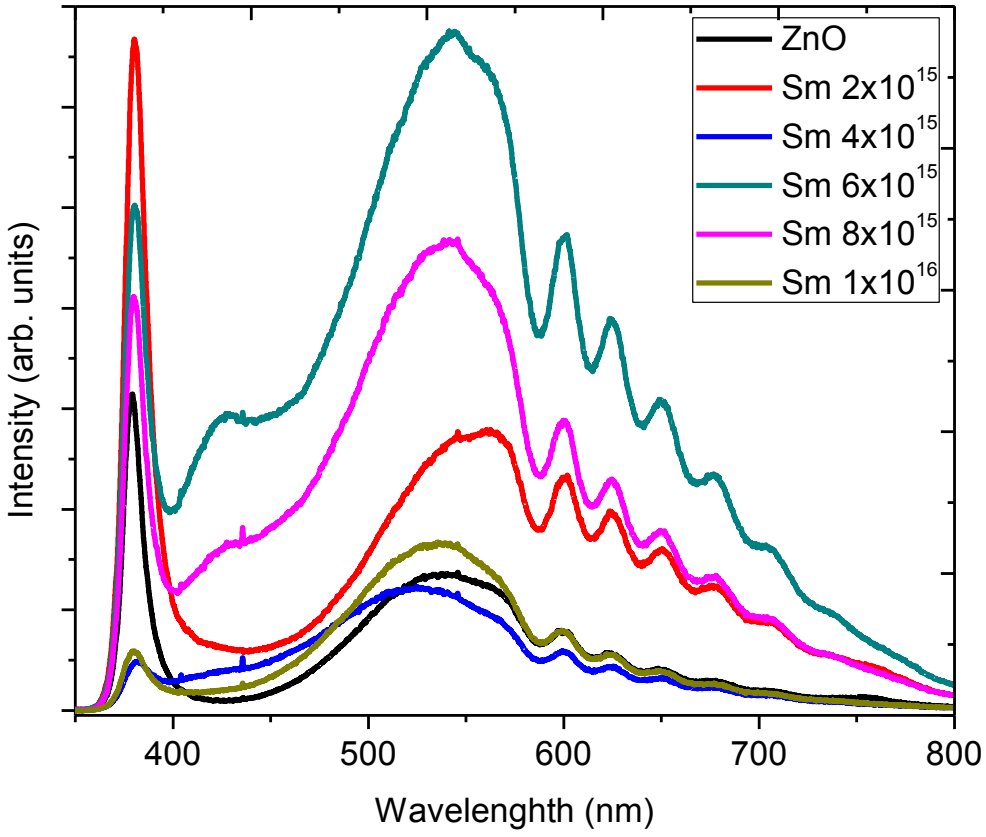


Figure 7-10: Room temperature PL spectra of the ZnO and Sm^{+}-doped ZnO thin films both of average thickness of 152 nm.

The broad green emission band range in the vicinity of 560 nm is associated with the various deep-level defects, such as zinc interstitial (Zn_i), oxygen interstitial (O_i), zinc vacancy (V_{Zn}), oxygen vacancy (V_O), or single-ionized oxygen vacancies in ZnO [34]. In addition there are yellow-orange induced from the recombination of a photogenerated hole with an electron that belongs to a singly ionized defect, such as oxygen vacancy or oxygen interstitial. Upon doping with Sm^{+} the possible substitution of Zn^{2+} site with low concentration Sm^{+} may enhance lattice distortion to compensate

for the charge imbalance and increase in the amounts of defects such as oxygen vacancies and oxygen interstitials leading to enhancement of the intensity of green, yellow and orange emission. These increased defects however led to the suppressing of the excitonic emission resulting in decrease of the near band edge emission intensity as the fluence increased beyond 6×10^{15} ions/cm^2. Figure 7-11 shows a schematic diagram of the energy level the ZnO:Sm$^+$ thin films. It seems that there is concentration based quenching for large fluences especially for the NBE emission,

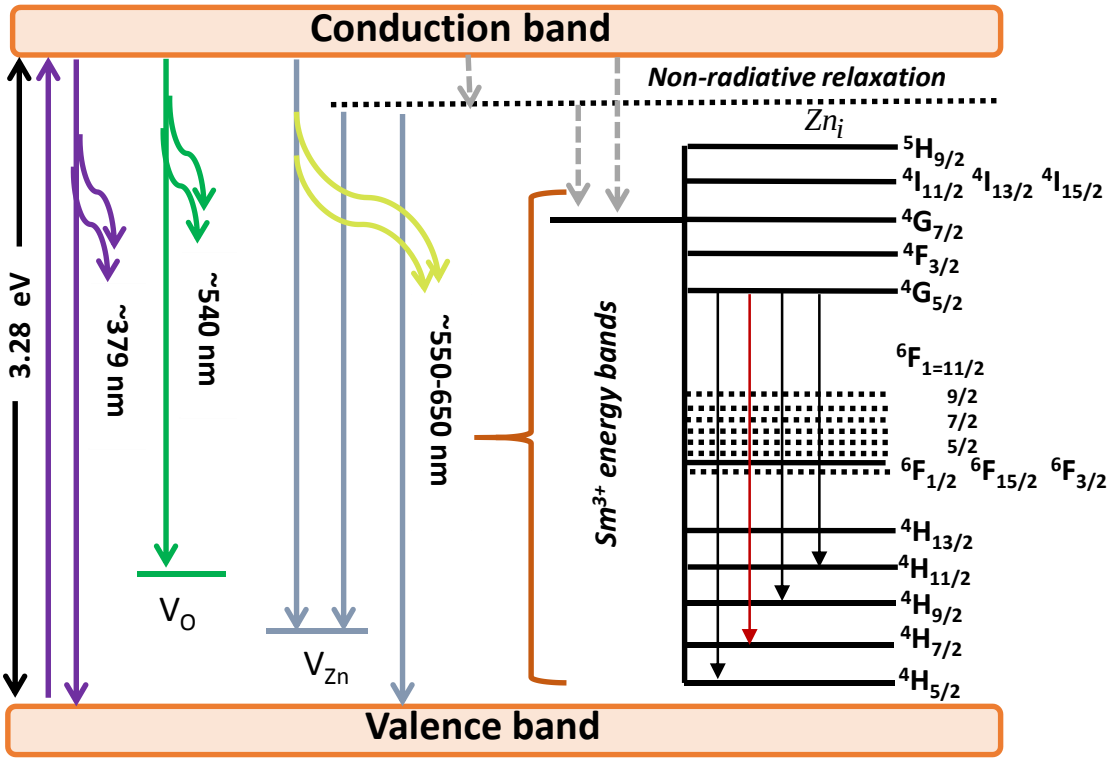


Figure 7-11: schematic of the energy level diagram of the ZnO:Sm$^+$ thin films.

Previous studies have been reported on PL properties of Sm$^+$ in ZnO polycrystalline pellets and their dependence on microstructure [11, 35, 36]. They reported that Sm$^+$ photoluminescence were only observed under the direct excitation or on impact excitation by hot electrons. However no energy transfer from ZnO to Sm$^+$ ions was observed. Moreover, Tsuji, Takahiro, *et al* [9] have

posited that the Sm^+ PL properties may depend on extrinsic effects since the ZnO:Sm^+ polycrystalline samples contain several grain boundaries and defects which usually act as non-radiative centers. In our study, we noted an additional shoulder at 427 nm and peaks at 435 and 544 nm which could be attributed to $^4G_{5/2}$–^6F_J (J = 11/2, 9/2, 7/2, 5/2) transition of Sm^+ ions. This indicates the contribution of the energy transfer from ZnO to Sm^+ since the ZnO:Sm^+ thin films are high-quality *c*-axis oriented thin films. There is also an enhancement of oscillatory excitations in the range of 600-750 nm, an indication of increase in defect levels as a result of Sm^+ ion implantation below the quenching limit which seems to kick in at an implantation fluence of 1×10^{16} ions/cm^2.

7.4. Conclusion

The effects of implantation of Samarium ions (Sm^+) on the properties of ZnO films grown on Si (001) substrate by RF sputtering system are presented. The films showed uniformly distributed homogeneous grains, an indication of the high packing density of the films. X-ray diffraction (XRD), atomic force microscope (AFM) and the Photoluminescence (PL) were employed to analyze the influence of the Sm^+ ions implantation into the ZnO matrix. The structural properties of undoped and Sm^+- doped ZnO thin films were investigated by Atomic force microscopy, Scanning Electron microscopy, Grazing incidence XRD and Raman scattering studies. Local lattice softening caused by the incorporation of highly mismatched Sm^+ (ionic radius 0.096 nm) into Zn antisites was detected as a red shift in E2 (high) mode and reduction in the crystallinity of the ZnO film. Photoluminescence on the pristine ZnO film has shown a strong near band gap (NBE) emission and an intrinsic defect related blue, green-orange emission. The NBE first increases after implantation of Sm^+ then suppressed while the blue, green – orange emission

intensities are enhanced as a result of increased structural defects with mismatched charge states. Moreover an additional shoulder at 427 nm and peaks at 435 and 544 nm are observed after ion implantation and they are most likely associated with the excitonic energy transfer from the host ZnO to the Sm^+ ions ($^4G_{5/2}$–^6F_J (J = 11/2, 9/2, 7/2, 5/2). The elucidation of the excitation lines due to energy transfer between ZnO and Sm^+ can be illustrated from room temperature PL measurements under reduced non radiative effects. The fluence was varied and the RBS data was in agreement with the projected range calculated for 80 keV Sm in ZnO using the SRIM simulation – a Monte Carlo simulation based on the binary collision approximation.

7.5. References (for chapter 7)

[1] P. Velusamy, R.R. Babu, K. Aparna, Effect of Sm doping on the physical properties of ZnO thin films deposited by spray pyrolysis technique, in: AIP Conference Proceedings, AIP Publishing, 2017, pp. 080085.

[2] D. Alsebaie, W. Shirbeeny, A. Alshahrie, M.S. Abdel-Wahab, Ellipsometric study of optical properties of Sm-doped ZnO thin films Co-deposited by RF-Magnetron sputtering, Optik-International Journal for Light and Electron Optics, 148 (2017) 172-180.

[3] W.E. Mahmoud, A. Al-Ghamdi, S. Al-Heniti, S. Al-Ameer, The influence of temperature on the structure of Cd-doped ZnO nanopowders, Journal of Alloys and Compounds, 491 (2010) 742-746.

[4] W.E. Mahmoud, A. Al-Ghamdi, The influence of Cd (ZnO) on the structure, optical and thermal stabilities of polyvinyl chloride nanocomposites, Polymer Composites, 32 (2011) 1143-1147.

[5] S. Lima, F. Sigoli, M. Jafelicci Jr, M.R. Davolos, Luminescent properties and lattice defects correlation on zinc oxide, International Journal of Inorganic Materials, 3 (2001) 749-754.

[6] G. Blasse, B. Grabmaier, A General Introduction to Luminescent Materials, in: Luminescent materials, Springer, 1994, pp. 1-9.

[7] F.A. Sigoli, C. de Oliveira Paiva-Santos, M. Jafelicci, M.R. Davolos, Study of crystallite size and strain as a function of morphological evolution in zinc oxide powder obtained from hydroxycarbonate precursor, Powder Diffraction, 16 (2001) 153-159.

[8] H. He, J. Fei, J. Lu, Sm-doping effect on optical and electrical properties of ZnO films, Journal of Nanostructure in Chemistry, 5 (2015) 169-175.

[9] T. Tsuji, Y. Terai, M. hakim bin Kamarudin, M. Kawabata, Y. Fujiwara, Photoluminescence properties of Sm-doped ZnO grown by sputtering-assisted metalorganic chemical vapor deposition, Journal of Non-Crystalline Solids, 358 (2012) 2443-2445.

[10] D. Kouyate, J.-C. Ronfard-Haret, J. Kossanyi, Electroluminescence of Sm3+ ions in semiconducting polycrystalline zinc oxide, Journal of Materials Chemistry, 2 (1992) 727-732.

[11] X. Zeng, J. Yuan, L. Zhang, Synthesis and photoluminescent properties of rare earth doped ZnO hierarchical microspheres, The Journal of Physical Chemistry C, 112 (2008) 3503-3508.

[12] J.F. Ziegler, J.P. Biersack, The stopping and range of ions in matter, in: Treatise on Heavy-Ion Science, Springer, 1985, pp. 93-129.

[13] J.F. Ziegler, M.D. Ziegler, J.P. Biersack, SRIM–The stopping and range of ions in matter (2010), Nuclear Instruments and Methods in Physics Research Section B: Beam Interactions with Materials and Atoms, 268 (2010) 1818-1823.

[14] S. Martinie, T. Saad-Saoud, S. Moindjie, D. Munteanu, J.-L. Autran, Behavioral modeling of SRIM tables for numerical simulation, Nuclear Instruments and Methods in Physics Research Section B: Beam Interactions with Materials and Atoms, 322 (2014) 2-6.

[15] A. Yen, W.-k. Chu, S. Tavares, J. Arruda-Neto, M. Goncßalves, V. Likhachev, J. Mesa, E. de Oliveira, S. de Pina, O. Rodriguez, Subject index of volumes 211–220, Nuclear Instruments and Methods in Physics Research B, 219 (2004) 92-121.

[16] M. Nastasi, J. Mayer, J.K. Hirvonen, Ion-solid interactions: fundamentals and applications, Cambridge University Press, 1996.

[17] S. Eshghi, M.H. Zadeh, M. Yari, E. Jafari-Khamse, The effect of nitrogen ion implantation on the corrosion resistance and microstructure of tantalum-coated stainless steel, The European Physical Journal Plus, 129 (2014) 117.

[18] D. Paramanik, S. Majumder, S. Sahoo, S. Varma, Nano Pattern Formation and Surface Modifications by Ion Irradiation, Defence Science Journal, 59 (2009) 413.

[19] C.A. Volkert, Stress and plastic flow in silicon during amorphization by ion bombardment, Journal of Applied Physics, 70 (1991) 3521-3527.

[20] P. Srivastava, V. Ganesan, O. Sinha, Evidence of plastic flow and recrystallization phenomena in swift (~ 100 MeV) Si 7+ ion irradiated silicon, Nuclear Instruments and Methods in Physics Research Section B: Beam Interactions with Materials and Atoms, 222 (2004) 491-496.

[21] S. Dey, C. Roy, A. Pradhan, S. Varma, Raman scattering characterization of Si (100) implanted with mega-electron-volt Sb, Journal of Applied Physics, 87 (2000) 1110-1117.

[22] U. Wahl, J. Correia, E. Rita, E. Alves, J. Soares, B. De Vries, V. Matias, A. Vantomme, I. Collaboration, Recent emission channeling studies in wide band gap semiconductors, Hyperfine Interactions, 159 (2004) 363-372.

[23] K. O'Donnell, B. Hourahine, Rare earth doped III-nitrides for optoelectronics, The European Physical Journal-Applied Physics, 36 (2006) 91-103.

[24] C. Lin, S. Young, C. Kung, L. Horng, H. Chen, M. Kao, Y. Shih, C. Ou, Phonon spectra and magnetic behaviors of hydrothermally synthesized Sm-doped ZnO nanorods, Vacuum, 87 (2013) 178-181.

[25] R. Al Asmar, J. Atanas, M. Ajaka, Y. Zaatar, G. Ferblantier, J. Sauvajol, J. Jabbour, S. Juillaget, A. Foucaran, Characterization and Raman investigations on high-quality ZnO thin films fabricated by reactive electron beam evaporation technique, Journal of Crystal Growth, 279 (2005) 394-402.

[26] J. Calleja, M. Cardona, Resonant Raman scattering in ZnO, Physical Review B, 16 (1977) 3753.

[27] M. Rajalakshmi, A.K. Arora, B. Bendre, S. Mahamuni, Optical phonon confinement in zinc oxide nanoparticles, Journal of Applied Physics, 87 (2000) 2445-2448.

[28] Y. Liu, H. Zhang, X. An, C. Gao, Z. Zhang, J. Zhou, M. Zhou, E. Xie, Effect of Al doping on the visible photoluminescence of ZnO nanofibers, Journal of alloys and compounds, 506 (2010) 772-776.

[29] K. Samanta, P. Bhattacharya, R.S. Katiyar, Raman scattering studies of p-type Sb-doped ZnO thin films, Journal of Applied Physics, 108 (2010) 113501.

[30] S. Limpijumnong, S. Zhang, S.-H. Wei, C. Park, Doping by large-size-mismatched impurities: the microscopic origin of arsenic-or antimony-doped p-type zinc oxide, Physical review letters, 92 (2004) 155504.

[31] S. Sharma, G. Exarhos, Raman spectroscopic investigation of ZnO and doped ZnO films, nanoparticles and bulk material at ambient and high pressures, in: Solid State Phenomena, Trans Tech Publ, 1997, pp. 32-37.

[32] F. Otieno, M. Airo, R.M. Erasmus, D.G. Billing, A. Quandt, D. Wamwangi, Structural and spectroscopic analysis of ex-situ annealed RF sputtered aluminium doped zinc oxide thin films, Journal of Applied Physics, 122 (2017) 075303.

[33] X. Meng, D. Zhao, D. Shen, J. Zhang, B. Li, X. Wang, X. Fan, ZnO nanorod arrays grown under different pressures and their photoluminescence properties, Journal of luminescence, 122 (2007) 766-769.

[34] Y. Wang, J. Piao, Y. Lu, S. Li, J. Yi, Intrinsic ferromagnetism in Sm doped ZnO, Materials Research Bulletin, 83 (2016) 408-413.

[35] J.-C. Ronfard-Haret, D. Kouyate, J. Kossanyi, Evidence for direct impact-excitation of luminescent rare-earth centers (Ho3+ and Sm3+) in semiconducting zinc oxide, Solid state communications, 79 (1991) 85-88.

[36] T. Ohtake, S. Hijii, N. Sonoyama, T. Sakata, Electrochemical luminescence of n-type ZnO semiconductor electrodes doped with rare earth metals under the anodic polarization, Applied Surface Science, 253 (2006) 1753-1757.

Chapter 8: Conclusion and future work

8.1. Conclusion

The aim of this project was to study the effect of Al and rare earth doping on the structural and spectroscopic properties of wide band gap oxide (ZnO) thin films.

The choice of the Terbium, Europium and Samarium dopant for such oxides to develop photon frequency downshifter materials necessitates foremost careful investigations to understand the effects of doping on the properties of the ZnO matrix. This led us to conduct a wide characterization of the properties of the undoped and doped ZnO films. The access to numerous and complementary analysis techniques was of fundamental importance for this study and allowed to establish the understanding basis of the structural and spectroscopic changes occurring in in ZnO.

We first carried out several variations of growth parameters in the RF sputtering technique such as deposition time, RF power and use of varied Oxygen pressure (0-15 sccm) introduced into the chamber while the Argon flow was kept at 13 sccm. The films were then subjected to ex-situ annealing in an Argon filled furnace at a temperature range of 500-1000 ˚C. Through XRD analysis, we have shown that the as-deposited thin films are highly textured with dominant (002) peak line of the hexagonal ZnO wurtzite phase. Upon annealing the ZnO thin films experienced an increase in the crystallite size. We have correlated these results to an increase of the crystallinity, which induces microvoids reduction. The effect of Al doping of the ZnO thereafter revealed the use of dopant our higher ionic radius, Al^{3+} (0.053 nm) compared to Zn^{3+} (0.074 nm) led to substitution of Zn^{2+} with Al^{3+} resulting into compression of the lattice hence a decrease in the lattice parameters as observed in chapter 5. There quality of films were observed to increase from the evident increase in XRD intensity with annealing temperature up to a temperature of 900 ˚C

while the full wavelength at half maxima (FWHM) reduced. Beyond 900 ˚C, the films showed cracks from the SEM measurements.

The RF sputtered ZnO was successfully used as a buffer layer in a Perovskite solar cell, in this type of device ZnO functions as an electron transport layer for an device architecture of the form ITO/ZnO/$CH_3NH3PbI_3$/P3HT/Au. The device characteristics have been extracted from the J-V curves thus giving a Jsc = 2.89 μA cm^{-2}, V_{oc} = 5.28 mV and FF = 23.3 % as a proof of concept. The device low FF could be attributed to the morphological changes in ZnO due to the acidic character of the perovskites upon exposure to standard conditions. It was a great challenge obtaining a working solar cell device with the limited facility and lack of glove box measurements. The use of ZnO as host material for potential application in optoelectronic devices such as solar cells was also investigated. Due to its wide bandgap of 3.37 eV and a strong exciton binding energy of 60 meV, ZnO is considered a suitable host material for doping with rare earth ions. The doping process either during growth or through ion implantation was extensively studied with a view to modify the electronic structures of ZnO material to achieve new or improved physicochemical, electronic and optical properties. The optical properties of rare earth ion doped ZnO were found to depend on many factors such as dopant concentration, host structure and also on the preparation parameters and ex-situ annealing. The dopants can segregate as a separate phase on the surface of ZnO film or or either find occupancy in substitutional or interstitial sites or both. This will be highlighted in the subsequent paragraphs.

Tb^{3+} doped ZnO was fabricated through RF sputtering of ZnO (97%): Tb (3%) (99.99% purity) target before ex-situ annealing in Argon filled furnace. All samples show the defect related emission with a major green emission peak at 543 nm and a few oscillations attributed to the emissions of Tb^{3+}. These occurred at 492, 543, 595, 624, 543 and 563 nm. These peaks represented

the $^5D_4$–$^7F_6$, $^5D_4$–$^7F_5$, $^5D_4$–$^7F_4$, $^5D_4$–$^7F_3$, $^5D_3$–$^7F_5$ and $^5D_3$–$^7F_4$ transitions of Tb^{3+}, respectively. The excitations were assigned to direct excitation of the Tb^{3+} through the f $\rightarrow$ d transitions. The undoped and Tb^{3+} doped ZnO thin films were then incorporated into organic solar cell with device structure ITO/ZnO:Tb^{3+}/P3HT:PCBM/PEDOT:PSS/Al. From the UV-Vis absorption measurement there was an increased absorption in the ultraviolet region from 300 – 400 nm with the introduction of ZnO thin film as a bi-functional layer before P3HT:PCBM blend. The optical properties of the Tb doped ZnO demonstrate increased absorption upon doping with Tb^{3+} and it leads to an increase in the number of photo-generated carriers after conversion of photons from the UV region into photons in the visible region.. This down-conversion process altered the UV properties of the solar cell under the solar emission spectrum enabling absorption of photons in the UV range and re-emitting light at a longer wavelength in visible region, where the organic solar cell has a considerably better response leading to enhanced short circuit current density, Jsc from 4.11 to 4.82 mA cm^{-2}.

ZnO:Eu^{3+} thin films were also grown using a similar process. The PL spectra contain peaks related to intrinsic defects in ZnO and those attributed to the transition in Eu^{3+} ions. The photoluminescence emission spectra of the films showed five intense band emissions at 576 nm, 594 nm, 613 nm, 651 nm, 703 nm that correspond to the intrinsic 4f $\rightarrow$ 4f transitions of Eu^{3+} in the ZnO host. The resulting intrinsic 4f $\rightarrow$ 4f transitions of Eu^{3+} were assigned to $^5D_0$ - $^7F_0$, $^5D_0$ - $^7F_1$, $^5D_0$ - $^7F_2$, $^5D_0$ - $^7F_3$, and $^5D_0$ - $^7F_4$ transitions of Eu^{3+} ions, respectively when excited with 244 nm wavelength. The decrease in intensity of both the near-band-edge emission and deep level defects emission at 372 nm and 536 nm respectively while increasing emission of the $^5D_0$ - $^7F_2$ transition at 613 nm was a confirmation of the energy transfer from ZnO to Eu^{3+} ions.

The films were then used to fabricate dye sensitized solar cells where it was used as a bi-functional layer for both transparent light absorption and spectral conversion layer.

ZnO was also implanted with Sm^+ ions where the NBE peak appeared to first increase then suppressed upon implantation of Sm^+ while the blue, green – orange emission intensities were enhanced as a result of increased structural defects with mismatched charge states. Moreover an additional shoulder at 427 nm and peaks at 435 and 544 nm were seen upon ion implantation and were attributed to excitonic energy transfer from the host ZnO to the Sm^+ ions ($^4G_{5/2}$–^6F_J (J = 11/2, 9/2, 7/2, 5/2). The elucidation of the excitation lines due to energy transfer between ZnO and Sm^+ were illustrated using room temperature PL measurements under reduced non radiative effects. The ion implantation fluence was varied and the experimental data was in agreement with the projected range calculated for 80 keV Sm in ZnO using the SRIM simulation – a Monte Carlo simulation based on the binary collision approximation.

8.2. Future work

Although the thin films were tested on perovskites, organic and dye sensitized solar cell, the efficiencies were still low. However these are not the upper limits possible. The efficiencies of the materials studied can be further improved. The used of rare earth doped AZnO can also be explored such that better electrical properties is coupled with better matching spectral absorption window.

Another aspect that requires further investigation is to determine doping mechanisms of polycrystalline ZnO involving (a) deposition of isolated islets on the surface, (b) spread of the dopants on the surface and within grain boundaries, (c) filling of grain boundaries leading to limited diffusion profile, (d) limited bulk transport leading to the formation of a concentration gradient, and (e) homogeneous distribution of the dopants within the film.

The energy transfer was reported from the reduced NBE and point defect emission in ZnO as well the emission lines attributed to the dopant rare earth. However precise energy transfer may be carried out using time-resolved photoluminescence studies. There is also need to study the incident photon-to-current efficiency (IPCE) spectra as a proof of enhancement from spectral conversion.

Appendix

Thermal evaporation process

Thermal evaporation of electrodes for the devices was carried out using thermal evaporator shown in figure 8-1. The chamber was first pumped using a rotary roughing pump then diffusion pump to a pressure of 2×10^{-5} mbar before Au evaporation with a voltage of 80-100 V across the tungsten 'boat' containing Au pellets. The thickness of the films deposited was monitored using quartz crystal monitor before verifying using a surface profilometer and RBS measurements.



Figure S-1: Picture of thermal evaporator during Au thin films deposition in Wits.



Figure S-2: Picture of the FEI Nova Nanolab 600 SEM measurement facility in Wits.